Microfluidics for the Detection of *Cryptosporidium*

Thesis

By: John McGrath
Supervised by: Dr. Helen Bridle

Thesis submitted to the School of Engineering and Physical Sciences (Postgraduate School) in conformity with the requirements for the degree of Doctor of Philosophy.

Institute of Biological Chemistry, Biophysics and Bioengineering (IB3)
Heriot-Watt University
Mountbatten Building
Edinburgh
EH14 4AS

January 2017

Abstract

This thesis details the development of microfluidics for the label-free sorting and/ or identification of waterborne pathogens which are commonly detected in contaminated drinking-water supplies using the United States Environmental Protection Agency method 1623.1 (USEPA 1623.1). This method recovers and detects pathogens of the *Cryptosporidium* and *Giardia* species, which can cause human gastroenteritis upon ingestion. USEPA 1623.1 is employed universally in developed regions (*e.g.*, Europe, North America, Australia, New Zealand).

Specifically, this thesis describes microfluidic systems that were developed with the objective of rapidly discriminating viable (*i.e.*, intact and apparently infectious), human-pathogenic *Cryptosporidium* oocysts from non-viable, human-pathogenic oocysts and/ or species which are considered non-hazardous to human health. Such a system would reduce the overall detection time and allow a more accurate assessment of the risk posed to human health.

A microfluidic setup incorporating dielectrophoresis was designed and employed for the viability-based sorting and enumeration of a human-pathogenic species of *Cryptosporidium*. This device enabled the sorting of untreated (live) and heat-inactivated (non-viable) sub-populations of the human pathogenic *Cryptosporidium parvum* with over 80% efficiency.

Existing Microfluidic Impedance Cytometry (MIC) and Microfluidic-enabled Force Spectroscopy (MeFS) technologies were adapted for the enumeration, detection and viability determination of human-pathogenic *Cryptosporidium* oocysts, plus the discrimination of *Cryptosporidium* species which pose a major risk to human health from those which pose little to no risk. Using MIC, it was possible to discriminate untreated and heat-inactivated *C. parvum* with over 90% certainty. Furthermore, populations of *C. parvum*, *Cryptosporidium muris* (low-risk, human pathogen) and *Giardia lamblia* (also recovered using USEPA 1623.1) were discriminated from one another with over 90% certainty.

Using MeFS, it was possible to differentiate temperature-inactivated (either by freeze- or heat-treatment) *C. parvum* from live *C. parvum* with a minimum of 78% efficiency. Finally, the high-risk, human pathogenic *C. parvum* was discriminated from *C. muris* with over 85% efficiency.

Upon further validation, *i.e.*, the analysis of other *Cryptosporidium* species and of oocysts which have been inactivated by other means (*e.g.*, ozonation, ultraviolet radiaton), it is hoped that water utilities will employ such method(s) to more accurately characterise the human-risk associated with contaminated supplies.

Contents

Chapter 1 – Motivation, Objective and Outline 1

1.1 Motivation 1

1.2 Objectives 3

1.3 Thesis Outline 4

1.4 References 6

Chapter 2 – *Cryptosporidium*: A Waterborne Pathogen 8

2.1 Introduction 8

2.2 Oocyst Properties 11

2.2.1 Oocyst Transmission 11

2.2.2 Oocyst Persistence 12

2.2.3 Oocyst Structure 13

2.3 Cryptosporidiosis 14

2.4 Monitoring for Cryptosporidium 16

2.4.1 Introduction 16

2.4.2 EPA 1622 and 1623.1 16

2.4.3 Species Prevalence 18

2.4.4 Additional Benchtop Molecular Genotyping 19

2.4.5 Alternative Benchtop Molecular Detection Methods 21

2.4.6 Infectivity/ Viability Testing 21

2.5 Summary 22

2.6 References 23

Chapter 3 – Microfluidics 27

3.1 Introduction and Motivation 27

3.2 Principles of Microfluidics 28

3.2.1 Basic Assumptions of Microfluidics 28

3.2.2 Laminar Flow 29

3.2.3 Resistance 31

3.2.4 Diffusion 32

3.2.5 Convection 33

3.2.6 Shear Stress 33

3.2.7 Surface Tension 34

3.3 On Chip Particle Manipulation and Detection 35

3.3.1 Introduction 35

3.3.2 Particle Separation in Continuous Flow 36
3.4 Detection of Cryptosporidium in Microfluidic Systems 39
3.4.1 Introduction.. 39
3.4.2 Discussion of Potential Detection Technologies 40
3.5 Summary 45
3.6 References 46
Chapter 4 – AC Electrokinetics... 51
4.1 Introduction 51
4.2 Theory 51
4.2.1 Dielectric Polarisation.. 51
4.2.2 Complex Permittivity.. 52
4.2.3 Interfacial Polarisation.. 54
4.2.4 Dielectric Relaxation 54
4.2.5 Maxwell’s Mixture Theory.. 56
4.2.6 Shell Model for Biological Particles... 56
4.2.7 The Shell Model for *Cryptosporidium*.. 57
4.3 Dielectrophoresis.. 58
4.3.1 DEP Principle and Theory 58
4.3.2 DEP Devices and Application 60
4.3.4 DEP Analysis of *Cryptosporidium* 62
4.4 Electrorotation 65
4.4.1 ROT Principle... 65
4.4.2 ROT Analysis of *Cryptosporidium*.. 66
4.5 Travelling Wave Dielectrophoresis.. 66
4.6 Electrical Impedance Spectroscopy... 68
4.6.1 EIS Principle 68
4.6.2 EIS Analysis of *Cryptosporidium*.. 70
4.7 Microfluidic Impedance Cytometry 70
4.7.1 Introduction.. 70
4.7.2 MIC Principle 71
4.7.3 MIC Theory 73
4.7.5 Advantages and Applications 74
4.8 Summary 75
4.9 References 76

Chapter 5 – Microfluidic-enabled Force Spectroscopy 80
  5.1 Atomic Force Microscopy 80
    5.1.1 Introduction 80
    5.1.2 Applications of AFM 81
    5.1.3 Force Spectroscopic Analysis of *Cryptosporidium* 82
  5.2 Microfluidics Meets AFM 83
  5.3 Microfluidic-enabled Force Spectroscopy 83
    5.3.1 Introduction 83
    5.3.2 MeFS Principle and Applications 84
    5.3.3 The Role of MeFS in this Research 86
    5.3.4 AFM Cantilever 86
    5.3.5 Deflection Detection 87
    5.3.6 Scanning Mode 87
    5.3.7 MeFS Cantilever 88
    5.3.8 Flow in the Cantilever 89
    5.3.9 Surface Forces 90
    5.3.10 Cantilever Spring Constant 90
    5.3.11 Experimental Spring Constant Calculation 91
    5.3.12 Force Spectroscopy 92
  5.4 Summary 95
  5.5 References 95
Chapter 6 – Methods for Force Spectroscopic Analysis of Waterborne Parasites 100
  6.1 Introduction 100
  6.2 Oocyst Preparation 100
  6.3 Force Spectroscopy 101
  6.4 Data Analysis 102
  6.5 Statistical Analysis 103
  6.6 Summary 105
  6.7 References 106
Chapter 7 – Results of Microfluidic-enabled Force Spectroscopy Analysis 107
  7.1 Introduction 107
  7.2 Single Cell Analysis 108
    7.2.1 Oocyst Selection and Force Measurement 108
    7.2.2 Force-Distance Curves 110

7.2.3 Multiple Measurements per Oocyst ... 111
7.2.4 Kinks in Force-Distance Curves ... 113
7.2.5 Effect of Suction Pressure ... 114
7.3 Batch Analysis ... 115
7.3.1 Inter-species Variation in Deformability and Height ... 115
7.3.2 Height and Deformability of Untreated and Temperature-inactivated *C. parvum* ... 117
7.4 Summary and Outlook ... 121
7.5 Author Contributions ... 122
7.6 References ... 122
Chapter 8 – Methods: Development of DEP Microfluidics ... 125
8.1 Introduction ... 125
8.2 Device Design ... 125
8.2.1 Chip Design ... 125
8.2.2 Baseplate Design ... 128
8.3 Device Fabrication ... 129
8.4 Sample Preparation ... 129
8.5 Experimental Set-Up and Procedure ... 130
8.6 Simulations/ Modelling ... 131
8.7 Data Analysis ... 132
8.8 Excystation Assay ... 133
8.9 Summary ... 134
8.10 References ... 134
Chapter 9 – Dielectrophoretic Analysis of *Cryptosporidium* ... 136
9.1 Introduction ... 136
9.2 Modelling and Theoretical Analysis ... 137
9.2.1 Modelling the Dielectric Response of *Cryptosporidium* ... 137
9.2.2 System Modelling ... 141
9.3 Experimental Results and Discussion ... 144
9.3.1 Critical Voltage ... 144
9.3.2 Focusing of *C. parvum* ... 147
9.3.3 Deflection of Oocysts at the Separation Electrodes ... 150
9.3.4 Mixed Sample Analysis ... 153
9.4 Conclusions and Outlook ... 156

9.5 Author Contributions 157
9.6 References 158
Chapter 10 – Methods: Microfluidic Impedance Cytometry System 160
10.1 Introduction 160
10.2 Chip Overview 160
10.3 Fabrication and Setup 161
10.4 Impedance Measurement 163
10.5 Accounting for Signal Attenuation 165
10.6 Sample Preparation, Introduction and Chip Cleaning 166
10.7 Inactivation of *C. parvum* Oocysts 167
10.8 Excystation Assay 168
10.9 Data Processing and Statistical Analysis 168
10.10 Flow Cytometry 169
10.11 References 169
Chapter 11 – Identification of Waterborne Parasites using Microfluidic Impedance Cytometry 171
11.1 Introduction 171
11.2 Dielectric Behaviour of Biological Cells 173
11.3 Impedance Analysis of Parasites 176
11.4 Frequency-dependent Modelling of Impedance Response 178
11.5 Impedance Analysis of Parasites in PBS 181
11.6 Discrimination of Untreated and Inactivated *C. parvum* 183
11.7 Species Analysis 185
11.8 Conclusion and Outlook 188
11.9 Author Contributions 189
11.10 References 190
Chapter 12 – Conclusions and Future Work 193
12.1 Introduction 193
12.2 Microfluidic-enabled Force Spectroscopy 194
12.3 Dielectrophoresis 195
12.4 Microfluidic Impedance Cytometry 196
12.5 Future Work 196
12.6 References 197
Appendix A – Dielectrophoresis Data Processing .... **Error! Bookmark not defined.**

Chapter 1 – Motivation, Objective and Outline

1.1 Motivation

Cryptosporidium, a protozoan parasite which causes gastroenteritis worldwide [1.1], was identified as a neglected disease by the World Health Organization (WHO) in 2004 [1.2]. Of all outbreaks of waterborne, parasitic protozoan illness that were recorded before 2009, 50.8% were attributed to *Cryptosporidium* and 23.7% were due to the consumption of *Cryptosporidium* contaminated drinking water which had passed through drinking water or distribution systems [1.3]. Although most recorded outbreaks were in North America and Europe, it is estimated that there are between 250-500 million global cases of cryptosporidiosis per annum [1.4]. *Cryptosporidium* is a problematic agent of waterborne illness as it is resistant to normal water treatments like chlorination, infective at extremely low doses and can be very persistent in water [1.1]. There are over 27 species and 60 genotypes of *Cryptosporidium* capable of causing illness in a variety of vertebrate hosts [1.5], making this pathogen a medical concern but also a veterinary concern.

The standard protocol for *Cryptosporidium* detection in drinking water, United States Environmental Protection Agency method 1623.1 (USEPA 1623.1) [1.6], is a highly manual procedure typically involving the processing of 1000 L of water to a 50 µL volume, before specialised microscopy techniques are used for oocyst detection (see Figure 2.2). In the UK, water distributors must test final treated water supplies to ensure that, on average, less than 10 *Cryptosporidium* oocysts are present per 100 L of supply [1.7]. This procedure can take up to three days which increases the risk of human infection and, importantly, the method gives no indication of oocyst viability or species. Consequently, the information obtained from USEPA 1623.1 is often likely to overestimate actual sample infectivity, as only a few of the 27 valid species and over 60 genotypes of *Cryptosporidium* are considered to pose a major risk to human health [1.8]. Furthermore, contaminated supplies are often likely to contain oocysts of mixed viability status [1.9]. For example, contamination events are typically seasonal and incidences of such events increase after severe weather events where, *e.g.*, flooding causes the direct contamination of source waters and ground waters with run-off and/ or sewage discharge [1.10]. In these instances, it is likely that any *Cryptosporidium* oocysts have remained dormant in the aquatic environment for a period of time before access to municipal water supplies became possible and that the average viability of the oocyst population decreased over time [1.11].

Cysts of *Giardia lamblia*, another protozoan parasite which causes human gastroenteritis upon ingestion, are also recovered using USEPA 1623.1 [1.6]. It is not regulatory for UK water utilities to monitor for the presence of *G. lamblia* cysts in treated drinking-water supplies [1.7]. Similarly, treated water in *e.g.* Canada is rarely tested for the presence of this pathogen [1.12], which demonstrates that *G. lamblia* is not considered to pose a similar risk level to *Cryptosporidium* in developed countries. Although this pathogen causes a similar human illness to *C. parvum*, it is generally less resistant to chlorination and removal by filtration and is thus, less commonly present in treated drinking-water. For example, using the typical dimensions of *C. parvum* (4 x 4.5 µm) and *G. lamblia* (8 x 12 µm) [1.12], one can easily approximate that the volume of a *C. parvum* oocyst is ~10% of the volume of a *G. lamblia* cyst, which explains why *Giardia* is less resistant to filtration removal. Therefore, the focus of this research will be directed towards identifying and discriminating human-pathogenic *Cryptosporidium* oocysts from non-human pathogenic/ low risk *Cryptosporidium* oocysts. Nonetheless, given that *Giardia* is recovered simultaneously using the same detection method, I will, where possible, show that *Cryptosporidium* and *Giardia* can be differentiated.

The ability to rapidly detect and discriminate *Cryptosporidium* oocysts based on viability status and/ or species would go beyond the capacity of the current detection method. This would help to more accurately assess the potential risk posed to humans by contaminated drinking water supplies, as sample infectivity would be overestimated less frequently. Consequently, water utilities may save numerous resources where risk mitigation procedures become unnecessary, *i.e.*, where it is rapidly identified that a contamination event is caused by a *Cryptosporidium* species which poses little or no risk to human health. In addition, a more targeted, streamlined and robust risk mitigation framework may then be continually redeveloped using new information as it becomes available.

1.2 Objectives

The aim of this work is to develop a microfluidic system that allows:

- rapid, label-free detection (*e.g.*, without the use of fluorescently-labelled antibodies which are used in the USEPA 1623.1) and enumeration of *Cryptosporidium* oocysts suspended in continuously flowing fluid.
- discrimination of viable (intact, apparently infectious), human-pathogenic *Cryptosporidium* oocysts from their non-viable counterparts
- discrimination of human-pathogenic *Cryptosporidium* oocysts from oocysts of other species of *Cryptosporidium* that pose no/ little risk to human health.

Microfluidics is often described as the intersection of engineering and several scientific disciplines including (but not limited to) physics, chemistry, biochemistry and biotechnology [1.13]. The field typically involves the study of manipulating and controlling fluid volumes within the volume range of microliters (10^{-6} L) to picoliters (10^{-12} L). The small dimensions that are characteristic of these devices enable operators to work at the scale of the typical biological cell and perform single cell analysis [1.14]. Microfluidics have proved to be useful tools for the high performance handling and sorting of cells and particles [1.14]. Thus, such systems offer the ideal platform for the rapid, automated detection of oocysts which are present in *Cryptosporidium*-contaminated drinking water [1.15-1.17].

The ideologies of “lab-on-a-chip” and “micro-total analysis systems”, which are commonly associated with microfluidics, refer to microsystems that perform several, automated processes (*e.g.*, sample transport, separation and detection) on one “chip” or “device”. The utilisation of microfluidics to perform integrated sorting/ discrimination and detection of the said waterborne parasites will be described in the remainder of this research thesis. The specific order in which each aspect will be addressed is described in the thesis outline that follows this section.

1.3 Thesis Outline

The layout of this thesis takes the form of the following outline:

Chapter 1 introduces the motivation of the research project and identifies the main subject areas concerned with the research project - *i.e.*, waterborne protozoa and microfluidics. The main objectives of the research project are also outlined in this chapter.

Chapter 2 uses published literature to identify why *Cryptosporidium* is a problematic agent of waterborne illness worldwide. It discusses the structural properties of *Cryptosporidium* oocysts, parasite transmission, the variety of valid species and the resulting infection – Cryptosporidiosis. This chapter also explains the stages involved in the existing detection method that is used universally by water utilities in developed countries and discusses the limitations of this procedure.

Chapter 3 introduces the field of microfluidics and presents the underlying microfluidic theory. This chapter also explores some of the published uses of microfluidics for cell/ particle sorting and detection. Chapter 3 concludes by identifying AC electrokinetics-based particle sorting techniques and size-based, passive particle sorting techniques as the key approaches to be employed throughout this research.

Chapter 4 explores AC electrokinetic theory and the reported uses of AC electrokinetics for sorting/ detection of cell populations. Specifically, particle manipulation technologies such as dielectrophoresis, electrorotation, travelling wave dielectrophoresis, electrical impedance spectroscopy and microfluidic impedance cytometry are discussed. Where applicable, publications which describe the processing of *Cryptosporidium* oocysts in AC electrokinetic microfluidics are discussed.

Chapter 5 describes microfluidic-enabled force spectroscopy (MeFS) – a recent technological adaptation of conventional atomic force microscopy (AFM) – and the underlying theory. This chapter describes how MeFS has been used previously to characterise the biomechanical properties (*i.e.*, size and/ or deformability) of cells/ particles. Chapter 5 explains that by characterising the biomechanical properties of the, *e.g.*, different *Cryptosporidium* species using MeFS, passive separation microfluidics can subsequently be developed, which utilise the knowledge gained to sort the species, if considerable variation exists between their biomechanical properties.

Chapter 6 describes the methods used to characterise the biomechanical properties of untreated (live) and temperature-inactivated sub-populations of the human-pathogenic *C. parvum* using MeFS. The methods detailed were also used to evaluate the size and deformability properties of different *Cryptosporidium* species, which varied in the level of risk they posed to human health.

Chapter 7 discusses the results attained using the methods given in Chapter 6. Chapter 7 discusses the inter- and intra-species variation in oocyst height and deformability and makes conclusions regarding the suitability of passive microfluidic sorting techniques which utilise deformability or size as a key parameter for sorting *Cryptosporidium* oocysts.

Chapter 8 explains the development of a microfluidic chip which utilises dielectrophoresis (DEP), an AC electrokinetic-based technique, to sort human-pathogenic *Cryptosporidium* oocysts based on their viability status.

Chapter 9 initially uses the literature-reported dielectric properties of *Cryptosporidium parvum* to model the behaviour of this pathogen when suspended in electrolytes of varying electrical conductivity. Using the methods described in Chapter 8, the dielectric properties of *C. parvum* oocysts are then estimated experimentally. Finally, the on-chip sorting of untreated and heat-inactivated *C. parvum* is performed.

Chapter 10 describes the microfluidic impedance cytometry (MIC) setup used to characterise the electrical impedance properties of *Cryptosporidium* oocysts of varying viability status and/ or species.

Chapter 11 details the use of MIC to detect single protozoan (oo)cysts within continuous flow. The biophysical properties of live and temperature-inactivated, human-pathogenic parasites are characterised and sample composition is assessed by analysing the electrical data. The detection of single *C. parvum* and *C. muris* oocysts, as well as *G. lamblia* cysts, is described.

Chapter 12 summarises the main conclusions of this research project and makes recommendations for future work.

1.4 References

1.1. Davies AP, Chalmers RM. Cryptosporidiosis. British Medical Journal. 2009;339.

1.2. World Health Organization. Guidelines for Drinking-water Quality - Third Edition: World Health Organization; 2006.

1.3. Karanis P, Kourenti C, Smith H. Waterborne transmission of protozoan parasites: A worldwide review of outbreaks and lessons learnt. Journal of Water and Health. 2007;5(1):1-38.

1.4. Snelling WJ, Xiao L, Ortega-Pierres G, Lowery CJ, Moore JE, Rao JR, et al. Cryptosporidiosis in developing countries. Journal of Infection in Developing Countries. 2007;1(3):242-56.

1.5. Bouzid M, Hunter PR, Chalmers RM, Tyler KM. Cryptosporidium Pathogenicity and Virulence. Clinical Microbiology Reviews. 2013;26(1):115-34.

1.6. USEPA. Method 1623.1: *Cryptosporidium* and *Giardia* in Water by Filtration/IMS/FA: United States Environmental Protection Agency; 2012.

1.7. Environment and Heritage Service. Guidance for the Monitoring of *Cryptosporidium* in Treated Water Supplies in Northern Ireland. 2003.

1.8. Chalmers RM, Katzer F. Looking for Cryptosporidium: the application of advances in detection and diagnosis. Trends in Parasitology. 2013;29(5):237-51.

1.9. Smith HV, Nichols RAB. Cryptosporidium: Detection in water and food. Experimental Parasitology. 2010;124(1):61-79.

1.10. USEPA. Cryptosporidium: Drinking Water Health Advisory. United States Environmental Protection Agency; 2015.

1.11. Chen F, Huang K, Qin S, Zhao Y, Pan C. Comparison of viability and infectivity of *Cryptosporidium parvum* oocysts stored in potassium dichromate solution and chlorinated tap water. Veterinary parasitology. 2007;150(1):13-7.

1.12. Health Canada. Guidelines for Canadian Drinking Water Quality. Guideline Technical Document. Enteric Protozoa: Giardia and Cryptosporidium. Minister of Health; 2012.

1.13. Tabeling P, Chen S. Introduction to Microfluidics: OUP Oxford; 2005.

1.14. Lenshof A, Laurell T. Continuous separation of cells and particles in microfluidic systems. Chemical Society Reviews. 2010;39(3):1203-17.

1.15. Bridle H, Kersaudy-Kerhoas M, Miller B, Gavriilidou D, Katzer F, Innes EA, et al. Detection of *Cryptosporidium* in miniaturised fluidic devices. water research. 2012;46(6):1641-61.

1.16. Bridle H. Waterborne Pathogens: Detection Methods and Applications: Elsevier Science; 2013.

1.17. Bridle H. Waterborne Pathogens : Detection Methods and Applications. Amsterdam: Elsevier; 2013.

Chapter 2 – *Cryptosporidium*: A Waterborne Pathogen

2.1 Introduction

Despite huge efforts to improve the quality of drinking water supplies worldwide, there are still an estimated 1.9 million deaths annually and over 3000 child mortalities occurring daily, due to the consumption of contaminated drinking water [2.1]. High mortality is not the only issue; waterborne disease is estimated to cause an economic burden of $20m per annum in the United States alone as a result of lost productivity [2.2]. As population densities and the demand for potable water continue to increase globally, it is likely that the spread and incidence of waterborne disease will rise accordingly. Therefore, improvement of drinking water standards and pathogen detection methods would help to reduce or limit the rise in morbidity and mortality rates worldwide, whilst also reducing or limiting the global, economic burden.

Cryptosporidiosis, the waterborne illness which results upon ingestion of an infectious dose of human-pathogenic *Cryptosporidium* oocysts, is considered the second greatest cause of diarrhoea and death in children after rotavirus [2.3]. Globally, the human disease burden for *Cryptosporidium* is estimated at 250-500 million cases per year and in the UK cases of cryptosporidiosis were increased in 2015, when compared to previous years [2.4]. In particular, approximately 300,000 homes in Lancashire, England were left without potable water in 2015 due to a *Cryptosporidium* contamination [2.5].

The genus *Cryptosporidium* is comprised of a group of intracellular parasites that are known to infect a range of vertebrate hosts [2.6]. This genus is contained within the class Coccidia, which in turn belongs within the phylum Apicomplexa, as indicated in Table 2.1. All apicomplexans are parasitic, of which there are over 4800 known species.

Table 2.1 Taxonomic Classification of *Cryptosporidium*

Classification	**Name**
Empire	Eukaryota
Kingdom	Protozoa
Phylum	Apicomplexa
Class	Coccidia
Order	Eucoccidiorida
Family	Cryptosporidiidae
Genus	*Cryptosporidium*

Characterisation of *Cryptosporidium* at species level is more complex as oocysts of several species are very similar in morphology, size and lack differential properties, making them indistinguishable from one another. Generally, *Cryptosporidium* species follow a similar lifecycle [2.7] upon ingestion by a vertebrate host but small variations in lifecycles and in morphology throughout the stages of the lifecycle can serve to determine speciation. For example, *C. baileyi* and *C. parvum* can be differentiated by analysing the schizont types present upon trophozoite division, however it is often impractical to examine infected tissues of host organisms for these variations [2.6].

Taxonomic classification of *Cryptosporidium* species is currently based on several factors including morphological variation, infection site, host preference and molecular methods [2.8, 2.9]. Improving molecular methods have aided the classification of numerous species in recent years. In the period 2008- 2013, 11 new species were given classification [2.10]. To date there are 27 distinct species of *Cryptosporidium* recognised, whilst over 60 other genotypes have been described [Ronald Fayer, USEPA, personal communication, 7th January 2015]. It is estimated that over 150 species of mammals, as well as fish, birds, amphibians and reptiles can be infected by *Cryptosporidium* [2.6]. Of the valid species indicated in Table 2.2, some are known only to infect one major host, whereas others like *C. parvum* and *C. meleagridis* infect several major and minor hosts. Generally, *Cryptosporidium* species that infect one type of vertebrate do not infect another type [2.6].

Table 2.2 Valid *Cryptosporidium* species, classification parameters and human health significance.

Valid Species	**Major Host**	**Minor Host**	**Infection site**	**Oocyst Dimensions (μm)**	**Public Health Significance**
C. andersoni	Cattle, Bactrian Camel	Sheep	Gastric	5.5 x 7.4	Minor
C. baileyi	Poultry	Quail, ostrich, duck	Intestinal	4.6 x 6.2	None
C. bovis	Cattle	Sheep	Intestinal	4.7-5.3 x 4.2-4.8	Minor
C. canis	Dog	Human	Intestinal	4.95 x 4.71	Minor
C. cuniculus	Rabbit, Human	Unknown	Intestinal	5.4 x 5.6	Moderate
C. ducismarci	Tortoise	Unknown	Intestinal	Unknown	None
C. fayeri	Marsupials	Unknown	Intestinal	4.5-5.1 x 3.8-5.0	Minor
C. felis	Cat	Human, cattle	Intestinal	4.5 x 5.0	Moderate
C. fragile	Black-spined toad	Unknown	Gastric	5.5 x 6.2	None
C. galli	Finch, chicken	Unknown	Gastric	8.25 x 6.3	None
C. hominis	Humans	Dugong, sheep	Intestinal	4.5 x 5.5	Major
C. macropodum	Eastern grey kangaroo	Unknown	Unknown	4.5-6.0 x 5.0-6.0	None
C. meleagridis	Turkey, human	Parrot	Intestinal	4.5-4.0 x 4.6-5.2	Moderate
C. molnari	Fish	Unknown	Gastric	4.7 x 4.5	None
C. muris	Rodents	Human, Rock Hyrax, Mountain Goat	Gastric	5.6 x 7.4	Minor
C. parvum	Cattle, livestock, human	Deer, mice, pig	Intestinal	4.5 x 5.5	Major
C. ryanae	Cattle, Bos taurus	Unknown	Unknown	2.94-4.41 x 2.94-3.68	None
C. scopthalmi	Fish	Unknown	Intestinal, Gastric	3.7-5.0 x 3.0-4.7	None
C. scrofarum	Pig	Unknown	Intestinal	Unknown	Minor

C. serpentis	Lizard, snake	Unknown	Gastric	5.6-6.6 x 4.8-5.6	None
C. suis	Pig	Human	Intestinal	4.9-4.4 x 4.0-4.3	Minor
C. tyzerri	Mice	Human	Intestinal	4.2 x 4.6	None
C. ubiquitum	Various mammals	Various mammals	Unknown	4.7 x 5.0	Moderate
C. viatorum	Human	Unknown	Unknown	4.7 x 5.4	Moderate
C. varanii	Lizard	Snake	Gastric, Intestinal	4.2-5.2 x 4.4-5.6	None
C. wrairi	Guinea pig	Unknown	Intestinal	4.9-5.0 x 4.8-5.6	None
C. xiaoi	Sheep	Yak, goat	Intestinal	2.94-4.41 x 2.94-4.41	None

Source: Compiled using data from refs [2.6, 2.8, 2.10-2.12]

2.2 Oocyst Properties

2.2.1 Oocyst Transmission

Cryptosporidium is transmitted in the form of the oocyst *via* the faecal-oral route (Figure 2.1). Oocysts are problematic agents of disease as upon ingestion by a suitable host and completion of the lifecycle, they are ejected in large numbers. It has been reported that experimental lambs eject approximately 10^9 oocysts per day for up to 14 days, whilst humans excrete 10^7 oocysts per gram of faeces [2.12]. If you consider that as little as ten oocysts of *C. parvum* can cause human infection [2.13, 2.14], then the risk associated with consumption of *Cryptosporidium* contaminated water is apparent. Ejected oocysts are capable of surviving in unfavourable environments for sustained durations. Chen *et al*. [2.15] demonstrated that *Cryptosporidium* oocysts can persist in chlorinated tap water at 4°C for up to 16 months.

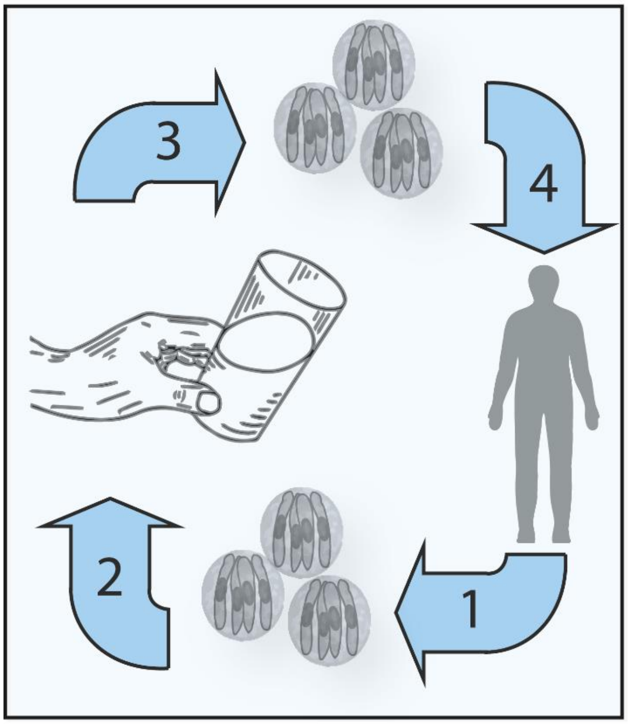

Figure 2.1: Typical Human-Human transmission route for *Cryptosporidium*. Step 1: Thick-walled, sporulated oocysts of *C. parvum* or *C. hominis* are excreted by human. Step 2: Oocysts enter drinking-water or recreational water supplies. Step 3: Oocysts are ingested by host. Step 4: Oocysts evade host immune response and reproduce within the gastrointestinal tract.

2.2.2 Oocyst Persistence

The *Cryptosporidium* oocyst has evolved to resist many natural stresses and manmade chemical disinfectants [2.6]. Additionally, its small dimensions and common presence in large quantities make it difficult to remove using physical, disinfection processes [2.1, 2.6]; numerous outbreaks have been reported in areas where systems incorporated 99.9% efficient filtration systems [2.6]. Combined, these factors make *Cryptosporidium* a global, problematic agent of waterborne infection.

Oocysts of *C. parvum* are most persistent in temperatures between 5 - 15°C but are able to survive at -5°C for at least four weeks and 30°C for two weeks, where they continue to exhibit 100% infectivity in experimental mice [2.6]. Heat treatments above 72.4°C for a minute and ultraviolet light (UV) treatments above 120 mJ cm^{-2} have been shown to render oocysts non-infectious [2.6], however, are not always practised or available universally. Despite this, water utilities throughout the UK (and elsewhere globally) are increasingly installing UV systems at treatment plants in order to improve *Cryptosporidium* disinfection standards, due to recent changes in legislation [Matt Bower, Drinking-Water Quality Regulator for Scotland, Personal communication, 21st June 2016]. C*ryptosporidium* oocysts also exhibit substantial resistance against most commercially available, chemical disinfectants, whilst the concentrations of the alternative, effective chemicals are typically not practical for use out of the laboratory setting [2.6].

2.2.3 Oocyst Structure

The robustness of the *C. parvum* oocyst is largely due to the presence of a multi-layered, outer wall. The outer layer of the wall, which is made of acidic glycoprotein, and the central layer, which consists of glycolipids and lipoproteins, are thought to give rigidity to the oocyst [2.16]. Meanwhile, the inner layer is mainly comprised of filamentous glycoprotein, but consists of outer and inner sections that give strength and flexibility [2.16, 2.17]. For *C. parvum* oocysts, the outer layer is approximately 10 nm in thickness, whereas the central layer is only 2.5 nm in thickness. The innermost layer has an outer section of 11.6 nm thickness and inner section of 25.8 nm thickness [2.6]. Contained within the multi-layered wall are four sporozoites (the infective organisms within the oocyst) and a large residual body – Figure 2.2. Within the residual body are a lipid body, a crystalline protein inclusion, amylopectin granules, ribosomes and cytomembranes [2.6]. The amylopectin granules provide energy reserves for persistence in harsh conditions but also for excystation (*i.e.*, the release of the infective organisms from the protective oocyst) and invasion of host cells [2.18]. Excysted *C. parvum* sporozoites are reported in literature to have typical dimensions of 3.8-5.2 x 0.6-1.2 µm [2.8], which indicates that the large, residual body occupies most of the volume within the oocyst.

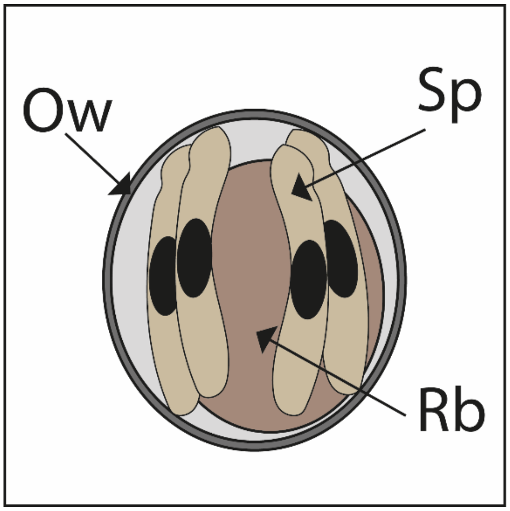

Figure 2.2: Main components of the *C. parvum* oocyst. A protective outer wall (Ow) encysts the parasitic, nuclei-containing sporozoites (Sp) and residual body (Rb).

The oocyst dimensions of different *Cryptosporidium* species (Table 2.2) are often similar, making it difficult to use size as a target for species separation within detection systems. The human-pathogenic *C. parvum* and *C. hominis* species, which pose the greatest risk to human health, are of similar dimensions and so cannot be separated using size-based separation techniques. However, size-based sorting may facilitate the discrimination of *Cryptosporidium* species which pose major or moderate human health significance (*C. hominis*, *C. parvum*, *C. meleagridis*, *C. cuniculus*, *C. felis*, *C. ubiquitum* and *C. viatorum*) from the larger species, *e.g. C. andersoni*, *C. baileyi*, *C. muris*, *C. galli* and smaller species, *e.g. C. ryanae* and *C. xiaoi*, which pose little or no risk to human health. Cysts of the human-pathogenic *Giardia lamblia*, a closely related protozoan pathogen that is simultaneously recovered using USEPA method 1623.1, are typically larger than all *Cryptosporidium spp.* oocysts and are reported in literature as 8 x 12 µm in size [2.19].

2.3 Cryptosporidiosis

Human Cryptosporidiosis is a gastroenteritic disease that results from the reproduction of *Cryptosporidium* at the epithelial cells of the gastrointestinal tract. This disease can infect immunocompetent humans and may be asymptomatic but is of greater danger to children under 2 years, elderly adults and immunocompromised individuals, where illness may manifest extraintestinally, may persist for a longer duration and have increased severity, morbidity and even mortality [2.6, 2.11, 2.20]. Typical symptoms include acute diarrhoea, persistent diarrhoea, stomach cramps, abdominal pain, fatigue, anorexia, vomiting, nausea and fever. The incubation period of illness in immunocompetent people usually ranges between 5 to 7 days and the duration of symptoms ranges from 4 to 14 days. In the case of infected young children, elderly adults and immunocompromised individuals, symptoms may last weeks or months and can result in persistent diarrhoea, weight loss and dehydration [2.6].

Nitazoxanide is licensed in the US and available on a named patient basis in the UK to help relieve the symptoms of cryptosporidiosis [2.20]. However, no treatment exists universally that limits oocyst production in infected hosts [2.6]. For immunocompromised patients, highly active antiviral treatment (HAART) may help to limit symptoms.

2.4 Monitoring for Cryptosporidium

2.4.1 Introduction

When monitoring for the presence of *Cryptosporidium* in drinking water, standard coliform testing is an unreliable indicator [2.6, 2.8, 2.21]. *In vitro* culture techniques are also not easily applicable to parasitic protozoa [2.12], as parasites require a vertebrate host to fulfil their lifecycle and replicate. Consequently, direct detection of oocysts is necessary and, due to the low infectious dose as well as to obtain a representative sample, large quantities of water must be sampled for the detection of *Cryptosporidium* oocysts. The most widely accepted and utilised methods of monitoring for *Cryptosporidium* are the USEPA methods 1622 [2.22] and 1623.1 [2.23]. Method 1622 monitors for *Cryptosporidium* only, whilst method 1623.1 monitors for *Cryptosporidium* and *Giardia* – another protozoan pathogen which is commonly transmitted in water supplies. In the following sections, I will describe the current detection procedures and some optional benchtop techniques that may be used by water utilities to determine the species or viability status of *Cryptosporidium* oocysts.

2.4.2 EPA 1622 and 1623.1

USEPA methods 1622 [2.22] and 1623.1 [2.23] require the filtering of small grab samples (10-50 L; *e.g.*, on site), or large volumes of water (1000 L; *e.g.*, at the treatment works) through specialised filters, which entrap *Cryptosporidium* oocysts with an average efficiency of 42% [2.22, 2.23]. The filter is then eluted and the eluate centrifuged to pellet oocysts (Fig. 2.3). The oocysts are then mixed with magnetic beads that are coated in *Cryptosporidium*-specific antibodies (and *Giardia*- specific for USEPA 1623.1) and separated from other debris by immunomagentic separation (IMS), where a magnet is used to withdraw the bead-oocyst complex to the side of a test tube. The supernatant is then removed by aspiration before oocysts are detached from the beads and stained on well slides with monoclonal antibodies (mAbs) and 4',6-diamidino-2-phenylindole (DAPI) fluorescent stain. The fixed slides are then examined qualitatively using differential interference contrast (DIC) microscopy to detect presence of oocysts, sporozoites and other morphological features but also to enumerate the number of oocysts recovered. This staining and microscopy combination offers advanced detection in comparison to conventional staining and microscopy techniques [2.24]. Methods 1622 and 1623.1 are able to recover *Cryptosporidium* oocysts from water samples, however do not indicate species or viability (*i.e.*, whether an oocyst is intact and appears capable of initiating infection) status [2.22, 2.23].

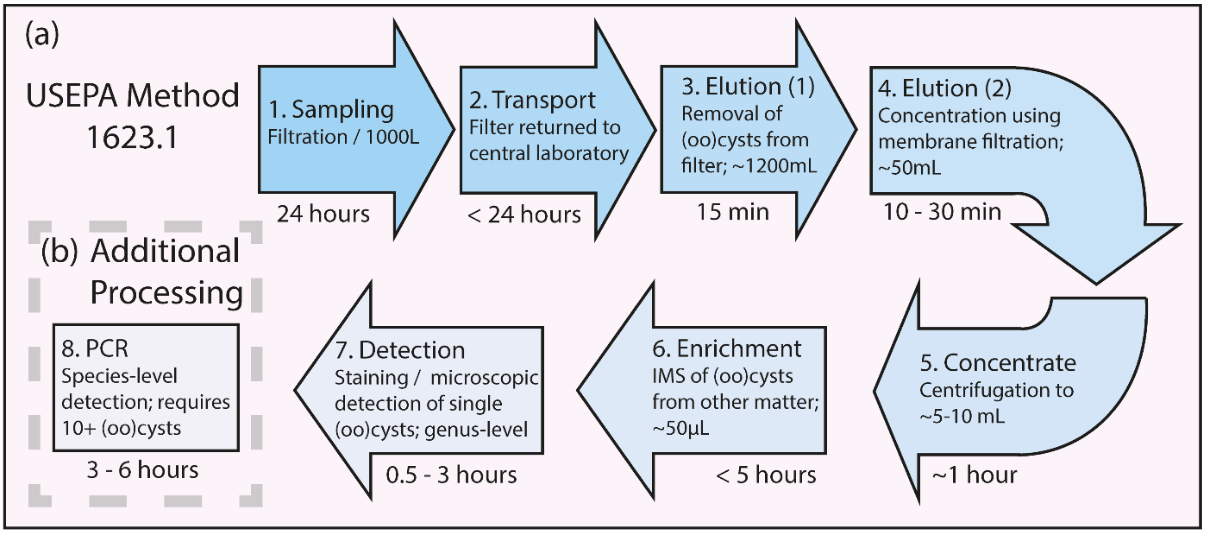

Figure 2.3: USEPA method 1623.1. **(a)** The regulated steps of the conventional detection method detect *Cryptosporidium* and *Giardia* at the genus level. **(b)** Water utilities in Scotland perform (b), a non-regulatory step, when the “alert reporting level” threshold (1 oocyst per 100L treated water) is breached. This additional processing *via* molecular genotyping is used to detect the species of the recovered parasites to identify whether the contaminating species poses a human health risk. Despite this, species-level detection is not practised universally throughout the UK. The whole process can take several days and still provides no information concerning the viability or species of recovered pathogens.

Immunomagnetic separation is useful in removing oocysts from raw solutions that may contain of inhibitors of downstream molecular genotyping [2.6] – IMS increases the sensitivity of the polymerase chain reaction (PCR) up to 1000-fold [2.6]. Moreover, IMS can purify very low numbers of oocysts from samples [2.12]. Purification of *Cryptosporidium* oocysts from water samples relies on the use of IMS beads, coated in mAbs that bind *Cryptosporidium* oocyst wall protein. Most commercially available IMS kits use an immunoglobulin M monoclonal antibody isotype (IgM MAb) which binds outer wall protein in favourable conditions but specificity and efficiency can be affected by factors such as pH and turbidity [2.6]; Dynabeads® (Life Technologies) are an example. Some other kits use an affinity matured IgG mAb isotype, capable of binding oocysts in more adverse conditions but the high affinity and specificity of binding makes dissociation more difficult. Binding of isotypes is species or genotype specific, for example some *Cryptosporidium* species bind isotypes with high affinity due to high density and specificity of epitope, whereas others may bind with low affinity or may not bind at all [2.6]. Dynabeads® is one of the most commonly employed IMS kits and although the affinity of this kit for particular species and genotypes has not been specifically tested, a range of *Cryptosporidium* oocysts have been recovered [Lihua Xiao, Centres for Disease Control and Prevention, personal communication, 24th February 2014]. In 2013, Scottish Water recovered *C. parvum, C. hominis, C. andersonii, C. muris, C. suis and C. ubiquitum* plus Fox, Muskrat 1 and Muskrat 2 genotypes, as well as novel genotypes SW1, SW2 and SW5 using this kit [James Green, Scottish Water, personal communication, 19th February 2014]. More detailed information regarding recoverable species and genotypes can be found in the following references [2.25-2.27].

2.4.3 Species Prevalence

Within the UK, continuous monitoring for the presence of *Cryptosporidium* is a regulatory requirement [2.28]. Water services must inform relevant health authorities immediately when the count exceeds the "alert reporting level" of 1 oocyst in 100L of treated drinking-water. If the count exceeds the "formal notification level" of 10 oocysts per 100L drinking-water then water utilities must also analyse operational procedures, investigate treatment and distribution systems, inspect and resample at the catchment area, and initiate disinfection procedures [2.28, 2.29]. Water utilities may even issue a "boil water" notice in the event of a severe contamination [2.28, 2.29], as occurred in Lancashire, England in 2015 [2.5].

Despite significant efforts in managing watershed and upgrading treatment/ distribution systems, the presence of *Cryptosporidium* is a challenge to the quality of treated water supplies in Scotland [2.11]. For example, during 22 months in the years 2006 – 2007, *Cryptosporidium* was detected in 26% of raw waters and 7% of final waters in Scotland and was detected at least once in 54% of sources. It was recognised that problematic catchment areas were those which were predominantly dry but experienced occasional, high rainfall that flushed oocysts into the supplies. Environmental samples are known to frequently contain a variety of *Cryptosporidium* species of which not all are hazardous to human health and which also portray a mixture in viability status [2.12]. Nichols *et al*. [2.26] documented that the major human-infectious species detected in final waters during this 22-month monitoring period were *C. parvum* (8.7%) and *C. hominis* (2.6%), the moderate human-infectious species were *C. ubiquitum* (15.4%) and the minor/ no risk species were *C. andersonii* (6.0%), *C. muris* (0.3%), *C. bovis* (0.1%) and *C. xiaoi* (< 0.1%). Notably, 19% of oocysts were unidentifiable as individual species/ genotypes and, thus, were categorised as of "mixed species/ genotype". The other oocysts detected, which belonged to valid species, were of no risk to human health, whilst the remainder were of recognised genotypes which are not associated with human Cryptosporidiosis. With only 26.7% of *Cryptosporidium* species detected in Scottish water supplies over a one-year period categorised as major and moderate risk to human health respectively, then it is reasonable to conclude that in many instances sample infectivity is overestimated by existing methods.

2.4.4 Additional Benchtop Molecular Genotyping

Current methods in the UK use staining and microscopy to observe distinguishing features and detect the presence of the genus *Cryptosporidium* [James Green, Scottish Water, personal communication, 9th October, 2013]. In Scotland, if 1 or more oocysts per 100 L water are detected using USEPA 1622 or 1623.1, then molecular methods may be used post-staining and detection to identify the contaminating species of *Cryptosporidium* [James Green, Scottish Water, personal communication, 19th August, 2016]. Species identification is useful for water utilities in water catchment and treatment, as most *Cryptosporidium* species do not pose a risk to human health. This also aids in determination of epidemiology, in case of an outbreak in humans or animals, and serves to provide an indication of likely transmission routes [2.8]. The result of such molecular genotyping can lead to action by the authorities depending on the species detected. However, genotyping is non-regulatory, often takes several hours and does not detect the viability status of recovered oocysts. Furthermore, the method denatures oocysts, meaning that it is no longer possible to perform a viability test.

The most common molecular methods used to realise species-level information are variations of PCR-based sequence amplification, where PCR is conducted and genomic sequences analysed for variation. Perhaps the most documented method is the PCR- restriction fragment length polymorphism (PCR-RFLP) nested analysis [2.30] which employs conventional PCR with specific primers [2.31, 2.32] to amplify extracted oocyst DNA. The primers target the 18s ribosomal ribonucleic acid (rRNA) gene loci and the procedure differentiates between most of the known human and livestock pathogens, plus many other species and genotypes [2.6]. This method has also been applied to amplify other genes including the *Cryptosporidium* outer wall protein gene (*COWP*) and heat shock protein 70 (*HSP70*), but only enabled differentiation between *C. meleagridis*, *C. hominis* and *C. parvum* [2.6].

Directly sequencing amplicons (replicated strands of DNA or RNA) rather than performing restriction digestion as in PCR-RFLP analysis is generally more expensive but can provide improved information that aids in the deciphering of species. Meanwhile, multiplex PCR offers a method of quickly differentiating between *C. hominis* and *C. parvum* oocysts using primers that amplify the dihydrofolate reductase (*DHFR*) gene sequence. This method is quicker and cheaper than PCR-RFLP analysis as no restriction digestion phase is required and amplicons can be run directly on an agarose gel, however this method cannot detect many other species [2.6]. Real-time quantitative PCR (RT-qPCR) technologies use oligonucleotides with attached fluorophores that fluoresce upon complimentary sequencing and amplification [2.33] or fluorescent dyes which emit light upon binding to double-stranded DNA. The light emitted is detectable and is quantified to measure the level of amplification occurring in a PCR cycle. As results are given in real-time, detection time is greatly reduced and the proficiency of the method improves qualitative diagnosis [2.6]. There is currently no standardised RT-qPCR method, but this method will likely be important in future diagnostics.

2.4.5 Alternative Benchtop Molecular Detection Methods

Immunological methods other than the direct immunofluorescent antibody (DFA) method using mAbs, which is incorporated into the USEPA methods described above, have been employed to detect *Cryptosporidium* oocysts. Immunochromatographic (IC) assays [2.34, 2.35] and enzyme-linked immunoassays (ELISA) have been developed with reported high specificity [2.36, 2.37] but again do not confer species or viability status. Immunofluorescent staining-flow cytometry has been described in literature with varying recovery rates but the specificity of currently available antibodies does not allow differentiation of species [2.24]. Fluorescent *in situ* hybridisation (FISH) uses labelled probes to bind specific target regions in DNA or RNA sequences but particularly RNA in the detection of *Cryptosporidium*. As RNA is degraded by RNAses after cell death, it was hypothesised that FISH could provide genus-level identification, plus the detection of whether an oocyst was dead or alive [2.38]. However, Vesey *et al*. [2.38] observed a transition state where oocysts that had recently died were still detectable by FISH as previously transcribed target RNA had not yet been fully degraded by RNAses, reducing the efficiency of the method.

2.4.6 Infectivity/ Viability Testing

At present, there is no known single method, or integration of multiple methods, which enables the simultaneous determination of oocyst viability status and uncovering of species-level information but many standalone infectivity and/ or viability tests exist. The actual infectivity of an oocyst differs from its viability – a viable oocyst can be defined as an oocyst which is apparently structurally intact, undamaged and thus, considered capable of initiating infection in a suitable host upon ingestion [2.39]. However, intact, viable oocysts may not necessarily cause an infection upon ingestion (such oocysts may even still excyst) due to *e.g.* internal oocyst damage or malfunction [2.39] which may not have been visibly apparent using microscopy. Measuring oocyst infectivity typically requires infecting an animal host *in vivo* with an inoculum of oocysts and then observing whether illness results [2.12, 2.39]. Although this type of study is considered the ‘gold standard’ test for oocyst infectivity, this clearly has many limitations, not least the time required before a result can be obtained and the number of oocysts required. An *in vitro* equivalent test is the cell culture (CC) study

[2.39], which basically involves inoculating cultured cell lines with oocysts and then using molecular methods to confirm invasion of the host cells. Both procedures are technically demanding [2.39], therefore, other tests are reported in the literature which either measure oocyst infectivity directly, or instead assess oocyst viability rather than infectivity.

As was outlined in the previous section, FISH can assess oocyst infectivity by labelling potentially infective oocysts [2.38], however this method does not correlate well with the *in vitro* infectivity assay or CC study [2.39]. The vital dye inclusion assay is also often used to assess oocyst viability [2.39]. This method is incorporated within the USEPA 1623.1 procedure [2.23], thus, was described in section 2.4.2 and typically involves assessing whether oocysts become stained by DAPI and/ or propidium iodide. Alternatively, *in vitro* excystation assays are often used to assess oocyst viability [2.40]. There are several variants of the *in vitro* excystation assay [2.39] however, the procedure generally involves subjecting oocysts to *in vitro* conditions which mimic transit through the gastrointestinal tract of vertebrates and subsequently measuring the oocyst excystation rate. Both the vital dye inclusion and *in vitro* excystation assays are rapid and cheap to perform [2.39], however, these tests overestimate actual sample infectivity as not all viable oocysts in a sample can cause infection.

2.5 Summary

Cryptosporidium is a problematic contaminant of water supplies in the UK and the two major risk, human-pathogenic species, plus the moderate risk species *C. ubiquitum*, have been identified as responsible for 26.7% of *Cryptosporidium* contamination events in Scotland using molecular methods. The ability to discriminate between major/ moderate risk pathogens and minor/ no risk pathogens, before enumerating viable, major/ moderate risk oocysts rapidly would reduce detection time, reduce labour demands, simplify the detection process, improve upon the information generated from existing methods and allow provision of safer drinking water. Microfluidic devices operate with very small fluid volumes and can potentially be utilised after the concentration or enrichment stages [2.41] in Figure 2.3, where sample volume becomes manageable, for the label-free detection of viable, human-pathogenic *Cryptosporidium*. This would indicate probable transmission routes and contamination sources, allowing rapid action where required. In addition, since *Giardia* cysts are typically larger than *Cryptosporidium* oocysts, the separation/ discrimination of *Giardia* cysts from *Cryptosporidium* oocysts may also be possible in such a device.

2.6 References

2.1. World Health Organization. Guidelines for Drinking-water Quality - Fourth Edition: World Health Organization; 2011.

2.2. Straub TM, Chandler DP. Towards a unified system for detecting waterborne pathogens. Journal of Microbiological Methods. 2003;53(2):185-97.

2.3. Ryan U, Hijjawi N. New developments in Cryptosporidium research. International journal for parasitology. 2015;45(6):367-73.

2.4. Public Health England. Health Protection Report. London: Public Health England; 2016.

2.5. BBC. Lancashire homes forced to boil water due to cryptosporidium bug. 2015 [Available from: http://www.bbc.co.uk/news/uk-england-lancashire-33816989]. Accessed: 08 October 2016.

2.6. Fayer R, Xiao L. Cryptosporidium and Cryptosporidiosis, Second Edition: Taylor & Francis; 2012.

2.7. Smith HV, Nichols RAB, Grimason AM. Cryptiosporidium excystation and invasion: getting to the guts of the matter. Trends in Parasitology. 2005;21(3):133-42.

2.8. Chalmers RM, Katzer F. Looking for Cryptosporidium: the application of advances in detection and diagnosis. Trends in Parasitology. 2013;29(5):237-51.

2.9. Fayer R. Taxonomy and species delimitation in Cryptosporidium. Experimental Parasitology. 2010;124(1):90-7.

2.10. Šlapeta J. Cryptosporidiosis and Cryptosporidium species in animals and humans: A thirty colour rainbow? International Journal for Parasitology. 2013;43(12–13):957-70.

2.11. Caccio S, Widmer G. Cryptosporidium: Parasite and Disease: Springer London, Limited; 2013.

2.12. Smith HV, Nichols RAB. Cryptosporidium: Detection in water and food. Experimental Parasitology. 2010;124(1):61-79.

2.13. Okhuysen PC, Chappell CL, Crabb JH, Sterling CR, DuPont HL. Virulence of three distinct Cryptosporidium parvum isolates for healthy adults. The Journal Of Infectious Diseases. 1999;180(4):1275-81.

2.14. King BJ, Monis PT. Critical processes affecting Cryptosporidium oocyst survival in the environment. PARASITOLOGY. 2007;134:309-23.

2.15. Chen F, Huang K, Qin S, Zhao Y, Pan C. Comparison of viability and infectivity of *Cryptosporidium parvum* oocysts stored in potassium dichromate solution and chlorinated tap water. Veterinary parasitology. 2007;150(1):13-7.

2.16. Harris JR, Petry F. Cryptosporidium parvum: structural components of the oocyst wall. The Journal of parasitology. 1999:839-49.

2.17. Jenkins MB, Eaglesham BS, Anthony LC, Kachlany SC, Bowman DD, Ghiorse WC. Significance of wall structure, macromolecular composition, and surface polymers to the survival and transport of Cryptosporidium parvum oocysts. Applied and environmental microbiology. 2010;76(6):1926-34.

2.18. Harris J, Adrian M, Petry F. Amylopectin: a major component of the residual body in Cryptosporidium parvum oocysts. Parasitology. 2004;128(3):269-82.

2.19. LeChevallier MW, Norton WD, Lee RG. Occurrence of Giardia and Cryptosporidium spp. in surface water supplies. Applied and Environmental Microbiology. 1991;57(9):2610-6.

2.20. Davies AP, Chalmers RM. Cryptosporidiosis. British Medical Journal. 2009;339.

2.21. Bridle H. Waterborne Pathogens: Detection Methods and Applications: Elsevier Science; 2013.

2.22. USEPA. Method 1622: *Cryptosporidium* in Water by Filtration/IMS/FA. United States Environmental Protection Agency; 2005.

2.23. USEPA. Method 1623.1: C*ryptosporidium* and Gia*rdia in* Water by Filtration/IMS/FA: United States Environmental Protection Agency; 2012.

2.24. Jex AR, Smith HV, Monis PT, Campbell BE, Gasser RB. Cryptosporidium — Biotechnological advances in the detection, diagnosis and analysis of genetic variation. Biotechnology Advances. 2008;26(4):304-17.

2.25. Yang W, Chen P, Villegas EN, Landy RB, Kanetsky C, Cama V, et al. Cryptosporidium source tracking in the Potomac River watershed. Applied and environmental microbiology. 2008;74(21):6495-504.

2.26. Nichols R, Connelly L, Sullivan C, Smith H. Identification of Cryptosporidium species and genotypes in Scottish raw and drinking waters during a one-year monitoring period. Applied and environmental microbiology. 2010;76(17):5977-86.

2.27. Jiang J, Alderisio KA, Xiao L. Distribution of Cryptosporidium genotypes in storm event water samples from three watersheds in New York. Applied and Environmental Microbiology. 2005;71(8):4446-54.

2.28. Scottish Water. Annual Water Quality Report 2013. 2013.

29. Environment and Heritage Service. Guidance for the Monitoring of *Cryptosporidium* in Treated Water Supplies in Northern Ireland. 2003.

2.30. Spano F, Putignani L, McLauchlin J, Casemore DP, Crisanti A. PCR-RFLP analysis of the Cryptosporidium oocyst wall protein (COWP) gene discriminates between C. wrairi and C. parvum, and between C. parvum isolates of human and animal origin. FEMS Microbiology Letters. 1997;150(2):209-17.

2.31. Xiao L, Morgan UM, Limor J, Escalante A, Arrowood M, Shulaw W, et al. Genetic diversity within Cryptosporidium parvum and related Cryptosporidium species. Applied and Environmental Microbiology. 1999;65(8):3386-91.

2.32. Nichols R, Campbell B, Smith H. Identification of Cryptosporidium spp. oocysts in United Kingdom noncarbonated natural mineral waters and drinking waters by using a modified nested PCR-restriction fragment length polymorphism assay. Applied and environmental microbiology. 2003;69(7):4183-9.

2.33. Burnet J, Ogorzaly L, Tissier A, Penny C, Cauchie H. Novel quantitative TaqMan real-time PCR assays for detection of Cryptosporidium at the genus level and genotyping of major human and cattle-infecting species. Journal of applied microbiology. 2013;114(4):1211-22.

2.34. Garcia LS, Shimizu RY. Detection of Giardia lamblia andCryptosporidium parvum Antigens in Human Fecal Specimens Using the ColorPAC Combination Rapid Solid-Phase Qualitative Immunochromatographic Assay. Journal of clinical microbiology. 2000;38(3):1267-8.

2.35. Garcia LS, Shimizu RY, Novak S, Carroll M, Chan F. Commercial assay for detection of Giardia lamblia and Cryptosporidium parvum antigens in human fecal specimens by rapid solid-phase qualitative immunochromatography. Journal of clinical microbiology. 2003;41(1):209-12.

2.36. Woods KM, Nesterenko MV, Upton SJ. Development of a microtitre ELISA to quantify development of Cryptosporidium parvum in vitro. FEMS microbiology letters. 1995;128(1):89-94.

2.37. Ungar B. Enzyme-linked immunoassay for detection of Cryptosporidium antigens in fecal specimens. Journal of clinical microbiology. 1990;28(11):2491-5.

2.38. Vesey G, Ashbolt N, Fricker E, Deere D, Williams K, Veal D, et al. The use of a ribosomal RNA targeted oligonucleotide probe for fluorescent labelling of viable Cryptosporidiumparvum oocysts. Journal of Applied Microbiology. 1998;85(3):429-40.

2.39. Robertson LJ, Gjerde BK. Cryptosporidium oocysts: challenging adversaries? Trends in parasitology. 2007;23(8):344-7.

2.40. Campbell A, Robertson L, Smith H. Viability of Cryptosporidium parvum oocysts: correlation of in vitro excystation with inclusion or exclusion of fluorogenic vital dyes. Applied and Environmental Microbiology. 1992;58(11):3488-93.

2.41. Bridle H, Kersaudy-Kerhoas M, Miller B, Gavriilidou D, Katzer F, Innes EA, et al. Detection of *Cryptosporidium* in miniaturised fluidic devices. water research. 2012;46(6):1641-61.

Chapter 3 – Microfluidics

3.1 Introduction and Motivation

In the 1980s, after the first successful attempts at miniaturisation of electro-mechanical systems were documented, the field of MEMS (Microelectro-mechanical systems) emerged. As the field grew, the range of MEMS applications became more complex, with MEMS also being designed to handle fluids for biological, biomedical and chemical functions. In the 1990s, this diversification naturally gave rise to Microfluidics [3.1]: an interdisciplinary subject constituting the intersection of science and engineering, which is defined as the study of simple or complex, monophasic or multiphasic flows circulating in artificial systems. The small dimensions that are characteristic of microfluidic systems give rise to predictable, low Reynolds number flow regimes which enable users to work at the microscale [3.2] – the scale of a typical biological cell. Consequently, microfluidic technology has since found application in various fields including chemical analysis, biotechnology and medical science [3.3]. Microfluidics has grown into a field of its own.

Another driving force behind the growth of Microfluidics is the synonymous ideologies of "Lab-on-a-chip" and Micro-total analysis systems (μTAS), which refer to the study of microfluidic integration. The development of integrated, microfluidic systems that perform several processes on one chip is estimated to have an economic worth of tens of billions of dollars per annum [3.1]. To be able to transport, mix and process a raw sample before detecting specific, single cells or molecules is the aspiration of many developers within the field [3.1]. With reference to this research project, microfluidics is believed to offer a platform which enables the processing of EPA 1622 and 1623.1 derived water samples to continuously separate and/or discriminate and detect recovered, single *Cryptosporidium* oocysts of differing species and/or viability status. Before exploring the specific microfluidic technologies which were employed to perform such tasks, the underlying theory of microfluidics will be considered.

3.2 Principles of Microfluidics

The typical microfluidic device consists of two layers: the top layer has small microchannels which define path(s) for fluid flow and the bottom layer acts as a seal or cover, enclosing the channels from the macro-environment. The top or bottom layer may then also have access holes, permitting the introduction and exit of fluid from the microchannels *via* tubing (see Figure 3.1).

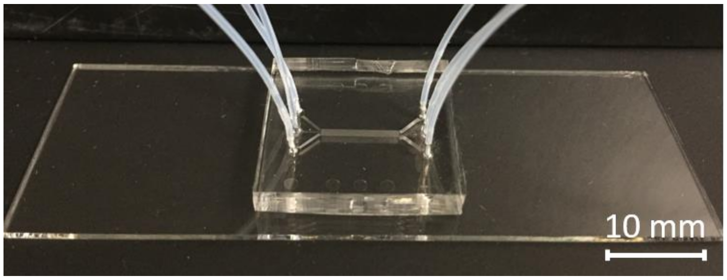

Figure 3.1: A typical microfluidic device. Tubing allows introduction/ exit of fluids to the device which is sealed from the macro-environment. The chip shown is manufactured of polydimethylsiloxane (PDMS), a polymer commonly used in microfabrication, and glass.

The characteristically small channel dimensions of microfluidics give the ideal conditions for manipulation of small fluid volumes and/or cells [3.4]. Many physical phenomena that have a lesser influence on macroscale fluid mechanics begin to increase in prominence at the microscale. Consequently, effects such as laminar flow, diffusion and resistance have a greater impact upon the flow of fluids in microchannels, thus outlining some of the areas to be discussed in the following sections.

3.2.1 Basic Assumptions of Microfluidics

Before discussing the theory of microfluidics, it should be noted that the following four assumptions are commonly applied to microfluidics [3.5] and thus, were applied to this thesis:

1. Continuum assumption: The discrete particles within a fluid are considered to form a continuous medium, which means that quantities such as density, pressure and

velocity are defined to be everywhere in space and to vary continuously between points [3.6]. The experimental work of Karniadakis *et al*. [3.7] demonstrates that the continuum assumption holds for water films as thin as 2 nm. Given that the microfluidic experiments reported in this thesis involved aqueous solutions and geometries considerably larger than 2 nm, it is reasonable to apply this assumption.

2. Newtonian Fluid: For Newtonian fluids, the stress and strain in a fluid are directly proportional and related by a viscosity constant [3.2, 3.8]. This assumption is valid for aqueous solutions and gas in normal lab conditions (*i.e.*, 20 °C, 1 atm).

3. Incompressible fluid: The liquid buffer has constant density and viscosity [3.9]. This assumption holds as long as fluid velocities are less than the speed of sound, which, in terms of microfluidics described in this research, applies.

4. No-slip boundary conditions: At the boundaries of the microchannel, *i.e.* the channel walls, the no-slip condition states that fluid at the wall has zero velocity [3.9]. Thus, at this boundary, particles do not slip along the wall, rather they are fixed to it. This effect can be problematic for very small particles, however for larger particles (*i.e. Cryptosporidium*), they protrude several micrometres from the wall and ‘bounce’ along the sidewall, as the hydrodynamic drag forces them to move with the fluid flow.

3.2.2 Laminar Flow

When dealing with fluids – substances which continually deform under the action of shear stress – the notion of describing their motion through a centre of mass cannot be accepted. Instead, a fluid must be considered as a continuous medium rather than a discrete mass. In doing this, quantities such as fluid density, pressure and velocity are defined to be everywhere in space and to vary continuously between points [3.6]. With this assumption applied, a range of established, theoretical approaches for flow characterisation have been derived and the governing, microscale phenomena recognised. The Navier-Stokes equation for motion of incompressible fluids is:

$$\rho\left(\frac{\partial v}{\partial t} + v\ \cdot \nabla v\right) = -\nabla p + \mu \nabla^2 v \qquad (3.1).$$

In equation 3.1, ρ is the fluid density [kg m^{-3}], v is the fluid velocity [m s^{-1}], t is time [s], p is the pressure [Pa] and μ is the fluid dynamic viscosity [Pa s]. At the microscale, viscous forces greatly exceed inertial forces, which rarely have any effect in microfluidic systems [3.8] and as a result, the non-linear terms on the left side of equation 3.1 can be disregarded, leaving the Stokes equation:

$$\rho\frac{\partial v}{\partial t} = -\nabla p + \mu \nabla^2 v \qquad (3.2).$$

Negligible inertia results in predictable, laminar flow upon fluid introduction. In fluid mechanics, the relationship between many forces is described using dimensionless numbers. A dimensionless number known as the Reynolds number (*Re*) can be derived from equation 3.2 [3.9], which is used to show the ratio of inertial force densities to viscous force densities and is given by:

$$Re = \frac{\rho v D_H}{\mu} \qquad (3.3).$$

In equation 3.3, D_H is the hydraulic diameter of the microchannel [m], which is approximated using:

$$D_H = 2wh/(w + h) \qquad (3.4),$$

where w and h are the width [m] and height [m] of the microchannel [3.10]. The Reynolds number is used to characterise the flow behaviour of fluid, where a value above 2300 is considered turbulent flow and below considered laminar flow. Non-inertial perturbations in flow are still possible at *Re* below 2300 but it is considered that *Re* below 30 guarantees no perturbations. At the microscale fluid flow is almost always laminar [3.11], allowing the design of channel geometries which create predictable flow lanes and facilitate precise control over the mixing of molecules and particles.

If we consider a microchannel with a width of 40 µm and depth of 40 µm as an example, the hydraulic diameter can be calculated as 40 µm. If we set *Re* to the largest acceptable value of 30 and flow water through the device at room temperature, then the flow velocity required through one channel can be calculated:

$$v = \frac{Re \cdot \mu}{\rho \cdot D_H} = \frac{30 \cdot 10^{-3}}{10^3 \cdot 40 \cdot 10^{-6}} = 0.75 \text{ ms}^{-1}.$$

This value, as demonstrated by Beech [3.12], is greatly in excess of the maximum, possible velocity for pressure-driven flow in microchannels of this order using standard equipment, leading us to conclude that Re will be below 30.

When flowing through a microfluidic device in pressure-driven flow, a particle experiences a drag force (F_{drag}) [N] which pulls a particle with the flow:

$$F_{drag} = -6\pi\mu r(v - v_p) \qquad (3.5),$$

where v_p is the particle velocity [m s^{-1}] and r the particle radius [m]. By quantifying particle displacement (dx) over time (dt), v_p can be calculated:

$$v_p = \frac{dx}{dt} \qquad (3.6).$$

3.2.3 Resistance

Resistance (R) [Pa m^{-3} s^{-1}] to the motion of a fluid within a channel increases as channel size decreases, due to an increase in friction between the channel walls and the fluid body [3.2, 3.8, 3.9]. Generally, as channel geometry becomes more complex and the surface-area-to-volume ratio increases, so too does the resistance and this can serve to restrict flow rate (Q) [m^3 s^{-1}]. For pressure-driven flow, the relationship between these properties can be deduced using:

$$Q = \frac{\Delta p}{R} \qquad (3.7),$$

where Δp is the pressure difference [Pa] along the channel. It is apparent that a larger value of R in the denominator would serve to decrease Q.

Resistance is dependent upon channel geometry but within a cylindrical channel can be approximated using:

$$R = \frac{8\mu l}{\pi {c_r}^4} \qquad (3.8).$$

In equation 3.8, the length of the channel is l [m] and c_r is the channel radius [m]. For rectangular microchannels with a high aspect ratio (*i.e.*, where the ratio of channel width and height is > 1), R is given by [3.2]:

$$R = \frac{12\mu l}{wh^3} \tag{3.9}$$

In a rectangular microchannel with low aspect ratio (*i.e.*, < 1), the following approximation can be used to calculate R [3.2]:

$$R = \left(\frac{h^3 w}{12\mu l}\left[1 - 0.63\frac{h}{w}\right]\right)^{-1} \tag{3.10}$$

The resistance of tubing or other macroscopic features which allow flow into and out of a microfluidic system can be neglected, as such fluidics operate at the macroscale, with dimensions several orders of magnitude larger than the typical microfluidic channel.

3.2.4 Diffusion

In the laminar flow regime, where flow perturbation is negligible, two parallel flow streams which are in contact may only mix by diffusion [3.2, 3.8, 3.9]. Diffusion is the movement of molecules from a region of high concentration to a region of low concentration until the concentration is equal throughout the solution. The diffusion or displacement of a molecule can be determined in one dimension using the equation [3.2]:

$$d^2 = 2Dt \tag{3.11}$$

where d is the distance [m] travelled between two points on the *x*-axis, D is the diffusion coefficient [$m^2\,s^{-1}$] and t is the time [s]. A Stokes-Einstein relation can be used to calculate D for spherical particles:

$$D = \frac{kT}{6\pi\mu a} \tag{3.12}$$

Of the terms in the numerator, k is the Boltzmann constant (1.38 x 10^{-23} J K^{-1}) and T is the absolute temperature [K]. For the undefined terms in the denominator, a is the hydrodynamic radius [m] of the particle or molecule.

3.2.5 Convection

In microfluidics, convection relates to the mass transfer that occurs due to the bulk movement of a fluid, *i.e.*, the flow of water causes the transport of suspended molecules. A dimensionless number known as the Peclet number (Pe) is used to give an indication of the ratio of the rates of convection and diffusion of particles and is estimated using the formula:

$$Pe = \frac{vw}{D} \qquad (3.13).$$

When Pe is high, the rate of convection greatly exceeds the rate of diffusion and this limits the mixing of fluids. The Peclet number is typically high in microchannels, from 10 - 10^5, and this coupled with low Re results in long mixing times for fluids, giving greater predictability of fluid flow [3.8].

Cryptosporidium oocysts are approximately 5 µm in diameter, thus, using equation 3.12 have diffusivity of 0.04 $\mu m^2 s^{-1}$, meaning that it would take an oocyst 12.5 seconds to diffuse 1 µm in water at room temperature. However, the utilisation of high flow rates in a low Re regime can serve to increase Pe and thus, minimise any undesired, diffusive effects.

3.2.6 Shear Stress

In a simple microfluidic channel, pressure-driven flow adopts a parabolic flow profile, according to the no-slip boundary condition, meaning that fluid in the centre of the channel is flowing at the greatest velocity but fluid flowing at the walls has zero velocity [3.13]. As such, particles contained within the central section of fluid encounter the greatest stress. The *Cryptosporidium* oocyst wall comprises both rigid and flexible elements and there is suggestion that the oocyst wall is somewhat deformable [3.14] – although the exact extent of such deformability remains underexplored. Red blood cells make to the transition from rigid particles to deformable particles at shear stress values of approximately 0.1 Pa [3.15], therefore it is conceivable that oocysts may deform, *e.g.*, within a complex channel geometry where high pressure is required to induce flow.

It has been reported that when particles encounter objects within a microchannel their orientation changes due to the shear forces present; such that they become orientated in a manner that makes their smallest dimension the critical dimension [3.15]. If oocysts are deformable in such regimes, then the effective size of this dimension may decrease and this could result in reduced device efficiency, *e.g.* in sized-based separation microfluidics if this deformability has not been characterised and/ or considered by the system designer.

3.2.7 Surface Tension

When the pressure, p [Pa], acting on one side of a tensioned surface, exceeds the pressure on the other side, a surface must deform or curve in order to balance the forces acting on each side. If we consider a droplet of liquid water, water molecules always attract one another, which means that the molecules contained within a droplet adapt/ deform the surface until external and internal forces are in equilibrium. Consequently, a surface tension, γ [N m^{-1}], is generated due to cohesion between the water molecules. The Young-Laplace equation describes the balancing of these forces and is given by:

$$\Delta p = \gamma \left(\frac{1}{r_1} + \frac{1}{r_2}\right) \qquad (3.14),$$

where Δp is the pressure difference required to deform the surface and r_1 and r_2 are the radii [m] or curvature in both axes that are parallel to the surface [3.2]. If the surface is spherical and r_1 and r_2 are equal, the relationship can be described by:

$$\Delta p = \frac{2\gamma}{r} \qquad (3.15).$$

Thus, allowing calculation of the pressure contained in a single liquid droplet.

If we consider the opposite scenario, where air enters a fluidic system, the air-water surface tension experienced causes air to form bubbles. This surface tension is relatively strong within microfluidics, meaning that considerable pressure is often required to remove air bubbles. It is therefore desirable to take care to limit the access of air to the fluidics, in order to avoid flow perturbations that may affect device efficiency and sample loss that may be associated with increasing sample flow rate to remove air bubbles.

3.3 On Chip Particle Manipulation and Detection

3.3.1 Introduction

It is imperative that the microfluidic technologies employed in this research project can discriminate between, *e.g.*, viable and non-viable *C. parvum* oocysts in continuous flow microfluidics to reduce the labour requirements and overall detection time of USEPA 1623.1 – should the prospective technology ever be incorporated within the existing detection protocol. To satisfy the research objectives (see section 1.2), a microfluidic device could be developed that firstly sorts the target particles based on a certain parameter(s) before detecting the different populations downstream. Alternatively, a technique could be employed that does not sort particles but instead detects differences in a certain parameter(s) to facilitate discrimination of the suspended populations. In the sections to follow, I will firstly discuss some of the particle separation/ manipulations technologies described in the literature and their suitability to this project. Secondly, a description will be provided of some technologies used by other researchers to detect *Cryptosporidium* in miniaturised devices. The applicability of each particle sorting and/ or detection technology to the scope of this research project will be discussed throughout.

3.3.2 Particle Separation in Continuous Flow

Cell separation and manipulation is an essential step in many biological and medical assays and many researchers are attempting to separate and manipulate biomolecules, cells and organisms from one another within microfluidic devices for use in a wide range of applications [3.3, 3.16-3.18]. There are numerous advantages of microfluidics in comparison to conventional, non-microfluidic, batch separation methods such as filtration, centrifugation, electrophoresis and chromatography. For example, microfluidic devices offer a platform for continuous flow separation and allow potential for quicker sample processing, reduced analysis time, lowered reagent use, fully integrated systems with less human intervention and higher sensitivity and spatial resolution [3.16, 3.19]. Consequently, a variety of microfluidic cell separation techniques have been widely explored and developed [3.3, 3.16, 3.17, 3.20].

Existing separation methods can be categorised as either active or passive, where active methods incorporate an external force and passive methods rely on carefully designed channel geometries and internal forces to separate differing particles [3.21, 3.22]. Parameters such as size, shape, deformability, compressibility and density have been explored in a range of techniques to separate particles within microfluidic systems. The dielectric, magnetic and adhesion properties of particles have also been used to facilitate separation. Some common, active, separation methods include AC electrokinetics-based techniques, acoustophoresis, immunomagnetic separation (IMS) and flow cytometry (Table 3.1). Alternatively, some familiar, passive methods adopted to differentiate between particles are the use of pillars, weirs and objects within microchannels (*e.g.* deterministic lateral displacement) [3.23], adhesion-based methods, pinched-flow fractionation (PFF) and inertial focusing. Microfluidic separation methods have been reviewed extensively by many authors, including Bhagat *et al.* [3.16], Autebert *et al.* [3.22], McGrath *et al*. [3.23] and more recently Sajeesh and Sen [3.17].

Table 3.1 Various separation techniques utilised within microfluidic systems

	Method	Separation mechanism	Separation parameters
Active	Acoustophoresis	Sound waves	Size, compressibility, density
	AC electrokinetics-based techniques	Inhomogeneous or travelling wave electric fields	Size, polarisability
	Electrophoresis	Homogeneous electric field	Size, charge density
	Flow cytometry (FACS)	Electrical charge	Fluorescent markers, forward and side scatter pulse area (FSC-A, SSC-A)
	Immunomagnetic separation	Magnetic field	Size, magnetic attraction
	Optical	Optical force	Size, refractive index, polarisability
Passive	Adhesion-based methods	Specific binding to fixed surface markers	Biochemical complex specificity
	Hydrodynamic filtration	Hydrodynamic force	Size
	Hydrophoretic filtration	Pressure field gradient	Size
	Inertial forces	Shear- and wall- induced lift	Size, shape
	Pillar and weir structures	Laminar flow	Size, deformability
	Pinched-flow fractionation	Hydrodynamic force (Parabolic flow profile)	Size

Source: Table compiled using refs [3.3, 3.16-3.18, 3.20, 3.22]

The microfluidic methods used in this project must reduce the labour demands of the existing USEPA 1623.1 detection method. Therefore, techniques included in Table 3.1 which typically require labelling/ staining of the target particles (*e.g.*, immunomagnetic separation and adhesion-based separation methods) do not satisfy the objectives of this research project. In addition, passive separation methods which typically rely on cell/ particle size or shape as the only separation parameter (*i.e.*, most of the remaining passive separation methods listed in Table 3.1) were similarly considered to be unsuited to the objectives of this research project as standalone techniques. Many researchers have assessed viable and non-viable sub-populations of *C. parvum* in microfluidics [3.24-3.26]. From these works, it is apparent that the size and shape of the *C. parvum* oocyst does not significantly change upon viability loss, meaning it is unlikely that a device which utilises size alone as the key separation parameter can enable the viability-based sorting of *e.g.*, *C. parvum*. Thus, if to be used, such techniques would require integration with another technique which sorts cells/ particles based on a different parameter.

The incorporation of pillar structures in a microchannel to separate cells/ particles based on their size and deformability properties has been described in the literature [3.23, 3.27, 3.28]. This technique, often termed deterministic lateral displacement (DLD) [3.23], could allow *e.g.*, the integrated deformability-based sorting of live and dead *C. parvum*, plus the size-based separation of *Cryptosporidium* species which vary in the level of risk they pose to human health. However, no published data was found in the literature which characterised the deformability and/ or size distributions of these respective pathogen populations. Thus, characterisation of the biomechanical properties of *Cryptosporidium* oocysts of different species and viability status is required before such systems can be reliably developed – this issue will be addressed in Chapters 6 and 7.

Of the remaining approaches listed in Table 3.1, which were not already discussed or discounted for the reasons given in earlier paragraphs (all of which are active sorting methods), many could have been considered applicable to this project. For example, the work of MacDonald *et al.* [3.29] demonstrated the use of optical forces within microfluidics to perform size-based separation of two populations (*e.g.*, imagine the separation of a human-pathogenic and non-human pathogenic *Cryptosporidium* species which differ in size), plus the separation of same-sized silica and polystyrene particles based on their refractive index (*e.g.*, consider the separation of viable and non-viable *C. parvum*). It should be stressed however, that, at present, there is no evidence in the literature to suggest that differences in the refractive indexes of, *e.g.*, viable and non-viable *C. parvum* may facilitate the efficient discrimination of these populations.

Using AC electrokinetics-based techniques like dielectrophoresis and electrorotation (both described in Chapter 4), several researchers have demonstrated that the frequency-dependent dielectric behaviour of viable and non-viable *C. parvum* differs in a range of experimental conditions [3.24, 3.25]. However, these analyses were performed in *e.g.*, batch-mode devices which did not separate the populations from one another in continuously flowing fluid. Consequently, a gap exists in the literature whereby new, novel work could be published showing the continuous sorting of unlabelled, viable and non-viable *C. parvum* based on differences in their dielectric properties.

AC electrokinetics-based approaches can also be used for label-free, size/ volume-based sorting [3.30-3.32] because the resulting electrical forces which act upon suspended particles are typically a function of particle size. Although the AC electrokinetics-based sorting of different *Cryptosporidium* species remains unreported in the literature, *Cryptosporidium* species which vary in size and the level of risk posed to human health could in theory be sorted using such methods. Therefore, AC electrokinetics-based sorting techniques will be used during this research project – the underlying theory and sorting mechanisms of such techniques will be introduced in Chapter 4.

3.4 Detection of Cryptosporidium in Microfluidic Systems

3.4.1 Introduction

In conjunction with the active or passive sorting of, *e.g.*, viable and non-viable *C. parvum*, a method of detecting and, thus, enumerating the separated oocysts must be incorporated downstream within the prospective microfluidic system(s). Perhaps the simplest solution in a microfluidic device which uses a particle sorting technique to focus two particle populations to different, defined flow paths would be to perform downstream microscopic detection. This could be achieved using, *e.g.*, a high-speed camera attachment and/ or standard particle tracking technologies which are readily, commercially available. The major drawback of such techniques is that, with respect to the analysis of *Cryptosporidium*-positive drinking-water samples, label-free microscopic detection would not allow the conclusive exclusion of same-sized particles with *Cryptosporidium*-like appearance that are similarly influenced by the sorting technique [3.26]. In addition, simple microscopic detection cannot conclusively detect the viability status or species of an oocyst. Nonetheless, these techniques could be used during initial validation experiments to provide an indication of the efficiency of the employed particle sorting technique – as described in Chapters 8 and 9 where an AC electrokinetics-based system was developed for the sorting of viable and non-viable *Cryptosporidium* oocysts.

3.4.2 Discussion of Potential Detection Technologies

Possible alternatives to detection using microscopic imaging, which can potentially satisfy the objectives of this research project (section 1.2), are given in Table 3.2. These detection techniques include microfluidic impedance cytometry (MIC) [3.33] and microfluidic Raman spectroscopy-based methods [3.34-3.36], which both have the capability to detect single cells/ particles. Before discussing these technologies, it should be noted that miniaturised molecular detection methods were excluded from Table 3.2 because other authors have already reported the miniaturisation of some benchtop molecular genotyping techniques [3.37, 3.38] and a benchtop immunofluorescent staining protocol [3.39, 3.40] for the detection and/ or viability determination of *Cryptosporidium* oocysts – see section 2.4 for discussion of benchtop detection techniques. Although only the final detection stages the miniaturised molecular detection protocols [3.37, 3.38] were performed on chip (*i.e.*, the there was considerable off-chip sample processing), there is little novelty associated with developing on-chip sample processing methods as several authors have already miniaturised the full PCR procedure [3.41, 3.42]. Alternatively, Taguchi *et al.* [3.39, 3.40] used microfluidics to perform immunofluorescent, genus-level, optical detection of *Cryptosporidium* on chip. In accordance with the objectives of this research project (see section 1.2), it is important that the developed techniques reduce the labour demands of USEPA 1623.1, *i.e.*, such methods should involve less sample processing than the detection procedure of USEPA 1623.1 (section 2.4.2), require minimal user input and be label-free. Thus, the miniaturisation of molecular genotyping protocols or immunofluorescent staining protocols are not considered central to this research.

Table 3.2 Comparison of potential microfluidic single-cell detection/ discrimination technologies.

Technology	Ability to determine oocyst viability	Ability to determine oocyst species	Continuous detection	Typical flow velocity	Sample processing stages involved
Microfluidic Raman spectroscopy-based methods	Yes [3.50]	Yes [3.50]	Has been demonstrated for other cell/ particle types [3.35, 3.36, 3.51]	< 400 µm s^{-1} [3.35, 3.36, 3.52]	Sample purification, sample labelling
Microfluidic impedance cytometry	Yes [3.53]	Unknown	Has been demonstrated for other cell/ particle types [3.54-3.57]	Up to 90 cm s^{-1} [3.57-3.59, Chapter 10]	Adjustment of sample conductivity

Note: brackets indicate source.

Other miniaturised detection technologies like fibre optic-based sensing [3.43, 3.44], surface plasmon resonance [3.45-3.47], mass-based detection techniques [3.48, 3.49] and microfluidic trapping combined with immunofluorescence detection [3.40], which have been used previously for the detection of *Cryptosporidium*, were considered incompatible with the objectives of this research. The reasons for excluding such methods from Table 3.2 included the view that a given technology could not uncover the viability status of oocysts and provide species-level information, or that a given technology required the use of *e.g.*, immunofluorescent labels – see a recent review article by Bridle *et al.* [3.26] which discusses the advantages and disadvantages of each excluded method.

Conventional microfluidic Raman and MIC detection technologies measure a certain parameter(s) (*e.g.*, Raman light scattering properties or electrical impedance properties of a cell/ particle) to discriminate (but not sort) single cells/ particles of different populations. In their conventional form, such technologies are of limited use if a user wishes to purify different cell types or perform further, post-separation analysis of the respective populations. However, if the user seeks only to characterise the properties of single cells within a suspension to make inference regarding the different populations which constitute a sample (*e.g.*, to identify and enumerate viable human-pathogenic *Cryptosporidium* oocysts), then such technologies are useful.

3.4.2.1 Raman Spectroscopy

Raman spectroscopy is a form of spectroscopy which uses incident monochromatic light to excite molecules into a vibrational state [3.26, 3.34, 3.35, 3.51]. Laser light is directed towards the sample (Figure 3.2) at a frequency which causes the molecules to vibrate (typically within the visible, near infrared or near ultraviolet ranges). Scattered light from the illuminated sample is then collected through a lens and sent through a monochromator. The majority of the scattered light is of similar frequency to the light source and is filtered out (using *e.g.* a notch filter), such that any inelastically scattered light can be detected. Inelastically scattered light is shifted in energy from the laser frequency due to interactions between the incident light and the vibrational energy levels of the molecules in the sample. However, different molecules enter this vibrational state at different light wavelengths depending on *e.g.*, their biochemical composition. Consequently, different cells tend to have a unique molecular vibrational frequency spectra, often termed a “Raman fingerprint” [3.26, 3.34, 3.35, 3.51]. Thus, Raman Spectroscopy can be used to detect different cell populations.

With respect to the detection of *Cryptosporidium*, the use of a technique known as surface enhanced resonance Raman spectroscopy (SERRS) to detect and discriminate viable and heat-inactivated (non-viable) *C. parvum* was reported in 2003 [3.50]. The same author also described the detection of three different *Cryptosporidium* species (*C. parvum*, *C. meleagridis*, *C. hominis*), plus the discrimination of 1-3 month-old *C. parvum* oocysts from 12 month-old oocysts [3.50]. SERRS is a label-free technology, thus, the Raman signal is relatively weak in comparison to other forms of Raman detection that use “Raman labels” [3.26] – nanogold particles conjugated with antibodies and dye molecules which enhance the Raman signal. This means that it reportedly takes 15-20 minutes, depending on the range of wavelengths used, to measure a single, immobilised (*i.e.*, the oocyst is anchored to a surface) oocyst [3.26]. The method used by Grow *et al*. [3.50] however, was not a continuous-flow microfluidic detection technology. The time required to detect one oocyst perhaps explains why water utilities have not, to date, incorporated SERRS within their *Cryptosporidium* detection protocols.

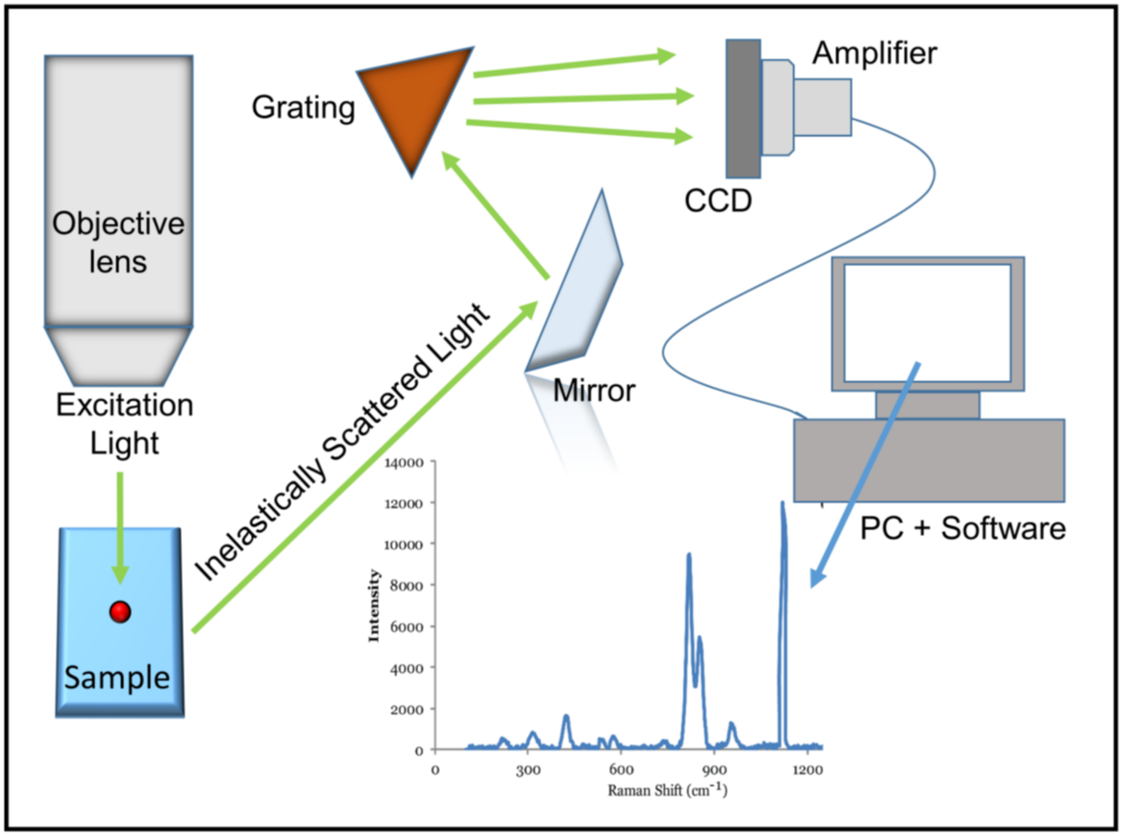

Figure 3.2: Diagram showing process of collecting a Raman signal. Monochromatic excitation light is directed upon a cell in sample at a wavelength which causes the molecules of the cell to vibrate. The inelastically scattered photons released by molecules upon excitation are detected by a detector such as a charge couple device (CCD). The Raman spectra of the sample is then processed and visualised using computer software.

A newer adaptation of Raman technology called coherent anti-Stokes Raman spectroscopy (CARS) can measure the Raman spectra of a single *Cryptosporidium* oocyst in a matter of seconds [3.60, 3.61]. One of the main reasons that CARS enables such rapid data acquisition is because target particles are firstly coated in a mixture containing “Raman labels”. Using CARS, Murugkar *et al.* [3.60, 3.61] have detected single *Cryptosporidium* oocysts to the genus level, but the discrimination of viable and non-viable sub-populations of one species, or the discrimination of different species was not demonstrated. The results of the SERRS-based *Cryptosporidium* analyses discussed previously do suggest however, that CARS can potentially be used for the viability and species detection of *Cryptosporidium* oocysts. Despite this, the CARS method used by Murugkar *et al.* [3.60, 3.61] cannot be considered a microfluidic technique etiher, rather a miniaturised detection technique, since oocysts were optically detected in a small liquid sample volume that was deposited on a microscope slide.

Many authors have reported the development of continuous-flow microfluidic Raman detection systems, which do not necessarily use the SERRS method, but which use physical traps or active, particle manipulation techniques (Table 3.1) to immobilise particles and thus, obtain a Raman signal [3.34, 3.35, 3.51, 3.62]. Clearly, the flow rate and particle immobilisation/ manipulation method(s) must be a critical consideration in such systems [3.35]. Raman detection techniques are also extremely sensitive to the presence of other cellular/ particulate matter which can bind to the target particle and influence the Raman signal, therefore, comprehensive sample filtering is often required [3.35]. Recently, label-free Raman-activated cell sorting (RACS) technology has been described in the literature [3.36, 3.52]. In principle, RACS devices operate like a fluorescence-activated cell sorter (FACS; see Table 3.1) system but the sorting parameter(s) differ and much slower flow rates are required, *e.g.*, the system of Zhang *et al.* [3.36] operates at a flow rate of 3 μL hr^{-1}. Interestingly, Zhang *et al.* [3.36] used AC electrokinetic-based particle manipulation techniques to trap particles for Raman measurement, before again using AC electrokinetics to sort particles based on their Raman spectra.

In the future, microfluidic Raman-based detection techniques will likely be very useful for environmental monitoring purposes. At present, due to the need for comprehensive sample filtering, sensitivity to interfering substances, integration of several microfluidic particle manipulation techniques and very low flow rates, it was deemed unlikely that microfluidic Raman-based methods could reduce the detection time and labour requirements of the existing EPA 1623.1 method.

3.4.2.2 Microfluidic Impedance Cytometry

In comparison to Raman spectroscopy, MIC is a technology which characterises the electrical properties (*e.g.*, membrane capacitance or cytoplasm resistance) of up to 1000 single cells/ particles per second when suspended in continuous flow [3.33] – see Table 3.2 for comparison of MIC and microfluidic-based Raman detection technologies. MIC is a label-free technology and has been used previously to discriminate between the different leukocyte populations within human blood [3.54], between different stem cell types [3.56] and to detect the viability of circulating tumour cells [3.57]. In such works, the respective populations were discriminated based on variations between their frequency-dependent, complex electrical impedance responses when suspended in an electrically conductive medium.

The use of MIC – a technological advancement of electrical impedance spectroscopy (EIS) – in the detection of *Cryptosporidium* has not been reported. EIS has however been used by Houssin *et al.* [3.53] to detect differences in the dielectric properties of viable and non-viable *C. parvum* populations (not single oocysts). Thus, I believe that there is a gap in the literature and an opportunity to publish novel material regarding the electrical impedance-based discrimination of *e.g.*, different *Cryptosporidium* species and viable/ non-viable sub-populations of a human-pathogenic species. Therefore, MIC and not Raman technology will be utilised for the detection of waterborne protozoa (Chapters 10 and 11) in this research project – MIC will be described in more depth in Chapter 4, after the underlying dielectric theory has been described.

3.5 Summary

In Chapter 3, the basic theory of microfluidics was introduced before many cell manipulation and/ or detection techniques were described. The low Reynolds number regimes and predictable flows of microfluidics offers the ideal platform for satisfying the objectives outlined in Chapter 1 of this thesis. Active, AC electrokinetics-based sorting techniques and passive, combined size/ deformability-based methods were highlighted as the key, label-free sorting approaches concerned with this research project. Furthermore, microfluidic impedance cytometry – an AC electrokinetics-based detection technology – was identified as the cell/ particle discrimination technology to be employed in this project. The specific mechanisms by which these approaches may facilitate the viability determination and species-level discrimination of *Cryptosporidium* oocysts will be described in the chapters to follow.

3.6 References

3.1. Tabeling P, Chen S. Introduction to Microfluidics: OUP Oxford; 2005.

3.2. Beebe DJ, Mensing GA, Walker GM. Physics and applications of microfluidics in biology. Annual Review of Biomedical Engineering. 2002;4:261-86.

3.3. Lenshof A, Laurell T. Continuous separation of cells and particles in microfluidic systems. Chemical Society Reviews. 2010;39(3):1203-17.

3.4. Jackson EL, Lu H. Advances in microfluidic cell separation and manipulation. Current Opinion in Chemical Engineering. 2013;2(4):398-404.

3.5. Ho CM. Micro/Nano Technology Systems for Biomedical Applications: Microfluidics, Optics, and Surface Chemistry: OUP Oxford; 2010.

3.6. Nguyen NT, Wereley ST. Fundamentals and Applications of Microfluidics: Artech House; 2002.

3.7. Karniadakis GE, Beskok A, Aluru N. Microflows and Nanoflows: Fundamentals and Simulation: Springer New York; 2006.

3.8. Squires TM, Quake SR. Microfluidics: Fluid physics at the nanoliter scale. Reviews of Modern Physics. 2005;77(3):977-1026.

3.9. Stone HA, Stroock AD, Ajdari A. Engineering flows in small devices: Microfluidics toward a lab-on-a-chip. Annual Review of Fluid Mechanics. 2004;36:381-411.

3.10. Hawkes JJ, Barber RW, Emerson DR, Coakley WT. Continuous cell washing and mixing driven by an ultrasound standing wave within a microfluidic channel. Lab on a Chip. 2004;4(5):446-52.

3.11. White FM. Viscous Fluid Flow: McGraw-Hill Higher Education; 2006.

3.12. Beech JP. Elastic Deterministic Lateral Displacement Devices. Sweden: Lund University; 2005.

3.13. Lauga E, Brenner MP, Stone HA. Microfluidics: the no-slip boundary condition. Experimental Fluid Mechanics: Springer; 2007.

3.14. Smith HV, Nichols RAB, Grimason AM. Cryptiosporidium excystation and invasion: getting to the guts of the matter. Trends in Parasitology. 2005;21(3):133-42.

3.15. Beech JP. Microfluidics Separation and Analysis of Biological Particles. Sweden: Lund University; 2011.

3.16. Bhagat AAS, Bow H, Hou HW, Tan SJ, Han J, Lim CT. Microfluidics for cell separation. Medical & biological engineering & computing. 2010;48(10):999-1014.

3.17. Sajeesh P, Sen AK. Particle separation and sorting in microfluidic devices: a review. Microfluidics and nanofluidics. 2014;17(1):1-52.

3.18. Shields IV CW, Reyes CD, López GP. Microfluidic cell sorting: a review of the advances in the separation of cells from debulking to rare cell isolation. Lab on a Chip. 2015;15(5):1230-49.

3.19. Pamme N. Continuous flow separations in microfluidic devices. Lab on a Chip. 2007;7(12):1644-59.

3.20. Kersaudy-Kerhoas M, Dhariwal R, Desmulliez M. Recent advances in microparticle continuous separation. IET Nanobiotechnology. 2008;2(1):1-13.

3.21. Bhagat AAS, Bow H, Hou HW, Tan SJ, Han J, Lim CT. Microfluidics for cell separation. Medical & biological engineering & computing. 2010;48(10):999-1014.

3.22. Autebert J, Coudert B, Bidard F-C, Pierga J-Y, Descroix S, Malaquin L, et al. Microfluidic: An innovative tool for efficient cell sorting. Methods. 2012.

3.23. McGrath J, Jimenez M, Bridle H. Deterministic lateral displacement for particle separation: a review. Lab on a Chip. 2014;14(21):4139-58.

3.24. Goater AD, Burt JP, Pethig R. A combined travelling wave dielectrophoresis and electrorotation device: applied to the concentration and viability determination of Cryptosporidium. Journal of Physics D-Applied Physics. 1997;30(18):L65.

3.25. Su Y-H, Tsegaye M, Varhue W, Liao K-T, Abebe LS, Smith JA, et al. Quantitative dielectrophoretic tracking for characterization and separation of persistent subpopulations of Cryptosporidium parvum. Analyst. 2014;139(1):66-73.

3.26. Bridle H, Kersaudy-Kerhoas M, Miller B, Gavriilidou D, Katzer F, Innes EA, et al. Detection of *Cryptosporidium* in miniaturised fluidic devices. water research. 2012;46(6):1641-61.

3.27. Adolfsson K. Deformability-based separation of erythrocytes with deterministic lateral displacement. Master's Thesis, Department of Solid State Physics, Lund Institute of Technology; 2011.

3.28. Beech JP, Holm SH, Adolfsson K, Tegenfeldt JO. Sorting cells by size, shape and deformability. Lab on a Chip. 2012;12(6):1048-51.

3.29. MacDonald M, Spalding G, Dholakia K. Microfluidic sorting in an optical lattice. Nature. 2003;426(6965):421-4.

3.30. Jones TB. Basic theory of dielectrophoresis and electrorotation. Engineering in Medicine and Biology Magazine, IEEE. 2003;22(6):33-42.

3.31. Pethig R. Review Article—Dielectrophoresis: Status of the theory, technology, and applications. Biomicrofluidics. 2010;4:022811.

3.32. Morgan H, Green NG. AC Electrokinetics: Colloids and Nanoparticles: Research Studies Press; 2003.

3.33. Sun T, Morgan H. Single-cell microfluidic impedance cytometry: a review. Microfluidics and Nanofluidics. 2010;8(4):423-43.

3.34. Chen L, Choo J. Recent advances in surface-enhanced Raman scattering detection technology for microfluidic chips. Electrophoresis. 2008;29(9):1815-28.

3.35. Chrimes AF, Khoshmanesh K, Stoddart PR, Mitchell A, Kalantar-zadeh K. Microfluidics and Raman microscopy: current applications and future challenges. Chemical Society Reviews. 2013;42(13):5880-906.

3.36. Zhang P, Ren L, Zhang X, Shan Y, Wang Y, Ji Y, et al. Raman-activated cell sorting based on dielectrophoretic single-cell trap and release. Analytical chemistry. 2015;87(4):2282-9.

3.37. Richmond KE, Li M-H, Rodesch MJ, Patel M, Lowe AM, Kim C, et al. Amplification and assembly of chip-eluted DNA (AACED): a method for high-throughput gene synthesis. Nucleic Acids Research. 2004;32(17):5011-8.

3.38. Nugen SR, Asiello PJ, Connelly JT, Baeumner AJ. PMMA biosensor for nucleic acids with integrated mixer and electrochemical detection. Biosensors and Bioelectronics. 2009;24(8):2428-33.

3.39. Taguchi T, Takeyama H, Matsunaga T. Immuno-capture of Cryptosporidium parvum using micro-well array. Biosensors and Bioelectronics. 2005;20(11):2276-82.

3.40. Taguchi T, Arakaki A, Takeyama H, Haraguchi S, Yoshino M, Kaneko M, et al. Detection of Cryptosporidium parvum oocysts using a microfluidic device equipped with the SUS micromesh and FITC-labeled antibody. Biotechnology and bioengineering. 2007;96(2):272-80.

3.41. Zhang C, Xu J, Ma W, Zheng W. PCR microfluidic devices for DNA amplification. Biotechnology Advances. 2006;24(3):243-84.

3.42. Jiang X, Jing W, Zheng L, Liu S, Wu W, Sui G. A continuous-flow high-throughput microfluidic device for airborne bacteria PCR detection. Lab on a Chip. 2014;14(4):671-6.

3.43. Kramer MF, Vesey G, Look NL, Herbert BR, Simpson-Stroot JM, Lim DV. Development of a Cryptosporidium oocyst assay using an automated fiber optic-based biosensor. Journal of biological engineering. 2007;1(1):1.

3.44. Wang X-D, Wolfbeis OS. Fiber-optic chemical sensors and biosensors (2008–2012). Analytical chemistry. 2012;85(2):487-508.

3.45. Kang CD, Lee SW, Park TH, Sim SJ. Performance enhancement of real-time detection of protozoan parasite, Cryptosporidium oocyst by a modified surface plasmon resonance (SPR) biosensor. Enzyme and microbial technology. 2006;39(3):387-90.

3.46. Kang CD, Cao C, Lee J, Choi IS, Kim BW, Sim SJ. Surface plasmon resonance-based inhibition assay for real-time detection of Cryptosporidium parvum oocyst. Water research. 2008;42(6):1693-9.

3.47. Homola J. Surface plasmon resonance sensors for detection of chemical and biological species. Chemical reviews. 2008;108(2):462-93.

3.48. Poitras C, Fatisson J, Tufenkji N. Real-time microgravimetric quantification of Cryptosporidium parvum in the presence of potential interferents. water research. 2009;43(10):2631-8.

3.49. Dixon MC. Quartz crystal microbalance with dissipation monitoring: enabling real-time characterization of biological materials and their interactions. Journal of biomolecular techniques: JBT. 2008;19(3):151.

3.50. Grow AE, Wood LL, Claycomb JL, Thompson PA. New biochip technology for label-free detection of pathogens and their toxins. Journal of Microbiological Methods. 2003;53(2):221-33.

3.51. Lim C, Hong J, Chung BG, Choo J. Optofluidic platforms based on surface-enhanced Raman scattering. Analyst. 2010;135(5):837-44.

3.52. Lau AY, Lee LP, Chan JW. An integrated optofluidic platform for Raman-activated cell sorting. Lab on a Chip. 2008;8(7):1116-20.

3.53. Houssin T, Follet J, Follet A, Dei-Cas E, Senez V. Label-free analysis of water-polluting parasite by electrochemical impedance spectroscopy. Biosensors and bioelectronics. 2010;25(5):1122-9.

3.54. Holmes D, Pettigrew D, Reccius CH, Gwyer JD, van Berkel C, Holloway J, et al. Leukocyte analysis and differentiation using high speed microfluidic single cell impedance cytometry. Lab on a Chip. 2009;9(20):2881-9.

3.55. Holmes D, Morgan H. Single cell impedance cytometry for identification and counting of CD4 T-cells in human blood using impedance labels. Analytical chemistry. 2010;82(4):1455-61.

3.56. Song H, Wang Y, Rosano JM, Prabhakarpandian B, Garson C, Pant K, et al. A microfluidic impedance flow cytometer for identification of differentiation state of stem cells. Lab on a Chip. 2013;13(12):2300-10.

3.57. Spencer D, Hollis V, Morgan H. Microfluidic impedance cytometry of tumour cells in blood. Biomicrofluidics. 2014;8(6):064124.

3.58. Spencer D, Morgan H. Positional dependence of particles in microfludic impedance cytometry. Lab on a Chip. 2011;11(7):1234-9.

3.59. Spencer D, Elliott G, Morgan H. A sheath-less combined optical and impedance micro-cytometer. Lab on a Chip. 2014;14(16):3064-73.

3.60. Murugkar S, Carrasco S, Evans C, Xie XS, Anis H, editors. Rapid detection of cryptosporidium parvum oocysts using coherent anti-Stokes Raman scattering (CARS) microscopy. Conference on Lasers and Electro-Optics; 2007: Optical Society of America.

3.61. Murugkar S, Evans CL, Xie XS, Anis H. Chemically specific imaging of cryptosporidium oocysts using coherent anti-Stokes Raman scattering (CARS) microscopy. Journal of microscopy. 2009;233(2):244-50.

3.62. Wang H-W, Bao N, Le TT, Lu C, Cheng J-X. Microfluidic CARS cytometry. Optics express. 2008;16(8):5782-9.

Chapter 4 – AC Electrokinetics

4.1 Introduction

The term alternating current (AC) electrokinetics is widely used to describe the study of particle behaviour whilst suspended in fluid and subjected to an AC electric field – *i.e.*, the study of electrically induced, particle motion and/ or rotation when an AC field causes electrical forces to act on both suspended particles and fluid. Typically, AC current periodically reverses in direction and the most common waveform used is the sine wave. Some of the earliest uses of AC electrokinetics include the demonstration of the existence of a cell membrane by Hoeber at the beginning of 20th century, or the calculation of the capacitance and thickness of a canine red blood cell (RBC) by Fricke in 1924 [4.1]. Generally, in a non-uniform, AC electric field a polarisable particle will undergo induced movement, whereas, in a rotating electric field a polarisable particle will be subjected to a rotating torque [4.2] – these are the foundations of label-free and non-invasive, AC electrokinetic separation/manipulation methods like dielectrophoresis [4.1-4.4], electrorotation [4.1, 4.2, 4.4, 4.5] and travelling wave dielectrophoresis [4.2, 4.5]. These cell manipulation technologies are the predecessors of electrical impedance-based cell detection technologies which were described in the literature more recently [4.1, 4.6]. Before discussing such techniques, the underlying AC electrokinetic theory will firstly be considered.

4.2 Theory

4.2.1 Dielectric Polarisation

When employing AC electrokinetics to analyse or manipulate particles, such particles are considered as dielectric materials (often just termed a “dielectric”), which are typically insulating materials or poor conductors of electricity. When an AC field is applied to *e.g.* an electrical insulator, electric charges (or current) do not flow through the material freely as they do in an ideal conductor because they have no loosely bound/ free electrons (or charges) that may drift through the material. Instead, charges slightly shift their average equilibrium positions. For instance, if a particle is more polarisable than the suspending medium, positive charges will be slightly displaced towards the regions of high field and intensity and negative charges will be displaced slightly in the opposite direction. Consequently, the charges form induced dipoles which align in parallel to the applied electric field and the material becomes polarised. The term dipole is used in AC electrokinetics to describe two equal, attracting charges of opposing sign which become separated by a (usually small) distance due to the application of an AC field. An induced dipole leads to the creation of a vector, termed a dipole moment, from the negative towards the positive charge. In a dielectric, the average dipole moment, $\mathbf{p}_{av}$ [C m], in each constituent molecule is proportional to the magnitude of the applied electric field [4.2]:

$$\mathbf{p}_{av} = \alpha \mathbf{E}' \qquad (4.1),$$

where $\mathbf{E}'$ is the local electric field [N C^{-1}] in the dipole's vicinity and α the polarisability, representing the response of the dielectric to an AC field (*i.e.*, the average dipole moment per unit field strength – units: C m^{2} V^{-1}).

4.2.2 Complex Permittivity

To understand the process of dielectric polarisation, the example of a parallel plate capacitor can be considered. If we place a conductor between two parallel plates (Figure 4.1), which are separated by distance d [m], then the impedance, Z [Ω], of the material (*i.e.*, the opposition to current flow by a material) is given by [4.1, 4.2]:

$$Z = \frac{d}{A\sigma} \qquad (4.2),$$

where A is the area [m^{2}] of the plate and σ the material's conductivity [S m^{-1}], which is related to the amount of unbound charges in the material.

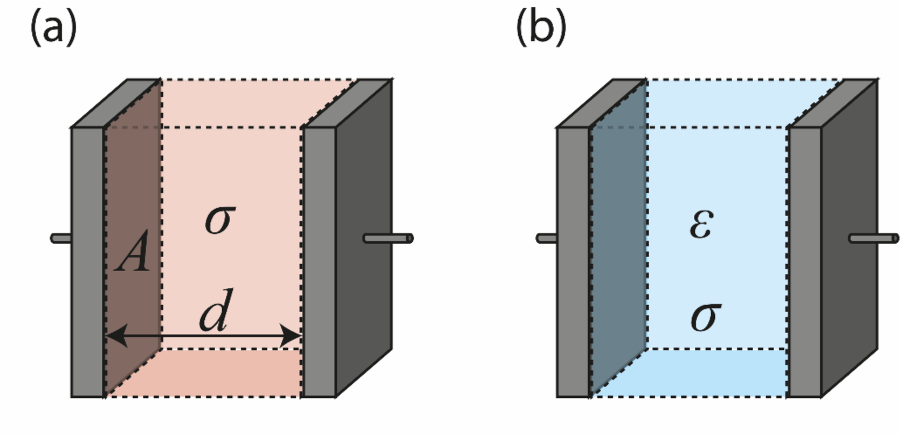

Figure 4.1: Diagram showing a parallel plate capacitor, with (**a)** a conductor and (**b)** a dielectric with unbound charge located between the two plates.

If a dielectric containing unbound charge, which has both permittivity and conductivity (Figure 4.1b), is positioned between the plates, its polarisation is dependent upon the frequency of the applied AC field. This scenario can be modelled as a loss-free capacitor and a resistor in parallel. Permittivity, ε [F m^{-1}], is given by [4.3]:

$$\varepsilon = \varepsilon_0 \varepsilon_r \tag{4.3}$$

and refers to the ability of a material to resist the formation of an electric field within itself, where ε_0 is the constant permittivity of vacuum (8.85 × 10^{-12} F m^{-1}) and ε_r the relative permittivity of the dielectric, which is dimensionless. In this model, the capacitor now exhibits a frequency dependent capacitance, $\tilde{C}$ [F], and the resistor a resistance, R [Ω], which can be approximated using [4.1, 4.2]:

$$\tilde{C} = \tilde{\varepsilon} \frac{A}{d} \tag{4.4}$$

$$R = \frac{1}{\sigma} \frac{d}{A} \qquad (4.5),$$

where $\tilde{\varepsilon}$ represents the complex permittivity of the dielectric, which is the dimensionless, frequency dependent permittivity of the dielectric. This is calculated using [4.3, 4.6]:

$$\tilde{\varepsilon} = \varepsilon_0 \varepsilon_r - j \frac{\sigma}{\omega} \qquad (4.6),$$

where j is the imaginary vector (j^2 = -1) and ω is the angular frequency ($\omega = 2\pi f$) of the applied electric field [rad s^{-1}].

The impedance, which is now the complex impedance of a parallel circuit positioned between the capacitor and resistor, is given by:

$$\tilde{Z} = \frac{1}{1/R + j\omega C} = \frac{d}{A(\sigma + j\omega\tilde{\varepsilon})} \qquad (4.7).$$

4.2.3 Interfacial Polarisation

Polarisation can occur at the interface between two materials with different dielectric properties when an AC field is applied. In the case of AC electrokinetics, this interface typically arises between a dielectric medium (an electrolyte) and dielectric particles in suspension. If an electric field, $\mathbf{E}$ [N C^{-1}], is applied across an electrolyte, charges will align at either side of each single, suspended particle, and the induced dipole moment of a particle, $\mathbf{p}$ [C m], can be calculated using:

$$\mathbf{p} = 4\pi r^3 \varepsilon_m \frac{\tilde{\varepsilon}_p - \tilde{\varepsilon}_m}{\tilde{\varepsilon}_p + 2\tilde{\varepsilon}_m}\mathbf{E} \qquad (4.8),$$

where $\tilde{\varepsilon}_p$ and $\tilde{\varepsilon}_m$ are the complex permittivities of the particle and medium, and r is the particle radius [m]. In terms of particle volume, V_p [L], rather than diameter, the dipole moment is given by:

$$\mathbf{p} = V_p \tilde{\alpha}\mathbf{E} \qquad (4.9),$$

where

$$\tilde{\alpha} = 3\varepsilon_m \frac{\tilde{\varepsilon}_p - \tilde{\varepsilon}_m}{\tilde{\varepsilon}_p + 2\tilde{\varepsilon}_m} = 3\varepsilon_m \tilde{f}_{CM} \qquad (4.10)$$

and $\tilde{f}_{CM}$ is the Clausius-Mossotti factor, which accounts for the complex permittivities of the particle and medium [4.1-4.3].

4.2.4 Dielectric Relaxation

The creation of an induced dipole moment during the polarisation of a dielectric requires the displacement of charges, which takes a certain time to occur. Similarly, upon the removal of an electric field, time is also required before charges relax and polarisation disappears. At low frequencies, dipoles have sufficient time to align with the field, however, the time available for alignment decreases with increasing frequency. This means that charges have less relaxation time (τ) [s]. Eventually, with increasing frequency, τ will equal the time required for maximum polarisation [4.1-4.3]. Going beyond this critical frequency means that maximum polarisation can no longer be achieved and at very high frequencies, polarisation ceases to exist at all, as the dipoles are no longer able to cope with the changing field. This frequency dependent decrease in the polarisability of a material is termed the dielectric relaxation.

The Clausius-Mossotti factor, a complex variable, indicates the frequency-dependent polarity of the system (*i.e.* it is a measure of the separation of positive and negative electrical charges in the system, or the effective dipole moment) and is influenced by the relaxation time. Separating the real ($\Re$) and imaginary ($\Im$) components of $\tilde{f}_{CM}$ gives the following Debye relaxation [4.2]:

$$\Re\left[\tilde{f}_{CM}\right] = \left(\frac{\varepsilon_p - \varepsilon_m}{\varepsilon_p +\ 2\varepsilon_m}\right) + \frac{\left(\frac{\sigma_p - \sigma_m}{\sigma_p + 2\sigma_m}\right) - \left(\frac{\varepsilon_p - \varepsilon_m}{\varepsilon_p +\ 2\varepsilon_m}\right)}{1 + \omega^2\tau^2} \qquad (4.11)$$

$$\Im\left[\tilde{f}_{CM}\right] = \frac{\left[\left(\frac{\sigma_p - \sigma_m}{\sigma_p + 2\sigma_m}\right) - \left(\frac{\varepsilon_p - \varepsilon_m}{\varepsilon_p +\ 2\varepsilon_m}\right)\right]\omega\tau}{1 + \omega^2\tau^2} \qquad (4.12),$$

where

$$\tau = \frac{\varepsilon_p +\ 2\varepsilon_m}{\sigma_p + 2\sigma_m} \qquad (4.13)$$

and σ_p and σ_m are the conductivity of the particle and medium.

The relaxation time describes the relaxation frequency of a suspending system containing individual cells (*i.e.* where polarisation occurs between a component of the cell and the suspending medium). Typically for biological cells, there are two relaxation frequencies: the first relaxation (time constant τ_1) often occurs at low frequencies up to 100 kHz due to polarisation between the interface of cell membrane and suspending fluid – the so called "α-dispersion"; the second relaxation (time constant τ_2) typically occurs in between 1 – 10 MHz due to the effective short-circuiting of the cell membrane, where polarisation occurs between the suspending medium and cell cytoplasm – commonly referred to as the “β-dispersion” [4.1].

4.2.5 Maxwell’s Mixture Theory

In the case where numerous particles are suspended in a dielectric medium, an approximation is required to measure the dielectric properties of the population. Maxwell’s Mixture Theory (MMT) is used to relate the complex permittivity of the cell and suspending medium with the volume fraction and the complex permittivity of the suspension. According to MMT [4.7], the complex permittivity of the mixture ($\tilde{\varepsilon}_{mix}$) is given by:

$$\tilde{\varepsilon}_{mix} = \frac{1+2\Phi\tilde{f}_{CM}}{1-\Phi\tilde{f}_{CM}} \text{ with } \tilde{f}_{CM} = \frac{\tilde{\varepsilon}_p-\tilde{\varepsilon}_m}{\tilde{\varepsilon}_p+2\tilde{\varepsilon}_m} \qquad (4.14),$$

where Φ is the volume fraction, which is in this instance the ratio of particle population volume [L] and the volume of all constituents of the suspension [L]. However, $\tilde{\varepsilon}_{mix}$ describes changes in the permittivity of the medium which occur due to a specific volume of particles. Therefore, this approximation can only be used when the volume fraction is small (*i.e.*, where $\Phi < 10\%$).

4.2.6 Shell Model for Biological Particles

In the case of a single cell suspended in an electrolyte, the spherical shell model [4.3, 4.8, 4.9] is generally used in conjunction with MMT to approximate the complex permittivity of the mixture (Figure 4.2a). Generally, cells have a complex structure, are multi-shelled (*i.e.*, they have a surrounding cell membrane and intricate internal structure) and often not spherical. Therefore, to precisely approximate the dielectric properties of a biological cell a double, or even multi-shelled model should be used [4.2, 4.10]. However, a simpler approximation in the form of a single-shelled model can be applied to many cells, such as RBCs and most mammalian cells, where cells are considered to consist of an insulating outer membrane and conductive cytoplasm (Figure 4.2b).

In the single-shell model, the complex permittivity of a biological cell ($\tilde{\varepsilon}_{cell}$) is influenced by the cell membrane permittivity, $\tilde{\varepsilon}_{mem}$, and cytoplasm permittivity, $\tilde{\varepsilon}_{cyt}$, and the relationship between these parameters is described by:

$$\tilde{\varepsilon}_{cell} = \tilde{\varepsilon}_{mem}\left[\frac{\left(\frac{r_2}{r_1}\right)^3 + 2\left(\frac{\tilde{\varepsilon}_{cyt} - \tilde{\varepsilon}_{mem}}{\tilde{\varepsilon}_{cyt} + 2\tilde{\varepsilon}_{mem}}\right)}{\left(\frac{r_2}{r_1}\right)^3 - \left(\frac{\tilde{\varepsilon}_{cyt} - \tilde{\varepsilon}_{mem}}{\tilde{\varepsilon}_{cyt} + 2\tilde{\varepsilon}_{mem}}\right)}\right] \tag{4.15}$$

The cell radius is denoted by r_2 [m] and the inner radius, which is the dimension from cell centre to outer boundary of the cytoplasm (also the inner boundary of the cell membrane), is denoted by r_1 [m].

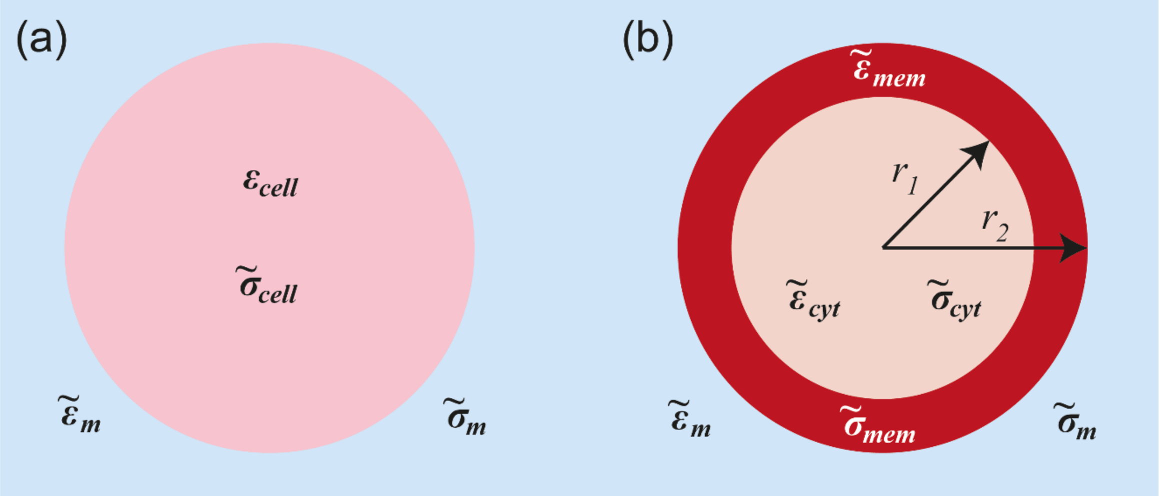

Figure 4.2: – **(a)** Representation of a simple, spherical model of a cell in a suspending medium, according to Maxwell's mixture theory. **(b)** Model of a single cell with a surrounding shell; the single-shell model.

4.2.7 The Shell Model for *Cryptosporidium*

The single-shell model (Figure 4.2b) has been used previously to determine the overall permittivity of the *Cryptosporidium* oocyst [4.5, 4.11, 4.12]. Presumably, the reason that no publications report a double- or even multi-shell model fitted to the *Cryptosporidium* oocyst is because the complex structure of the parasite makes this process very challenging. For example, fitting a double- (illustrated in Figure 4.3) or multi-shell model requires an understanding of the radius of each successive cell layer and the thickness of the shell or membrane surrounding this layer. However, the typical *Cryptosporidium* oocyst is comprised of a multi-layered outer wall that surrounds four, nuclei-containing sporozoites and a membrane-enclosed residual body [4.13]. Furthermore, the typical dimensions of these internal components are not well, if at all, characterised in the literature. Thus, several assumptions must be made if applying a double- or multi-shell model, which limits confidence in the result.

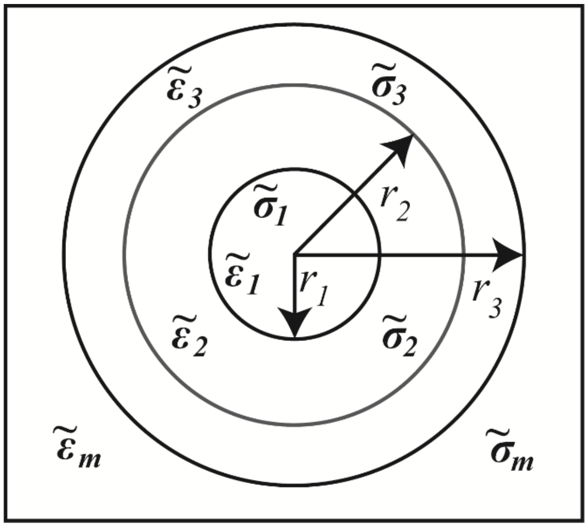

Figure 4.3: Double-shell model for spherical particles. From inside to out, the double-shell model can be made the equivalent of a single-shell model using a two-step calculation of Equation 4.15, based on the model developed by Huang *et al*. [4.14]. For multi-shelled particles with *n* shells (*i.e.*, *n* shells surrounding a conductive interior), an *n*-step calculation would be performed. An adaptation of Huang's model by Yang *et al*. [4.15], allows the approximation of the dielectric properties of particles which are ellipsoidal, not spherical, in shape.

4.3 Dielectrophoresis

4.3.1 DEP Principle and Theory

Dielectrophoresis (DEP) was first described by Pohl [4.16] in 1951 and was then defined as "the motion of suspensoid particles relative to that of the solvent resulting from polarisation forces produced by an inhomogeneous electric field". As described previously, when a polarisable particle is subjected to an AC electric field, the induced motion of charges leads to the formation dipoles which align in parallel to the applied electric field [4.3]. In a uniform electric field, each half of a dipole experiences similar Coulombic forces, consequently there is no net force acting upon the dipole; see Figure 4.4a which shows the separation of charges in a dielectric sphere when subjected to a homogenous AC field. Contrastingly, in a non-uniform electric field each half of a dipole experiences unequal forces and a net force acts upon the dipole [4.3]; see Figure 4.4b. A polarisable particle moves along an electric field gradient towards regions of high field intensity when more polarisable than the surrounding medium, often referred to as positive dielectrophoresis (pDEP) [4.17], and away from regions of high field intensity when experiencing negative dielectrophoresis (nDEP) [4.17].

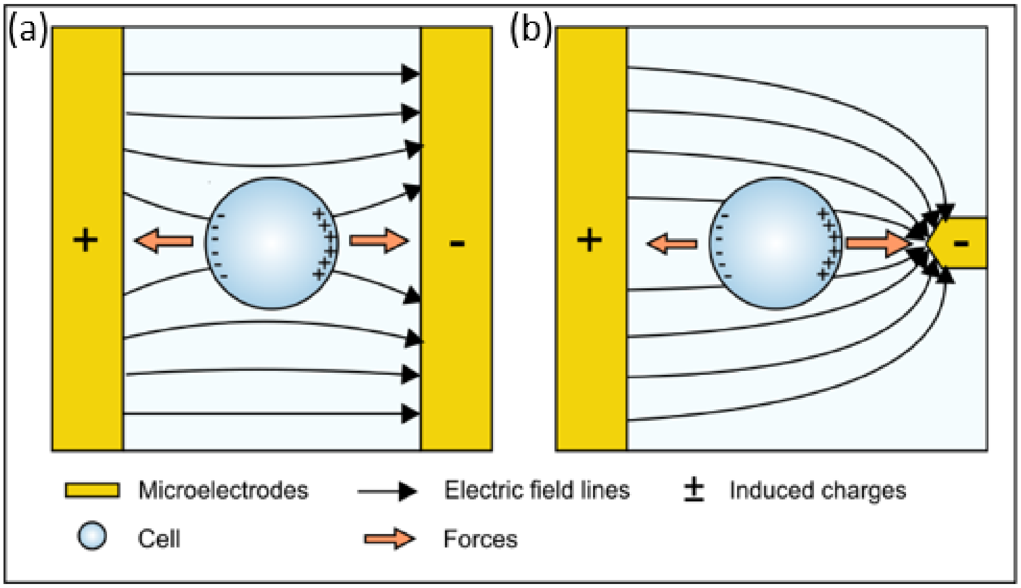

Figure 4.4: Dielectrophoretic-induced motion of polarisable particles. **(a)** In a uniform electric field, a particle with an equal amount of charges experiences no net force or movement. **(b)** In a non-uniform electric field, each half of the formed dipoles experiences unequal forces, as a result the particle undergoes a net movement.

The time-averaged dielectrophoretic force ($\langle F_{DEP} \rangle$) applied on a spherical particle suspended in electrolyte is given by [4.3, 4.4]:

$$\langle F_{DEP} \rangle = 2\pi r^3 \varepsilon_m \Re[\tilde{f}_{CM}] \nabla \mathbf{E^2} \qquad (4.16).$$

The real, in-phase component of the Clausius-Mossotti factor, $\Re[\tilde{f}_{CM}]$, governs the frequency dependence and direction of dielectrophoretic force acting upon a particle. $\Re[\tilde{f}_{CM}]$ can have a value between -0.5 and 1, with a value greater than 0 symbolising pDEP, *i.e.*, positive polarisability and a value below 0 indicating nDEP [4.11], *i.e.*, negative polarisability.

For biological cells, the direction of DEP motion is frequency dependent and there are typically one or two distinct crossover frequencies when the sign of motion changes (*i.e.*, nDEP or pDEP) [4.3]. The effects of electrically induced fluid flow and diffusion within a system make it difficult to measure/characterise the F_{DEP} directly, instead, the dielectrophoretic crossover frequency (f_{cross}) can be measured [4.1-4.3]:

$$f_{cross} = \frac{1}{2\pi}\sqrt{\frac{(\sigma_m - \sigma_p)(\sigma_p + 2\sigma_m)}{(\varepsilon_p - \varepsilon_m)(\varepsilon_p + 2\varepsilon_m)}} = \frac{1}{\sqrt{2\pi}}\sqrt{\frac{\sigma_m - \sigma_p}{\varepsilon_p - \varepsilon_m}}f_{MW} \qquad (4.17),$$

with:

$$f_{MW} = \frac{1}{2\pi\tau} \qquad (4.18),$$

where f_{MW} is the Maxwell-Wagner relaxation frequency [Hz] and, in the case of a biological cell, τ represents time constant τ_2 [s], as the crossover back to nDEP behaviour typically occurs in the MHz frequency range due to the effective short-circuiting of the cell membrane.

The DEP force acting upon a cell is also influenced by cell size, shape, membrane conformation and internal structure [4.18], which all typically differ between species and are usually distinct in infected and normal or viable and non-viable bacteria or cells [4.11, 4.14, 4.17, 4.19, 4.20]. For instance, DEP has been used to differentiate between different bacterial species such as *E. coli* and *Bacillus* spp. [4.21] and protozoa like *Cryptosporidium* and *Giardia* [4.11]. Therefore, with the correct signal frequency, amplitude and suspending medium, DEP can be used to sort a range of biological cells. Some applications of DEP in microfluidics will be described in the following sections.

4.3.2 DEP Devices and Application

Dielectrophoresis has been applied within many fields including medical diagnostics, biosensors, cell therapies, drug discovery and microfluidics [4.3] and is the most widely documented AC electrokinetic-based, manipulation technique in the literature. When employed in continuous-flow microfluidic systems, DEP has demonstrably enabled fast, highly sensitive manipulation (*i.e.*, trapping, isolation and sorting of specific particles from others) and label-free detection of target particles.

Advances in microfabrication technologies and procedures mean that almost any microelectrode design can be implemented in a microfluidic system. Consequently, a variety of operating strategies have been employed in DEP systems to facilitate particle sorting in continuous flow including (but not limited to): gravitational field-flow fractionation, multi-step, lateral sorting, barrier-assisted, pulsed DEP, medium conductivity gradient, immuno-assisted and marker specific devices [4.3, 4.17, 4.22]. Generally, these devices/ strategies either: 1. Induced opposing, dielectrophoretic motion on two populations to facilitate separation; or 2. Utilised the difference in the magnitude of DEP force experienced by two populations (where the direction of DEP force experienced is similar) to facilitate volume-sensitive separation.

A simple representation of a common DEP device is annotated in Figure 4.5, which shows a lateral sorting device. In this device, interdigitated, planar microelectrodes are positioned at an angle to the flow and the sample flow stream is focused narrowly by a sheath flow. At the correct frequency, signal amplitude and buffer conductivity, a polarisable particle will experience nDEP force which is greater than the magnitude of the hydrodynamic drag force within the continuously flowing fluid. Consequently, the particle will be repelled from regions of high field intensity. The resulting effect is that such particles will be deviated laterally and vertically out of the sample stream and across the sheath flow to the opposite side of the channel. Alternatively, particles which experience no or little nDEP force will experience minimal lateral and vertical deviation and thus, separation can be achieved within the channel.

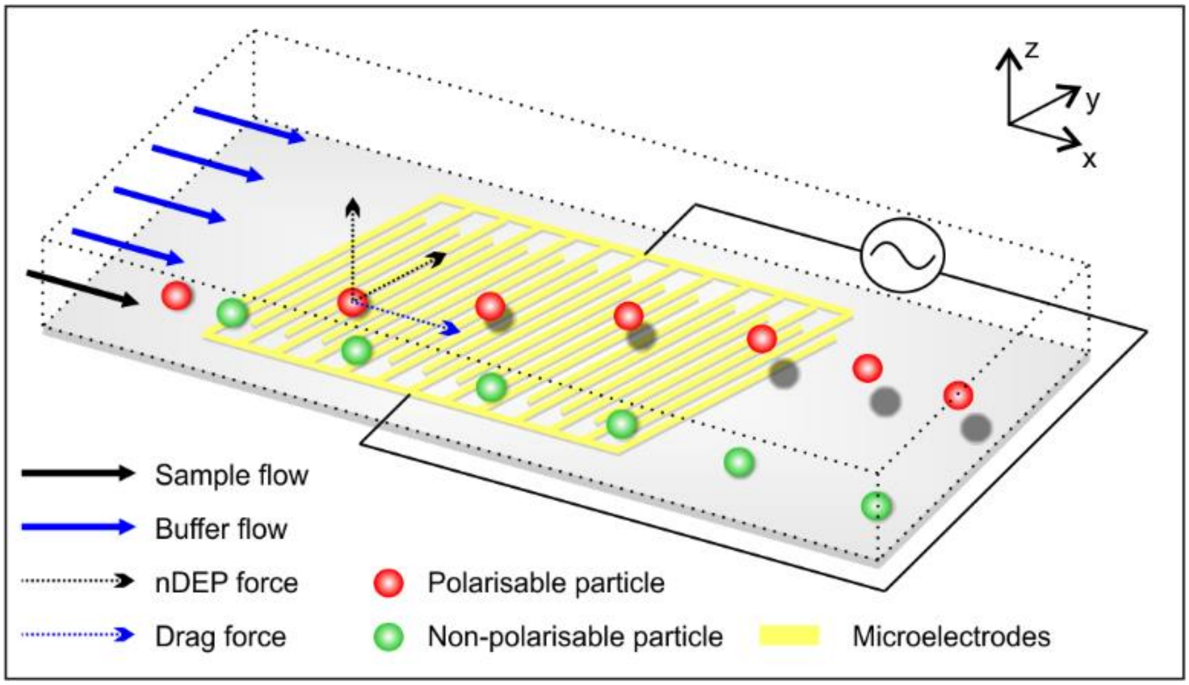

Figure 4.5: A lateral sorting DEP device. Interdigitated, planar microelectrodes facilitate the lateral deviation of polarisable particles contained within the sample flow. Consequently, polarisable particles are forced into the sheath flow and are, thus, separated from non-polarisable particles in the device.

4.3.4 DEP Analysis of *Cryptosporidium*

The dielectrophoretic behaviour of *Cryptosporidium* has been characterised by several researchers using microfluidics [4.11, 4.12, 4.23]. Su *et al.* [4.12] characterised the DEP responses of viable and treated *C. parvum* oocyst populations in a low conductivity deionised (DI) water-based buffer within the 10 – 15 frequency MHz range. In this work, *C. parvum* sub-populations were inactivated using heat-treatment (exposure to 90°C for 10 mins) but were also exposed to silver nanoparticles (AgNP) at varying concentrations – the use of AgNP for water disinfection purposes has drawn increased attention in recent years, but dielectric analysis of AgNP-treated *Cryptosporidium* oocysts has rarely been reported. The device utilised a technique known as insulator-DEP to facilitate the characterisation of the DEP response of the pathogens – see Figure 4.6. A narrowing constriction was fabricated using PDMS (an insulating material commonly used in microfabrication), which was bonded to a glass slide and electrodes inserted at either pole of the device to allow the application of an electric field. With no flow induced in the microchannel (*i.e.*, experiments were performed in batch mode), the DEP motion of oocysts was easily tracked and the time-averaged DEP response curve plotted. A notable finding was that within the frequencies of 10 – 15 MHz and in low conductivity media (σ_m = 2 mS m^{-1}), heat-inactivated oocysts experienced limited DEP force but untreated oocysts experienced considerable negative DEP force, thus, highlighting ideal conditions for separation of these sub-populations.

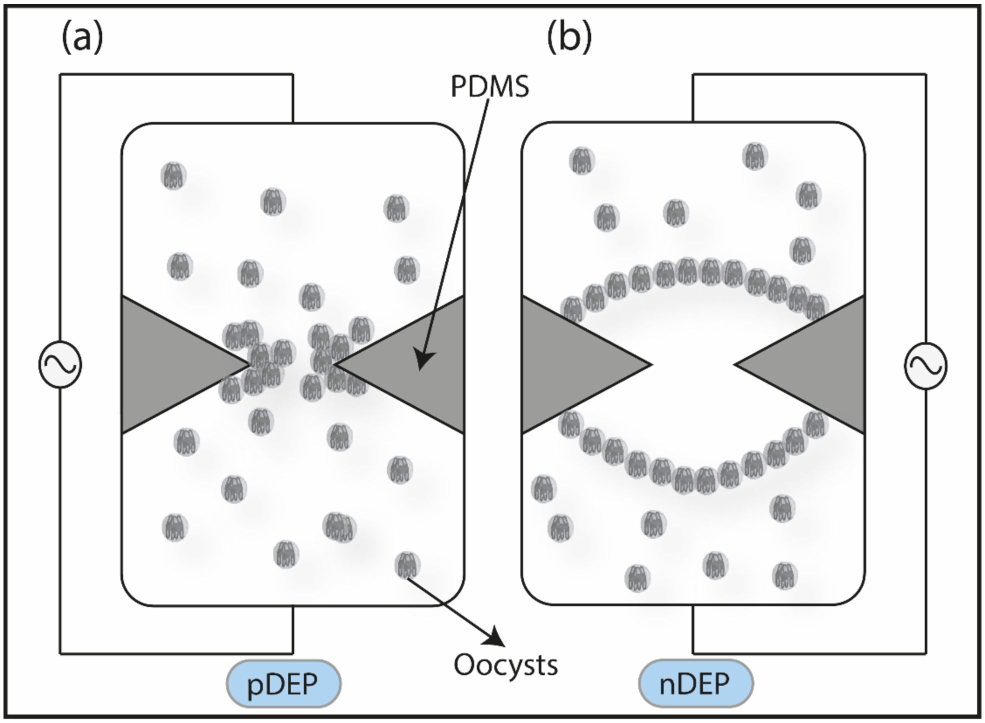

Figure 4.6: Schematic representation of insulator-DEP device of Su *et al*. [4.12]. A PDMS-glass device which has a narrowing constriction is filled with sample, sealed and an AC signal applied. **(a)** Positively polarised oocysts suspended in DI water migrate towards the regions of high field intensity – the tips of the PDMS features. **(b)** Oocysts experiencing nDEP are repelled from the regions of high intensity.

Using batch mode microfluidics, Quinn *et al.* [4.23] showed that the ratio of dielectrophoretic collection of *C. parvum* oocysts in DI water at two frequencies (100 kHz and 10 MHz) decreased, in comparison to untreated oocysts, upon exposure to increasing dosages of UV light. This device consisted of a fluid chamber with parallel microelectrodes patterned on the bottom surface, which could be filled with a solution and sealed, before DEP analysis was performed. The authors speculated that the reduction in collection at the highest UV dosages occurred due to a change in the internal conductivity of UV-treated oocysts. This hypothesis is feasible given that in low conductive buffer (*i.e.*, DI water) at frequencies of 10 MHz or more, the "β-dispersion" range of the outer membrane of the typical biological cell is usually surpassed (see section 4.2.4). Consequently, membrane perforation would lead to ion exchange between the oocyst interior and external media (unless isosmotic conditions), thus altering the internal conductivity of the oocyst. Despite this, the use of the dielectrophoretic collection ratio at two frequencies as an indicator of efficiency appears misleading, as it does not give an indication of the overall collection efficiency or recovery rates within the system.

While useful insight can be gained from the work of Su *et al*. [4.12] and Quinn *et al.* [4.23], the devices operated in batch mode and, thus, required considerable user input to facilitate sorting. Furthermore, the device required microscopic observation by skilled personnel to monitor the DEP response of the pathogens. Therefore, the device has limited use to water utilities, who seek automated detection devices that operate in continuous mode to advance from the requirement of current methods (EPA 1622 and 1623.1) for highly-skilled microscopists (James Green, Scottish Water, Personal Communication, 11 September 2015).

In another study, Unni *et al*. [4.11] used a continuous flow microfluidic system to separate *C. parvum* oocysts and *Giardia lamblia* cysts whilst suspended in DI water. This device similarly used a parallel microelectrode array which was positioned on the bottom surface of the microchannel. The method of separation involved trapping *G. lamblia* cysts at the microelectrode surface, whilst suspended *C. parvum* oocysts continued with the flow outwards from the device – these pathogens are often isolated simultaneously from treated water supplies using the EPA 1623.1 detection procedure.

Although there are numerous positive aspects of the work of Unni *et al*. [4.11], the authors were unable to separate two different species of *Cryptosporidiu*m (*C. parvum* and *C. muris*) and did not perform analysis of viable and non-viable sub-populations. Therefore, further analysis of the inter-species DEP response and viability-based separation of *Cryptosporidium* using DEP is merited – this issue will be addressed in Chapters 8 and 9.

4.4 Electrorotation

4.4.1 ROT Principle

Electrorotation (ROT) is a popular single-cell analysis technique that enables the monitoring of subtle, biophysical differences in cells by observing their ROT behaviour and ROT rate under an applied electric field. This technique has been used to measure the dielectric properties of many different biological cells [4.5, 4.14, 4.24, 4.25].

When located between quadruple electrodes which each have 90° advancing phase (*i.e.*, 0° - 90° - 180° - 270°) a polarisable particle will be subjected to a rotating electrical field (see Figure 4.7). An induced dipole forms across such a particle and consequently, the particle either rotates in a similar direction to that of the field (co-field) or against the direction of the field (anti-field) depending on the sign of the imaginary component of the Clausius-Mossotti factor ($\Im\left[\tilde{f}_{CM}\right]$; see equation 4.20). This imaginary, out-of-phase component governs the electrorotation spectrum of the cell/ particle as it accounts for the dielectric properties of the particle and media, but also the frequency of the field. Using co-field rotation as an example (where $\Im\left[\tilde{f}_{CM}\right] > 0$), this phenomenon occurs due to the induced dipole lagging behind the turning field vector, which causes the particle to constantly attempt to re-align itself with the electric field, such that it is subjected to a rotational torque (Γ_{ROT}). The time-averaged electrorotational torque, Γ_{ROT}, experienced by a particle is given by [4.1, 4.4]:

$$\langle\Gamma_{ROT}\rangle = -4\pi r^{3\varepsilon_m}\Im[\tilde{f}_{CM}]\mathbf{E}^2 \qquad (4.19),$$

however, $\langle\Gamma_{ROT}\rangle$ is usually measured indirectly by means of the rotation rate (angular velocity) [4.4]:

$$R_{ROT} = -\frac{\varepsilon_m\Im[\tilde{f}_{CM}]\mathbf{E}^2}{2\mu}K \qquad (4.20),$$

where R_{ROT} is the rotation rate, μ is the viscosity [Pa s] of the suspending medium and K is a scaling factor.

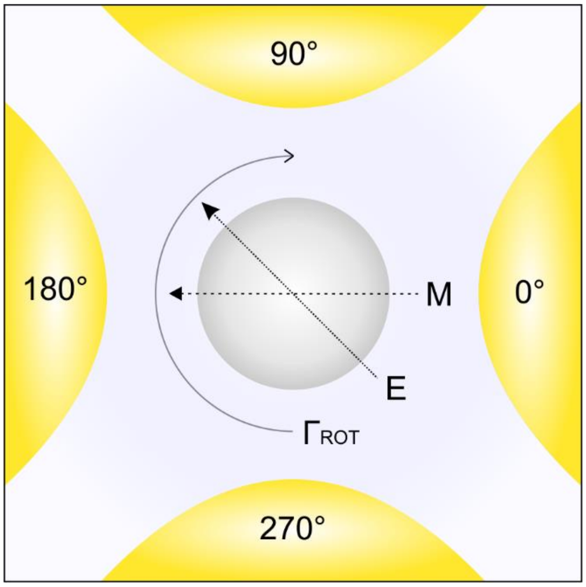

Figure 4.7: Induced anti-field electrorotation of a polarisable particle. Four-pole electrode structure which creates a rotating electric field (**E**), due to the phase-shifted voltage excitation. If the field rotates sufficiently quickly, the induced dipole moment (M) will lag behind the electric field at an angle related to its relaxation time (the time taken for the dipole to form), which induces a rotating torque (Γ_{ROT}) upon the particle. Adapted from ref [4.4].

4.4.2 ROT Analysis of *Cryptosporidium*

The use of ROT to indicate the viability status of *Cryptosporidium* oocysts has been reported [4.5], where system conditions were identified which compelled viable and non-viable oocysts to rotate in opposing directions. Despite this, ROT devices typically operate in batch mode as the forces generated are too small to resist the hydrodynamic drag forces created in continuous flow systems [4.26]. Therefore, ROT devices do not permit high and continuous sample throughput, which are key specifications (section 1.2) of the *Cryptosporidium* detection device proposed as part of this research.

4.5 Travelling Wave Dielectrophoresis

The use of sequentially-actuated parallel arrays of planar microelectrodes with phase-shifted signals to manipulate particle motion was firstly described by Masuda *et al*. [4.27]. This method, commonly referred to as travelling wave dielectrophoresis (TWD), has since been used in continuous flow microfluidic devices to separate different cell/ particle populations based on their dielectric properties [4.28-4.30]. There are no reports of TWD analysis of *Cryptosporidium* in the literature. The TWD (F_{TWD}) force acting upon a particle is given by:

$$F_{TWD} = \frac{-4\pi^2 \varepsilon_m r^3}{\lambda} \Im[\tilde{f}_{CM}]\mathbf{E}^2 \qquad (4.21),$$

where λ is the wavelength of the travelling field [m]; the distance covered between four planar electrodes when the phase shifts in the direction 0° - 90° - 180° - 270°.

Like ROT, particles move in a co-field direction towards the smaller phase regions when $\Im[\tilde{f}_{CM}] > 0$ and move in anti-field direction towards the higher phase regions when $\Im[\tilde{f}_{CM}] < 0$. Particle separation by means of TWD also relies on the nDEP principle (where $\Re[\tilde{f}_{CM}] < 0$), which is required to ensure that particles are repelled from regions of high field intensity (*i.e.* the microelectrode edges) and effectively levitate in the channel – this stops particle sedimentation or trapping in the channel.

A schematic representation of the TWD device used by van den Driesche *et al.* [4.30] is represented in Figure 4.8. In this example, the smaller, sample inlet is pinched by a larger, sheath flow and entering cells are subjected to a non-uniform, phase-shifted electric field. At the correct signal frequency, magnitude and medium conductivity, particles experience nDEP and levitate but move in co-field direction towards the smaller phase regions ($\Im[\tilde{f}_{CM}] > 0$) in response to the travelling field. Eventually, the particles traverse across the width of the channel, whilst other, unaffected particles continued through the channel facilitating separation.

In comparison to DEP, more complex signal generation equipment is required to create a phase-shifted electric field within TWD and ROT devices. This equipment was not readily accessible within my research institute, thus, TWD was not explored any further during this project.

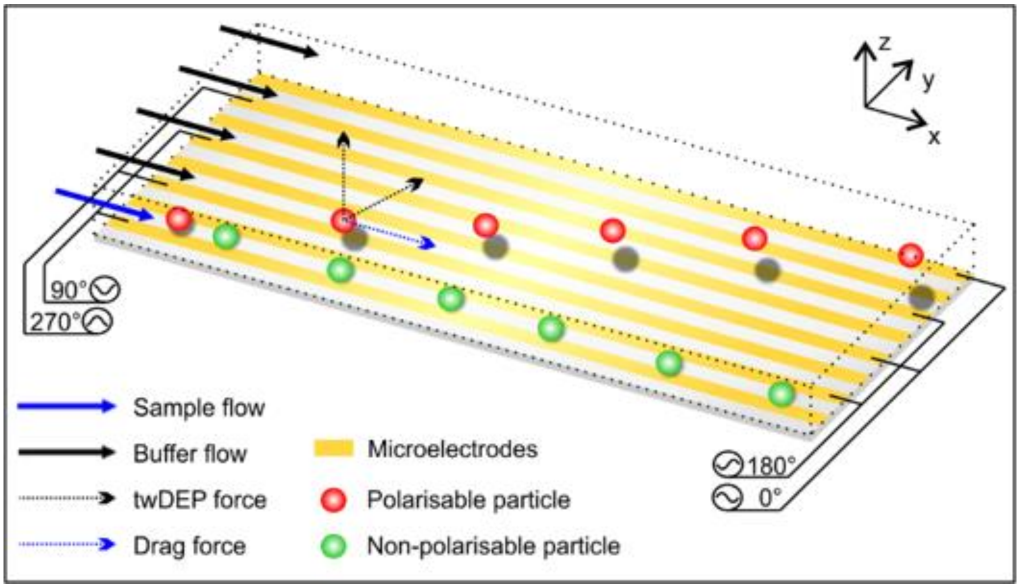

Figure 4.8: Particle separation by travelling wave dielectrophoresis. Sample is injected at the left side of the chip by pressure-driven flow. Polarisable cells exposed to a non-uniform phase-shifted TWD field move against the direction of field travel (0° – 270° – 180° – 90°) to leave the device at the opposite side.

4.6 Electrical Impedance Spectroscopy

4.6.1 EIS Principle

In DEP, ROT and TWD, there is no reason to acknowledge the volume fraction, since the polarisability of individual particles is measured directly. Despite this, the limitations of such techniques are evident. For example, to measure fully the real and imaginary components of the Clausius-Mossotti factor, both the DEP crossover frequency and ROT torque of a cell would need to be measured. Additionally, to obtain the ROT properties of a single cell typically takes several seconds per cell, making this technique impractical when measuring cells from highly concentrated samples.

Electrical impedance spectroscopy (EIS), in comparison, allows the rapid measuring of the complex impedance properties of a bulk suspension, whereby large numbers of cells in suspension are measured.

In conventional EIS, the dielectric properties of the system are obtained by applying a frequency-dependent AC signal and measuring the system response. A small AC voltage ($\tilde{V}(j\omega)$) [V], which is frequency-varied, is applied and the electrical current response ($\tilde{I}(j\omega)$) [A], is measured, from which the complex impedance ($\tilde{Z}$) [Ω] can be calculated [4.1, 4.6]:

$$\tilde{Z}(j\omega) = \frac{\tilde{V}(j\omega)}{\tilde{I}(j\omega)} = \Re(\tilde{Z}) + j\Im(\tilde{Z}) \qquad (4.22),$$

where $\Re(\tilde{Z})$ and $\Im(\tilde{Z})$ represent the real and imaginary components of the complex impedance, j is the imaginary vector (j^2 = -1) and ω is the angular frequency ($\omega = 2\pi f$) of the applied electric field [rad s^{-1}]. The components $\Re(\tilde{Z})$ and $\Im(\tilde{Z})$ are commonly referred to as the resistance and reactance. The magnitude and phase angle of the complex impedance are given by [4.1]:

$$|\tilde{Z}| = \sqrt{\Re(\tilde{Z})^2 + \Im(\tilde{Z})^2} \qquad (4.23)$$

and

$$\angle\tilde{Z} = \arctan\left(\frac{\Im(\tilde{Z})}{\Re(\tilde{Z})}\right) \qquad (4.24),$$

respectively.

When measuring the impedance of a suspension, the complex impedance of the system (*i.e.*, a mixture) is [4.1, 4.6]:

$$\tilde{Z}_{mix} = \frac{1}{j\omega\tilde{C}_{mix}G} \qquad (4.25),$$

where $\tilde{C}_{mix}$ is the complex capacitance of the system. The variable G is a geometric constant, which for an ideal, parallel plate electrode system is simply the ratio of electrode area to electrode separation distance (*A*/*d*) [m] – see Figure 4.1.

Equation 4.25, together with equation 4.14, allows the complex permittivity of a suspension to be calculated from the frequency-dependent impedance measurements. For a suspension where the dielectric properties of the medium and particle concentration are known, the calculated complex permittivity of the mixture can then be used to approximate the average dielectric properties of a single particle [4.1, 4.6].

4.6.2 EIS Analysis of *Cryptosporidium*

The only use of an electrical impedance spectroscopy system to discriminate viable and non-viable *C. parvum* oocysts was demonstrated by Houssin *et al*. [4.31]. Results showed a 15% difference in impedance magnitude of a low conductive buffer containing either viable or non-viable *C. parvum*, with a reported detection limit of less than 10 oocysts μL^{-1}. In follow up work, Dibao-Dina *et al.* [4.32] used a similar system to differentiate between the different parasitic stages of *C. parvum* upon infection of mammalian cells. In both works, measurements were made in bulk, where aliquots containing oocysts, either viable or non-viable, were loaded into sample wells and the impedance was then measured and compared to the control (previously obtained values of the suspending fluid alone). However, oocysts recovered using EPA 1623.1 could be of mixed viability [4.33], therefore, it is a necessity that any impedance system used for this purpose can discern the viability status of single oocysts. To date, there are no reports of the impedance analysis of different *Cryptosporidium* species, or the simultaneous impedance analysis of *Cryptosporidium* and *Giardia*.

4.7 Microfluidic Impedance Cytometry

4.7.1 Introduction

Technological advances, plus the emergence of microfluidics, has facilitated the development of novel microsystems that measure the dielectric properties of single cells at high speed [4.1, 4.6]. Microfluidic Impedance Cytometry (MIC) measures the dielectric properties of single particles and suspension but also performs enumeration and discrimination of detected particles. Commercial products are available which enumerate and discriminate single particles. For example, conventional flow cytometers detect particles and measure size and internal complexity depending on how a particle alters the forward and side scattered light signals emitted by the detection system – discrimination may then be achieved by analysing the retrieved values but no sorting occurs. Additionally, the Beckman Coulter Counter®, which requires laminar flow conditions for successful operation (this condition also applies in flow cytometry), typically measures the change in DC resistance between two electrolyte filled, electrically isolated chambers to discriminate particles without sorting. In this system, electrolyte is drawn from one chamber to the other via a microchannel and a transient drop in current is recorded, upon the passing of a suspended particle to the second chamber, which is proportional to the amount of displaced fluid within the microchannel *i.e.* particle volume (see diagram in Figure 4.9). Nonetheless, these systems and even modern fluorescence-activated cell sorting (FACS) machines, which can analyse and sort thousands of cells per second based on their optical and/ or fluorescence properties, are costly and generally unsuitable for the handling of small fluid volumes.

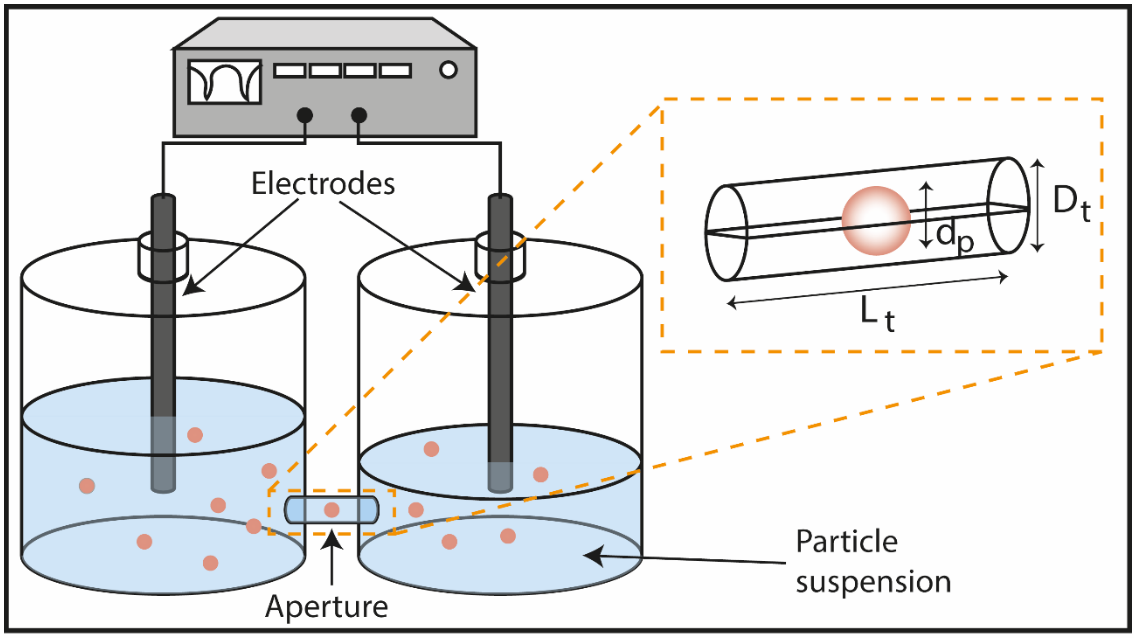

Figure 4.9: Schematic of the Coulter counter. Two electrodes are positioned at either side of an aperture. As a particle suspended in an electrolyte of known resistivity passes through a cylindrical aperture of known length (D_t) and diameter (L_t), it displaces conductive fluid and measurably changes the flow of current. The magnitude of this current change is proportional to the amount fluid displaced, *i.e.*, cell size (d_p).

4.7.2 MIC Principle

In MIC, suspended cells flow through a microchannel which has microelectrode pairs located at the top and bottom boundaries (see Figure 4.10), thus, allowing the application of an AC field across the channel [4.1, 4.6]. When no particle is present between the electrode pairs (*i.e.*, steps t_0, t_2 and t_4 in Figure 4.10b), the electrolyte can be modelled as a capacitor in parallel with a resistor (see Figure 4.1b), which has a complex impedance according to equation 4.7. The complex impedance being measured is altered when a suspended particle passes between the electrode pairs (*i.e.*, steps t_1 and t_3), as current flow is disrupted.

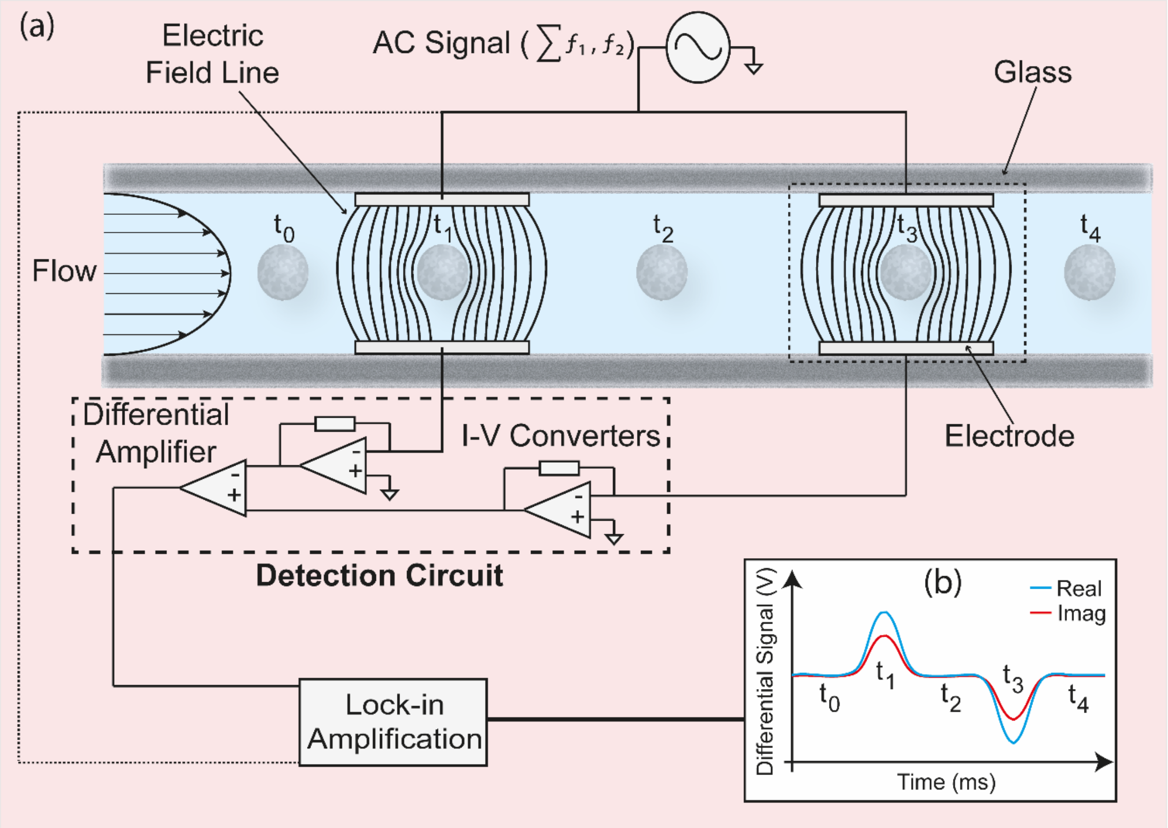

Figure 4.10: Microfluidic impedance cytometry system. **(a)** Two AC signals of discrete frequencies (*e.g.*, low and high) are summed and applied to the microelectrodes. The impedance response of a suspended particle (steps t_1 and t_3) is calculated by measuring the change in current received at the bottom microelectrodes as the particle flows by. The detection circuitry is then used to convert the current to voltage (I-V converters), retrieve a single output signal and suppress any common voltage (both processes performed by differential amplifier). Lock-in amplification is then used to separate out the real and imaginary components of the response at each applied frequency. **(b)** Shows the idealised signal (real and imaginary components) retrieved when a particle passes centrally through the microchannel. Corresponding steps of the sequences in (a) and (b) are annotated t_0, t_1, t_2, t_3, t_4.

The difference in current measured at the detection volume (first microelectrode pair) as a particle passes is compared to that measured at the reference volume (second microelectrode pair) where no particle is present to measure the particle impedance. The current flowing through the bottom electrodes is converted to voltage using transimpedance amplifiers. A differential amplifier is then used to retrieve a single output signal and suppress common voltage. Afterwards, lock-in amplification is required to separate out (demodulate) the magnitude and phase responses at each applied frequency, based on the real and imaginary impedance components, which gives a response signal for the particle being analysed (Figure 4.10b). If we consider a suspended, polystyrene microparticle or cell passing the first electrode pair: A positive impedance is detected as the particle passes, which is a consequence of a drop in the current being measured in comparison to the current measured for the electrolyte only, with the opposite occurring at the second pair. Retrieving the signal allows the plotting of population distribution, modelling and also estimation of dielectric parameters for detected particles.

4.7.3 MIC Theory

Like in electrical impedance spectroscopy (EIS), Maxwell's mixture theory (MMT; see section 4.2.5 and 4.2.6) can be used with MIC to approximate the complex permittivity of the particle and electrolyte, which in turn allows calculation of the dielectric properties of the mixture. However, in contrast to EIS, there is typically only a single particle (and not a whole particle population) between the electrodes of the microfluidic impedance cytometer. Therefore, the dielectric properties of single particles can be derived.

In the microfluidic impedance cytometer, the volume fraction (the ratio of particle volume and the volume of all constituents of the suspension) is typically much larger than in conventional EIS, since the area between the electrodes is less [4.1, 4.6]. For example, the detection region of the impedance cytometer used in this research had cross sectional dimensions of 40 μm height and 30 μm width – described later in Chapter 10. Therefore, the volume fraction is often considerably larger than 10% in an impedance cytometer. Furthermore, the electric field is no longer uniform but divergent [4.1, 4.6], since the field is not generated by two electrodes as in EIS. Therefore, the corrected volume fraction can be calculated using the following equation which also accounts for the non-uniform field [4.1, 4.6]:

$$\Phi = \frac{4}{3}\pi r^3 \frac{1}{\kappa w l h} \qquad (4.26),$$

where

$$\kappa = \frac{K(k)}{K'(k)} \qquad (4.27)$$

and

$$k = \tanh\left(\frac{\pi w}{2h}\right) \qquad (4.28).$$

In equations 4.26 and 4.27, κ is the cell constant which is dependent on the geometry of the cytometer detection region. The width [m] and height [m] of detection region are given by w and h, while the electrode length is l [m]. $K(k)$ is the complete elliptic integral of the first kind, $K'(k)$ is the complementary integral and k is the modulus of the elliptic function [4.6]. Consequently, the complex impedance of the system becomes:

$$\tilde{Z}_{mix} = \frac{1}{j\omega\tilde{\varepsilon}_{mix} l k} \qquad (4.29),$$

where $\tilde{\varepsilon}_{mix}$ is the complex permittivity of the mixture.

In conjunction with equation 4.14, the known dielectric properties of the medium and a shell model (see section 4.2.6) which accurately represents the structure of the measured particle(s), equation 4.29 allows the calculation of the dielectric properties of single particles.

4.7.5 Advantages and Applications

Suspended particles flow through the MIC system at high speed, for example flow rates of ~40 µL min^{-1} are typically employed using the systems currently described in the literature [4.34]. Therefore, in comparison to other continuous microfluidic separation/discrimination technologies [4.35, 4.36], MIC offers rapid sample processing and high throughput. This technology is also label-free, requires minimal sample processing (it is sometimes necessary to manipulate sample conductivity) and allows the impedance measurement of up to 1000 particles per second [4.37].

To date, MIC has been used for the viability determination of circulating tumour cells (CTCs) [4.34], plus the discrimination of different types of leukocytes [4.38, 4.39] and stem cells [4.40]. The mechanism of discrimination relies on the principle that due to the variations in the inherent properties of different cell types (*i.e.*, the biochemical composition, size and structure of cells), or similar cells in different states (*e.g.*, differentiated *vs* undifferentiated cells or sporulated *vs* unsporulated cysts), the impedance response differs. The analysis of pathogens which are typically isolated using the USEPA 1623.1 detection procedure however, has not been investigated using MIC. In Chapters 10 and 11, the impedance properties of such pathogens will be investigated.

4.8 Summary

The principle, theory and reported applications of several AC electrokinetics-based cell manipulation technologies were reviewed within this chapter. In addition, the reported uses of these technologies which concerned the analysis of *Cryptosporidium* and *Giardia* were described. For example, Su *et al.* [4.12] observed differences in the high-frequency DEP responses of viable and heat-inactivated *C. parvum*, whilst Unni *et al*. [4.11] sorted *Cryptosporidium* and *Giardia* in a continuous-flow microfluidic device. The DEP response of *Cryptosporidium* has been characterised by several authors, thus, methods for analysing the electrical data gained using DEP experiments are well developed. Furthermore, this technique enables continuous sample throughput. Therefore, DEP is considered a more suitable technology for the viability determination of *Cryptosporidium* oocysts than, *e.g.*, ROT or TWD.

MIC is a relatively new detection technology, thus, the suitability of MIC to the discrimination and detection of waterborne protozoa remains unexplored. Despite this, the use of EIS by Houssin *et al*. [4.31] to detect differences in the impedance response of viable and non-viable sub-populations of *C. parvum* provides an indication that MIC may facilitate the discrimination of such pathogens. MIC has also been used previously for the discrimination of a variety of different cell types [4.38, 4.39, 4.41], plus the viability determination of similar cell types [4.34], thus, the application of this technology to the detection and discrimination of waterborne pathogens is an interesting proposition. Furthermore, the biophysical characterisation of the dielectric properties of *Cryptosporidium spp*. and *Giardia* at the single-oocyst level using impedance-based methods remains unreported in the literature.

Later in this thesis, the research performed to separate waterborne pathogens based on viability using DEP is discussed (Chapters 8 and 9). In addition, the evaluation of the suitability of MIC to the species- and/or viability-based discrimination of waterborne protozoa, plus the biophysical characterisation of waterborne protozoa, is described in Chapters 10 and 11.

4.9 References

4.1. Morgan H, Sun T, Holmes D, Gawad S, Green NG. Single cell dielectric spectroscopy. Journal of Physics D: Applied Physics. 2007;40(1):61.

4.2. Morgan H, Green NG. AC Electrokinetics: Colloids and Nanoparticles: Research Studies Press; 2003.

4.3. Pethig R. Review Article—Dielectrophoresis: Status of the theory, technology, and applications. Biomicrofluidics. 2010;4:022811.

4.4. Jones TB. Basic theory of dielectrophoresis and electrorotation. Engineering in Medicine and Biology Magazine, IEEE. 2003;22(6):33-42.

4.5. Goater AD, Burt JP, Pethig R. A combined travelling wave dielectrophoresis and electrorotation device: applied to the concentration and viability determination of Cryptosporidium. Journal of Physics D-Applied Physics. 1997;30(18):L65.

4.6. Sun T, Morgan H. Single-cell microfluidic impedance cytometry: a review. Microfluidics and Nanofluidics. 2010;8(4):423-43.

4.7. Maxwell JC. A treatise on electricity and magnetism: Clarendon press; 1881.

4.8. Hanai T. Theory of the dielectric dispersion due to the interfacial polarization and its application to emulsions. Kolloid-Zeitschrift. 1960;171(1):23-31.

4.9. Pethig R. Dielectric and electrical properties of biological materials. Journal of Bioelectricity. 1985;4(2):vii-ix.

4.10. Irimajiri A, Hanai T, Inouye A. A dielectric theory of “multi-stratified shell” model with its application to a lymphoma cell. Journal of theoretical biology. 1979;78(2):251-69.

4.11. Unni HN, Hartono D, Yung LYL, Ng MM-L, Lee HP, Khoo BC, et al. Characterization and separation of Cryptosporidium and Giardia cells using on-chip dielectrophoresis. Biomicrofluidics. 2012;6:012805.

4.12. Su Y-H, Tsegaye M, Varhue W, Liao K-T, Abebe LS, Smith JA, et al. Quantitative dielectrophoretic tracking for characterization and separation of persistent subpopulations of Cryptosporidium parvum. Analyst. 2014;139(1):66-73.

4.13. Fayer R, Xiao L. Cryptosporidium and Cryptosporidiosis, Second Edition: Taylor & Francis; 2012.

4.14. Huang Y, Holzel R, Pethig R, Wang X-B. Differences in the AC electrodynamics of viable and non-viable yeast cells determined through combined dielectrophoresis and electrorotation studies. Physics in medicine and biology. 1992;37(7):1499.

4.15. Yang C, Lei U. Quasistatic force and torque on ellipsoidal particles under generalized dielectrophoresis. Journal of Applied Physics. 2007;102(9):094702.

4.16. Pohl HA. The motion and precipitation of suspensoids in divergent electric fields. Journal of Applied Physics. 1951;22(7):869-71.

4.17. Khoshmanesh K, Nahavandi S, Baratchi S, Mitchell A, Kalantar-zadeh K. Dielectrophoretic platforms for bio-microfluidic systems. Biosensors and bioelectronics. 2011;26(5):1800-14.

4.18. Beech JP, Jonsson P, Tegenfeldt JO. Tipping the balance of deterministic lateral displacement devices using dielectrophoresis. Lab on a Chip. 2009;9(18):2698-706.

4.19. Shafiee H, Sano MB, Henslee EA, Caldwell JL, Davalos RV. Selective isolation of live/dead cells using contactless dielectrophoresis (cDEP). Lab on a Chip. 2010;10(4):438-45.

4.20. Pysher MD, Hayes MA. Electrophoretic and dielectrophoretic field gradient technique for separating bioparticles. Analytical chemistry. 2007;79(12):4552-7.

4.21. Lapizco-Encinas BH, Simmons BA, Cummings EB, Fintschenko Y. Insulator-based dielectrophoresis for the selective concentration and separation of live bacteria in water. Electrophoresis. 2004;25(10-11):1695-704.

4.22. Voldman J. Electrical forces for microscale cell manipulation. Annu Rev Biomed Eng. 2006;8:425-54.

4.23. Quinn C, Archer G, Betts W, O'Neill J. Dose-dependent dielectrophoretic response of Cryptosporidium oocysts treated with ozone. Letters in applied microbiology. 1996;22(3):224-8.

4.24. Dalton C, Goater A, Pethig R, Smith H. Viability of Giardia intestinalis cysts and viability and sporulation state of Cyclospora cayetanensis oocysts determined by electrorotation. Applied and environmental microbiology. 2001;67(2):586-90.

4.25. Dalton C, Goater A, Burt J, Smith H. Analysis of parasites by electrorotation. Journal of Applied Microbiology. 2004;96(1):24-32.

4.26. Gascoyne PR, Vykoukal JV. Dielectrophoresis-based sample handling in general-purpose programmable diagnostic instruments. Proceedings of the IEEE. 2004;92(1):22-42.

4.27. Masuda S, Washizu M, Kawabata I. Movement of blood cells in liquid by nonuniform traveling field. IEEE transactions on Industry Applications. 1988;24(2):217-22.

4.28. Morgan H, Green NG, Hughes M, Monaghan W, Tan T. Large-area travelling-wave dielectrophoresis particle separator. Journal of micromechanics and Microengineering. 1997;7(2):65.

4.29. van den Driesche S, Rao V, Puchberger-Enengl D, Witarski W, Vellekoop MJ. Continuous separation of viable cells by travelling wave dielectrophoresis. Procedia Engineering. 2010;5:41-4.

4.30. Van den Driesche S, Rao V, Puchberger-Enengl D, Witarski W, Vellekoop MJ. Continuous cell from cell separation by traveling wave dielectrophoresis. Sensors and Actuators B: Chemical. 2012;170:207-14.

4.31. Houssin T, Follet J, Follet A, Dei-Cas E, Senez V. Label-free analysis of water-polluting parasite by electrochemical impedance spectroscopy. Biosensors and bioelectronics. 2010;25(5):1122-9.

4.32. Dibao-Dina A, Follet J, Ibrahim M, Vlandas A, Senez V. Electrical impedance sensor for quantitative monitoring of infection processes on HCT-8 cells by the waterborne parasite Cryptosporidium. Biosensors and Bioelectronics. 2015;66:69-76.

4.33. Smith HV, Nichols RAB. Cryptosporidium: Detection in water and food. Experimental Parasitology. 2010;124(1):61-79.

4.34. Spencer D, Hollis V, Morgan H. Microfluidic impedance cytometry of tumour cells in blood. Biomicrofluidics. 2014;8(6):064124.

4.35. McGrath J, Jimenez M, Bridle H. Deterministic lateral displacement for particle separation: a review. Lab on a Chip. 2014;14(21):4139-58.

4.36. Bhagat AAS, Bow H, Hou HW, Tan SJ, Han J, Lim CT. Microfluidics for cell separation. Medical & biological engineering & computing. 2010;48(10):999-1014.

4.37. Spencer D, Elliott G, Morgan H. A sheath-less combined optical and impedance micro-cytometer. Lab on a Chip. 2014;14(16):3064-73.

4.38. Holmes D, Pettigrew D, Reccius CH, Gwyer JD, van Berkel C, Holloway J, et al. Leukocyte analysis and differentiation using high speed microfluidic single cell impedance cytometry. Lab on a Chip. 2009;9(20):2881-9.

4.39. Han X, van Berkel C, Gwyer J, Capretto L, Morgan H. Microfluidic lysis of human blood for leukocyte analysis using single cell impedance cytometry. Analytical chemistry. 2011;84(2):1070-5.

4.40. Song H, Wang Y, Rosano JM, Prabhakarpandian B, Garson C, Pant K, et al. A microfluidic impedance flow cytometer for identification of differentiation state of stem cells. Lab on a Chip. 2013;13(12):2300-10.

4.41. Holmes D, Morgan H. Single cell impedance cytometry for identification and counting of CD4 T-cells in human blood using impedance labels. Analytical chemistry. 2010;82(4):1455-61.

Chapter 5 – Microfluidic-enabled Force Spectroscopy

5.1 Atomic Force Microscopy

5.1.1 Introduction

The first AFM system [5.1] used a mechanical probe, typically pyramidal in shape and assembled to a cantilever, to scan and generate a topographical image of a surface. This mechanical probe was coupled to a scanning tunnelling microscope (STM) that incorporated small piezoelectric elements to control the *x*-*y*-*z* position of the probe [5.2] – see sections 5.3.5 and 5.3.6. A small voltage was applied to such elements causing the separation of the contained charges and the subsequent contraction or extension of the piezo. Like microfluidics, atomic force microscopy (AFM) technology made considerable advances in the late 20th century, due to progression of microfabrication techniques. In modern systems and upon voltage application, the piezoelectric effect changes the length of an element by less than 0.2%, thus very precise control of probe movement is possible – AFM enables sub-nanometre spatial resolution [5.3]. When scanning a surface, any deflections of the flexible probe (which typically acts as a spring), in response to tip-surface interactions, are monitored using a laser beam and photodiode detector [5.4] – Figure 5.1.

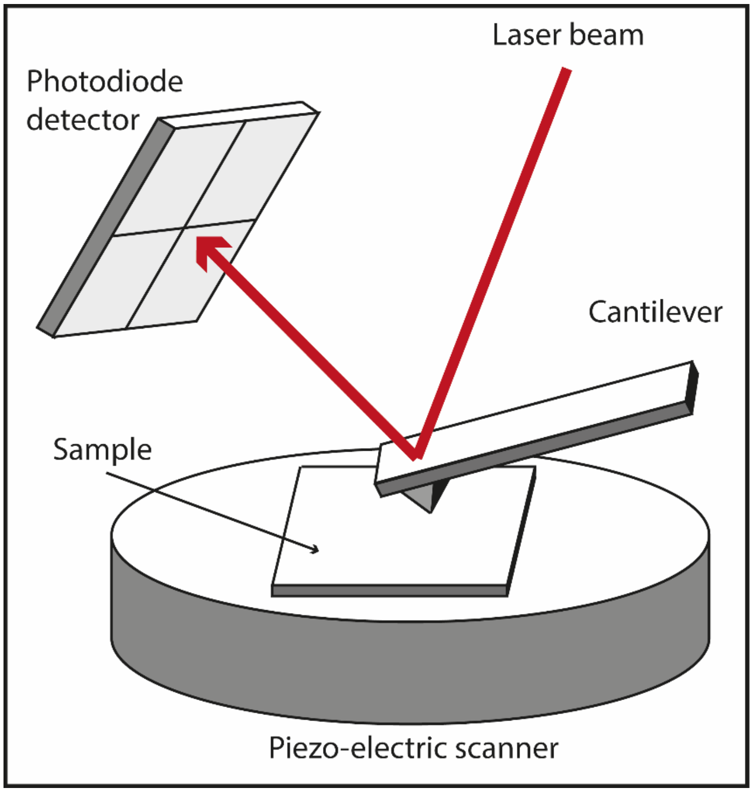

Figure 5.1: Optical beam detection of AFM cantilever deflection using a photo-detector.

5.1.2 Applications of AFM

Since invention, AFM has been used in a plethora of different applications, *e.g.*, on top of gaining a topographical image of a surface, AFM has been used to gather information concerning the physical [5.5], chemical [5.6, 5.7], thermal [5.8], magnetic [5.9] or contact potential [5.10] properties of a substrate, sometimes using specifically designed probes. Furthermore, in a method known as colloidal probe AFM [5.11], the elastic properties of a spherical particle can be measured, when the subject is immobilised (typically using glue) at the tip of a flat cantilever and pressed against a surface. The chemical interaction between the immobilised particle and surface can also be analysed using this method.

Although mostly utilised in surface and material science, AFM has also become a useful tool in biology. For example, AFM has been employed in microbiology to mechanically manipulate and study eukaryotic and prokaryotic cells [5.12-5.16]. Due to the high resolution of AFM technology, the unfolding [5.17, 5.18] and binding kinetics [5.19] of single proteins can be studied. High speed AFM [5.20] even permits the monitoring of protein movement and conformational change in real-time [5.21].

5.1.3 Force Spectroscopic Analysis of *Cryptosporidium*

Cryptosporidium is a problematic agent of waterborne disease and to date, filtration is the most efficient barrier to oocyst contamination of treated water supplies. As such, numerous colloidal probe AFM analyses have been performed to investigate the adhesion of *Cryptosporidium* oocysts to sand-like materials, as sand-bed filtration is one of the most widely utilised filtration methods. Generally, the scope of such articles bears no relevance with regards to this thesis. Despite this, some valuable insight can be gained from these articles regarding the mechanical properties of the oocyst, the outer wall and the extending network of molecules that protrude from the wall. For example, the biochemical composition and structure of *Cryptosporidium* oocyst (specifically the outer wall) may affect the force measurement.

The surface topography of the *C. parvum* oocyst was mapped by Considine *et al*. [5.22, 5.23] using AFM, who found a rough surface containing a collapsible, brush-like layer of lateral protrusions between 50 – 250 nm in height, which extended from the surface of the outer wall. The overall deformability of the oocyst was also quantified by Considine *et al*. [5.22], in terms of an interfacial spring constant. Although the sample size was relatively small ($n = 5$), *C. parvum* oocysts reportedly had low spring constants (indicative of high deformability) on the order of 0.1 – 4 N m^{-1}. In addition, it was found that the extending layer induced a steric repulsion to sand surfaces, likely due to the presence of an electrical double layer (EDL), and an overall negative charge of the oocyst in aqueous conditions [5.23, 5.24] – this feature possibly explains the mechanism by which *Cryptosporidium* evades filtration. Bryd and Walz [5.25, 5.26] later found that the extending layer of the outer wall was on average 115 nm thick and likely consisted of uncharged glycoprotein. This may appear contradictory to the previous findings that oocysts exhibit an overall negative charge, however, surface steric and EDL forces operate at larger ranges than Van der Waals forces [5.27], and thus, steric and EDL forces, which are repulsive in nature, dominate the surface interaction response of an oocyst.

5.2 Microfluidics Meets AFM

In the year 1999, the first successful integration of fluidic components within the cantilever tip of an AFM system was demonstrated. This technology, then termed dip pen nanolithography [5.28, 5.29], employed an AFM cantilever covered in ink to deposit ink on a substrate material by capillary forces, however the effects of thermal evaporation limited the functionality of this method. Many researchers designed systems which incorporated liquid reservoirs at the cantilever, to reduce the negative impacts of such evaporation [5.30-5.32]. An interesting solution was that of Deladi *et al.* [5.31], which utilised a hollow aperture in the cantilever tip, to reduce the surface area of the liquid-air interface and thus, reduce the rate of liquid evaporation. Despite this, all designs included an unprotected reservoir at the cantilever, thus, making it impossible for the cantilever to work when submerged within liquid buffer.

5.3 Microfluidic-enabled Force Spectroscopy

5.3.1 Introduction

In 2009, a new technology called microfluidic-enabled force spectroscopy (MeFS) was firstly described in published literature [5.33]. This technology combined the principles of conventional AFM with that of the microchanneled cantilever previously developed by Deladi *et al.* [5.31], to create a new syringe- or pipette-like probe for application in single cell microbiology settings. The principle of MeFS, based on the published work of Meister *et al.* [5.33], is illustrated in Figure 5.2a.

In the MeFS system, a microfluidic channel flows from the apex of the cantilever tip, through the microfluidic chip until it reaches a drilled probe holder (together these components are termed the FluidFM Micro Pipette®). This microchannel then continues through to the opposite side of the probe holder into a large fluid reservoir (also fabricated within the probe holder). The subsequent connection of tubing to the fluid reservoir/ probe holder allows the application of pressure from an external pressure controller. This water-tight pipeline enables the full immersion of the cantilever in solution, such that the only contact point between the fluid filled cantilever and solution is at the apex of the tip.

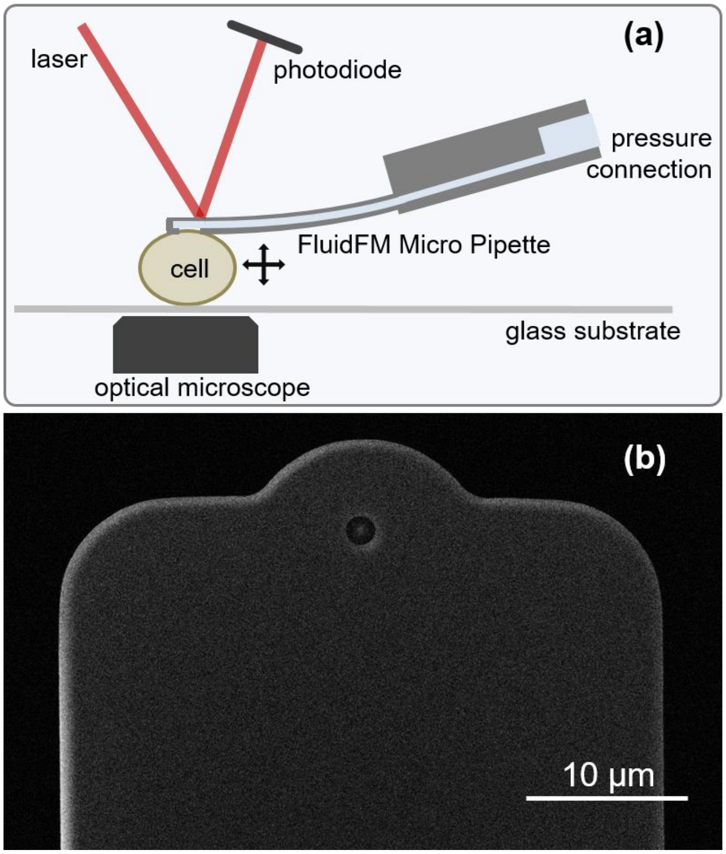

Figure 5.2: Schematic of MeFS measurement process. **(a)** The water-tight pipeline of the chip and cantilever assembly allows application of pressure from an external pressure supplier. **(b)** Using suction, target particles can be isolated at the hollow aperture of the cantilever and their biomechanical properties measured using a deflection measurement. Cantilever deflection is measured using optical beam detection.

5.3.2 MeFS Principle and Applications

In Figure 5.2b, the hollow aperture at the apex of a flat cantilever is shown which enables pipette-like function, upon precise control from an external pressure supply. Other tip designs however, can enable different functions, *e.g.*, pyramidal (Figure 5.3) or triangular tips with an aperture at the apex allow syringe-like function. Regardless of tip geometry, the ability to precisely dispense small amounts of liquid at a confined area with the resolution and force feedback of an AFM, give MeFS great versatility. For example, by applying negative pressure or vacuum to a cantilever with pipette-like function, which is immersed in a cell suspension, it is possible to attract and immobilise a cell at the cantilever aperture. Like in conventional and colloidal probe AFM studies, a force measurement can then be performed on the immobilised subject, which gathers information regarding the bio- physical, chemical and mechanical properties (list not exhaustive) of the cell, before positive pressure can be applied to facilitate cell release. The whole measurement procedure can be visualised because the probe is mounted directly above the lens of an inverted microscope. The ability to pick, measure, release and even relocate cells allows the capacity for rapid, single cell force spectroscopy in comparison to conventional AFM [5.2, 5.33].

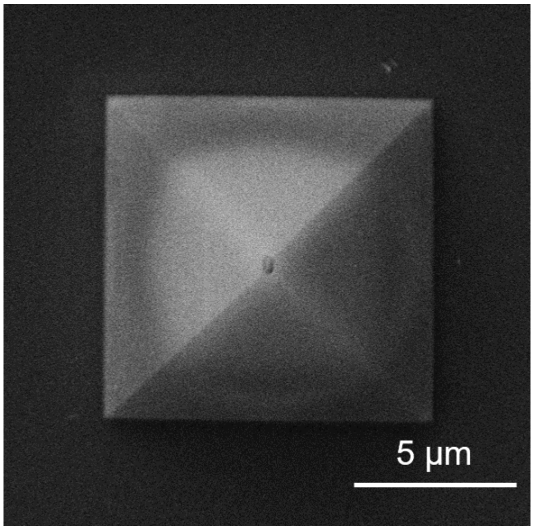

Figure 5.3: MeFS cantilever with pyramidal tip which incorporates a sub-micron aperture. Pyramidal, or triangular tips, with sub-micron apertures can be used to perform functions such as micro-injection of substances to a biological cell.

The micro-pipette and syringe functions which were described above have enabled the use of this technology in the fields of biology, material science and physics. Some applications include local liquid dispensing [5.33-5.35] in nanolithography, cell manipulation and displacement [5.36, 5.37] and the intracellular injection (*i.e.*, nucleic and cytosolic) of chemicals [5.38]. More recently, MeFS has been used in the quantification of bacterial adhesion [5.39] and monitoring of the deformation of beating cardiac cells [5.40].

5.3.3 The Role of MeFS in this Research

With regards to this research, the ability to immobilise cells/ particles at a hollow aperture and gather information concerning the biomechanical properties of each subject, before displacing/ relocating cells based on the results of such measurements is of particular interest. For example, characterisation of the variance in size and deformability of *e.g.*, *Cryptosporidium* oocysts of different species has not been described in the literature. Therefore, microfluidic-enabled force spectroscopy provides a platform through which such properties can be assessed. Consequently, the applicability of size- and/ or deformability-based (passive) microfluidic separation systems to the objectives of this research can be determined. Before discussing the related research however (Chapters 6 and 7), the principle and underlying mechanical theory of MeFS systems will be considered further.

5.3.4 AFM Cantilever

To understand fully the properties and principle of the microfluidic-enabled cantilevers described later in this chapter, it is necessary to firstly consider the development of the conventional AFM cantilever – the predecessor of the microfluidic-enabled cantilever. The AFM cantilever is commonly assembled using several components which are fabricated using a derivative of the standard computer chip fabrication process. The cantilever is part of a larger chip which is secured in a probe holder before being fitted onto the AFM system. AFM cantilever designs most commonly incorporate the rectangular geometry [5.41] – which is the predecessor of the rectangular MeFS cantilever used in this research – or the V-shaped geometry [5.42], which is more tolerant to torsional force. The cantilever is often manufactured from silicon or silicon nitride and coated with a reflective, metallic layer (required for detecting cantilever deflection) – chrome, gold, aluminium and platinum-iridium are commonly used and layer thickness is typically on the order of tens of nanometres [5.43]. One of the final steps of the fabrication process involves the anisotropic etching of a tip onto the cantilever surface. Due to the nature of the etching process, such tips are always pyramidal in shape. Using modern microfabrication technology, the tip apex typically has width of ~10 nm, however, it is possible to manufacture tips with an apex width of 1 nm [5.43]. Furthermore, sharp tips with high aspect ratio can also be manufactured. Tips are regularly manufactured from the same material as the cantilever, before a chemical or metallic covering is applied, however it is possible to buy *e.g.* magnetic or electrically conductive tips [5.43]. Colloidal probe tips, which have a spherical particle pre-glued to the tip, are also commercially available.

5.3.5 Deflection Detection

The sensing mechanism employed in MeFS, which is the most common sensing mechanism used in AFM systems (Figure 5.2), is optical beam detection (OBD) [5.44]. Using this mechanism, cantilever deflection is typically detected by monitoring changes in the reflection of a laser beam that is initially directed onto the top, free surface of the cantilever. The force-dependent angle of the cantilever is then quantified using a photo-detector, thus gathering information regarding the nature of the deflection. Changes in both the vertical and lateral directions can be measured using a quadrant photo-detector (Figure 5.1), however only vertical deflection was measured in this thesis, as this aspect of deflection contained information concerning the biomechanical properties of interest to this research (oocyst height and deformability; reasoning discussed in section 5.3.12). Some other detection sensing mechanisms used in AFM include optical interference, tuning fork, piezoresistive and capacitive methods [5.12, 5.43, 5.45, 5.46], however none of these methods were utilised when acquiring the data contained in this thesis.

5.3.6 Scanning Mode

Using an AFM system, a 100 μm^2 area can typically be scanned in a few minutes, where the rectangular area is scanned in a line-by-line order. This scanning either takes place in DC mode, where a static change is measured, or AC mode, where resonant changes are measured at high frequencies [5.2, 5.33]. The MeFS system used in this research operates in DC mode, thus, the variations of DC mode will be discussed.

The first ever AFM measurement mode was presented by Binnig *et al.* [5.1] and is now commonly termed the constant height mode. During such measurements, the cantilever approaches a surface in the *z*-direction until the tip makes contact, where it then remains before a scan in the *x*-*y* directions is initiated.

A more modern DC mode, the constant force mode, is now the most common measurement mode used in AFM [5.2]. This method is an improvement on the constant height mode because it incorporates an active feedback loop to constantly measure the force between a surface and probe. Consequently, the z-position of the probe can be continuously adjusted to maintain a similar force relationship between the cantilever and substrate throughout a complete surface scan. Contrastingly, changes in this force when using the constant height mode (where no feedback loop exists) can have detrimental effects on the cantilever tip, thus the constant force mode was preferred for all relevant experiments described in this thesis.

5.3.7 MeFS Cantilever

The MeFS cantilever has a rectangular design and is 37 µm wide, 200 µm long and 1.7 µm thick (Figure 5.4). The cantilever interior is manufactured from silicon nitride, which is in turn coated with a layer of silicon. The microchannel within the central region of the cantilever is 30 µm wide x 1 µm high and contains two rows of pillars, which increase cantilever stability. Due to the small dimensions, the cantilever is bound to a glass wafer to improve ease of handling when gluing the cantilever to the chip. Using sand blasting, a microchannel is fabricated in the glass in order to connect the fluidics of the cantilever and chip. The chip contains a 15 µL liquid reservoir, to which tubing can be easily connected with the aid of luer-lok™ fittings.

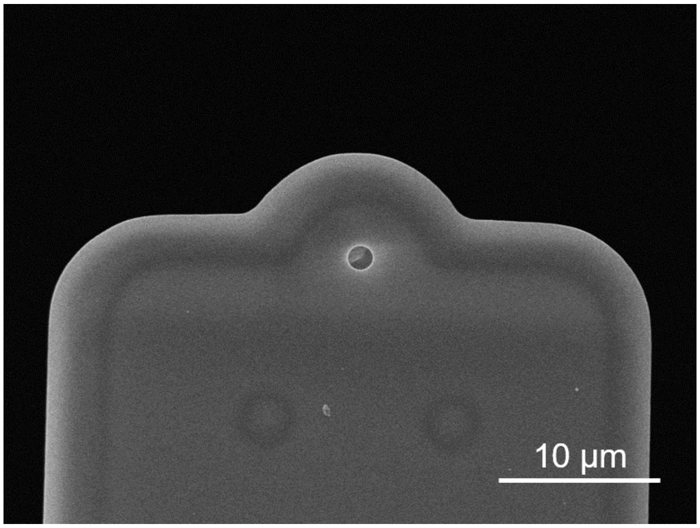

Figure 5.4: MeFS cantilever with 2 µm hollow aperture. Also apparent are the first set of pillars, which each belong to a row of pillars that stretches the length of the cantilever to provide stability.

Although the probe or aperture of MeFS can take the form of a variety of designs, cantilevers incorporating hollow apertures were utilised in this research. Such cantilevers are available commercially with apertures ranging from 100 nm to 8 µm in diameter.

5.3.8 Flow in the Cantilever

The maximal flow velocity (v_{max}) [m s^{-1}] at which flow through the hollow aperture of the cantilever can still be within the laminar regime (see section 3.2.2) is given by:

$$v_{max} = \frac{2300\mu}{\rho D_H} \qquad (5.1),$$

where μ is fluid dynamic viscosity [Pa s], ρ fluid density [kg m^{-3}] and D_H the hydraulic diameter [m] of the aperture (see equation 3.4).

The maximum volumetric flow rate for laminar conditions is therefore [5.43]:

$$Q_{max} = \frac{2300\mu}{\rho D_H}\frac{\pi {D_H}^2}{4} \qquad (5.2).$$

As mentioned in the previous section, the smallest tip aperture that can be purchased is 100 nm in diameter, thus, for water at room temperature Q_{max} = 100 nL s^{-1} in a MeFS system, according to equation 5.2. The MeFS experiments performed in this research typically utilised flow rates on the order of several nL s^{-1} (*i.e.*, < 10 nL s^{-1}), therefore, it can be assumed that flow was laminar.

Using equations 3.4 and 5.2 and the channel dimensions stated in section 5.3.7, the cantilever microchannel has D_H = 2 µm. The maximum volumetric flow rate in the rectangular microchannel ($Q_{\max\_c}$) is given by:

$$Q_{\max\_c} = \frac{2300\mu}{\rho D_H} w_c t_c = 30\ \mu\text{L}\ s^{-1} \qquad (5.3),$$

where w_c and t_c are the width [m] and height [m] of the channel – flow in the channel is also within the laminar regime.

5.3.9 Surface Forces

When the cantilever tip is positioned close to a substrate surface, it experiences attractive and repulsive surface forces. Attractive forces are typically in the form of Van der Waals forces [5.47], where nearby atoms or molecules experience electron coupling reactions and repulsive forces are described by the Pauli exclusion principle [5.48], where atomic orbitals start to overlap. These forces (V) can be approximated using the Lennard-Jones pair potential equation:

$$V = 4\varepsilon\left\{\left(\frac{\sigma}{r}\right)^{12} - \left(\frac{\sigma}{r}\right)^{6}\right\} \qquad (5.4),$$

where the distance [m] between two atoms or molecules is given by r, the distance [m] at which the potential equals zero by σ and the depth [m] of the potential well (*i.e.*, the region surrounding a local minimum of potential energy which is unable to convert to another type of energy and is, thus, captured) by ε. The force is then equal to the gradient of this potential.

5.3.10 Cantilever Spring Constant

Due to the small dimensions of cantilevers and to variations in precision of cantilever microfabrication, the spring constant (*i.e.* the stiffness = force applied / displacement) of similar cantilevers is often highly variable. In order to measure and correctly interpret the mechanical properties of a surface, it is necessary to first quantify the vertical spring constant of the cantilever and thus, calibrate the measurement system. The vertical spring constant, k [N m^{-1}] of a solid cantilever with uniform cross section can be devised using [5.49]:

$$k = \frac{3EI}{L^3} \qquad (5.5),$$

where E is the elastic modulus [Pa], I the moment of inertia [kg m^2] of the cantilever cross section and L the length of the cantilever [m]. When using a solid, rectangular cantilever, I is given by [5.49]:

$$I = \frac{wt^3}{12} \qquad (5.6),$$

where w is the width [m] and t is the thickness [m] of the cantilever. Consequently, the following expression results:

$$k = \frac{Ewt^3}{4L^3} \qquad (5.7).$$

For a hollow cantilever which incorporates a microchannel centrally along its length, I_c is given by [5.43]:

$$I_c = \frac{wt^3 - w_c {t_c}^3}{12} \qquad (5.8)$$

with w_c and t_c representative of the width [m] and height [m] of the microchannel. Using the rational described for equations 5.6-5.8, the vertical spring constant [N m^{-1}] of a hollow cantilever, k_h, is therefore [5.43]:

$$k_h = \frac{E}{4L^3}(wt^3 - w_c {t_c}^3) \qquad (5.9).$$

5.3.11 Experimental Spring Constant Calculation

In AFM studies, cantilever thickness is typically less than 1 µm and as shown in equation 5.6, thickness is cubed during the calculation of the spring constant. Given that it is challenging to fabricate sub-micron features with precision, small variations in cantilever thickness can therefore significantly impact the cantilever spring constant. Consequently, the experimental method developed by Sader *et al.* [5.41] is commonly used to calculate the spring constant. Sader *et al.* [5.41] identified that the spring constant (k) and the fundamental resonance frequency [Hz] of the cantilever in vacuum (ω_{vac}) are related using:

$$k = M_e \rho_{ct} w t L \omega_{vac}^2 \qquad (5.10),$$

where ρ_{ct} and M_e are the density [kg m^{-3}] and effective mass [kg] of the cantilever. In this scenario, the effective mass of the cantilever is the apparent mass of the cantilever when responding to force. Numerical methods are required to calculate the geometry dependent M_e:

$$M_e = \frac{k}{m\omega_{vac}^2} \qquad (5.11),$$

where m is the mass [kg] of the cantilever. For a long rectangular cantilever (L/w > 5), like those used in this research, Sader *et al.* [5.50] identified that M_e = 0.243. Sader *et al.* [5.41] later related ω_{vac} and ρ_{ct} to the aqueous buffer and cantilever quality factor (Q_f) using the following equation:

$$k = 0.1906 \rho_f w^2 L Q_f \Gamma(\omega_{vac}) \omega_{vac}^2 \qquad (5.12),$$

where ρ_f, ω and the dimensionless Γ are the density [kg m^{-3}], measurement frequency [Hz] and frequency dependent hydrodynamic function of the fluid. The lumped constant 0.1906 still accounts for the effective mass [5.41]. For the equation to provide an accurate estimation, Q_f must be > 1.

The resonant frequency (ω_r) of the cantilever and Q_f can be calculated by measuring the cantilever's thermal noise spectrum. Furthermore, L and w can be easily calculated using standard microscopy. Based on previous experimental works using MeFS cantilevers [5.36, 5.43], ω_r is typically between 73 – 85 kHz, Q_f is ~110 and k is between 0.2 and 2 N m^{-1}.

5.3.12 Force Spectroscopy

5.3.12.1 Force-Distance

The deflection of the cantilever upon contact with a surface is quantified during a force spectroscopy measurement. When contact is made with a surface, the angle of the cantilever changes and this is monitored using a photo-detector, which registers the signal as a voltage (V). This voltage has to be converted to distance in order to give an understandable readout, therefore the deflection sensitivity (S) is obtained by performing a force measurement on a hard substrate (*e.g.* glass) to give a value with units nm V^{-1}. Using the previously attained k value, the force exerted on the tip can be calculated using [5.2]:

$$F = VSk \tag{5.13}$$

Depending on the chemical and mechanical properties of probe and substrate, interface effects such as chemical attraction and electrical potential, for example, can become increasingly influential when a probe nears contact with a substrate. Despite such dependencies, a force-spectroscopy curve generally exhibits the following features (see Figure 5.5) [5.2]: The curve is flat where no contact is made between probe and substrate; when probe and surface are almost in contact a "snap-in" can be observed, where interface effects cause a strong attraction and contact is initiated; when contact is made the cantilever deflection increases depending on the mechanical properties of substrate and cantilever. Thus, data concerning the elasticity and/or deformability of a substrate is within this phase; upon retraction, the cantilever typically sticks slightly to the substrate due to the adhesion force – the value of this force can be easily extracted from a force-spectroscopy curve.

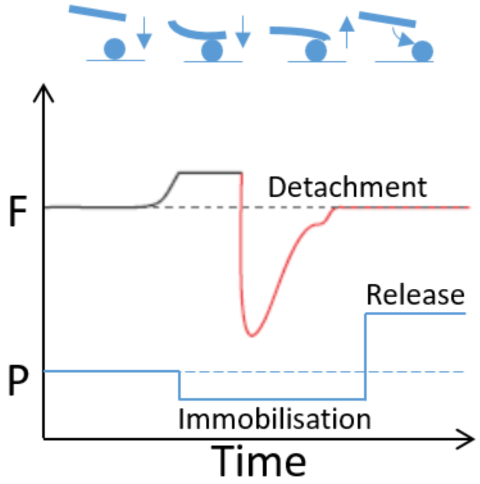

Figure 5.5: Force Spectroscopy Measurement. Force (F; black-red line) and pressure (P; blue line) progress during a force measurement using a cantilever with a hollow aperture. The black line indicates approach and initial contact stages of the force measurement. The red line indicates the typical force curve upon and after the initiation of deflection. The position of the cantilever at each stage of the measurement, with reference to the particle, is indicated using the small series of diagrams shown above the plot. Figure adapted from ref [5.2].

5.3.12.2 Elastic Modulus

In 1882, Henrich Hertz [5.51] developed a classical contact model for calculating the elastic modulus of a substrate (information gathered during contact phase of force measurement). According to this model, the non-adhesive contact between a flat surface and spherical colloid can be described using the following equation:

$$A = \sqrt{Rd} \qquad (5.14),$$

where A is the radius [m] of the contact area, R is the radius of the colloid [m] and d is the depth [m] for which the colloid is forced towards the surface. The applied force (F) [N] can be related to R and d using:

$$F = \frac{4}{3}E^{*}R^{\frac{1}{2}}d^{\frac{3}{2}} \qquad (5.15),$$

where the effective elastic modulus (E^{*}) is:

$$E^{*} = \left(\frac{1-\upsilon_1^2}{E_1} + \frac{1-\upsilon_2^2}{E_2}\right)^{-1} \qquad (5.16).$$

In equation 5.16, E_1 and E_2 are the elastic moduli [N m^{-2}] and υ_1 and υ_2 are the Poisson's ratio (the ratio of the transverse contraction strain and the longitudinal extension strain acting on a surface – which is dimensionless) associated with each component.

The Hertz model makes numerous assumptions which do not hold for many biological cells, *e.g.*, that the substrate is a homogenous substance, which is not true for the complex physiology of the *Cryptosporidium* oocyst. Therefore, it may not be possible to calculate the elastic modulus of an oocyst using the Hertz model. Despite this, in instances where there is a linear increase in force during the contact phase of a force measurement, a linear fit with the units of a spring constant (N m^{-1}) can be attributed to a force-spectroscopy curve. Consequently, an apparent spring constant can be used as an empirical parameter to describe the deformability, rather than elasticity, of the substrate.

5.4 Summary

Information regarding the height and deformability of a biological cell can be obtained using force spectroscopy. As highlighted in Table 2.2, the typical dimensions of *Cryptosporidium* oocysts vary depending on species, therefore, the ability to characterise oocyst size may enable species-level discrimination/ separation. For example, the MeFS platform is capable of motion in *x*-*y*-*z* directions, thus, it may be possible to relocate/ separate oocysts based on size, or the results may simply provide a basis for which to develop passive, microfluidic separation systems. Furthermore, it has been reported that *Cryptosporidium* oocysts are deformable [5.22, 5.23]. Variations in oocyst deformability, likely due to differences in oocyst biochemical composition and size, may again facilitate inter-species discrimination or discrimination between viable and non-viable sub-populations of a single species. The research associated with quantifying the mechanical properties of *Cryptosporidium* and in testing these hypotheses will be detailed later in the chapters to follow.

5.5 References

5.1. Binnig G, Rohrer H, Gerber C, Weibel E. Surface studies by scanning tunneling microscopy. Physical review letters. 1982;49(1):57.

5.2. Guillaume-Gentil O, Potthoff E, Ossola D, Franz CM, Zambelli T, Vorholt JA. Force-controlled manipulation of single cells: from AFM to FluidFM. Trends in biotechnology. 2014;32(7):381-8.

5.3. Müller DJ, Dufrene YF. Atomic force microscopy as a multifunctional molecular toolbox in nanobiotechnology. Nature nanotechnology. 2008;3(5):261-9.

5.4. Albrecht TR, Akamine S, Carver T, Quate CF. Microfabrication of cantilever styli for the atomic force microscope. Journal of Vacuum Science & Technology A. 1990;8(4):3386-96.

5.5. Chasiotis I, Knauss WG. A new microtensile tester for the study of MEMS materials with the aid of atomic force microscopy. Experimental Mechanics. 2002;42(1):51-7.

5.6. Tamayo J, Humphris AD, Miles MJ. Piconewton regime dynamic force microscopy in liquid. Applied Physics Letters. 2000;77(4):582-4.

5.7. Smith D, Connell S, Robinson C, Kirkham J. Chemical force microscopy: applications in surface characterisation of natural hydroxyapatite. Analytica chimica acta. 2003;479(1):39-57.

5.8. Majumdar A, Carrejo J, Lai J. Thermal imaging using the atomic force microscope. Applied Physics Letters. 1993;62(20):2501-3.

5.9. Saenz J, Garcia N, Grütter P, Meyer E, Heinzelmann H, Wiesendanger R, et al. Observation of magnetic forces by the atomic force microscope. Journal of applied physics. 1987;62(10):4293-5.

5.10. Nonnenmacher M, o'Boyle M, Wickramasinghe H. Kelvin probe force microscopy. Applied physics letters. 1991;58(25):2921-3.

5.11. Dörig P, Ossola D, Truong AM, Graf M, Stauffer F, Vörös J, et al. Exchangeable colloidal AFM probes for the quantification of irreversible and long-term interactions. Biophysical journal. 2013;105(2):463-72.

5.12. Dufrêne YF. Atomic force microscopy, a powerful tool in microbiology. Journal of bacteriology. 2002;184(19):5205-13.

5.13. Aeschimann L, Meister A, Akiyama T, Chui BW, Niedermann P, Heinzelmann H, et al. Scanning probe arrays for life sciences and nanobiology applications. Microelectronic Engineering. 2006;83(4):1698-701.

5.14. Franz CM, Taubenberger A, Puech P-H, Muller DJ. Studying integrin-mediated cell adhesion at the single-molecule level using AFM force spectroscopy. Science Signaling. 2007;2007(406):pl5-pl.

5.15. Taubenberger A, Cisneros DA, Friedrichs J, Puech P-H, Muller DJ, Franz CM. Revealing early steps of α2β1 integrin-mediated adhesion to collagen type I by using single-cell force spectroscopy. Molecular biology of the cell. 2007;18(5):1634-44.

5.16. Beaussart A, El-Kirat-Chatel S, Herman P, Alsteens D, Mahillon J, Hols P, et al. Single-cell force spectroscopy of probiotic bacteria. Biophysical journal. 2013;104(9):1886-92.

5.17. Rief M, Gautel M, Oesterhelt F, Fernandez JM, Gaub HE. Reversible unfolding of individual titin immunoglobulin domains by AFM. science. 1997;276(5315):1109-12.

5.18. Carrion-Vazquez M, Oberhauser AF, Fowler SB, Marszalek PE, Broedel SE, Clarke J, et al. Mechanical and chemical unfolding of a single protein: a comparison. Proceedings of the National Academy of Sciences. 1999;96(7):3694-9.

5.19. Fritz J, Katopodis AG, Kolbinger F, Anselmetti D. Force-mediated kinetics of single P-selectin/ligand complexes observed by atomic force microscopy. Proceedings of the National Academy of Sciences. 1998;95(21):12283-8.

5.20. Ando T, Kodera N, Naito Y, Kinoshita T, Furuta Ky, Toyoshima YY. A High-speed Atomic Force Microscope for Studying Biological Macromolecules in Action. ChemPhysChem. 2003;4(11):1196-202.

5.21. Kodera N, Yamamoto D, Ishikawa R, Ando T. Video imaging of walking myosin V by high-speed atomic force microscopy. Nature. 2010;468(7320):72-6.

5.22. Considine RF, Drummond CJ, Dixon DR. Force of interaction between a biocolloid and an inorganic oxide: complexity of surface deformation, roughness, and brushlike behavior. Langmuir. 2001;17(20):6325-35.

5.23. Considine RF, Dixon DR, Drummond CJ. Oocysts of Cryptosporidium parvum and model sand surfaces in aqueous solutions: an atomic force microscope (AFM) study. Water Research. 2002;36(14):3421-8.

5.24. Lytle DA, Johnson CH, Rice EW. A systematic comparison of the electrokinetic properties of environmentally important microorganisms in water. Colloids and Surfaces B: Biointerfaces. 2002;24(2):91-101.

5.25. Byrd T, Walz J. Interaction force profiles between Cryptosporidium parvum oocysts and silica surfaces. Environmental science & technology. 2005;39(24):9574-82.

5.26. Byrd T, Walz J. Investigation of the interaction force between Cryptosporidium parvum oocysts and solid surfaces. Langmuir. 2007;23(14):7475-83.

5.27. Tufenkji N, Dixon DR, Considine R, Drummond CJ. Multi-scale Cryptosporidium/sand interactions in water treatment. Water research. 2006;40(18):3315-31.

5.28. Jaschke M, Butt H-J. Deposition of organic material by the tip of a scanning force microscope. Langmuir. 1995;11(4):1061-4.

5.29. Piner RD, Zhu J, Xu F, Hong S, Mirkin CA. " Dip-pen" nanolithography. science. 1999;283(5402):661-3.

5.30. Meister A, Liley M, Brugger J, Pugin R, Heinzelmann H. Nanodispenser for attoliter volume deposition using atomic force microscopy probes modified by focused-ion-beam milling. Applied Physics Letters. 2004;85(25):6260-2.
5.31. Deladi S, Tas N, Berenschot J, Krijnen G, De Boer M, De Boer J, et al. Micromachined fountain pen for atomic force microscope-based nanopatterning. Applied physics letters. 2004;85(22):5361-3.
5.32. Kim KH, Moldovan N, Espinosa HD. A Nanofountain Probe with Sub-100 nm Molecular Writing Resolution. Small. 2005;1(6):632-5.
5.33. Meister A, Gabi M, Behr P, Studer P, Vörös Jn, Niedermann P, et al. FluidFM: combining atomic force microscopy and nanofluidics in a universal liquid delivery system for single cell applications and beyond. Nano letters. 2009;9(6):2501-7.
5.34. Grüter RR, Vörös J, Zambelli T. FluidFM as a lithography tool in liquid: spatially controlled deposition of fluorescent nanoparticles. Nanoscale. 2013;5(3):1097-104.
5.35. Stiefel P, Schmidt FI, Dörig P, Behr P, Zambelli T, Vorholt JA, et al. Cooperative vaccinia infection demonstrated at the single-cell level using FluidFM. Nano letters. 2012;12(8):4219-27.
5.36. Dörig P, Stiefel P, Behr P, Sarajlic E, Bijl D, Gabi M, et al. Force-controlled spatial manipulation of viable mammalian cells and micro-organisms by means of FluidFM technology. Applied Physics Letters. 2010;97(2):023701.
5.37. Potthoff E, Guillaume-Gentil O, Ossola D, Polesel-Maris J, LeibundGut-Landmann S, Zambelli T, et al. Rapid and serial quantification of adhesion forces of yeast and mammalian cells. PLoS One. 2012;7(12):e52712.
5.38. Guillaume-Gentil O, Potthoff E, Ossola D, Dörig P, Zambelli T, Vorholt JA. Force-Controlled Fluidic Injection into Single Cell Nuclei. Small. 2013;9(11):1904-7.
5.39. Potthoff E, Ossola D, Zambelli T, Vorholt JA. Bacterial adhesion force quantification by fluidic force microscopy. Nanoscale. 2015;7(9):4070-9.
5.40. Ossola D, Amarouch M-Y, Behr P, Vörös Jn, Abriel H, Zambelli T. Force-controlled patch clamp of beating cardiac cells. Nano letters. 2015;15(3):1743-50.
5.41. Sader JE, Chon JW, Mulvaney P. Calibration of rectangular atomic force microscope cantilevers. Review of Scientific Instruments. 1999;70(10):3967-9.
5.42. Stark RW, Drobek T, Heckl WM. Thermomechanical noise of a free v-shaped cantilever for atomic-force microscopy. Ultramicroscopy. 2001;86(1):207-15.

5.43. Dörig P. Manipulating cells and colloids with FluidFM. Zurich: ETH Zurich; 2013.

5.44. Meyer G, Amer NM. Novel optical approach to atomic force microscopy. Applied physics letters. 1988;53(12):1045-7.

5.45. Danzebrink H-U, Koenders L, Wilkening G, Yacoot A, Kunzmann H. Advances in scanning force microscopy for dimensional metrology. CIRP Annals-Manufacturing Technology. 2006;55(2):841-78.

5.46. Geisse NA. AFM and combined optical techniques. Materials today. 2009;12(7):40-5.

5.47. Bautsch H, Bohm J. Kleber: Einführung in die Kristallographie, 18. Auflage, Verlag Technik Berlin. 1998.

5.48. Hunklinger S, Kittel C. Einführung in die Festkörperphysik. 2005.

5.49. Bhushan B, Marti O. Scanning probe microscopy–principle of operation, instrumentation, and probes. Springer handbook of nanotechnology: Springer; 2010. p. 573-617.

5.50. Sader JE, Larson I, Mulvaney P, White LR. Method for the calibration of atomic force microscope cantilevers. Review of Scientific Instruments. 1995;66(7):3789-98.

5.51. Hertz H. Über die Berührung fester elastischer Körper. Journal für die reine und angewandte Mathematik. 1882;92:156-71.

Chapter 6 – Methods for Force Spectroscopic Analysis of Waterborne Parasites

6.1 Introduction

This chapter describes the microfluidic-enabled force spectroscopy (MeFS) system parameters, experimental methods and analytical procedures used to characterise the biomechanical properties (*i.e.*, height and deformability) of viable and non-viable oocysts of the human-pathogenic *C. parvum*. Similar methods were used to characterise the biomechanical properties of *Cryptosporidium* species which pose either a major (*C. parvum*) or minor risk to human health (*C. muris*). This work was carried out to assess whether the differences in size and/ or deformability between different oocyst populations were large enough such that passive, microfluidic separation systems, *e.g.*, deterministic lateral displacement (DLD) devices [6.1], could be developed to efficiently sort the populations. The findings have been published in PLOS One [6.2] and an author contribution statement is provided in section 7.5 .

6.2 Oocyst Preparation

Samples containing either 1.25 x 10^6 *C. parvum* or *C. muris* oocysts mL^{-1} PBS + antibiotics + 0.01% Tween 20 were obtained from Waterborne Inc. (US) and stored at 4 °C until use. Experiments were performed within 2 months of receiving the stock suspensions. To perform measurements using inactivated oocysts, samples containing *C. parvum* were incubated at 70 °C in a heating block for 10 min [6.3]. Additional samples were inactivated using a freeze-thaw treatment that consisted of an overnight cycle of freezing at -18^0 C for 18 hr [6.3], in order to assess whether oocysts displayed similar behaviour despite a different inactivation procedure.

6.3 Force Spectroscopy

In order to perform microfluidic-enabled force spectroscopy a FluidFM (Cytosurge AG, Switzerland) was used. Access to this technology was gained by contacting and subsequently establishing a collaboration with Dr. Jos Quist, a postdoctoral researcher in the group of Professor Serge Lemay at the University of Twente, Netherlands. The FluidFM system includes a Zeiss Axio Observer.Z1 inverted microscope (Figure 6.1), onto which a FlexAFM 5 scan head (both Nanosurf AG, Switzerland) is secured – see section 5.3 to recap on terminology. In order to minimise the effects of background noise on measurements, the system was positioned on top of a passive vibration isolation table. Microchannelled force spectroscopy cantilevers (Cytosurge) – which were actuated using a pressure controller – were used to immobilise single oocysts and perform deflection measurements. Due to the difference in typical dimensions of *C. parvum* and *C. muris* oocysts (see Table 2.2, Chapter 2), cantilevers with 2 μm or 4 μm apertures were used respectively. For each set of measurements, a 4 μL aliquot of suspension containing ~5000 oocysts was dispensed into a petri dish containing 7-8 mL of PBS – a buffer volume of this order was required to ensure that the cantilever tip was fully submerged.

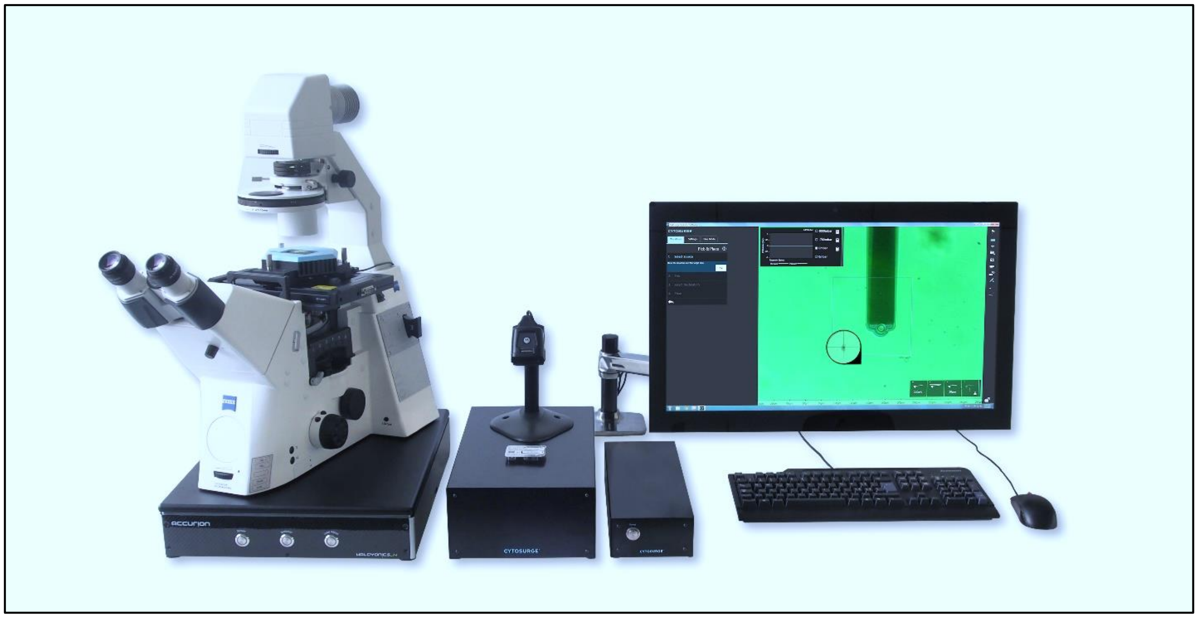

Figure 6.1: The FluidFM setup. Image provided by and reproduced with the permission of Cytosurge (https://www.cytosurge.com).

Custom CyUI software developed by Cytosurge permitted the simultaneous control of microscopy, pressure and force spectroscopy. In order to calibrate the system before performing experiments, the Sader method [6.4] was used to measure the spring constant of an unfilled cantilever (typically ~2 N m^{-1}), which was then corrected for the 11° angle of the cantilever [6.5]. The deflection sensitivity of a water-filled cantilever was measured through hard contact with the substrate (petri dish surface), whilst suspended in PBS. Force spectroscopy measurements of immobilised oocysts were conducted by using suction (applied *via* the external pressure controller) to hold the subject/ oocyst at the cantilever aperture before approaching the cantilever with the substrate at a speed of 600 nm/s. A slow approach speed was used to firstly ensure that the cantilever slowly approached and did not crash into the surface. Secondly, slow approach ensures that the attachment and detachment of the subject to a surface can be more accurately measured. All measurements were performed at room temperature (21 °C).

6.4 Data Analysis

Matlab version R2015a (Mathworks, USA) was used to convert deflection measurements to force-distance (F-D) curves and perform the subsequent data analysis. To minimise the effects of noise artefacts, curves were binned over 16 or 40 data points for *C. parvum* or *C. muris* – whereby the original sample frequencies were 2400 and 6000 Hz, respectively – giving one data point per 4 nm of the retrieved F-D curve. In order to obtain the height of an oocyst (compressed) at each datapoint, piezo displacement was subtracted from the initial cantilever-substrate separation, before this value was corrected for cantilever deflection. To give an accurate estimate of the point of first contact between surface and an immobilised subject, a threshold of 0.1 nN was used on the approach curves. The corresponding cantilever-substrate separation then gave an indication of oocyst height – the difference in distance at the point of first contact without and then with an oocyst attached. In instances where the F-D curve contained a kink (discussed in more depth in section 7.2.4), the data points on and above the kinks were not included in the analysis. To estimate deformability (*i.e.*, the effective spring constant) of subjects, a linear fit was applied to the upper section of the F-D curves. Figure 6.2 gives an overview of the steps involved in the data analysis.

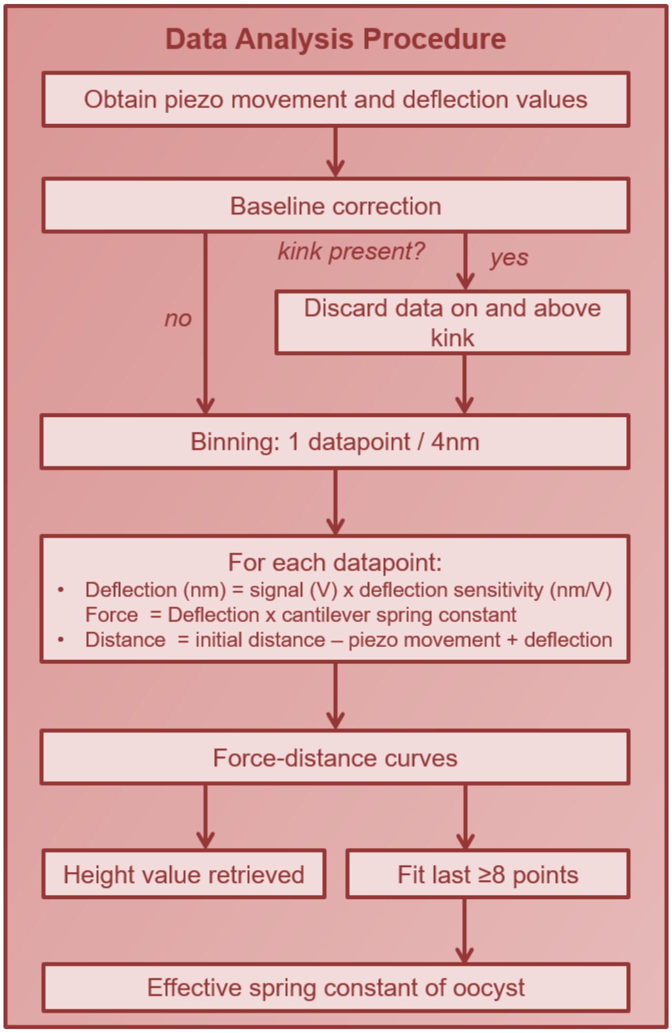

Figure 6.2: Data analysis procedure for force spectroscopy data. Adapted from McGrath *et al.* [6.2] with permission (https://creativecommons.org/licenses/by/4.0/legalcode).

6.5 Statistical Analysis

Height and deformability data for untreated, heat-treated and freeze-thaw treated *C. parvum* were tested for distribution normality and equal variance using SPSS Statistics (Version 22, IBM) to assess the applicability of statistical tests which were designed for use with parametric data. In particular, data normality was assessed using the Kolmogorov-Smirnov and Shapiro-Wilk tests – due to the presence of skewness in spring constant distributions, data are frequently discussed using median and quartile values (unless stated otherwise). Levene's F test was used to test data for homogeneity of variance. As a result, Welch's F test and the Games-Howell test were used –both are commonly used in connection with Levene's F test for *post-hoc* analysis – to compare the deformability data of the differing oocyst populations. Since the assumption of homogeneity of variances was met for oocyst height data, a one-way analysis of variance test was utilised for comparison of the respective data. Significance was recorded at the 0.05 confidence level ($p < 0.05$).

A custom script was developed using Matlab (R2015a) to quantify the discrimination efficiency of the oocyst populations on the basis of height or spring constant distribution where relevant (*e.g.*, it was not necessary to quantify the overlap of height data for untreated vs temperature-inactivated *C. parvum* as all populations demonstrated considerable distribution overlap or similarity in values). Due to the non-normal distribution of some datasets, non-parametric methods of estimation were used to calculate the discrimination probability. Specifically, a kernel probability density function (PDF) was applied to height or spring constant data of two populations to determine the overlapping area (see Figure 6.3). The probability that an oocyst from either population may plot within the region of overlap was calculated using the respective cumulative distribution functions (CDFs). Discrimination probability (DP) was calculated using: 1 – the probability of the overlapping area x 100 (%).

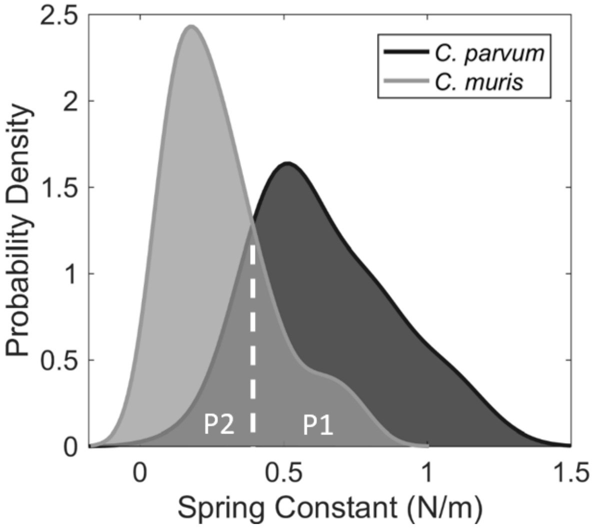

Figure 6.3: Example of calculation of discrimination efficiency between two populations. Using spring constant data as an example: the discrimination probability (DP) was estimated by firstly calculating the probability density function (PDF) of *C. parvum* (light grey) and *C. muris* (black) data; non-parametric PDFs (*i.e.*, Kernel PDFs) were used due to skewness (non-normality) of data distribution. The probability of finding a *C. muris* oocyst within the *C. parvum* population (P1) plus the probability of finding a *C. parvum* oocyst within the *C. muris* population (P2) was then calculated; this is the probability of the overlapping area. Finally, the DP was calculated by finding the percentage of the total area which was completely discrete; DP = 1 - (P1 + P2) x 100%. Adapted from McGrath *et al*. [6.2] with permission under the CCBY 4.0 license: (https://creativecommons.org/licenses/by/4.0/legalcode).

6.6 Summary

The system hardware, system parameters, experimental methods and data analysis procedure used to characterise the biomechanical properties of waterborne pathogens were described within this chapter. The findings of this work are detailed in Chapter 7.

6.7 References

6.1. McGrath J, Jimenez M, Bridle H. Deterministic lateral displacement for particle separation: a review. Lab on a Chip. 2014;14(21):4139-58.

6.2. McGrath JS, Quist J, Seddon JR, Lai SC, Lemay SG, Bridle HL. Deformability Assessment of Waterborne Protozoa Using a Microfluidic-Enabled Force Microscopy Probe. PloS one. 2016;11(3):e0150438.

6.3. Fayer R, Xiao L. Cryptosporidium and Cryptosporidiosis, Second Edition: Taylor & Francis; 2012.

6.4. Sader JE, Chon JW, Mulvaney P. Calibration of rectangular atomic force microscope cantilevers. Review of Scientific Instruments. 1999;70(10):3967-9.

6.5. Heim L-O, Kappl M, Butt H-J. Tilt of atomic force microscope cantilevers: effect on spring constant and adhesion measurements. Langmuir. 2004;20(7):2760-4.

Chapter 7 – Results of Microfluidic-enabled Force Spectroscopy Analysis

7.1 Introduction

Cryptosporidium-contaminated environmental samples are known to frequently contain a variety of *Cryptosporidium* species not all hazardous to human health [7.1] and which also portray a mixture in viability status [7.2]. If the deformability and/ or size of *Cryptosporidium* oocysts varies considerably between, *e.g.*, different species, and should such variation be quantifiable at the single-oocyst level, then the resulting analysis techniques would be of considerable interest to water utilities. For instance, if different *Cryptosporidium* species could be efficiently discriminated using a new technique, then treatment, detection and risk mitigation frameworks could be optimised by water utilities to save numerous resources.

Therefore, in this chapter the characterisation of the size and deformability of human-pathogenic and non-human pathogenic species, plus the deformability of viable and heat-inactivated oocysts of the same human-pathogenic species has been undertaken using MeFS [7.3, 7.4]. The results are detailed below. One option for exploiting the potential differences would be to directly use MeFS for the sorting of, *e.g.*, human-pathogenic and non-human pathogenic oocysts, as subjects can be immobilised and relocated in the *x*-*y*-*z* planes. Nonetheless, such a procedure would likely be labour-intensive (unless an automated platform can be developed), given that an operator is required to direct system processing. Therefore, it is more likely that the findings of such research may provide a basis for the development of alternate technologies which perform size- and/ or deformability-based sorting – *e.g*, microfluidics [7.5-7.8] – to more accurately evaluate the risk associated with *Cryptosporidium*-contaminated drinking-water samples. In addition, similar methods may then be employed for the sorting of viable and non-viable sub-populations of the same human-pathogenic species, should the degradation of oocyst wall and internal structures upon viability loss result in a measurable change in deformability. Therefore, the quantification of size and deformability of human-pathogenic and non-human pathogenic species, plus the deformability between viable and non-viable oocysts of the same human-pathogenic species, are of considerable interest to optimise treatment, detection and risk mitigation frameworks.

The use of colloidal probe microscopy (previously introduced in section 5.1.2) to analyse the biomechanical properties of the outer wall of the human-pathogenic *C. parvum* (*CP*) has been reported previously [7.9-7.13]. Such works mainly investigated the colloidal properties of *CP* (*e.g.,* oocyst interactions with sand particles), but provided little, valuable information concerning the overall deformability of oocysts. For example, Considine *et al*. [7.9] reported highly variable effective spring constants of *CP* oocysts, however, sample size (n = 5) was small, thus limiting confidence in the stated values. Furthermore, no comparison was made between viable and non-viable human-pathogenic oocysts or different *Cryptosporidium* species. Thus, the development of a force spectroscopy method for routinely measuring the biomechanical properties of *Cryptosporidium* oocysts is desirable.

In this work, a FluidFM (introduced in Chapter 5) was used for force spectroscopy on relatively large numbers of individual oocysts (n > 50) to assess the effect of temperature-based inactivation treatments on *CP* and the inter-species deformability of *CP vs. C. muris* (*CM*). Oocyst immobilisation and release were achieved by applying negative or positive pressure, respectively, and individual oocysts were measured in rapid sequence and in multiple orientations, demonstrating considerable advance over traditional colloidal probe microscopy.

7.2 Single Cell Analysis

7.2.1 Oocyst Selection and Force Measurement

Oocysts were attracted towards the cantilever and immobilised by applying a suction pressure of -300 to -500 mbar and finally a force measurement was performed (Figure 7.1). The cantilever was then relocated to an arbitrary position and the subject released using a pressure pulse up to 100 mbar. When sampling, over 50 oocysts were measured per hour when performing single measurements of each subject and over 200 discrete measurements were performed per hour when five measurements were performed on each oocyst. USEPA 1623.1 (7.14) derived, *Cryptosporidium*-positive samples typically contain between 1 – 90 oocysts per 1000 L filtered drinking-water [7.1], which is concentrated to a 50 µL detection volume. Therefore, in principle, this force spectroscopy method enables the simultaneous measuring of the height and deformability of all oocysts within 1.5-2 hours, which is equivalent to the existing staining and microscopic detection method. Furthermore, automation of the sample replacement and oocyst selection procedure could enable a throughput of several samples per hour and significantly reduce labour demands.

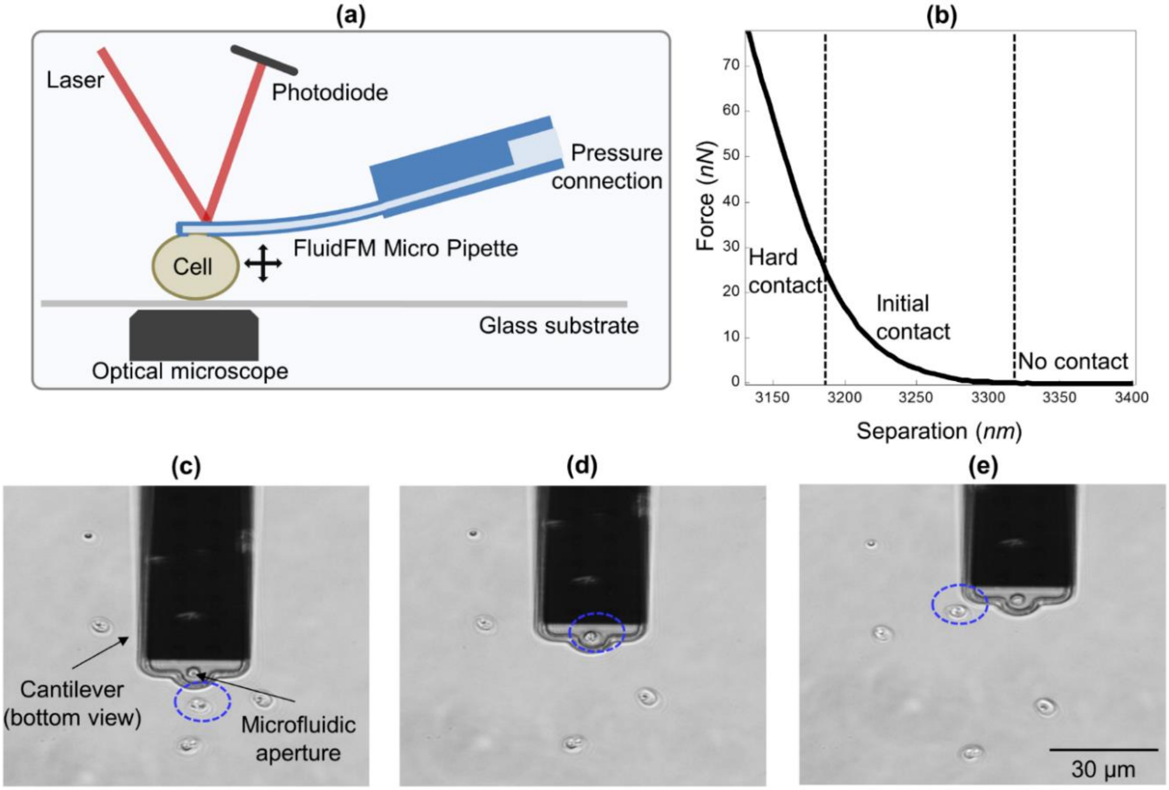

Figure 7.1: Force measurement of *Cryptosporidium*. **(a)** Schematic representation of FluidFM setup. **(b)** Typical Force-distance (F-D) curve showing zero (no contact), exponential (initial contact), and linear (hard contact) increase of force. An oocyst (indicated by dashed blue oval) is **(c)** attracted and immobilised, **(d)** measured and **(e)** subsequently released. Reproduced from McGrath *et al*. [7.15] with permission (https://creativecommons.org/licenses/by/4.0/legalcode).

7.2.2 Force-Distance Curves

The force-distance (F-D) curve retrieved upon measurement of a *Cryptosporidium* oocyst typically comprised of three elements: zero force under no contact between the oocyst and glass surface, at initial contact with the surface there was an exponential-like increase in force and a linear increase was evident upon hard contact – see Figure 7.1b. Tufenkji *et al.* [7.12] have previously attributed the exponential-like element of the F-D curve to the extending layer of glycoprotein which protrudes from the oocyst outer wall. We attribute the linear element of the F-D curve to the deformation of the oocyst body, based on the assumption that the glycoprotein layer is fully collapsed during hard contact with the surface. As repulsive, electrostatic interactions become shorter-ranged with increasing ionic strength of buffer, any effects of electrostatic repulsion between the oocyst and the glass surface were considered negligible (Debye screening length < 1 nm) due to the high ionic content of the buffer (~ 0.15 mol L^{-1}).

The deformation of the *Cryptosporidium* oocyst can be estimated using a linear fit (mean $R^2 > 0.99$), whereby the slope of this fit has the units of a spring constant (N m^{-1}). Although this method of estimation has also been employed by other researchers [7.9, 7.10], the physical basis by which this linear deformation occurs is not well understood: oocysts are spheroidal in shape, thus, the contact area increases during compression with the surface, and one would expect a 3/2 power relationship, *i.e.*, as described in the Hertz model for the deformation of elastic spheres [7.16]. Despite this, several assumptions which hold for the elastic spheres described by the Hertz model, do not hold for oocysts (and indeed most biological objects) – see section 5.3.12. For example, an oocyst generally contains four sporozoites and a large residual body, which is indicative of an intricate, internal structure, thus, an oocyst cannot be described as a homogeneous substance. Due to the lack of an underlying physical model, the obtained apparent spring constant of an oocyst was used as an empirical measure of oocyst deformability.

If the initial, exponential-like element of the F-D curve is considered, the glycoprotein layer that protrudes the outer wall might be modelled as a neutral polymer brush, as described by the de Gennes model [7.11, 7.17]. If adopting this model, an F-D curve must be corrected for the deformations of the oocyst body. However, linear deformation of the oocyst body during the initial contact element cannot be assumed, *e.g.*, increase of contact area might play a significant role. Consequently, it is difficult to efficiently differentiate between the contributions of the collapse of the protruding glycoprotein layer and oocyst body deformation during initial contact. Thus, the initial element of the F-D curves was not included in further analysis – the following sections will discuss the characteristics of and parameters which can be extracted from the remaining elements of the F-D curve.

7.2.3 Multiple Measurements per Oocyst

Upon the completion of a force measurement, an individual oocyst can be released, re-attracted, immobilised and measured multiple times without damaging its structure (*i.e.*, there is no systematic trend or observable change in subsequent measurements). Subsequently, experiments were completed to evaluate the variability in height and spring constant of *CP*, whereby an oocyst was immobilised, five force measurements performed and the oocyst released, before this full process was repeated a successive four times using the same oocyst. The orientation in which a subject was immobilised and/ or re-immobilised was assumed to be random, due to the use of a pressure-based attract and release mechanism. Shown in Figure 7.2 are a series of F-D curves obtained from one untreated *CP* oocyst – each colour represents a set of five measurements performed without releasing the subject. For each measurement set, the shape of the F-D curves was highly reproducible, which indicates that an elastic rather than plastic deformation of the oocyst occurs during force measurement. Random shifts of 50-100 nm, which we consider to be evidence of mechanical drift, are observable between the curves of each measurement set. Such drift is likely a consequence of the large mechanical loop between the sample and the cantilever in the FluidFM. For an AFM-based method this level of drift is relatively large, however, it does not seriously affect the analysis or conclusions of this work.

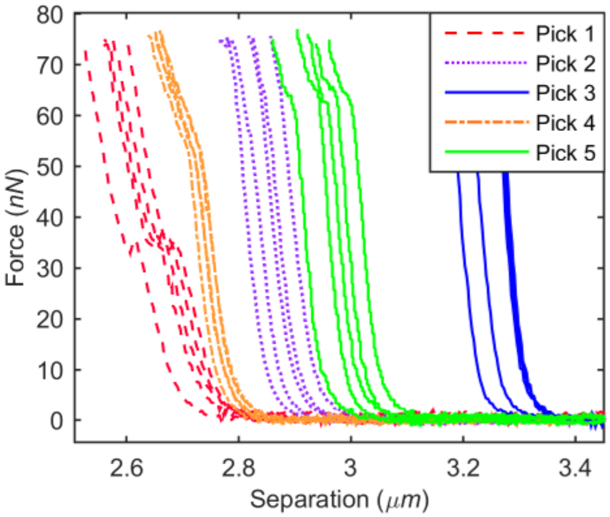

Figure 7.2: Force-distance curves for five sets of force measurements with a single *CP* oocyst. With an oocyst immobilised, five measurements were performed in sequence and a single colour was assigned to the resulting force-distance curves; after release and subsequent re-immobilisation another colour assigned to the next set of five force measurements. Adapted from McGrath *et al.* [7.15] with permission under license (https://creativecommons.org/licenses/by/4.0/legalcode).

Figure 7.2 shows that the calculated height for a single oocyst varied between ~2.7 – 3.3 µm, which indicates that orientation changed frequently between measurement sets. *Cryptosporidium* oocysts are generally spheroidal in shape, *e.g.*, *CP* oocysts reportedly have minor and major axes of lengths 4.5 µm and 5.5 µm, respectively [7.18]. Therefore, it is conceivable that different heights would be recorded when an oocyst is released and re-immobilised between measurements. The hollow aperture – a feature of all cantilevers used in this study – makes it possible to immobilise oocysts, however the pressure-based mechanism causes a portion of the subject to be held within the aperture during measurements. Consequently, the reported height values are an underestimation of the actual dimensions of oocysts. Nonetheless, use of this technology allows the user to rapidly measure individual pathogens many times and in several orientations.

7.2.4 Kinks in Force-Distance Curves

Several of the sets of F-D curves shown in Figure 7.2 (*i.e.*, “Pick 1” and “Pick 5”) displayed highly reproducible kinks when multiple measurements were completed without releasing an oocyst. This behaviour may be explained by a reorientation of the oocyst at the aperture of the cantilever during the initial contact element of the force measurement, or perhaps by a reversible change of the oocyst structure (*e.g.*, the inward folding of the oocyst wall) under influence of the applied force – incidentally, a common feature of curves which displayed kinks was that they provided a lower effective spring constant on average (Figure 7.3).

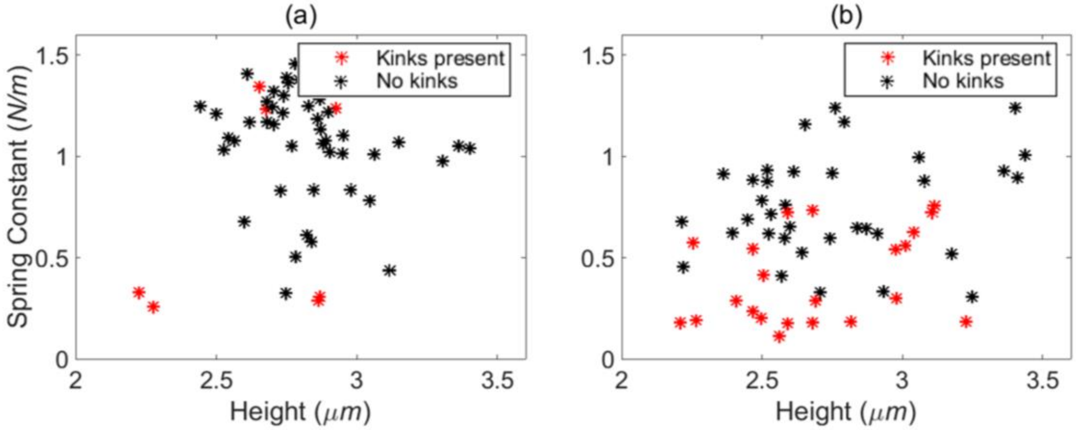

Figure 7.3: Occurrence of kinks in force-distance curves. Distribution of effective spring constant *vs*. height values for untreated **(a)** and freeze-thawed **(b)** *CP*; the relative occurrence of kinks (indicated by red ‘*’) is higher for lower apparent spring constants, possibly because of a sliding movement of the oocysts during the measurement. Adapted from McGrath *et al*. [7.15] with permission under license (https://creativecommons.org/licenses/by/4.0/legalcode).

The type of structural transition, or motion, which corresponds with the observable kinks in Figure 7.2 was not always identifiable, given the limited resolution of optical microscopy. Despite this, in some instances it was possible to correlate kinks with a rotational movement of the oocyst during force spectroscopy – see Video S1 at reference [7.15] which corresponds with Figure 7.4.

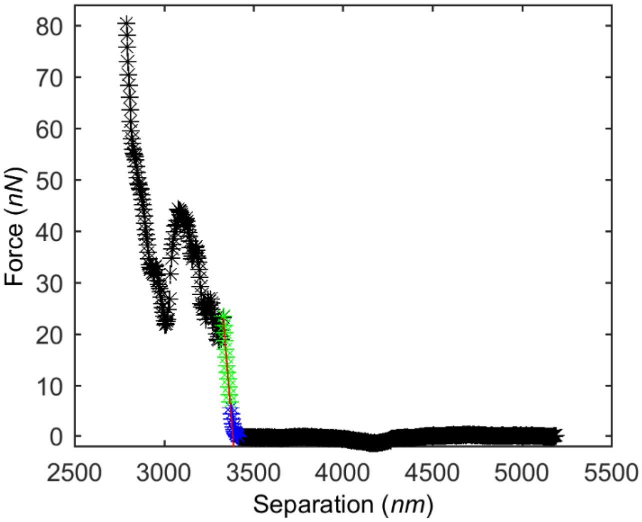

Figure 7.4: Force-distance curve for oocyst that underwent rotational movement during measurement. Visit reference [7.15] to see S1 Video which corresponds with this F-D curve. The apparent kink is representative of the force profile gathered upon the rotational movement of the oocyst during measurement. A linear fit (red line) is applied to data gathered during hard contact and represents the effective spring constant of the oocyst. The data on/ above the kink were excluded from the linear fit. Green points are fitted points and correspond to hard contact. Blue points correspond to the early, exponential-like contact phase. The rightmost blue point (force starts to exceed a 0.1 nN threshold) indicates the measured oocyst height. Adapted from McGrath *et al*. [7.15] with permission under license (creativecommons.org/licenses/by/4.0/legalcode).

7.2.5 Effect of Suction Pressure

Due to the versatility of the pressure controller, it was possible to attract and immobilise subjects using a variety of suction pressures. To assess whether varying suction pressure influenced oocyst deformability, multiple force measurements were conducted at a range of suction pressures (50 – 700 mbar) using two oocysts – Figure 7.5. At each pressure, up to eight force measurements were performed and oocysts were released between measurements to account for the effects of any changes in orientation. Although there was a large difference between the average effective spring constant values of each oocyst, it appeared that the measured spring constant was independent of suction pressure, except for the lowest pressures (50 – 100 mbar). However, the frequency of kinks increased at these low suction pressures (there was also a decrease in the average force threshold at which these events occurred): it appears that when immobilised loosely, it is easier for an oocyst to reorient during measurement.

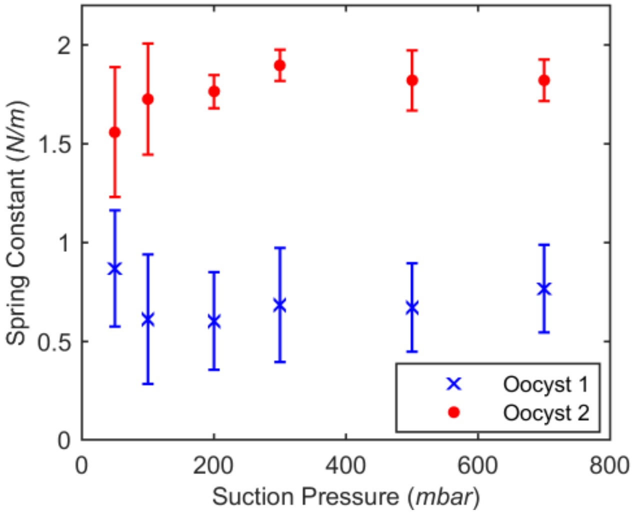

Figure 7.5: Effective spring constant values calculated whilst two different oocysts were immobilised at the cantilever using a variety of suction pressures. Adapted from McGrath *et al*. [7.15] with permission under CCBY 4.0 license (https://creativecommons.org/licenses/by/4.0/legalcode).

7.3 Batch Analysis

7.3.1 Inter-species Variation in Deformability and Height

Effective spring constant and height values for untreated *CM* or *CP* oocysts were retrieved using the respective force spectroscopy measurements, which were performed using a suction pressure of 300 mbar. The scatter plot in Figure 7.6a shows height *vs.* spring constant values for *CM* and *CP* oocysts. Figure 7.6b displays a histogram of spring constant distribution, meanwhile Figure 7.6c shows height distribution. The results suggest that *CP* oocysts are generally less deformable (median spring constant = 0.59 N m^{-1}) than *CM* oocysts (median

= 0.24 N m^{-1}). In addition, more variance existed in the heights of *CM* oocysts than *CP* – this is likely due to difference between the typical minor and major axis dimensions of *CM* (on average 5.6 μm x 7.4 μm) [7.18] being nearly a factor of two larger than that of *CP* (4.5 μm x 5.5 μm) [7.18]. Using the height data, we estimate a coefficient of variance (CV) of 9.7% and 12.1% for *CP* and *CM*, respectively.

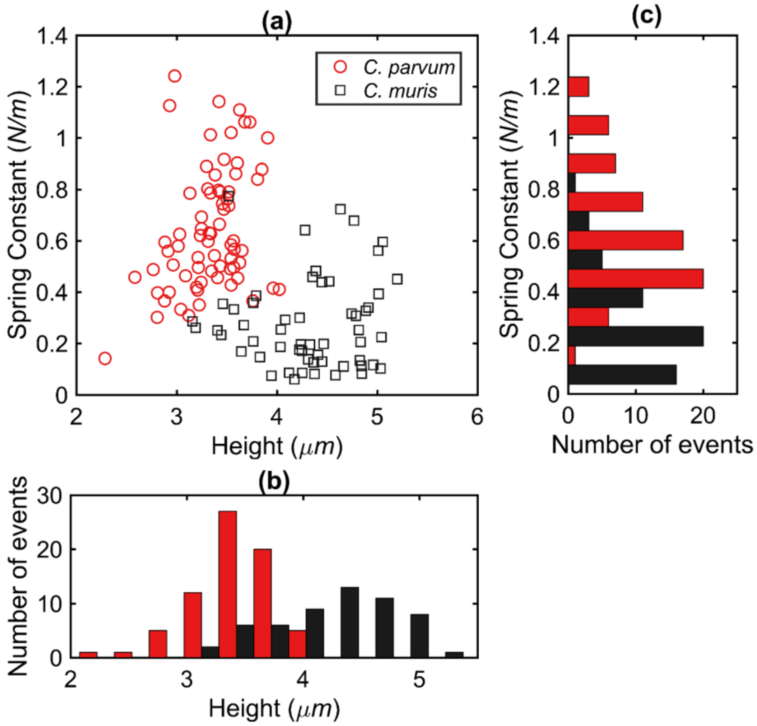

Figure 7.6: Deformability and height of untreated *CM* and *CP* oocysts. **(a)** Height and spring constant data for single oocysts of *CP* (*n* = 71) and CM (*n* = 56) are plotted along with side histograms, which show spring constant **(b)** and height **(c)** distributions independently. The human pathogenic *CP* is represented in red and *CM* in black. Adapted from McGrath *et al*. [7.15] with permission under CCBY 4.0 license (https://creativecommons.org/licenses/by/4.0/legalcode).

To calculate the level of discrimination achieved, based on either spring constant or height data, non-parametric probability density estimations were used. This process involved firstly fitting a kernel probability density function (PDF) to the data to define the overlapping area between the PDFs. Next, the respective cumulative distribution functions (CDFs) were used to calculate the probability that an oocyst was within the overlapping region and, thus, indicate the level of discrimination (*i.e.*, the percentage of the oocyst population which did not plot within the overlapping region) – see Figure 6.3 for an overview of the procedure. Using height data, *CP* (median = 3.38 µm) was discriminated from *CM* (median = 4.36 µm) with 86% efficiency, whilst a discrimination efficiency of 81% was calculated for the same populations using on spring constant data. Despite the existence of overlap between the distributions of spring constant or height data, the level of discrimination between *CP* and *CM* is improved in the scatterplot of height *vs.* spring constant (Figure 7.6), where discrimination is dependent on both characteristics.

Our results imply that near complete separation of these *Cryptosporidium* species may be difficult to achieve in, *e.g.*, size-based and/ or deformability-based microfluidic systems. For example, our findings show that *CM* is more deformable than *CP*, however *CP* is typically smaller than *CM*. Thus, I anticipate that, when experiencing sufficient fluidic pressure within a microchannel, the deformation of *CM* oocysts will occur before *CP*. Consequently, CM oocysts would effectively become smaller and the efficiency of the separation would likely be reduced. Despite this, FluidFM could be used for the same purpose, as the method utilises the size and deformability properties independently to facilitate discrimination. Furthermore, oocysts can be easily immobilised, therefore, they can be removed from the sample or placed at a defined location to enable sorting. The "major" human-pathogenic species (*C. hominis*, *C. parvum*, *C. meleagridis*, *C. cuniculus*, *C. felis* and *C. canis*) of *Cryptosporiidum* are typically similar in size (~4.0 – 5.5 µm) – see Table 2.2, thus, analysis could potentially be performed to discriminate between oocysts of the "major" species and others that are out with this size range (*e.g., C. xiaoi, C. muris, C. andersoni* and *C. baileyi*).

7.3.2 Height and Deformability of Untreated and Temperature-inactivated *C. parvum*

Force measurements were performed using sub-populations of untreated, heat-treated and freeze-thawed *C. parvum* – distributions of height and spring constant data are displayed in Figure 7.7. For each sub-population, 30 separate oocysts were measured in up to eight discrete orientations at a constant suction pressure of 500 mbar. Distributions of height data for each sub-population are presented in Figure 7.7a. It is evident in Figure 7.7c that the distributions of heat-treated, freeze-thawed and untreated *C. parvum* completely overlap, which indicates that oocyst size does not provide a marker for viability – as stated in section 3.3.2.

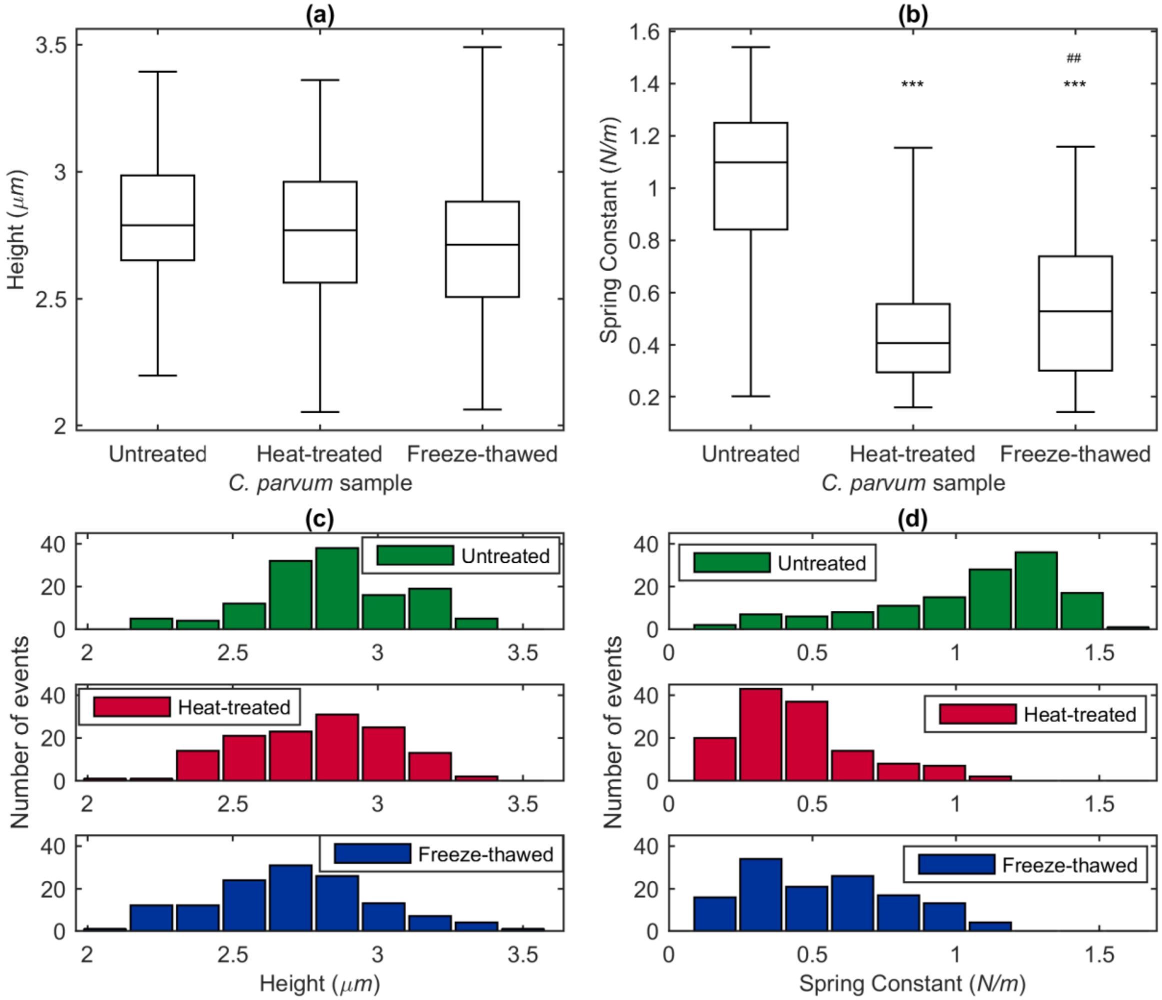

Figure 7.7: Height and spring constant data for sub-populations of untreated and temperature-inactivated *C. parvum*. Height **(a)** and spring constant **(b)** data for untreated (*n* = 184), heat-treated (*n* = 224) and freeze-thawed *C. parvum* (*n* = 131) are represented by boxplots which display medians and quartiles for the respective distributions; the upper and lower error bar caps are indicative of the maximum and minimum recorded values. *** Significantly different from untreated group ($p < 0.001$). $^{\#\#}$ Significantly different from heat-treated group ($p < 0.01$). The distributions of height **(c)** and spring constant **(d)** are presented using histograms. Reproduced from McGrath *et al.* [7.15] with permission – license (https://creativecommons.org/licenses/by/4.0/legalcode).

The distributions of spring constant data shown in Figure 7.7b suggest that temperature-inactivated oocysts are more deformable than untreated oocysts. Upon inactivation, the degradation of internal structures, for example membranes and organelles of the sporozoites contained within an oocyst, may contribute to the measured deformability increase. Alternatively, the structure and rigidity of the oocyst outer wall may have been compromised. The composition of the inner [7.19] and central [7.20] layers of the trilaminar *C. parvum* outer wall are considered to contribute to the overall elasticity of the oocyst outer wall. Upon temperature-inactivation, the responsible proteins within these layers may have become damaged.

A statistically significant difference between the deformability of untreated and temperature-inactivated *C. parvum* was indicated by the Welch's F test; $F\ (2,290) = 192.62$, $p < 0.001$. Additionally, *post-hoc* means analysis using the Games-Howell test revealed a statistically significant decrease in spring constant for freeze-thawed (mean difference = 0.46 N m^{-1}, $p < 0.001$) and heat-treated (mean difference = 0.56 N m^{-1}, $p < 0.001$) *C. parvum* in comparison to untreated oocysts (mean = 1.03 N m^{-1}). Using a similar method to that outlined previously, a discrimination efficiency of 85% was estimated using the spring constant data of untreated and heat-treated oocysts. Furthermore, 78% discrimination of untreated and freeze-thawed oocysts was achieved using spring constant data. A statistically significant difference was also measured between the spring constants of heat-treated and freeze-thawed oocysts using a Games-Howell test (mean difference = 0.10, $p < 0.01$), which, although comparably less, suggests that deformability is influenced by the method of temperature-based inactivation. A discrimination efficiency below 20% was calculated using the spring constant data of the two, temperature-inactivated sub-populations.

The spring constant distributions of untreated and temperature-inactivated *C. parvum* are displayed in Figure 7.7d. For untreated *C. parvum*, the distribution appears bivariate, since there are two peaks. Interestingly, the smaller, low spring constant peak corresponds to the peak of the temperature-inactivated populations, which may provide evidence for the existence of a smaller, naturally occurring, non-viable subpopulation within the untreated sample. Using the corresponding PDF (Figure 7.8), we estimated an 86% viability rate for the untreated sample, which agrees with the 92% viability rate calculated by the supplier for this sample using a conventional excystation assay [7.21].

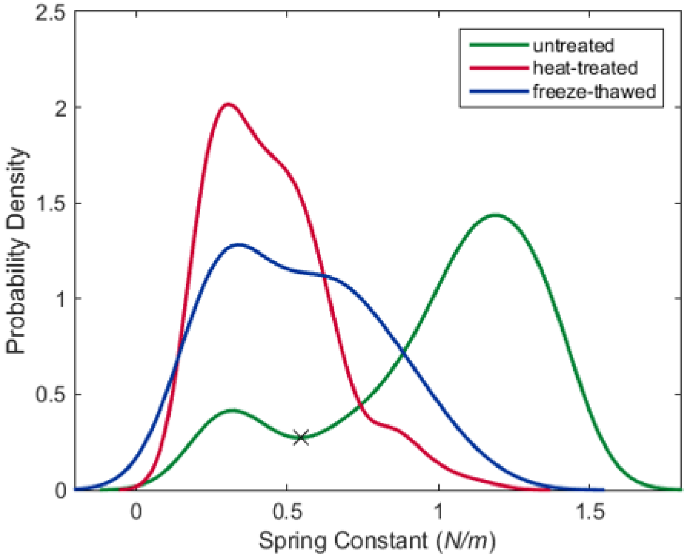

Figure 7.8: Probability density estimation of spring constant data for untreated and temperature-inactivated *C. parvum*. Spring constant data has been fitted with a kernel probability density function (PDF) – a non-parametric estimation of the PDF – due to data skewness. For untreated *C. parvum*, the smaller peak of the PDF occurs at similar spring constant values to the peaks of the PDFs for temperature-inactivated oocysts. Sample viability of the untreated sample was estimated at 86% due to 14% of oocysts being distributed to the left side of the minima (indicated by black cross) between the two peaks of the PDF. Reproduced from McGrath *et al*. [7.15] with permission under license (https://creativecommons.org/licenses/by/4.0/legalcode).

7.4 Summary and Outlook

This chapter describes the use of a novel, MeFS method that permits the immobilisation, manoeuvring, and force measurement of more than 50 single oocysts in an hour, but that has the capacity to perform more than 200 measurements per hour. Using the data retrieved from force measurements, the height and deformability distributions of untreated, heat-treated and freeze-thawed *C. parvum* were characterised – after temperature-based inactivation, *C. parvum* oocysts appear to exhibit increased deformability. Although a statistically relevant difference was identified between the overall deformability of each sub-population, the respective distributions were overlapping (as were the height distributions) – this suggests that deformability- and/ or size-based separation methods (including DLD), *e.g.*, the passive microfluidic systems described in Table 3.1, cannot be used for the complete sorting of viable and non-viable sub-populations of *C. parvum*.

For the discrimination of *Cryptosporidium* species (*i.e.*, discerning between the major human-pathogenic and little/ no risk *Cryptosporidium* species) however, the simultaneous plotting of spring constant and deformability data, that are retrieved in synchrony using MeFS, allows the discrimination of *C. parvum* and *C. muris*. The exact efficiency of this discrimination should be validated further using, *e.g.*, the benchtop molecular speciation methods described in Chapter 2. It is doubtful that microfluidic techniques which utilise both size and deformability in synchrony to sort particles (*e.g.*, DLD) would enable more efficient sorting of *C. parvum* and *C. muris* than solely size- or deformability-based techniques. For example, *C. muris* is larger and more deformable than *C. parvum*, thus, under deformation it is likely that *C. muris* would become smaller and consequently, overall sorting efficiency would be reduced. Even a combinatorial device which links, for example, a deformability-based separation technique with a downstream, size-based technique would unlikely be able to reliably sort these pathogens, since their size or deformability distributions were overlapping.

Other future work should explore how inter-batch variability, ageing and environmental influences (*e.g.*, exposure of oocysts to UV light) affect the deformability of *Cryptosporidium* oocysts. To verify the finding that inactivated oocysts are generally more deformable than untreated oocysts, MeFS can be used to sort *Cryptosporidium* into sub-populations with high or low deformability, followed by *e.g.*, animal infectivity assays (discussed in Chapter 2). Finally, the methods used in this research may be applied to other waterborne pathogens and single-celled organisms to characterise their biomechanical properties.

7.5 Author Contributions

The following authors contributed to the completion of this work: John McGrath (JM), Dr. Jos Quist (JQ), Dr. James Seddon (JS), Dr. Stanley Lai (SCL), Prof. Serge Lemay (SGL) and Dr. Helen Bridle (HB). JM and HB are currently based at Heriot-Watt University (UK). At present, JQ, JS, SCL and SGL are based at the University of Twente (Netherlands). In order of level of contribution, the following aspects of this work were completed by:

1. Conceived and designed the experiments: JM JQ
2. Performed the experiments: JM JQ
3. Analysed the data: JM JQ
4. Contributed reagents/ materials/ analysis tools: HB SGL SCL JS
5. Wrote up results: JM JQ JS SCL SGL HB

7.6 References

7.1. Nichols R, Connelly L, Sullivan C, Smith H. Identification of Cryptosporidium species and genotypes in Scottish raw and drinking waters during a one-year monitoring period. Applied and environmental microbiology. 2010;76(17):5977-86.

7.2. Smith HV, Nichols RAB. Cryptosporidium: Detection in water and food. Experimental Parasitology. 2010;124(1):61-79.

7.3. Meister A, Gabi M, Behr P, Studer P, Vörös Jn, Niedermann P, et al. FluidFM: combining atomic force microscopy and nanofluidics in a universal liquid delivery system for single cell applications and beyond. Nano letters. 2009;9(6):2501-7.

7.4. Guillaume-Gentil O, Potthoff E, Ossola D, Franz CM, Zambelli T, Vorholt JA. Force-controlled manipulation of single cells: from AFM to FluidFM. Trends in biotechnology. 2014;32(7):381-8.

7.5. Hou HW, Bhagat AAS, Chong AGL, Mao P, Tan KSW, Han J, et al. Deformability based cell margination—a simple microfluidic design for malaria-infected erythrocyte separation. Lab on a Chip. 2010;10(19):2605-13.

7.6. Hur SC, Henderson-MacLennan NK, McCabe ER, Di Carlo D. Deformability-based cell classification and enrichment using inertial microfluidics. Lab on a Chip. 2011;11(5):912-20.

7.7. McGrath J, Jimenez M, Bridle H. Deterministic lateral displacement for particle separation: a review. Lab on a Chip. 2014;14(21):4139-58.

7.8. Bhagat AAS, Bow H, Hou HW, Tan SJ, Han J, Lim CT. Microfluidics for cell separation. Medical & biological engineering & computing. 2010;48(10):999-1014.

7.9. Considine RF, Drummond CJ, Dixon DR. Force of interaction between a biocolloid and an inorganic oxide: complexity of surface deformation, roughness, and brushlike behavior. Langmuir. 2001;17(20):6325-35.

7.10. Considine RF, Dixon DR, Drummond CJ. Oocysts of Cryptosporidium parvum and model sand surfaces in aqueous solutions: an atomic force microscope (AFM) study. Water Research. 2002;36(14):3421-8.

7.11. Byrd T, Walz J. Interaction force profiles between Cryptosporidium parvum oocysts and silica surfaces. Environmental science & technology. 2005;39(24):9574-82.

7.12. Tufenkji N, Dixon DR, Considine R, Drummond CJ. Multi-scale Cryptosporidium/sand interactions in water treatment. Water research. 2006;40(18):3315-31.

7.13. Byrd T, Walz J. Investigation of the interaction force between Cryptosporidium parvum oocysts and solid surfaces. Langmuir. 2007;23(14):7475-83.

7.14. USEPA. Method 1623.1: C*ryptosporidium* and Gia*rdia in* Water by Filtration/IMS/FA: United States Environmental Protection Agency; 2012.

7.15. McGrath JS, Quist J, Seddon JR, Lai SC, Lemay SG, Bridle HL. Deformability Assessment of Waterborne Protozoa Using a Microfluidic-Enabled Force Microscopy Probe. PloS one. 2016;11(3):e0150438.

7.16. Hertz H. Über die Berührung fester elastischer Körper. 1882.

7.17. De Gennes P. Polymers at an interface; a simplified view. Advances in Colloid and Interface Science. 1987;27(3):189-209.

7.18. Smith HV, Nichols RAB, Grimason AM. Cryptiosporidium excystation and invasion: getting to the guts of the matter. Trends in Parasitology. 2005;21(3):133-42.

7.19. Reduker D, Speer C, Blixt J. Ultrastructure of Cryptosporidium parvum oocysts and excysting sporozoites as revealed by high resolution scanning electron microscopy. The Journal of protozoology. 1985;32(4):708.

7.20. Harris JR, Petry F. Cryptosporidium parvum: structural components of the oocyst wall. The Journal of parasitology. 1999:839-49.

7.21. Blewett D, editor Quantitative techniques in Cryptosporidium research. Proceedings of the First International Workshop on Cryptosporidiosis Edinburgh: The Animal Disease Research Association; 1989.

Chapter 8 – Methods: Development of DEP Microfluidics

8.1 Introduction

This chapter describes the development of a microfluidic system incorporating a dielectrophoretic field (principle outlined in section 4.3) – *i.e.*, an active, microfluidic separation technique. This device was designed for manipulating the trajectory of waterborne pathogens depending on their viability status. Firstly, device design, in terms of the inherent fluidics and electronics, and fabrication are considered, before the experimental methods used to realise the findings of Chapter 9 are described.

8.2 Device Design

8.2.1 Chip Design

A microfluidic chip was designed using AutoCAD 2016 (Autodesk Inc., US) with the features annotated in Figure 8.1. The buffer and sample inlet channels were 300 µm and 100 µm wide, respectively and converged into a main channel of 400 µm width x 4.5 mm length, which divided into three outlets of equal width (~133 µm). All channels were designed with a depth of 40 µm.

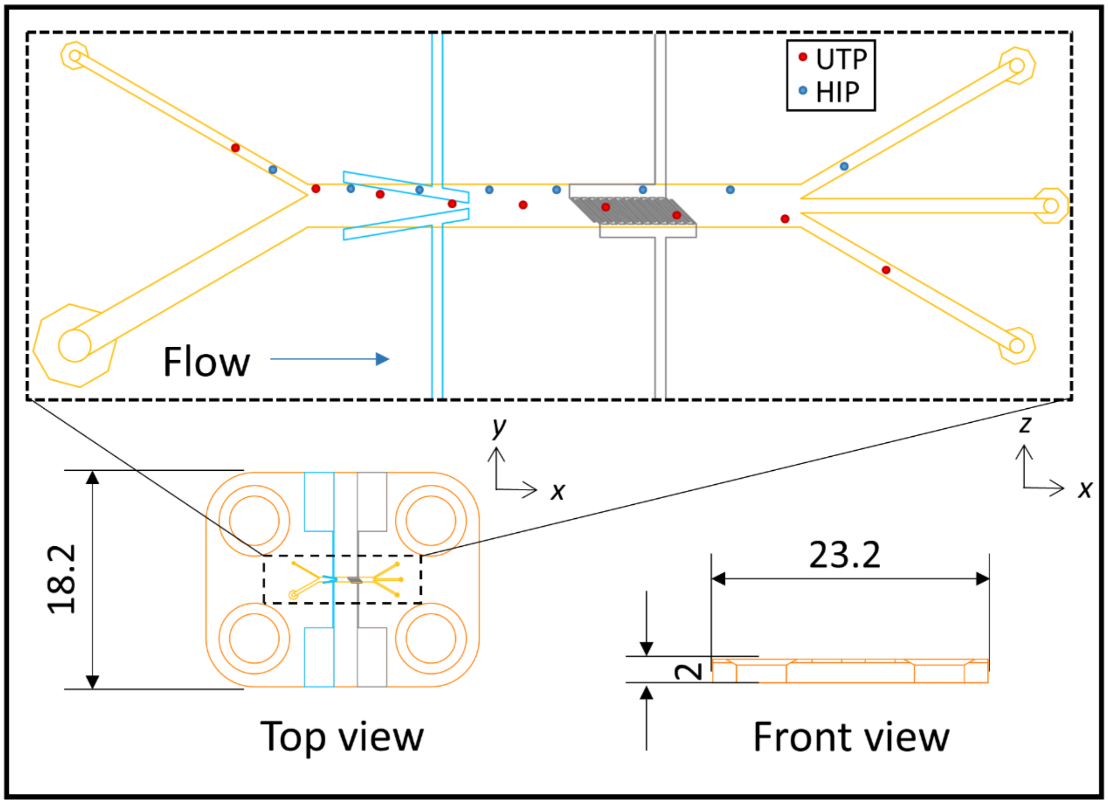

Figure 8.1: Design of microfluidic chip and ideal operation. The chip of dimensions 23.2 x 18.2 x 2 mm is shown in orange, the fluidic channel in yellow, the focusing electrodes in blue and the interdigitated, lateral separation electrodes are grey. All dimensions are in mm. Untreated *C. parvum* (UTP; red circles) should be focused into a stream of narrow width in the centre of the channel after passing the focusing electrodes. UTP should then be deflected across the width of the device by the angled, interdigitated electrode array. The motion of heat-inactivated *C. parvum* (HIP; blue circles) should not be affected significantly by the electric field.

By fabricating interdigitated electrodes at an angle to the fluid flow direction, several authors have generated a lateral, negative dielectrophoresis (DEP) effect within a microfluidic constriction to manipulate the trajectory of a target particle/ cell population [8.1-8.4]. At the time of writing, it is possible to purchase microparticles with diameters of 1- 250 μm (Microparticles GmbH, Germany), which have a small coefficient of variance (CV) of < 2% from the average particle size. Since the F_{DEP} experienced by a polarisable particle is a function of particle size – outlined in section 4.3.1 – then, immediately after passing the electrode array of a lateral separation device (illustrated previously in section 4.3.2), polystyrene particles are often dispersed within a flow stream of narrow width – this phenomenon is apparent in the works of Park *et al*. [8.1] and Han *et al*. [8.2]. However, the typical biological cell population usually has a much larger CV from the average size (see section 7.3.1). Consequently, biological cells are generally dispersed in wider flow streams than *e.g.*, polystyrene particles after passing an interdigitated electrode array – again see Park *et al*. [8.1] and Han *et al*. [8.2]. This means that the final in-channel positions of biological cells are more difficult to predict. To have greater control over the final in-channel positions of oocysts, a pre-focusing element was added upstream of the angled, interdigitated electrode array. By focusing oocysts into a narrower stream than the width of the sample inlet stream (100 µm), it is likely that oocysts will be less dispersed across the device width upon exiting the interdigitated electrode array. Furthermore, the inclusion of a pre-focusing element means that a large sample to buffer volume ratio (1:3) can be maintained (*i.e.*, rather than simply reducing the width of the sample inlet to achieve focusing), thus, allowing greater sample throughput.

Focusing electrodes have been used previously by several authors to concentrate target particles into a narrow flow stream [8.5-8.7] and were therefore included in the design. The symmetrical, focusing electrode array was designed as shown in Figure 8.1 (represented by blue features) to focus particles into the central region of the microchannel. This electrode array consisted of two, facing electrodes with width of 100 µm and length of 1.17mm, which converged until a 50 µm gap existed between the electrodes.

The downstream region of the microfluidic device was designed so that after focusing, suspended particles flow centrally towards an array of interdigitated, lateral electrodes. This electrode array consisted of 12 finger pairs which were located on the floor of the main channel at 45° to the flow direction. Electrode fingers were 20 µm wide with a 20 µm gap between each finger - when measured perpendicularly between parallel fingers. Each electrode finger was 318 µm long, however, given the 45° angle, electrode fingers spanned across 225 µm of the 400 µm wide channel. When passing this electrode array, particles experiencing negative DEP (nDEP) should be deviated laterally across the device in accordance with the 45° angle of the electrodes. Large contact pads at the perimeter of the chips (Figure 8.1) allowed the application of an AC signal to each electrode set.

8.2.2 Baseplate Design

A baseplate was designed to facilitate to connection of the microfluidic chip to the macroscale environment and allow the leak-free introduction/ exit of fluid (Figure 8.2). The fluidic inlets and outlets of the baseplate were designed to align with the access holes of the microfluidic chip. The central outlet incorporated a slalom design, ensuring that the fluidic resistance of the outflow channels was similar. The larger, macroscopic fittings shown in red (Figure 8.2) permitted, firstly, the fixing of the chip to the baseplate, and secondly, the entry/ exit of fluid from the baseplate. The assembly of these components is described in greater detail in section 8.5.

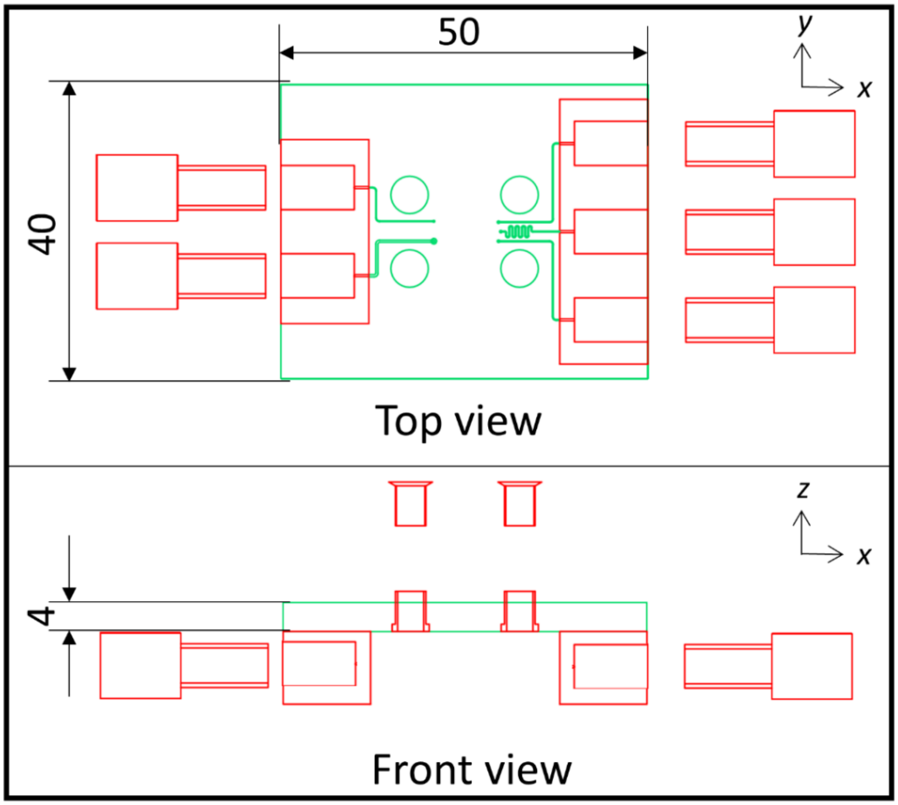

Figure 8.2: Device baseplate and fittings. The baseplate design is shown in green and the larger macroscale fittings are shown in red. The smaller fittings (red) shown in the front view of the device enable the fixing assembly of the chip and baseplate. The larger screws (also red) apparent in both the top and front views have through holes which enable the connection of tubing to the baseplate. These screws are inserted within the PMMA blocks that are fixed to the underside of the baseplate. All dimensions are in mm.

8.3 Device Fabrication

The microfluidic chips and baseplate were manufactured by Epigem (UK). The chips consisted mainly of Polymethyl-methacrylate (PMMA) and SU-8. Specifically, an 18 µm layer of SU-8 (Microchem, USA) was spin-coated on a 2 mm layer of PMMA, before microchannels of 40 µm depth were defined on this surface (also SU-8). This layer was bonded to another construction which consisted of a 0.5 mm cover layer of PMMA, which had embedded, 6 µm thick nickel electrodes and another 18 µm layer of SU-8. The electrodes were patterned using an acetate photomask and the 18 µm thick, covering layer of SU-8 was fabricated in the chip to limit the effects of joule heating/ electrolysis.

8.4 Sample Preparation

C. parvum oocysts (Moredun strain) obtained from Moredun Scientific (Edinburgh, UK) at a concentration of 1 x 10^8 oocysts mL^{-1} PBS + antibiotics were diluted to a concentration of 1 x 10^6 oocysts mL^{-1} and washed twice in DI water before introduction to the chip. Washing was performed by centrifugation, whereby oocysts were spun down at 13,000 rpm for 15 s using an Eppendorf MiniSpin centrifuge (Eppendorf, Germany), the supernatant decanted and oocysts resuspended in buffer. The buffer consisted of a low conductive, DI water solution ($\sigma = 2.75 \times 10^{-4}$ S m^{-1}), which contained 0.15 – 0.16 g mL^{-1} sucrose to density match the mixture and thus, minimise particle sedimentation effects. For analysis of heat-treated oocysts, samples were prepared as above then heated to 70°C and held for 5 minutes in a block heater (Stuart Scientific, UK), before a further wash step was completed. Samples were drawn into 1 mL plastic syringes via luer-lok™ attached dispensing tips (Becton, Dickinson and Company, USA). A separate syringe containing only buffer fluid was prepared for use as a sheath fluid. Untreated and heat-treated oocysts were firstly assessed separately, to accurately characterise their behaviour. Mixed samples containing equal numbers of viable and non-viable oocysts (in total 2 x 10^6 oocysts mL^{-1}) were then prepared and assessed later to measure whole device efficiency.

8.5 Experimental Set-Up and Procedure

The dielectrophoretic chip was mounted to the custom designed baseplate (Figure 8.3) ensuring that fluidic entry/ exit holes were aligned and the spring-loaded electrical pins of the baseplate were in contact with the on-chip metallised pads (apparent in Figure 8.3b). Ferrules manufactured of PTFE (Epigem, UK) were used at each fluidic junction between the baseplate and chip to limit fluid leakage. Syringes were fixed within Fusion 100 syringe pumps (Chemyx, USA) and connected to 1/16” OD PTFE (Dolomite, UK) tubing using female slip-luer PEEK adapters (IDEX, USA), which each had a 10-32 thread for insertion of a PEEK finger tight nut (IDEX, USA). The finger tight nuts had a 1/16” through-hole for insertion of tubing. The opposite end of the tubing was connected to chip using PEEK nuts with 1/16” through-holes which screwed into the on-chip compatible 10-32 thread female adaptors; use of flangeless ferrules ensured tubing could not retract from the PEEK nuts (all parts obtained from Epigem, UK). Tubing was connected to the chip outlets using similar parts (Figure 8.3a). Sample was introduced to the system at a flow rate of 0.2 – 0.3 $\mu L\ min^{-1}$ and buffer at a rate of 0.6 – 0.9 $\mu L\ min^{-1}$.

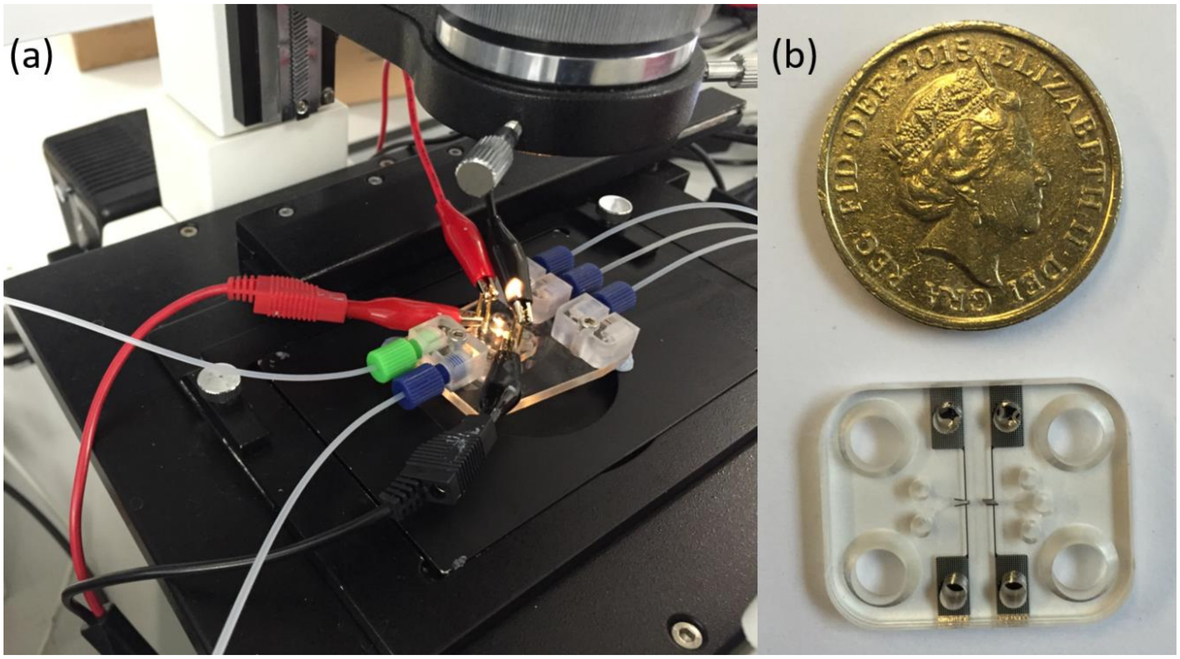

Figure 8.3: Chip assembly and electrical connection. **(a)** Microfluidic chips were fixed to the baseplate ensuring that the contact pins and fluidic access holes of the baseplate were aligned with the matching holes of the chip – apparent in **(b)**, which shows a chip beside a UK £1 coin.

To independently control the signal frequency and amplitude applied to each electrode set, two function generators (TTi, UK) were each connected to a high-power amplifier (LZY-22+, MiniCircuits, USA) which had an average voltage gain factor of 141.25 between 0.1 – 200 MHz – Figure 8.4. The output of each amplifier was connected to the spring-loaded, contact pins of the chip baseplate using coaxial cables with crocodile clip attachments. Signals were typically applied within the range of 0 – 30 MHz. The setup was mounted onto the Phase Contrast 2 EWLD 0.3 inverted microscope (Nikon, Japan) with a ProGres® CF USB high-speed camera attachment (Jenoptik, Germany) used to gather images, which were viewed using a laptop computer.

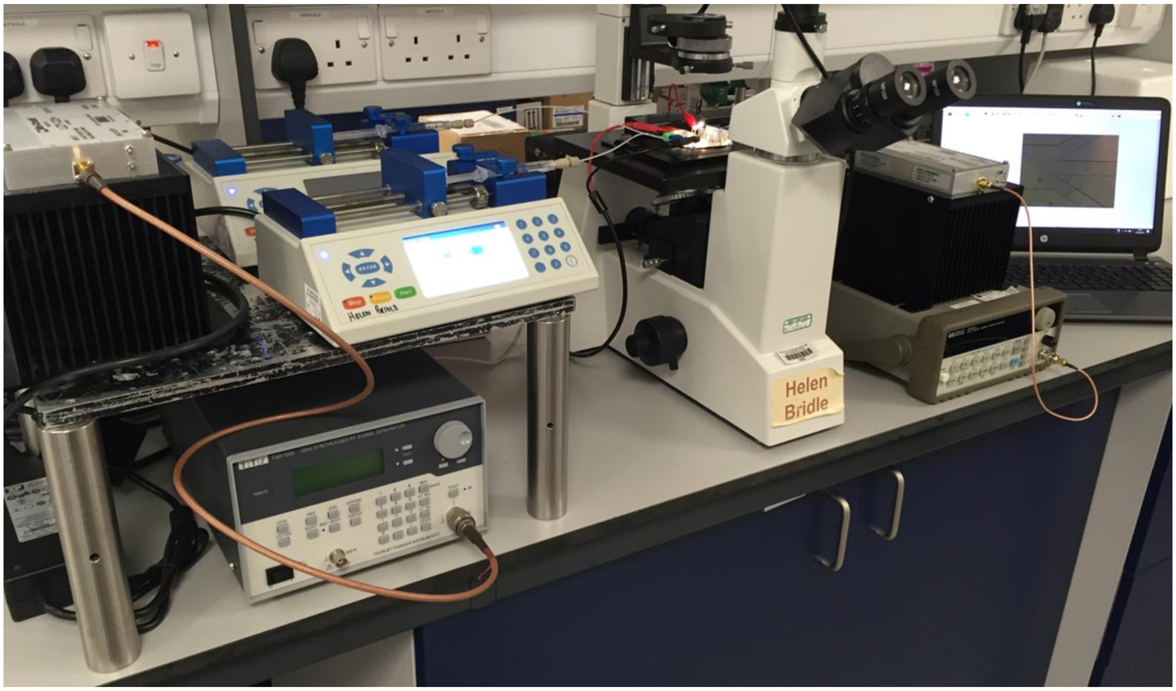

Figure 8.4: Dielectrophoretic chip with all fluidic and electrical connections assembled. Positive pressure from the syringe pumps allowed the introduction of fluid *via* the sample and buffer inlets, respectively.

8.6 Simulations/ Modelling

3-D simulations of the fluid flow within the DEP chip were modelled using the creeping flow module in COMSOL Multiphysics version 5.2 (COMSOL, Inc., USA). The electric field gradient generated by the interdigitated, planar electrode array was modelled in 2-D using the electrostatics module. The chips were modelled as a microfluidic channel with two insulating layers of SU-8 at the top and bottom channel walls. In addition, nickel electrodes were modelled beneath the bottom SU-8 layer. Cover layers of PMMA were then added to the top and bottom of the model to ensure accurate estimation of the electrical parameters (see section 8.3). Given that the DEP chip is fabricated of materials commonly used in microfabrication, the inbuilt material properties of the software were used for PMMA, SU-8 and nickel. The properties of the fluid were input manually and reflected the experimental medium conditions described in section 8.4 at 20°C. For example, medium viscosity (μ_m) = 1 x 10^{-3} Pa s, density (ρ_m) = 1155 kg m^{-3}, relative permittivity (ε_m) = 72 and electrical conductivity (σ_m) = 2.72 x 10^{-4} S m^{-1}. Specifically, ρ_m is slightly greater than the actual density of water due to the addition of sucrose, plus the relative permittivity is less because the addition of sucrose to water reduces the relative permittivity by ~10% [8.8].

Modelling of the frequency-dependent Clausius-Mossotti factor, which governs the direction of the dielectrophoretic force and electrorotational torque experienced by a particle, was performed in Matlab (v R2016a, Mathworks, USA) using a single-shell model (see section 4.2). This code used the medium electrical properties given in the previous paragraph and used the average of the literature-reported values for the parasites' electrical properties – these parameters and modelling will be discussed in more depth in Chapter 9.

8.7 Data Analysis

A custom script was written in Matlab (R2016a) for the analysis of images gathered within the DEP chip. Briefly, from a set of 100 individual images, an image which contained no oocysts was used as the reference image. The remaining images were then subtracted from the reference image to identify differences (*i.e.*, oocysts and any other suspended particles). Upper and lower thresholds were then selected to exclude any particles which appeared smaller or larger in size than the oocysts. The in-channel *y*-positions (*i.e.*, transverse to flow direction) of oocysts were then stored and used in the generation of figures and separation efficiency calculations. An example script is shown in Appendix A.

8.8 Excystation Assay

The viability rates of the oocysts eluted from each chip outlet were estimated using an *in vitro* excystation assay developed at Moredun Research Institute (UK) [8.9] to evaluate the sorting efficiency of the device. The assay typically requires a high oocyst concentration of 1 x 10^6 *C. parvum* oocysts per 1 mL solution. Thus, the fluid eluted from each outlet was collected at the end of each experiment set and stored at 5°C until all experiments were performed. With respect to each outlet, the eluted, stored oocysts were then concentrated and combined in a single container to achieve the maximum possible oocyst concentration. Thus, the viability rates attained demonstrate the average achieved across all mixed sample experiments.

The assay involved spinning a stock suspension containing *C. parvum* oocysts at 500 g for 5 mins (note all centrifugation steps were in these conditions), removal of supernatant and resuspension of the pellet in 40 µL of Hanks Buffered Salt Solution (HBSS). To this, 50 µL of 1% Trypsin (pH 3.0) was added and vortexed thoroughly before incubating at 37°C for 60 mins in a water bath. The mixture was then centrifuged, the supernatant was discarded and the pellet resuspended in 90 µL HBSS + 10 µL of 2.2% Sodium Bicarbonate + 10 µL 1% Sodium Deoxycholate. The mixture was vortexed and incubated at 37°C for 40 mins in a water bath, centrifuged and then resuspended in 50 µL PBS. From the sample, 10 µL was pipetted onto a glass slide and covered using a cover slip. The cover slip edges were coated with mineral oil to limit evaporation of the sample. Oocysts were visualised using a differential interference contrast (DIC) microscope (BX50, Olympus) – the number of intact oocysts and empty shells were counted until 250 events had been recorded. The following formula was used to calculate excystation percentage: number of empty shells / (number of empty shells + number intact oocysts). Additionally, the ratio of sporozoites to shells (Sp/ Sh) as an additional parameter for evaluating sample quality and device efficiency.

8.9 Summary

The design and fabrication process of the DEP chip used in this research has been outlined in this chapter. The experimental set-up, data analysis, plus the modelling of the DEP chip and parasite response to an applied field were also discussed. The results of this work are detailed in the following chapter.

8.10 References

8.1. Park S, Zhang Y, Wang T-H, Yang S. Continuous dielectrophoretic bacterial separation and concentration from physiological media of high conductivity. Lab on a Chip. 2011;11(17):2893-900.

8.2. Han K-H, Frazier AB. Lateral-driven continuous dielectrophoretic microseparators for blood cells suspended in a highly conductive medium. Lab on a Chip. 2008;8(7):1079-86.

8.3. Han K-H, Han S-I, Frazier AB. Lateral displacement as a function of particle size using a piecewise curved planar interdigitated electrode array. Lab on a Chip. 2009;9(20):2958-64.

8.4. Han S-I, Lee S-M, Joo Y-D, Han K-H. Lateral dielectrophoretic microseparators to measure the size distribution of blood cells. Lab on a Chip. 2011;11(22):3864-72.

8.5. Fiedler S, Shirley SG, Schnelle T, Fuhr G. Dielectrophoretic sorting of particles and cells in a microsystem. Analytical chemistry. 1998;70(9):1909-15.

8.6. Müller T, Gradl G, Howitz S, Shirley S, Schnelle T, Fuhr G. A 3-D microelectrode system for handling and caging single cells and particles. Biosensors and Bioelectronics. 1999;14(3):247-56.

8.7. Dürr M, Kentsch J, Müller T, Schnelle T, Stelzle M. Microdevices for manipulation and accumulation of micro-and nanoparticles by dielectrophoresis. Electrophoresis. 2003;24(4):722-31.

8.8. Padua GW. Proton NMR and dielectric measurements on sucrose filled agar gels and starch pastes. Journal of food science. 1993;58(3):603-4.

8.9. Blewett D, editor Quantitative techniques in Cryptosporidium research. Proceedings of the First International Workshop on Cryptosporidiosis Edinburgh: The Animal Disease Research Association; 1989.

Chapter 9 – Dielectrophoretic Analysis of *Cryptosporidium*

9.1 Introduction

In Chapter 7, it was concluded that the efficient sorting of viable and non-viable *C. parvum*, or different *Cryptosporidium* species using size- and/ or deformability-based, passive microfluidic separation methods would not be possible. Subsequently, an active, microfluidic method of cell/ particle was sought to sort the different pathogen populations.

When integrated in continuous-flow microfluidics, dielectrophoresis (DEP) has demonstrably enabled the fast, highly sensitive, label-free sorting of target particles [9.1]. At a carefully selected signal frequency and amplitude, DEP can be used to differentiate between cell populations based on a range of characteristics such as volume, shape and internal structure [9.2]. For instance, DEP has been used to differentiate between different bacterial species such as *E. coli* and *Bacillus* spp. [9.3] and protozoa like *Cryptosporidium* and *Giardia* [9.4], as well as to separate live and dead cells of the same type [9.5].

The dielectrophoretic behaviour of *C. parvum,* specifically, has been characterised by several researchers [9.4, 9.6, 9.7]. The work of Su *et al.* [9.7] is notable in that both untreated and heat-treated *C. parvum* oocyst populations were analysed. In this study, Su *et al.* [9.7] identified differences in the high frequency (> 10 MHz) DEP responses of these pathogen populations, however, were unable to continuously separate the pathogens in their batch-mode operated chip. In this chapter, I describe the use of a DEP chip, an active microfluidic separation technique, which continuously sorts untreated and heat-inactivated *C. parvum* by exploiting variations in their internal dielectric properties. To my knowledge, this is the first microfluidic device which separates viable and non-viable *Cryptosporidium* oocysts in continuous flow.

To gain insight into the performance of the DEP chip and optimise experimental parameters, the Clausius-Mossotti factor ($\tilde{f}_{CM}$) of *C. parvum*, which governs the direction and magnitude of the dielectrophoretic force experienced by the pathogen, was firstly modelled based on the literature-reported dielectric parameters of *C. parvum*. The hydrodynamic forces which influence particle motion within the chip were also simulated before the DEP sorting of untreated and heat-inactivated *C. parvum* populations was performed.

9.2 Modelling and Theoretical Analysis

9.2.1 Modelling the Dielectric Response of *Cryptosporidium*

The use of AC electrokinetics-based microfluidics in conjunction with Maxwell's mixture theory (MMT) and the single shell model (all described in Chapter 4) to estimate the dielectric properties of *C. parvum* has been described in the literature [9.4, 9.7, 9.8]. The dielectric properties of *C. parvum* which influence $\tilde{f}_{CM}$, as described in the literature, are shown in Table 9.1. Using the average of these values and a single shell model, the real and imaginary components of $\tilde{f}_{CM}$ for untreated (UTP) and heat-inactivated *C. parvum* (HIP) were simulated in the frequency range of 10 Hz-100 MHz in a variety of medium conductivities (Figure 9.1). Only a single report of the dielectric properties of HIP was identified and thus, the values used in our simulations for HIP are those reported by Su *et al*. [9.7]. It should be noted, however, that at frequencies on the order of tens of MHz or greater, which penetrate further into the internal structure of the oocyst, the relevance of the single shell model becomes reduced due to the intricacy of oocyst interior. The single shell model does not account for any further dielectric dispersions, often termed Maxwell-Wagner polarisations [9.9], that take place after the polarisation of the cell cytoplasm (outlined in section 4.7.4).

Table 9.1. Literature-reported values for the relative permittivity (ε) and electrical conductivity (σ) of the untreated (viable) and heat-inactivated *Cryptosporidium* oocyst wall (ε_{wal} and σ_{wal}) and interior (ε_{int} and σ_{int}).

	ε_{int} [1]	ε_{wal} [1]	σ_{int} [S m^{-1}]	σ_{wal} [S m^{-1}]
Goater *et al.* [9.8] – untreated	56.65	8.73	0.052	3.46×10^{-7}
Unni *et al.* [9.4] – untreated	61.35	9.84	0.047	1.86×10^{-7}
Su *et al.* [9.7] – untreated	55.00	8.00	0.055	6.00×10^{-7}
Su *et al.* [9.7] – heat-treated	78.00	8.00	0.005	5.00×10^{-5}
Average – all untreated	57.67	8.86	0.051	3.77×10^{-7}

Note: square brackets denote units; 1 indicates dimensionless parameter.

The direction of DEP force experienced by a particle is governed by the sign of the real component of $\tilde{f}_{CM}$. In the calculations, $\Re[\tilde{f}_{CM}]$ was estimated using complex permittivities of the oocyst ($\tilde{\varepsilon}_{cyst}$) and medium ($\tilde{\varepsilon}_m$) by:

$$\Re[\tilde{f}_{CM}] = \frac{\tilde{\varepsilon}_{cyst} - \tilde{\varepsilon}_m}{\tilde{\varepsilon}_{cyst} + 2\tilde{\varepsilon}_m} \tag{9.1}$$

where

$$\tilde{\varepsilon}_{cyst} = \tilde{\varepsilon}_{wal}\left[\frac{\left(\frac{r_2}{r_1}\right)^3 + 2\left(\frac{\tilde{\varepsilon}_{int} - \tilde{\varepsilon}_{wal}}{\tilde{\varepsilon}_{int} + 2\tilde{\varepsilon}_{wal}}\right)}{\left(\frac{r_2}{r_1}\right)^3 - \left(\frac{\tilde{\varepsilon}_{int} - \tilde{\varepsilon}_{wal}}{\tilde{\varepsilon}_{int} + 2\tilde{\varepsilon}_{wal}}\right)}\right] \tag{9.2}$$

and

$$\tilde{\varepsilon}_i = \varepsilon_{i,0} - j\frac{\sigma_i}{\omega} \tag{9.3}$$

In equation 9.2, r is the oocyst radius (r = 2.15 μm; see section 11.7) and the inner radius, which is the dimension from oocyst centre to inner boundary of the oocyst wall, is denoted by r_1 [m] – see section 4.2.6. $\tilde{\varepsilon}_{int}$ and $\tilde{\varepsilon}_{wal}$ are the complex permittivities of the oocyst interior and outer wall, respectively. In equation 9.3, ε and σ are the permittivity [F m^{-1}] and conductivity [S m^{-1}] of a given component (i) of the mixture, while ε_0, j and ω are the constant permittivity of free space (8.85×10^{-12} F m^{-1}), the imaginary vector ($j^2 = -1$) and the angular frequency of the applied electric field [rad s^{-1}].

The ROT behaviour of a particle is concerned with the imaginary component of the $\tilde{f}_{CM}$, thus, will not be explored in the DEP chip. Despite this, the model of the $\Im[\tilde{f}_{CM}]$ force profile shows electrorotational peaks (Figure 9.1b) that correspond with the direction of the simulated $\Re[\tilde{f}_{CM}]$ profiles and which occur immediately prior to each crossover of $\Re[\tilde{f}_{CM}]$ (Figure 9.1a). This phenomenon occurs because the phase factor by which the cell/ particle's induced dipole moment lags the field is typically at its maximum at each $\Re[\tilde{f}_{CM}]$ crossover, whereby the polarisation of a successive cell layer takes place [9.9-9.11].

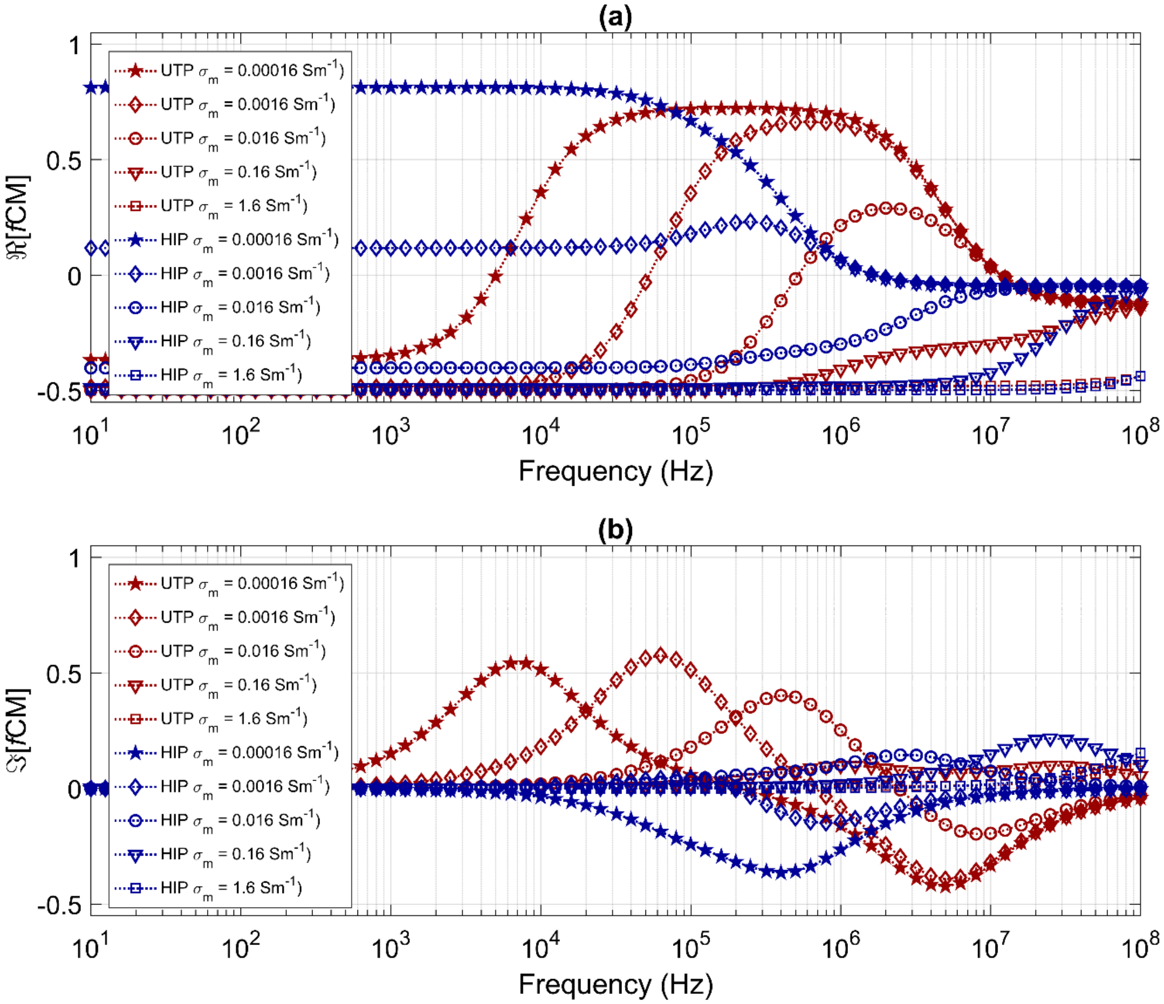

Figure 9.1: Model of the dielectric response of untreated and heat-inactivated *C. parvum* using literature-reported dielectric properties. **(a)** The real part of the Clausius-Mossotti factor ($\Re[\tilde{f}_{CM}]$), which governs the dielectrophoretic force profile of the oocysts, was simulated in a variety of media conductivities. **(b)** The imaginary part of the Clausius-Mossotti factor ($\Im[\tilde{f}_{CM}]$) was simulated in the same conditions and governs the electrorotational force profile of the oocysts.

For untreated *C. parvum* and indeed most living biological cells, there are typically two DEP crossover frequencies (f_{cross_n}; discussed in section 4.2.4). The first crossover, f_{cross_1}, is the initial transition from nDEP to pDEP that occurs due to polarisation between the suspending medium and cell membrane [9.10]. At frequencies below f_{cross_1}, the oocyst typically appears insulating and is less polarisable than the surrounding media, thus, the direction of DEP force is experienced is negative. f_{cross_1} is a strong function of the medium conductivity and in low conductive media (*e.g.*, σ_m = 1.6 x 10^{-4} S m^{-1}), where less charge exists within the system, this crossover occurs at low frequency (~ 50 kHz). With ever increasing media conductivity, f_{cross_1} shifts towards higher frequencies. For example, in media of physiological conductivity (*e.g.*, 1.6 S m^{-1}), which is generally highly conductive, crossover does not occur within the frequency range shown in Figure 9.1a and biological cells typically experience only nDEP. The second crossover (*i.e.*, the transition back to nDEP motion; f_{cross_2}) occurs at higher frequencies due to the effective short-circuiting of the cell membrane capacitance [9.10], where polarisation occurs between the suspending medium and cell cytoplasm. At low conductivities (*e.g.*, 1.6 x 10^{-4} – 1.6 x 10^{-2} S m^{-1}; indicated by stars, diamonds and circles in Figure 9.1a), f_{cross_2} appears to be frequency independent.

To facilitate the sorting of UTP and HIP (or indeed any two, different cell populations) a regime must be created in which the populations experience DEP force in opposing directions or where the magnitude of DEP force experienced by each population varies. At frequencies more than f_{cross_2}, a greater degree of control over the induced forces is possible because the electrical properties of the interior components are more influential in the overall DEP response, *e.g.*, see the difference between the electrical properties of oocyst exterior and interior shown in Table 9.1. Thus, high frequency DEP analysis in a low conductive buffer, whereby f_{cross_2} is frequency independent, was used to control and/or manipulate the trajectory of the suspended parasites.

Using finite element modelling software (COMSOL Multiphysics v5.2, COMSOL, USA), the fluid flow and electric field within the designed DEP chip were simulated. Pressure-driven flow within microfluidics typically adopts a parabolic flow profile (discussed in section 3.2), meaning that particles within the central region of the flow travel at greater velocity than those near to the channel boundaries. Figure 9.2 shows the modelled, parabolic flow profile within the DEP chip when fluid flow is established at a total volumetric flow rate (Q) of 0.8 or 1.2 µL min^{-1} – the minimum and maximum values of Q used in this research (see section 8.5). In the DEP chip, these flow rates correspond with an average fluid velocity of 1.1 or 1.6 cm s^{-1}, which gives rise to Reynolds number (Re) values of 0.42 and 0.64, respectively.

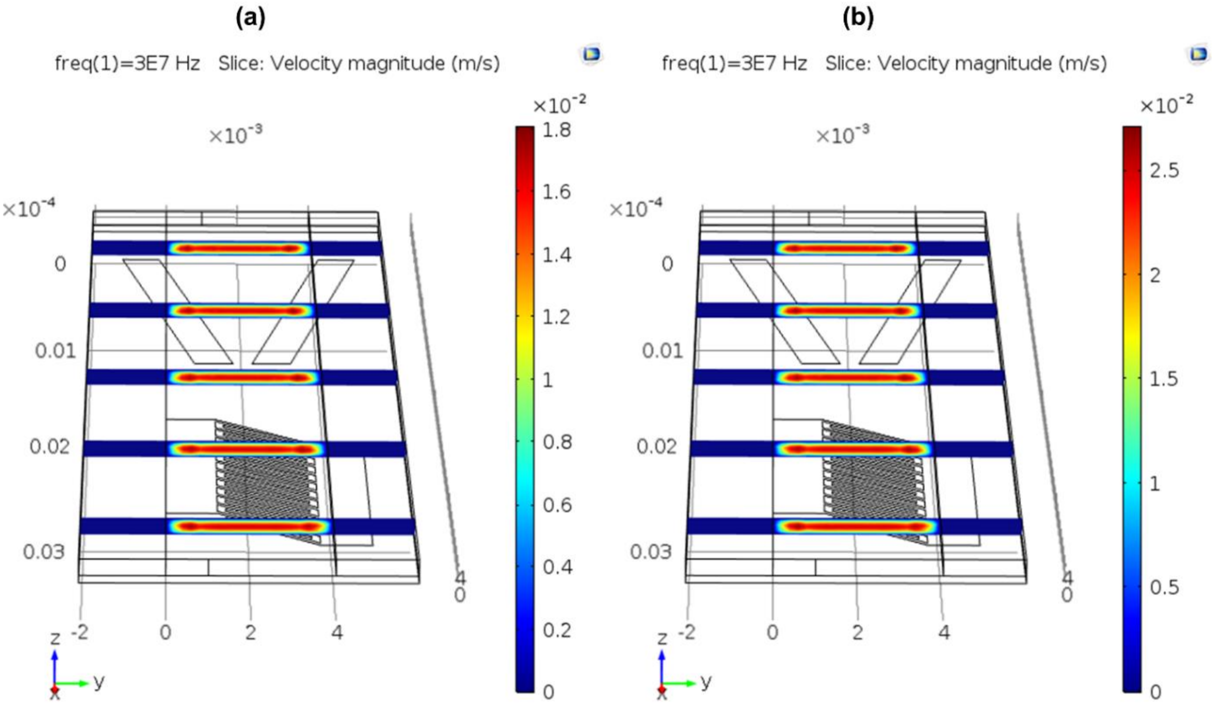

Figure 9.2: Model of fluid flow within system at a total volumetric flow rate of **(a)** Q = 0.8 µL min^{-1} or **(b)** Q = 1.2 µL min^{-1}. Fluid velocity is greatest in the central region of the established parabolic flow profile.

Due to the low Re values, viscous forces are considered to dominate within the chip, such that the viscous drag force is [9.12, 9.13]:

$$F_{drag} = -6\pi r\mu(v_p - v) \tag{9.4}$$

where r, μ, v_p and v are the oocyst radius [m], fluid viscosity [kg m^{-3}], particle velocity [m s^{-1}] and fluid velocity [m s^{-1}], respectively. Gravitational forces acting upon the particle are neglected, since the solution is density matched. For a particle which is within one particle radius of the channel top, *e.g.*, an oocyst which is repelled from the regions of high field strength under nDEP, the local fluid velocity is given by [9.13]:

$$v_f = \frac{6r(h-r)}{h^3 w}Q \tag{9.5}$$

where h, w are the channel height [m] and width [m].

For a fixed flow rate and frequency of applied electric field, a critical voltage (V_c) exists within a DEP chip with interdigitated electrodes whereby the hydrodynamic drag force and *x*-directional (parallel to flow) dielectrophoretic force acting on a particle are balanced ($v_p = 0$), such that [9.4, 9.12, 9.13]:

$$F_{drag} + F_{DEP} = 0 \tag{9.6}$$

where

$$F_{DEP} = 2\pi r^3 \varepsilon_m \varepsilon_0 \Re[\tilde{f}_{CM}] \nabla \mathbf{E}_x^2 \tag{9.7}$$

and $\nabla \mathbf{E}_x^2$ is the *x*-component of the electric field gradient vector. In the chip presented here, V_c can be described as the voltage [V] at which oocysts firstly become trapped at the DEP minima between the interdigitated electrode finger pairs, whereby F_{drag} is no longer dominant over F_{DEP}. Thus, at steady state, the real component of $\tilde{f}_{CM}$ is given by [9.12, 9.13]:

$$\Re[\tilde{f}_{CM}] = \frac{6\pi r\mu v_f}{2\pi r^3 \varepsilon_m \varepsilon_0 \nabla \mathbf{E}_x^2} \tag{9.8}.$$

In this work, a simplified chip model was used to accurately calculate $\nabla \mathbf{E}_x^2$ for each set of experimental conditions (see section 9.3.1). In the *x*-plane, a cross section including one electrode finger pair from the interdigitated electrode array was replicated for modelling purposes. Firstly, the electric potential [V] was calculated in the chip model. Figure 9.3a shows the electric potential when V_c = 10 V and signal frequency = 30 MHz. For the same signal conditions, the local electric field ($\mathbf{E}$), *i.e.*, the average $\mathbf{E}$ within one oocyst radius from the channel top, was calculated (Figure 9.3b). The local $\mathbf{E}$ is important because negatively polarised oocysts will levitate towards the DEP minima at the channel top, between electrode finger pairs, due to the *z*-directional component of F_{DEP} [9.4, 9.12-9.14]. Finally, the *x*-directional, local electric field gradient, $\nabla\mathbf{E}_x^2$, was calculated (Figure 9.3c) in order to approximate $\Re[\tilde{f}_{CM}]$ using equation 9.8.

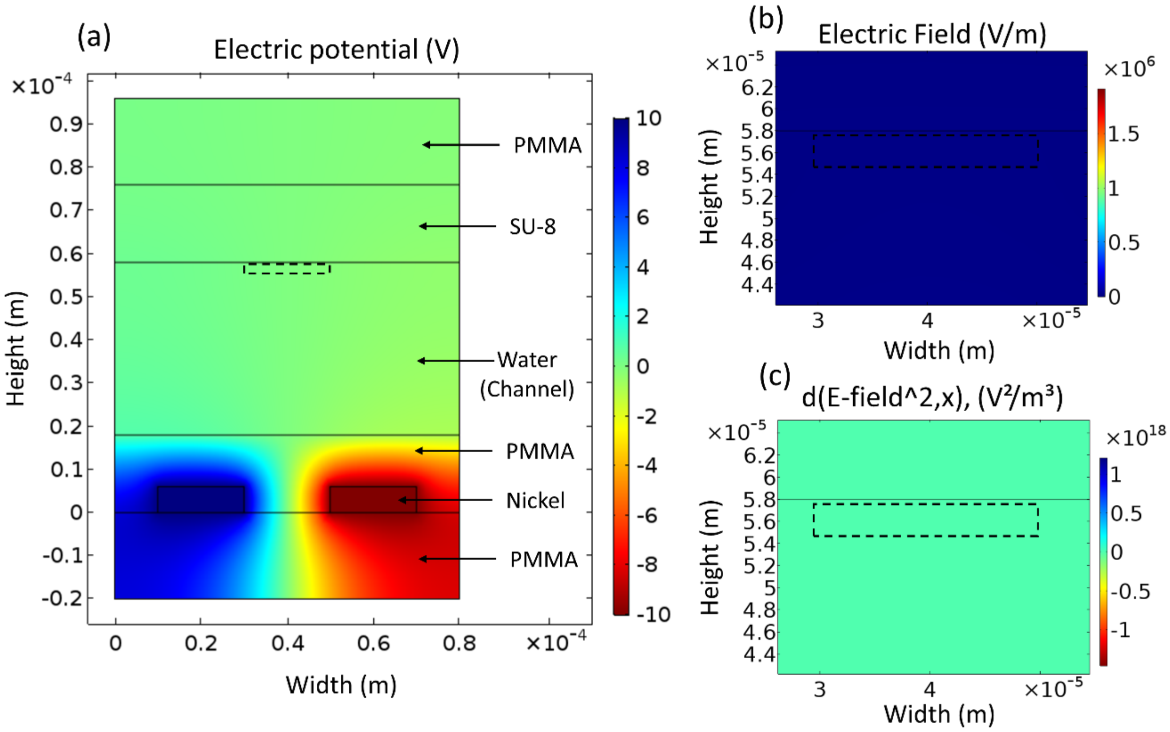

Figure 9.3: Electric field distribution in the DEP chip as modelled using COMSOL Multiphysics. **(a)** A 2-D model of the chip was replicated and electric potential calculated when an AC signal of 10 V amplitude was applied to the electrodes at a frequency of 30 MHz. To properly calculate the electric potential within the chip, all chip materials were included in the model. The dashed box has a width the same as the electrode spacing and a height the same as the radius of a *C. parvum* oocyst (~2.15 µm – see Table 2.2). **(b)** Local electric field ($\mathbf{E}$) within the channel; $\mathbf{E}$ = 4770 V m^{-1}. **(c)** $\nabla\mathbf{E}_x^2$ calculated within the same section of the microchannel. The average local field gradient within the dashed box was extracted from the calculations for use in experimental approximation of $\Re[\tilde{f}_{CM}]$; $\nabla\mathbf{E}_x^2$ = 9.25 x 10^{-15} V^2 m^{-3}.

9.3 Experimental Results and Discussion

9.3.1 Critical Voltage

Firstly, the interdigitated electrode array was used to quantify the critical voltage required to capture/trap oocysts within the DEP field. As was described previously, the combination of high frequency and low conductive media means that live *C. parvum* experience nDEP. Thus, analysis of the critical voltage required to capture oocysts was performed at a series of frequencies higher than f_{cross_2} (~10 MHz) – see Figure 9.4. A sample containing UTP suspended in low conductive buffer (σ_m = 1.6 x 10^{-4} S m^{-1}), plus a buffer flow, were introduced simultaneously into the DEP chip at a total volumetric flow rate of 0.8 μL min^{-1} and the V_c required to capture UTP was measured upon flow stabilisation. With increasing frequency, the V_c required for oocyst capture decreased, until signal frequency was > 32 MHz. The subsequent increase in V_c at frequencies > 32 MHz suggests that the oocysts became less negatively polarised under the applied field.

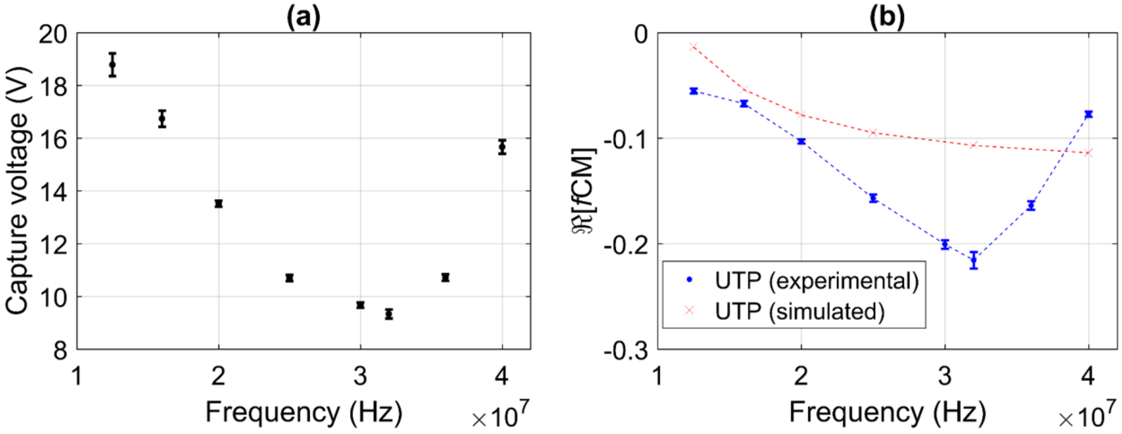

Figure 9.4: Capturing *C. parvum* oocysts in the DEP field. **(a)** The critical voltage (V_c) required to capture untreated *C. parvum* (UTP) was measured at a variety of frequencies above f_{cross_2}, where the sign of $\Re\left[\tilde{f}_{CM}\right]$ is negative. Each data point shows the mean ± SD of a minimum of ten oocysts. **(b)** $\Re\left[\tilde{f}_{CM}\right]$ of UTP (blue circles) was calculated using the experimental V_c values in (a) plus the model-derived $\nabla\mathbf{E}^2$ values. Also shown is the simulated $\Re\left[\tilde{f}_{CM}\right]$ for UTP in a medium with conductivity (σ_m) = 2.72 x 10^{-4} S m^{-1} (red crosses), based on the literature-reported dielectric parameters of the pathogen (see Table 9.1 and equation 9.1).

Using the average of the model-derived, local $\nabla\mathbf{E}^2$ values for each combination of capture voltage and frequency, equation 9.8 was solved to estimate $\Re[\tilde{f}_{CM}]$ for UTP. Table 9.2 shows an example of the values used in relation to V_c at 30 MHz. In Figure 9.4b, the post-f_{cross_2}, experimentally approximated $\Re[\tilde{f}_{CM}]$ values (blue circles) appear to show that the initiation of a further dielectric dispersion occurred at ~16 MHz, *i.e.*, where a large decrease in $\Re[\tilde{f}_{CM}]$ is evident. This finding implies that the single shell model is generally too simplistic to accurately approximate the high-frequency dielectric properties of *Cryptosporidium* (red crosses). This apparent dielectric dispersion which occurred between 16 – 32 MHz may be reflective of polarisation between the suspending medium and the sporozoite and/ or residual body membrane(s), which are contained within the oocyst interior (discussed in section 2.2.3). Dielectric dispersions of the surrounding membranes of internal organelles often only induce small changes to the DEP force profile of a typical cell and are thus, difficult to observe [9.9]. Therefore, it is possible that the signal may have penetrated further into the conductive organelles of the oocyst interior. For example, $\Re[\tilde{f}_{CM}]$ may be a measure of the dielectric properties of the interior residual body and/ or nuclear envelopes and/ or nuclei – each of the four, membrane-enclosed sporozoites contains a nucleus.

Table 9.2. Values used in approximation of $\Re[\tilde{f}_{CM}]$ at 30 MHz for untreated *C. parvum*.

Parameter	*Value*
h	40 µm
w	400 µm
Q	0.8 µL min^{-1}
r	2.15 µm
μ	1e-3 Pa s
ε_0	8.85e-12 F m^{-1}
ε_m	72
$\nabla\mathbf{E}^2$(V_c = 9.68 V, f = 30 MHz)	1.29e15 V^2 m^{-3}

As the signal frequency exceeded 32 MHz, the experimentally calculated $\Re[\tilde{f}_{CM}]$ values approached 0, which indicates that there was a large reduction in the conductivity of the oocyst layer being probed by the high frequency signal. Although this finding was unexpected, there is a large lipid body present within the residual-body of the *Cryptosporidium* oocyst [9.15]. Lipid is generally considered as an electrically insulating material [9.16, 9.17], *i.e.*, a poor conductor of electricity. Thus, this apparent reduction in conductivity may be representative of polarisation occurring between the medium and the lipid body, which is contained within the residual body.

For HIP, it was not possible to capture oocysts between 12 – 20 MHz. At 25 MHz however, it was possible to capture HIP at the maximum power output of the function generator/ high-power amplifier setup (70.62 V). This equates to a $\Re[\tilde{f}_{CM}]$ value of -0.004, which indicates that HIP oocysts were experiencing minimal nDEP force. Despite this, very soon after application of the signal, significant electrolysis at the electrodes was evident, thus, no further high field strength experiments were performed to capture HIP.

9.3.2 Focusing of *C. parvum*

Given the small difference in $\Re[\tilde{f}_{CM}]$ at 30 and 32 MHz, which were -0.20 and -0.22 specifically (Figure 9.4b), the on-chip focusing (and separation – see section 9.3.3) of *C. parvum* was performed at 30 MHz to reduce the chance that any oocysts may exhibit the apparent decrease in conductivity that was described in the previous section. Figure 9.5a shows the percentage of UTP focused at 30 MHz by the focusing electrode array under a variety of flow rates and applied voltages. For each flow rate, a range of voltages were selected nearby the voltage which appeared (by eye) to be the optimal voltage for focusing UTP oocysts. A similar ratio (3:1) of buffer to sample flow rate was maintained at all flow rates – the sample stream flows within the top quarter of the device (Figure 9.5b-c) and is, therefore, ~100 µm wide assuming steady flow. Thus, oocysts were considered focused if their in-flow *y*-position (transverse to the flow) was greater than the width of the sample stream (*i.e.*, > 100 µm) upon exiting the focusing electrode array. The effects of diffusion were neglected since *Cryptosporidium* oocysts have a low diffusivity of ~0.04 $\mu m^2\ s^{-1}$ (see section 3.2.5). Therefore, at the average flow velocities stated in section 9.2.2, oocysts pass through the main channel in less than 0.5 s, giving them insufficient time to diffuse even a few microns across the channel width. The *y*-position of the ideally focused UTP oocyst within the chip should have been between 175-225 µm – *i.e.*, within the central region of the microchannel width. The maximum voltage at which oocysts were focused but did not become immobilised at the focusing array was termed the maximal efficiency voltage. The focusing efficiency of HIP at the identified maximal efficiency voltage for UTP is also plotted in Figure 9.5a for each sample flow rate.

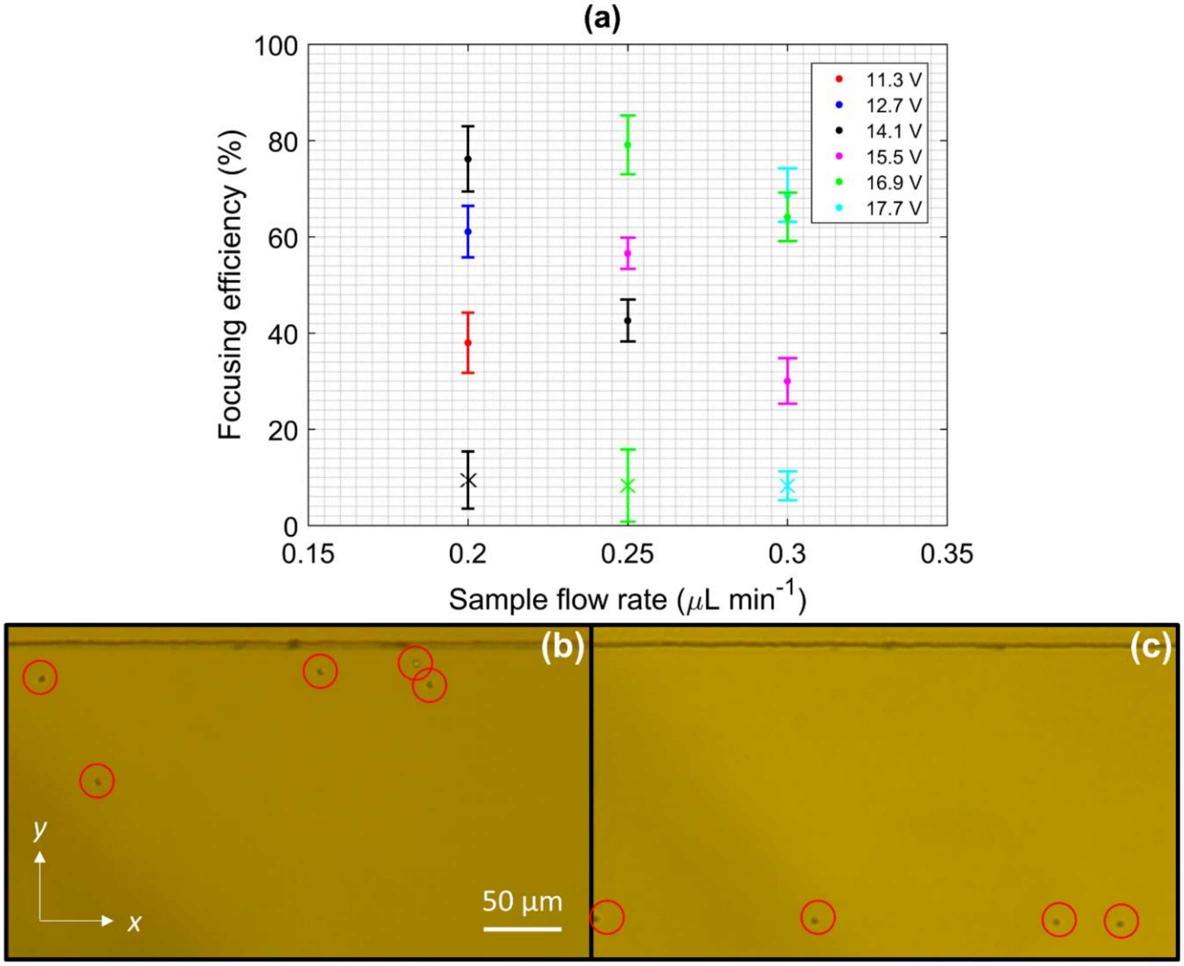

Figure 9.5: DEP focusing of *C. parvum* at 30 MHz. **(a)** The focusing efficiency of untreated (dots) and heat-inactivated oocysts (crosses) was measured at a variety of sample flow rate and applied voltage combinations. Each data point indicates the average of a minimum of three independent analyses. Legend shows voltage amplitude. **(b)** Heat-inactivated oocysts leaving the electrode focusing array in the sample stream, which were detected (indicated by red ellipses) using the custom script described in section 8.7. A signal of 16.9 V was applied to the focusing electrodes at a frequency of 30 MHz, whilst sample was entering the device at a flow rate of 0.25 µL min^{-1}. Top half of channel is shown as no oocysts were detected in bottom half. **(c)** Untreated, focused oocysts detected in the buffer stream when under the same experimental conditions described in (b). Upon focusing, UTP were contained within a narrow flow stream (as intended during the design stage – section 8.2.1) and travelled towards the interdigitated array of electrode finger pairs.

Generally, less than 10% of HIP were considered focused at the maximal efficiency voltage for each flow rate, demonstrating that the *y*-position of HIP was minimally influenced by the magnitude of the DEP force (Figure 9.5b) – *i.e.*, $\Re\left[\tilde{f}_{CM}\right]$ of HIP was near to 0. This means that the focusing of UTP effectively initiates the separation of UTP and HIP in the device. For UTP, the lowest focusing efficiency of all maximal efficiency voltages (68.7 ± 5.6%) was recorded at a sample flow rate of 0.30 µL min^{-1}, whereby a voltage of 17.7 V was the maximum before DEP trapping/ immobilisation of oocysts occurred. Average focusing efficiencies of 76.2 ± 6.8% and 79.1 ± 6.1% (Figure 9.5c) were the best recorded at sample flow rates of 0.20 or 0.25 µL min^{-1}, respectively.

The decrease in focusing efficiency at a sample rate of 0.30 µL min^{-1} and the inability to focus the whole UTP populations at the slower sample flow rates may be in part due to a larger difference existing between the velocities of particles suspended within the parabolic profile of the flow (discussed previously in section 9.2.2). For example, the flow velocity at the sidewalls and channel top (*i.e.*, for oocysts experiencing nDEP) is near zero according the no-slip boundary condition (Figure 9.2), however, particles within the central region of the flow travel at higher velocities when introduced at a sample flow rate of 0.30 µL min^{-1} compared to 0.25 µL min^{-1}. Consequently, the difference between the voltages required to manipulate the position of the slowest and fastest moving oocysts becomes larger. Therefore, there is an increased probability that slower moving oocysts may eventually become immobilised at the DEP minima between the electrodes before the motion of larger particles is significantly influenced. Similarly, as F_{DEP} is a function of particle size, it is possible that due to the large CV of *C. parvum* (~9.7% - see section 7.3.1), many of the largest oocysts became trapped at the electrodes before the F_{DEP} magnitude was enough to significantly influence the motion of the smallest oocysts.

Alternatively, the greater field strength required to manipulate particle trajectory at increased flow rates may have increased the local nDEP force experienced by oocysts near to the channel sidewalls. Park *et al.* [9.19], have shown that in a device where the channels are manufactured of an electrically insulating material (*e.g.*, SU-8, PDMS, PMMA), the local nDEP effect near the sidewalls becomes more significant with increasing particle levitation height in comparison to the nDEP effect experienced at the electrodes. Due to the parabolic flow profile, fluid velocity is slowest in the device at the join between the sidewalls and top/ bottom boundaries. Thus, at the highest field strengths (*i.e.*, 17.7V at 30 MHz), particles which enter near to the sidewalls may become levitated towards the low flow velocity regions and effectively become trapped at the local DEP minima of the channel sidewall-top boundary. This phenomenon was observed at some of the higher field strengths used in this study, however, care was taken to ensure that minimal oocyst trapping occurred at the DEP minima of both the sidewalls and electrode arrays. To reduce the effect of particle-sidewall interactions in future generations of the DEP device, an additional buffer inflow could be used to ensure that the sample stream enters more centrally in the *y*-direction, between two buffer flows.

9.3.3 Deflection of Oocysts at the Separation Electrodes

Upon identification of the optimal focusing conditions, these parameters were utilised and the efficiency of the separation electrodes investigated. For each set of flow conditions, the focusing electrodes were actuated with a signal at the maximal efficiency voltages identified in section 9.3.2, while a variety of voltages were applied to the separation electrodes to identify the most suitable conditions for oocyst deflection. All signals were applied at a frequency of 30 MHz. Figure 9.6a shows the average percentage of UTP which were detected flowing towards the bottom outflow of the chip (*i.e.*, *y*-position > 266.7 µm), downstream of the separation electrodes, in a variety of voltage-sample flow rate combinations. By increasing flow rate, the overall efficiency of the device to laterally deflect oocysts across the width of the device became reduced, *e.g.*, the minimum error between measurements was recorded at a sample flow rate of 0.20 µL min^{-1}. It is likely that at the increased power requirements, differences in particle flow velocities and the large population CV (as explained in section 9.3.2) significantly contributed to the reduction in device efficiency for increasing flow rates. In Figure 9.6a, the maximal efficiency voltages for the separation electrodes were identified as 9.5 V at a sample flow rate of 0.20 µL min^{-1}, 10.2 V at 0.25 µL min^{-1} and 10.9 V at 0.30 µL min^{-1}. Furthermore, in each of these sets of conditions, an average of 71.8 ± 3.1%, 60.7 ± 4.4% and 46.7 ± 2.5% of UTP were detected flowing towards the bottom outflow upon focusing and deflection. The electrode spacing between the interdigitated electrodes (20 µm) was smaller than that of the focusing electrodes (50 µm), therefore, the signal amplitude required to manipulate oocyst motion at the interdigitated electrodes was less for a given sample flow rate.

For the best result of 71.8 ± 3.1%, Figure 9.6b shows the average percentage of all oocysts which were detected flowing towards the upper (outlet 1), middle (outlet 2) or lower (outlet 3) channel outlets – the idealised, negatively polarised oocyst should be positioned within the lower third of the channel when exiting (Figure 9.6c). The findings of section 9.3.2 demonstrated that the optimum focusing efficiency achieved at an applied voltage of 16.9 V and sample flow rate of 0.25 µL min^{-1} (79.1 ± 6.1%) – whereby only the focusing electrodes were actuated – was marginally better than at a sample flow rate of 0.20 µL min^{-1} when 14.1 V was applied (76.2 ± 6.8%). Despite this, use of the lowest sample flow rate enabled the deflection of an additional ~11% of the total UTP towards the bottom outflow upon the synchronous actuation of both the focusing and separation electrode arrays (Figure 9.6a). Thus, a sample flow rate of 0.20 µL min^{-1} was chosen as the optimal flow rate for the remaining experiments.

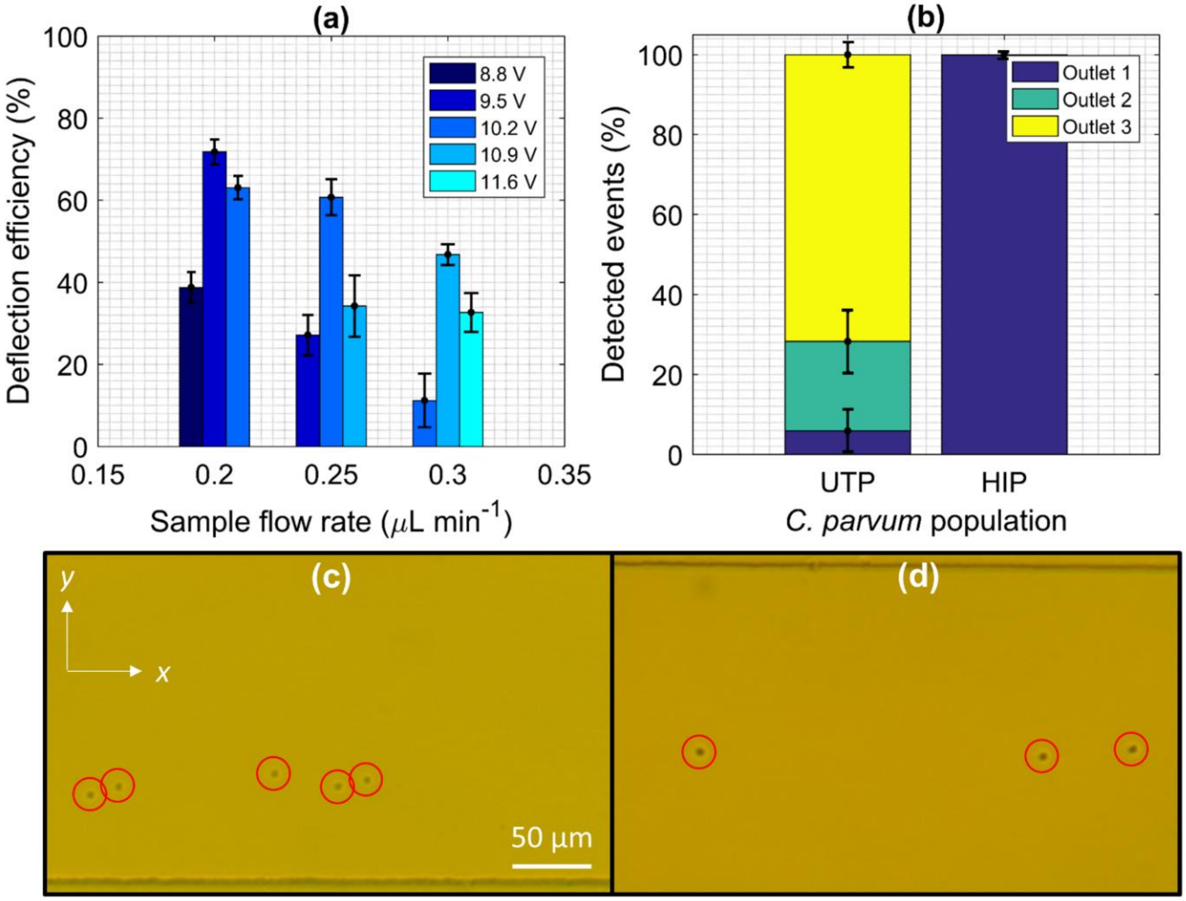

Figure 9.6: Synchronous focusing and deflection of untreated or heat-inactivated *C. parvum*. **(a)** Deflection efficiency of UTP in a variety of voltage-flow rate combinations was measured by quantifying the proportion of oocysts flowing towards the bottom outlet (outlet 3) upon actuation of both sets of electrodes. See section 9.3.2 for description of signal voltage applied to focusing electrodes for each flow rate. Each datapoint represents the average of a minimum of three datasets (*n* = 3). **(b)** The mean percentage (± standard deviation) of all detected UTP or HIP flowing towards each outlet was quantified when exposed to the optimum conditions identified in (a), whereby flow rate = 0.20 µL min^{-1}, voltage applied to focusing electrodes = 14.1 V and voltage applied to separation electrodes = 9.5 V (both voltages applied at frequency of 30 MHz). Same data as Each datapoint represents the average of a minimum of three datasets (*n* = 3). **(c)** Image showing typical positions of focused UTP in the bottom half of channel. **(d)** HIP in top half of channel which were minimally affected by the applied field.

The in-channel y-positions of the HIP was also monitored whilst separate signals of 14.1 V and 9.5 V were applied to the focusing and separation arrays at a frequency of 30 MHz. Figure 9.6b compares the quantity of UTP and HIP detected flowing towards each of the three channel outputs upon application of the electric field – see also Figure 8.1 which shows ideal trajectory of UTP and HIP in device. In agreement with the results presented in section 9.3.2, a low average of ~9.0% of HIP were found to be positioned within the buffer stream (*i.e.*, HIP oocysts that were considered focused). However, only ~0.1% of all HIP oocysts were detected flowing towards the middle and bottom outflows upon passing the separation electrodes (*i.e.*, y-position > 133 µm; see Figure 9.6d). This finding indicates that although the motion of HIP was slightly influenced by F_{DEP} at the focusing electrodes (*i.e.*, ~9% of HIP had y-position > 100), the magnitude of this force was generally too low to significantly deflect HIP into the flow lanes which travelled directly above the separation electrodes.

9.3.4 Mixed Sample Analysis

Samples which contained UTP and HIP were introduced to the chip to validate whole chip function. Figure 9.7 displays the percentage of all oocysts which were detected flowing towards each outlet after passing both electrode arrays, where each data point represents the average across ten independent datasets. The fluid eluted from each outlet was gathered for use in a conventional excystation assay [9.18]. This assay is often used to assess the viability rate of *C. parvum* oocysts, whereby the numbers of excysted (*i.e.*, oocysts which were viable) oocysts and still intact (*i.e.*, oocysts which were non-viable) oocysts are quantified after exposure to conditions which mimic transit through the human gastrointestinal tract [9.20]. The method for calculating overall oocyst viability rate is detailed in section 8.8. The ratio of sporozoites to shells (Sp/ Sh) was also calculated to provide an indication of sample quality – see Table 9.3. For example, a low Sp/ Sh ratio may indicate that many of the excysted oocysts had released their contents prior to the assay, due to, *e.g.*, exposure to environmental stimulants and/ or that apparently intact, viable oocysts did not excyst due to, *e.g.*, DNA damage. Alternatively, a high Sp/ Sh ratio may be indicative of the opposite scenario. The original viability rate and Sp/ Sh ratio, as calculated by the supplier, are given in Table 9.3 as a reference for comparison. The ideal, 100% viable *C. parvum* sample should give an Sp

/Sh ratio of 4, thus, the low Sp/ Sh ratio of the original sample indicates a high proportion of empty (damaged/ excysted) shells.

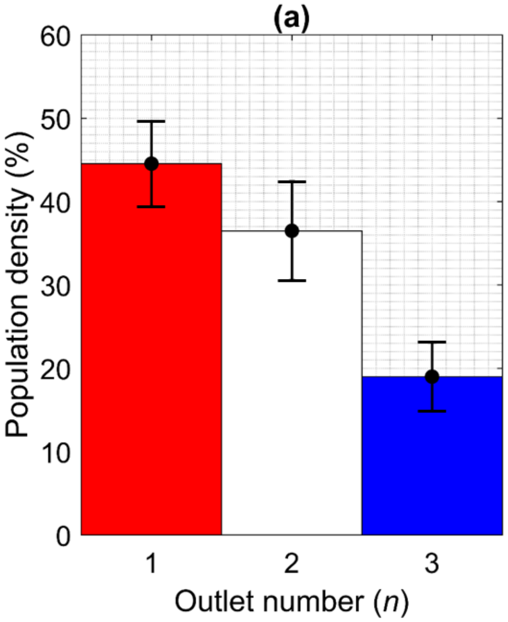

Figure 9.7: Dielectrophoretic sorting of oocysts of mixed viability status. **(a)** The percentage of the oocysts contained within a mixed sample that were detected flowing towards each outlet, upon focusing and deflection, was quantified. Each data point represents the mean ± SD across ten datasets.

The data in Figure 9.7 shows that 44.5 ± 5.1% of the total detected events exited the device *via* Outlet 1 and that 5.9 ± 1.4 % of these oocysts were considered viable using the excystation assay, *i.e.*, an average of 5.9% shell presence. In contrast, 81.8 ± 7.0% and 88.4 ± 3.4% of the oocysts which left *via* Outlet 2 and Outlet 3, respectively, were deemed viable using the excystation assay. Interestingly, the Sp/ Sh ratios calculated for these deflected oocysts were greater than the suppliers original value, demonstrating the ability of the chip to purify UTP oocysts. Nonetheless, an average 55.5% of all events left the device *via* these exits, which, means that some HIP were deflected laterally within the device. Therefore, the actual sorting efficiency of the device (*i.e.*, where the device was left operating for several hours) was less than may have been implied in sections 9.3.2 and 9.3.3, where UTP and HIP populations were assayed independently.

Table 9.3. Excystation assay results for *C. parvum* oocysts exiting DEP chip outlets.

	Viability (%)	*Sp/ Sh*
Outlet 1	5.9 ± 1.4	0.1 ± 0.0
Outlet 2	81.8 ± 7.0	2.4 ± 0.1
Outlet 3	88.4 ± 3.4	2.9 ± 0.5
Original Stock	89.7	2.1

Values show mean ± standard deviation of 3 counts (n = 3).
Sp = sporozoite, Sh = shell.

Due to the high limit of detection of the excystation assay, *i.e.*, where a high concentration of oocysts is desirable for the successful completion of the assay, sample concentration was doubled for mixed sample analysis. Thus, the reduction in whole device efficiency when assaying mixed samples may be due to the influence of oocyst-oocyst interactions. Cell-cell binding in DEP devices can be problematic as agglomerates effectively appear as larger particles [9.21], meaning that they are more likely to influenced by the F_{DEP}. Furthermore, "pearl chain" formations between attracting particles in DEP chips [9.7, 9.9, 9.22] were observed at some of the very high electric field strengths (but not in the optimal conditions) used in this study. Consequently, device efficiency may be negatively affected if agglomerates which contain oocysts of mixed viability status do not flow to the desired output. Despite this, it is likely that actual oocyst concentration would be several orders of magnitude less in a *Cryptosporidium*-contaminated drinking-water sample than that used in this research. Therefore, oocyst-oocyst adhesion effects should be less influential.

9.4 Conclusions and Outlook

In this chapter, $\Re[\tilde{f}_{CM}]$ of *C. parvum* was simulated using the literature-reported dielectric properties of the pathogen but was also estimated experimentally using capture voltage analysis. Generally, the simulated values demonstrated less negative polarisability of oocysts than the experimentally calculated $\Re[\tilde{f}_{CM}]$ values – this probably occurs because the single-shell model used in the simulations does not accurately represent the high-frequency DEP properties of *C. parvum*. By estimating $\Re[\tilde{f}_{CM}]$, the optimum conditions for the dielectrophoretic sorting of untreated and heat-inactivated *C. parvum* were identified. Specifically, at a sample flow rate of 0.20 µL min^{-1}, optimal sorting was achieved by applying signals of 14.1 V and 9.5 V to the focusing and separation arrays at a frequency of 30 MHz, respectively. Ultimately, it was possible to sort a sample containing oocysts of mixed viability into populations which had less than 10% or greater than 80% viability, as indicated using a conventional excystation assay, when the focusing and separation electrodes were actuated simultaneously. Despite this, the error calculated across most measurements was relatively large, probably due to the sensitivity of DEP to *e.g.* particle-particle interactions and small perturbations in flow rate. Furthermore, since the excystation assay is a subjective, *in vitro* assay [9.23], the ability/ experience of the operator to perform the assay may have influenced the results.

The DEP chip typically operated for multiple hours each day – without any evidence of heating, electrode fouling or general device degradation in the identified optimal conditions for oocyst sorting – thus, it would take ~4 hours to process the 50 µL product volume of EPA 1623.1 (see section 2.4.2) at a sample flow rate of 0.20 µL min^{-1}. This is generally too slow and would likely increase the duration of the existing EPA 1623.1 procedure if incorporated. The design of a custom baseplate however, which *e.g.*, accommodates two chips and has common electrical contacts for each type of electrode array, would halve the time required for processing the EPA 1623.1 product volume. Parallelisation of such devices would reduce detection time further, however, the equipment and power requirements would become larger and likely result in a bulky setup, which might be unattractive to water utilities.

In future generations of the device design, the sample should be introduced more centrally across the width of the channel to limit oocyst losses that may have occurred due to the local nDEP attraction forces at channel sidewalls. Furthermore, the fabrication of electrodes on top and bottom channel surfaces would reduce the effects of DEP field dissipation in the upper regions of the microchannel. Consequently, sample throughput may be larger in each single device, since the device height could be greater.

To increase the applicability and relevance of future devices, work should be performed to separate samples of *Cryptosporidium* oocysts which pose little/ no risk to human health from those which are moderate/ high risk pathogens. Unfortunately, due to the large lead time needed recently by the only known supplier (Waterborne Inc., US) of a minor/ no risk *Cryptosporidium* species – *C. muris* – I was unable to perform such work before the conclusion of this research. Despite this, it was shown in Chapter 7 that *C. muris* and *C. parvum* (a high risk pathogen) have overlapping size distributions, plus Unni *et al.* [9.4] have demonstrated that these pathogens also exhibit similar DEP profiles. Therefore, it may be difficult to efficiently sort, *e.g.*, *C. parvum* and *C. muris* using a DEP chip.

9.5 Author Contributions

The following authors contributed to the completion of this work: John McGrath (JM), Ameya Vaidya (AV), Ben Horton (BH), Dr. Helen Bridle (HB) and Epigem (a microfabrication company based in the UK). JM, AV, BH and HB are currently based at Heriot-Watt University (UK). BH is an employee of Moredun Scientific (UK). In order of contribution level, the following aspects of this work were completed by:

1. Designed and fabricated the system: JM (design) Epigem (fabrication)
2. Conceived and designed the experiments: JM
3. Performed the experiments: JM AV BH
4. Analysed the data: JM
5. Contributed reagents/ materials/ analysis tools: HB
6. Wrote up the results: JM

9.6 References

9.1. Khoshmanesh K, Nahavandi S, Baratchi S, Mitchell A, Kalantar-zadeh K. Dielectrophoretic platforms for bio-microfluidic systems. Biosensors and bioelectronics. 2011;26(5):1800-14.

9.2. Beech JP, Jonsson P, Tegenfeldt JO. Tipping the balance of deterministic lateral displacement devices using dielectrophoresis. Lab on a Chip. 2009;9(18):2698-706.

9.3. Lapizco-Encinas BH, Simmons BA, Cummings EB, Fintschenko Y. Insulator-based dielectrophoresis for the selective concentration and separation of live bacteria in water. Electrophoresis. 2004;25(10-11):1695-704.

9.4. Unni HN, Hartono D, Yung LYL, Ng MM-L, Lee HP, Khoo BC, et al. Characterization and separation of Cryptosporidium and Giardia cells using on-chip dielectrophoresis. Biomicrofluidics. 2012;6:012805.

9.5. Doh I, Cho Y-H. A continuous cell separation chip using hydrodynamic dielectrophoresis (DEP) process. Sensors and Actuators A: Physical. 2005;121(1):59-65.

9.6. Quinn C, Archer G, Betts W, O'Neill J. Dose-dependent dielectrophoretic response of Cryptosporidium oocysts treated with ozone. Letters in applied microbiology. 1996;22(3):224-8.

9.7. Su Y-H, Tsegaye M, Varhue W, Liao K-T, Abebe LS, Smith JA, et al. Quantitative dielectrophoretic tracking for characterization and separation of persistent subpopulations of Cryptosporidium parvum. Analyst. 2014;139(1):66-73.

9.8. Goater AD, Burt JP, Pethig R. A combined travelling wave dielectrophoresis and electrorotation device: applied to the concentration and viability determination of Cryptosporidium. Journal of Physics D-Applied Physics. 1997;30(18):L65.

9.9. Pethig R. Review Article—Dielectrophoresis: Status of the theory, technology, and applications. Biomicrofluidics. 2010;4:022811.

9.10. Sun T, Morgan H. Single-cell microfluidic impedance cytometry: a review. Microfluidics and Nanofluidics. 2010;8(4):423-43.

9.11. Jones TB. Basic theory of dielectrophoresis and electrorotation. Engineering in Medicine and Biology Magazine, IEEE. 2003;22(6):33-42.

9.12. Kralj JG, Lis MT, Schmidt MA, Jensen KF. Continuous dielectrophoretic size-based particle sorting. Analytical chemistry. 2006;78(14):5019-25.

9.13. Wu L, Yung L-YL, Lim K-M. Dielectrophoretic capture voltage spectrum for measurement of dielectric properties and separation of cancer cells. Biomicrofluidics. 2012;6(1):014113.

9.14. Han K-H, Frazier AB. Lateral-driven continuous dielectrophoretic microseparators for blood cells suspended in a highly conductive medium. Lab on a Chip. 2008;8(7):1079-86.

9.15. Fayer R, Xiao L. Cryptosporidium and Cryptosporidiosis, Second Edition: Taylor & Francis; 2012.

9.16. Crowley JM. Electrical breakdown of bimolecular lipid membranes as an electromechanical instability. Biophysical journal. 1973;13(7):711.

9.17. Schwan H, editor Electrical properties of tissues and cell suspensions: mechanisms and models. Engineering in Medicine and Biology Society, 1994 Engineering Advances: New Opportunities for Biomedical Engineers Proceedings of the 16th Annual International Conference of the IEEE; 1994: IEEE.

9.18. Blewett D, editor Quantitative techniques in Cryptosporidium research. Proceedings of the First International Workshop on Cryptosporidiosis Edinburgh: The Animal Disease Research Association; 1989.

9.19. Park S, Zhang Y, Wang T-H, Yang S. Continuous dielectrophoretic bacterial separation and concentration from physiological media of high conductivity. Lab on a Chip. 2011;11(17):2893-900.

9.20. Campbell A, Robertson L, Smith H. Viability of Cryptosporidium parvum oocysts: correlation of in vitro excystation with inclusion or exclusion of fluorogenic vital dyes. Applied and Environmental Microbiology. 1992;58(11):3488-93.

9.21. Zahn JD. Methods in Bioengineering: Biomicrofabrication and Biomicrofluidics: Artech House; 2009.

9.22. Voldman J. Electrical forces for microscale cell manipulation. Annu Rev Biomed Eng. 2006;8:425-54.

9.23. Robertson LJ, Gjerde BK. Cryptosporidium oocysts: challenging adversaries? Trends in parasitology. 2007;23(8):344-7.

Chapter 10 – Methods: Microfluidic Impedance Cytometry System

10.1 Introduction

This chapter provides an overview of the design, fabrication and operation of the Microfluidic Impedance Cytometer (MIC) system used in this research as a tool to enumerate and characterise the electrical properties of populations of waterborne pathogens that differ in their species or viability status and are recovered using EPA 1623.1 (see section 2.4). In addition, it provides details concerning the preparation, quality assessment and introduction of samples containing waterborne pathogens to the system and the subsequent data analysis.

10.2 Chip Overview

The design of the MIC chip and system has undergone continual development since initial conception by the research group of Professor Hywel Morgan at the University of Southampton (UK), with whom this research was performed in collaboration – a statement of author contributions to this study is provided in Chapter 11. Despite this, the fluidics remain relatively simple in comparison to many other microfluidics that can be found by simply searching through the literature concerned with the field. The MIC chip used in this research consisted of a single microfluidic channel with one inlet and one outlet, through which sample entered and left. The fluidic constriction had a symmetrical design (Figure 10.1), which included a wider region cross-sectional dimensions 200 µm width x 30 µm height that narrowed into a detection region of 40 µm width x 30 µm height. Sets of microelectrodes pairs were fabricated in the microchannel; each pair included microelectrodes which were positioned on either the top or bottom surfaces of the microchannel and which overlapped by the width of the detection region (Figure 10.1).

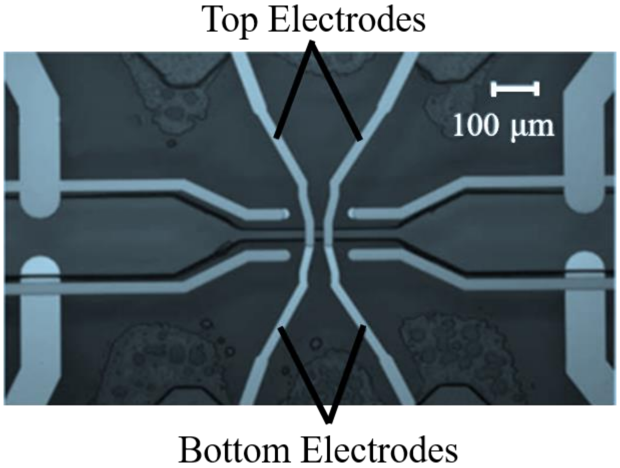

Figure 10.1: Impedance chip detection region. Two identically processed wafers were fabricated and then thermally-bonded to ensure there were electrodes on the top and bottom surfaces of the microchannel.

10.3 Fabrication and Setup

The process of fabrication for the microfluidic chips – which involved standard photolithography and full wafer thermal bonding – has been outlined previously [10.1-10.3]. Nonetheless, the process used was as follows: Firstly, H_2SO_4 was used to clean 500 µm thick 4” Pyrex wafers (Schott, Switzerland), which were then rinsed with distilled water and dried using nitrogen. An EVG150 spin coater was used to deposit a double-layer resist on the wafer, which was then dehydrated. A layer of LOR5A (Microchem, USA) photoresist with 0.45 µm thickness was spun onto the wafers at 4000 rpm, before baking was completed at 183 °C for 8 min. A further 1 µm thick layer of S1813 photoresist (Shipley, US) was spun onto the wafers at 6000 rpm and baked at 115 °C. Using Microposit metal-ion-free developer (MF-319; Shipley, US), the resist layer was patterned photolithographically (Karl Suss MA-6 Mask Aligner, Germany). A 100 nm thick layer of platinum was then evaporated onto the patterned wafer (LAB-600H; Laybold Optics, Germany). Unwanted metal and the resist layer were washed off by ultrasonication in Microposit Remover 1165 (Shipley, US) to define two platinum electrodes with 30 µm width and 50 µm spacing between.

SU-8 negative photoresist (Microchem, USA) was spin coated (2500 rpm) on top of the platinum electrodes at a thickness of 15 µm, followed by a soft bake (5 min at 60 °C), in order to define the microfluidic channel. Two identical wafers were then aligned and thermally bonded (200°C for 30 min) under 5 bars of pressure in air using a Karl Suss MA-6 Mask Aligner (Germany), followed by another bake at 300 °C for 1 h in N_2. Upon the bonding of two identical wafers, the contained chips had microchannel heights of 30 µm. The wafers were divided into single microfluidic chips by dicing with a diamond saw (DAD321, Disco Corporation) and inlet/ outlet holes were cut using a CO_2 laser (Mini 18, Epilog Laser).

The MIC chip was clamped within a custom built, 3D-printed holder (Figure 10.2), with miniature O-rings placed within the laser cut input/ output holes, at the interface of the holder and chip, to limit the risk of leakage. Input and exit holes were machined in the holder at identical positions to the chip design, such that tubing could be inserted, sealed and then fixed using a gasket, to permit the leak-free inflow and exit of fluid to the clamped MIC chip. Spring loaded electrical clips were mounted to the holder as to make connection with the electrical contacts of the chip. The chip holder was then placed on a printed circuit board (PCB) which contained the impedance detection circuitry, before the entire set-up was mounted onto a microscope with camera attachment that allowed visualisation of the detection region.

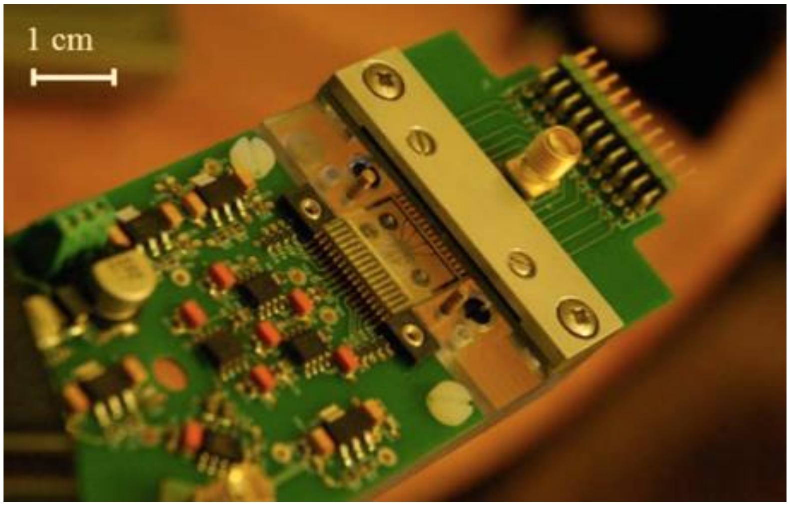

Figure 10.2: MIC chip mounted within 3D-printed holder. The holder houses fluidic and electrical connections and is mounted to a PCB which contains the impedance detection circuitry. Upon connecting the impedance analyser (HF2LI, Zurich Instruments, Switzerland), an AC signal can be applied to the microelectrodes of the MIC chip.

10.4 Impedance Measurement

With sample flow initiated (details of sample preparation and introduction described later in section 10.6), sinusoidal voltages were applied at two simultaneous frequencies (f_1, f_2; see Figure 10.3a) to the top two electrodes using a digital impedance analyser (H2FLI, Zurich Instruments, Switzerland). The first voltage, termed the reference frequency, was applied to the top electrodes at 18.3 MHz. A frequency of 18.3 MHz was the maximum frequency which could be applied before signal collection became attenuated by the input and output filters of the lock-in amplifier (see section 10.5). Furthermore, this reference signal was applied at high frequency, beyond the outer wall relaxation frequency of the parasites, so that any differences in the internal composition of untreated and heat-treated *C. parvum* would be exposed [10.1, 10.4]. Dielectric polarisation of the outer membrane typically occurs at a few MHz for biological cells (discussed in section 4.2.4). The second frequency, termed the probe frequency, was applied at 24 discrete frequencies between 0.25 to 50 MHz to characterise the impedance response of the sampled pathogens over a wide frequency range. The voltage applied ranged from 0.75 Vpp to 10 Vpp depending on buffer conductivity – lower power was used with increasing buffer conductivities to prevent system overload.

The difference in current flowing through the bottom electrodes was measured by the custom detection circuit (Figure 10.3a). The circuit consists of transimpedance amplifiers, which convert current (I) to voltage (V), and a differential amplifier, which amplifies the difference between the two input voltages and suppresses any common voltage. Lock-in amplification (HF2LI, Zurich Instruments) was then used to separate the magnitude and phase at each frequency, based on the real and imaginary parts of the signal, with the input signal used as a reference (indicated by dotted line from "AC signal" to "Lock-in Amplification"). Data were recorded for approximately 30 s, before the probe frequency was increased incrementally. The resulting impedance data was stored for subsequent data analysis.

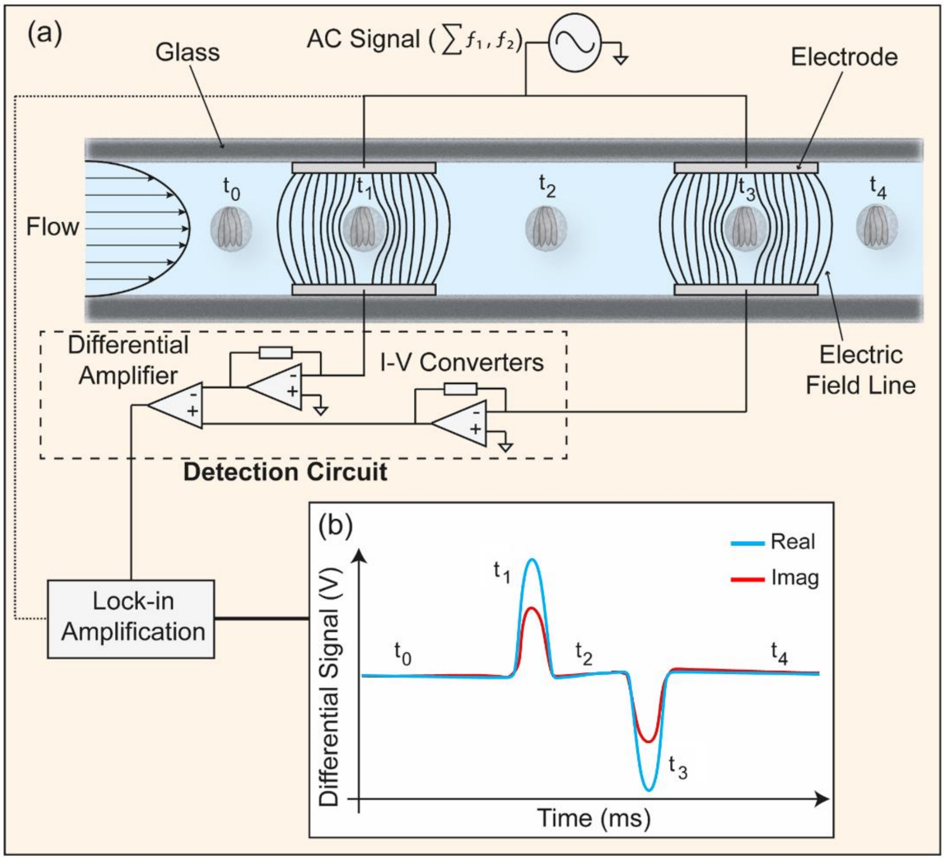

Figure 10.3: Schematic showing the concept structure of the microfluidic impedance cytometer chip. **(a)** The detection region consists of pairs of parallel facing electrodes which are 30 μm wide and separated by 50 μm. The electrodes are fabricated within a microfluidic channel which is 40 μm wide x 30 μm high. Waterborne pathogens suspended in PBS (*C. parvum* illustrated) are driven through the channel by pressure-driven flow. Sinusoidal voltages at two discrete frequencies (f_1, f_2) are applied to the top electrodes and the difference in current flowing through the bottom electrodes is measured by the custom detection circuit. **(b)** The idealised differential impedance signal that results when an oocyst passes the center of the detection region – annotated steps correlate with oocyst positions shown in (a).

When a suspended particle, with diameter on the order of a few microns, passes the detection region, it measurably disrupts the current flow. Shown in Figure 10.3b is a representation of the idealised differential signal that results when a *Cryptosporidium* oocyst (or any particle generally) passes the center of the detection region. The corresponding steps of this sequence are annotated, *e.g.*, t_0 represents the impedance signal measured before the suspended particle reaches the first electrode pair, while t_2 and t_4 are indicative of the particle passing the first and then second electrode pairs. Thus, for each passing particle, impedance is measured at two discrete frequencies.

As was demonstrated by Spencer *et al.* [10.5], particles experience inertial focusing when flowing at a rate of 40 µL min^{-1} through a rectangular geometry with dimensions on the order of those given in section 10.2. In this environment, particles pass through the detection region in two equilibrium positions, which are typically a factor of 0.4 multiplied by the distance from the channel centre to upper or lower channel walls [10.5, 10.6]. In contrast, particle position is more disperse within the flow when flow rate is below that required for inertial focusing. With the inertial focusing effect in place, the CV in the measured impedance signal is negligible, as it becomes smaller than the CV of any cell or particle population. This means that data retrieved from passing particles of a single population, at either equilibrium position, displays consistent form. Furthermore, a characteristic of MIC sensing is that particles which pass closer to the current sensing (bottom) electrodes have greater impedance *(i.e.,* they offer more resistance to current flow) than those which pass near the current injection (top) electrodes. Consequently, it is possible to determine, based on the magnitude of the impedance signal, at which of these two positions a particle is located. By measuring the time between a particle's impedance measurements at the first and second electrodes, which have a known distance, it is also possible to calculate a particle's flow velocity. Therefore, using MIC it is possible to extract details about the position, velocity and electrical properties of a particle, in addition to traditional cytometric parameters.

10.5 Accounting for Signal Attenuation

When using the system, signal collection is attenuated by the input and output filters of the lock-in amplifier at frequencies above 20 MHz, with -6dB at 50 MHz. Therefore, for frequencies ≥ 20 MHz, the applied voltage was increased incrementally to account for the consequent signal loss. The average signal magnitude for the 3 frequencies prior to 20 MHz was firstly calculated ($\bar{Z}_{<20\ MHZ}$). Then, the increment factor to be applied was calculated by dividing this average value by the average magnitude signal for each frequency (*e.g.*, $factor_{50\ MHZ} = \bar{Z}_{<20\ MHZ}/\bar{Z}_{50\ MHZ}$ for 50 MHz). An example can be found in Figure 10.4. By increasing the voltage applied with the necessary factor, signal loss was minimised without affecting data collection or analysis.

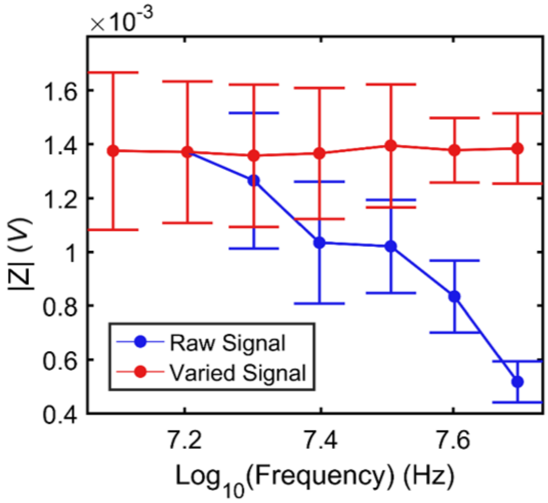

Figure 10.4: Attenuation of signal loss. High frequency impedance magnitude of 7 µm polystyrene beads with (red) and without (blue) correcting for signal attenuation.

10.6 Sample Preparation, Introduction and Chip Cleaning

Four different stock samples were used in the analysis of untreated (UTP) and heat-inactivated parasites (HIP). At the time of analysis, the first batch of calf-sourced *C. parvum* (WC1) was used within one month of propagation. A second batch of calf-sourced *C. parvum* (WC2) and a batch of mouse-sourced *C. parvum* (WM) obtained from Waterborne Inc. (Iowa strain; US) were used within 1-2 months of oocyst propagation. Calf-sourced *C. parvum* (MC) obtained for Moredun Scientific (Moredun Strain; UK) was used when aged approximately 2-3 months. All oocysts were obtained in suspensions containing PBS + 2% antibiotics + 0.01% Tween 20.

From each stock, samples containing UTP or HIP were independently prepared and the impedance measured separately. In each sample, oocysts were diluted to a final concentration of ~100 oocysts µL^{-1} of PBS. Various PBS concentrations were used as the suspending buffer to explore the effect of varying sample conductivity – medium conductivity (σ_m) ranged from

0.76 – 7.10 S m^{-1}; each buffer also contained 0.1% Tween 20. Additionally, polystyrene beads of 7 µm diameter (Microparticles GmbH) were added to each sample to a final concentration of 100 beads μL^{-1}. Polystyrene beads have a known size and electrical properties [10.1], and have a constant impedance across the frequency range used in these experiments. The measured impedance signal of each cell is therefore normalised with respect to the bead by dividing with the mean impedance of the polystyrene beads for each frequency, thus removing any non-linear system response. Prior to measurement, the sample was mixed in the containing Eppendorf tube using a vortex mixer, before being carefully drawn into a syringe and pumped through the MIC at 40 µL min^{-1} using a syringe pump (Fusion 400, Chemyx).

For impedance analysis of live pathogens which are typically recovered using the existing EPA 1623.1 detection protocol (*i.e.*, *Cryptosporidium* spp. and *G. lamblia*; see section 2.4), individual samples containing *C. parvum*, *C. muris* or *G. lamblia* (all Waterborne Inc.) were prepared in PBS + 0.1% Tween 20 (σ = 1.60 S m^{-1}). Mixed samples were diluted to contain a total of ~100 (oo)cysts and 100 beads μL^{-1} of sample; mixed samples were prepared to include equal numbers of each pathogen. All samples were introduced to the system and impedance measured according to the steps described earlier in section 10.4.

Between samples, the chips were flushed with 1 mL ethanol (70%) and 1 mL DI water using a syringe. Electrode surfaces were cleared of debris daily by introducing 1 M sodium hydroxide into the system at 50 µL min^{-1} for ~4 mins, before 1 mL DI water was again rinsed through.

10.7 Inactivation of *C. parvum* Oocysts

To inactivate oocysts, samples prepared as described for UTP in section 10.6 were subjected to a heat-treatment of 70°C for 5 mins in a heating block (Stuart Scientific, UK) before introduction to the system. This treatment is reported in the literature as the minimum treatment required for loss of infectivity in the mouse model [10.7, 10.8].

10.8 Excystation Assay

The viability rates of the live *C. parvum* stock samples were estimated using an *in vitro* excystation assay as described earlier in section 8.8. Approximately, 1 x 10^6 oocysts were used for each assay.

10.9 Data Processing and Statistical Analysis

Custom script was generated in Matlab (R2016a) for processing and statistical analysis of gathered impedance data. In order to make reliable statistical inference regarding each population, samples containing each population were first measured separately. Using the UTP population as an example, impedance scatter plots of impedance magnitude *vs* phase were plotted at reference frequency (18.3 MHz) – data retrieved using the real and imaginary parts of the signal, respectively – before the 7 µm polystyrene beads were gated from the contained *C. parvum* population and smaller debris. As was highlighted in section 10.6, polystyrene beads have frequency independent dielectric properties within the frequency range used in this research, thus, can be used to normalise the impedance signal across the probe frequency range and remove system non-linearities. Upon normalisation, UTP could then be gated relative to the impedance of the polystyrene beads – again at reference frequency. Consequently, the normalised impedance response of gated pathogens at the probe frequency could then be plotted and statistically analysed.

By considering the spread and orientation of the data, it was possible to estimate the level of discrimination achieved across both impedance dimensions, at a given frequency, between any two populations. Firstly, the covariance matrix was calculated to identify the directions in which the 2-D data of a single population varied the most – the largest and smallest eigenvectors of the matrix indicated the directions of the spread of the data and the magnitude of these vectors corresponded with the largest and smallest eigenvalues of the matrix. Secondly, with respect to spread and orientation of each population, confidence ellipses containing all events within 1 – 3 SDs of the mean were plotted to identify the positions of equal probability deviation between two clusters, *i.e.*, at the intersection of the equivalent confidence ellipses is where a data point has equal probability of belonging to either population. A segregating line was then fitted to the points of intersection and subsequently, the efficiency of discrimination was calculated – *i.e.*, by counting the number of oocysts from each population that plotted either side of the segregating line.

10.10 Flow Cytometry

To provide an equivalent, label-free comparison to MIC, flow cytometric analysis of parasite suspensions was carried out at 35 µL min^{-1} using a BD Accuri C6 flow cytometer (BD Biosciences) containing two lasers (488 nm and 640 nm). Flow cytometry data were exported as standard FCS files and the forward and side scattered light (FSC and SSC) signals were analysed and plots generated using Matlab.

10.11 References

10.1. Spencer D, Hollis V, Morgan H. Microfluidic impedance cytometry of tumour cells in blood. Biomicrofluidics. 2014;8(6):064124.

10.2. Holmes D, Pettigrew D, Reccius CH, Gwyer JD, van Berkel C, Holloway J, et al. Leukocyte analysis and differentiation using high speed microfluidic single cell impedance cytometry. Lab on a Chip. 2009;9(20):2881-9.

10.3. Holmes D, She JK, Roach PL, Morgan H. Bead-based immunoassays using a micro-chip flow cytometer. Lab on a Chip. 2007;7(8):1048-56.

10.4. Song H, Wang Y, Rosano JM, Prabhakarpandian B, Garson C, Pant K, et al. A microfluidic impedance flow cytometer for identification of differentiation state of stem cells. Lab on a Chip. 2013;13(12):2300-10.

10.5. Spencer D, Morgan H. Positional dependence of particles in microfludic impedance cytometry. Lab on a Chip. 2011;11(7):1234-9.

10.6. Amini H, Lee W, Di Carlo D. Inertial microfluidic physics. Lab on a Chip. 2014;14(15):2739-61.

10.7. Fayer R. Effect of high temperature on infectivity of Cryptosporidium parvum oocysts in water. Applied and environmental microbiology. 1994;60(8):2732-5.

10.8. Su Y-H, Tsegaye M, Varhue W, Liao K-T, Abebe LS, Smith JA, et al. Quantitative dielectrophoretic tracking for characterization and separation of persistent subpopulations of Cryptosporidium parvum. Analyst. 2014;139(1):66-73.

Chapter 11 – Identification of Waterborne Parasites using Microfluidic Impedance Cytometry

11.1 Introduction

The standard method of isolation and detection for *Cryptosporidium* oocysts present in treated water supplies, EPA 1623.1 [11.1], typically involves the processing of 50-1000 L of water to a 50 µL volume, before highly-skilled microscopists confirm detection using specialised techniques [11.2] – see Chapter 2. This process also simultaneously recovers cysts of the *Giardia* genus – protozoan parasites that may cause gastroenteritis if ingested by humans [11.1]. Generally, EPA 1623.1 is labour intensive, time consuming and does not confer the viability status (*i.e.* cannot discriminate between oocysts which are capable or incapable of initiating infection) or species of recovered oocysts [11.2].

Monitoring for the presence of *Cryptosporidium* is a regulatory requirement within the UK [11.3]. Water services must perform compulsory procedures if the count exceeds 10 oocysts per 100 L [11.3, 11.4]. These procedures are carried out regardless of the viability status or species of detected oocysts because existing methods do not provide this information [11.1]. Although issuance is rate, water utilities may issue a "boil water" notice in the event of a severe contamination [11.3, 11.4] – as occurred in Lancashire, England in 2015, where over 300,000 homes were without potable water for almost one month.

To characterise the electrical properties of and discern between live and temperature-inactivated *C. parvum*, several published works have employed AC electrokinetic techniques (see Chapter 4). In these studies, the dielectrophoretic [11.5, 11.6] – as was investigated in Chapter 9 – or electrorotational [11.7, 11.8] responses of *C. parvum* were investigated. Measurements were either performed in batch [11.5, 11.7, 11.8], required long processing times [11.6] or required microscopy to assess the oocyst response to an applied field [11.5-11.8]. As *Cryptosporidium* is often present in very low numbers (typically < 100 oocysts are recovered from 1000 L filtered drinking-water in *Cryptosporidium*-positive samples) [11.9], conventional staining and enumeration would still be required for confirmation of presence.

Therefore, incorporation of such techniques into EPA 1623.1 would increase the duration of the process further [11.2].

AC electrokinetic techniques have been utilised for sorting at the genus level, *e.g.*, *Cryptosporidium* and *Giardia*. The work of Unni *et al*. [11.10] demonstrated the dielectrophoretic separation of *Cryptosporidium muris* and *Giardia lamblia* on-chip, in batch mode, but did not report a limit of detection. However, such approaches have not, to our knowledge, been used for the discrimination of alternate species of *Cryptosporidium* and it has been suggested that the separation of *C. parvum* and *C. muris* might not be possible, as both show a minor difference in dielectric properties [11.10].

In the literature, a single example of an electrical impedance analysis system to characterise the electrical properties of viable and non-viable *C. parvum* oocysts was published by Houssin *et al*. [11.11]. The authors reported a 15% difference in impedance magnitude of a low conductive buffer containing either viable or non-viable *C. parvum*. However, oocysts recovered using EPA 1623.1 could be of mixed viability [11.12]; therefore, it is a necessity that any impedance system used for this purpose can discern the viability status of single oocysts. To our knowledge, there are no reports of the impedance analysis of different *Cryptosporidium* species, or the simultaneous impedance analysis of *Cryptosporidium* and *Giardia*.

The ability to rapidly enumerate and discriminate *Cryptosporidium* oocysts on the basis of viability status and/ or species in an automated process would reduce the detection time of EPA 1623.1, reduce the level of human intervention required, aid in better assessing the risk posed to human health and contribute to the saving of numerous resources [11.13].

In this chapter, the use of Microfluidic Impedance Cytometry (MIC; see Chapter 4) to detect single protozoan (oo)cysts within continuous flow is detailed. The biophysical properties of live and temperature-inactivated, human-pathogenic parasites was also characterised and sample composition was assessed by analysing the electrical data. Single *C. parvum* and *C. muris* oocysts, as well as *G. lamblia* cysts were detected. Detection and viability/ species analysis of oocysts in continuous flow using MIC offers a significant advance over other approaches, both in terms achieving this information at the single (oo)cyst level and the speed of data collection. Following validation studies, MIC could offer the high sensitivity needed for the detection and discrimination of highly infectious, waterborne pathogens. Furthermore, it offers the advantage of ease of incorporation into the existing framework.

11.2 Dielectric Behaviour of Biological Cells

To assist in the interpretation of the gathered electrical impedance data concerning waterborne parasites (discussed from section 11.3 onwards), the impedance response of the typical biological cell will firstly be discussed. Generally, biological cells are insulating at low frequencies (kHz), due to the presence of the lipid cell membrane, but become increasingly conductive at higher frequencies (MHz) due to the short circuiting of the membrane capacitance (so called β-dispersion/ -relaxation) [11.11, 11.14, 11.15] – see Figure 11.1. Impedance magnitude at low frequencies (< 1 MHz) is typically a measure of cell volume, meaning that intact cells or solid objects of similar size cannot be easily distinguished at low frequencies. In the MHz regime, cell impedance firstly becomes a function of the membrane capacitance (typically occurs at frequencies 1 – 10 MHz) before cytoplasm conductivity strongly influences the response at high frequencies (> 10 MHz) [11.16]. Consequently, cells of similar size may show differences in their impedance responses, due to variations in the biochemical composition and/ or structure of the membrane and cytoplasm. For example, impedance phase is the angle by which current flow lags the applied voltage. Cells which have a high lipid content, for instance, are more electrically insulating [11.14, 11.17] and thus, induce greater lag to the signal than those which have a lower lipid content. As signal frequency increases further, *i.e.*, typically > 30 MHz, impedance becomes a measure of the biochemical complexity of the cell interior [11.16]. For example, the initiation frequency and rate at which the dielectric relaxation of internal organelles (such as sporozoites in the case of *Cryptosporidium*), nuclei and other membrane-bound organelles occurs is dependent upon the structure and biochemical composition of such entities.

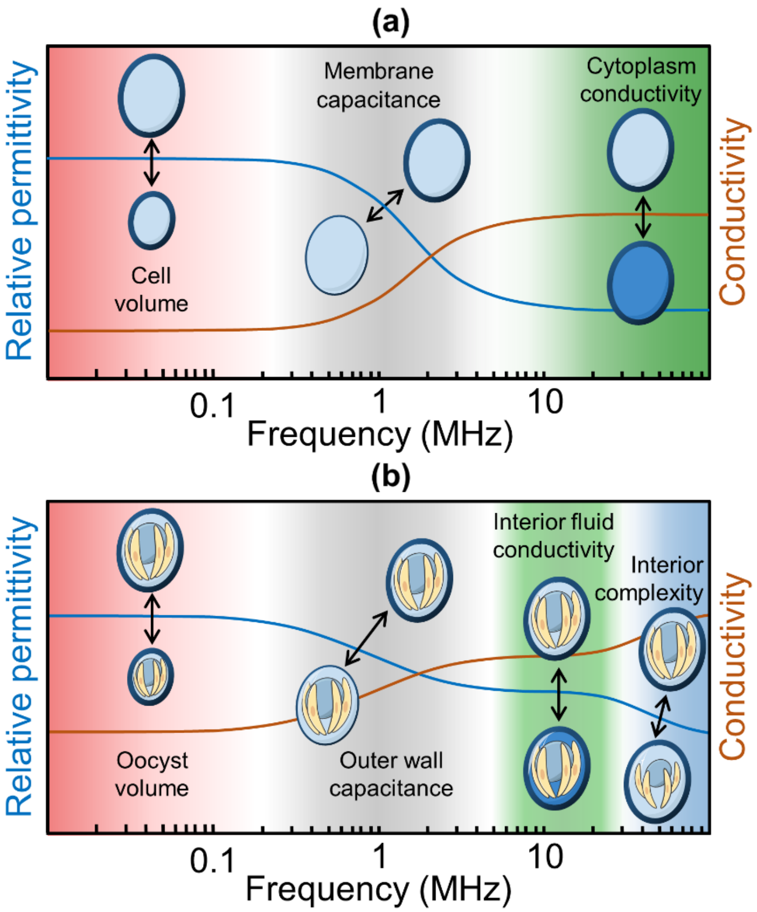

Figure 11.1: The frequency-dependent dielectric response of a single-shelled particle *vs* a *C. parvum* oocyst. **(a)** A simplified, single shell model is sometimes used to approximate the dielectric properties of cells/ particles. A cell/ particle which is surrounded by a single shell typically experiences a single dielectric dispersion, often termed a Maxwell-Wagner polarisation, within the frequency range of 1 – 10 MHz, due to the polarisation of the cell/ particle cytoplasm. **(b)** For more complex biological structures, like the *C. parvum* oocyst, a simplified single-shell model cannot accurately calculate the dielectric properties of the oocyst components. For example, *C. parvum* oocysts are likely to experience multiple Maxwell-Wagner polarisations due to the polarisation of successive cell layers by an AC signal of increasing frequency. The initiation and rate at which such polarisations occurs is dependent upon the biochemical composition and structure of the probed oocyst layer.

Upon viability loss, the physical disruption of the outer membrane (Figure 11.2a) results in biological cells becoming electrically leaky, which manifests as changes in the lower frequency impedance [11.15]. Therefore, non-viable cells may appear smaller in volume because of membrane disruption. Despite this, the apparent change in volume is usually small, since the surrounding membrane is relatively thin in comparison to the size of the typical cell cytoplasm, meaning that discrimination of non-viable and viable cells is often not possible. Although inconclusive, due to the limitations of microscopy, the outer wall of HIP (Figure 11.2c) generally appears less convoluted than that of the untreated oocysts (Figure 11.2b), which suggests that the outer wall became denatured during the inactivation treatment.

Non-viable cells also generally become incapable of regulating ion transfer and maintaining osmotic pressure as efficiently as viable cells [11.15, 11.18] – Figure 11.2a. A contributing factor to the ability of viable oocysts to persist in the environment for long durations is their strict regulation of ion transfer. Upon inactivation, oocysts no longer regulate ion transfer as efficiently as untreated oocysts. Thus, the internal composition of the inactivated oocyst becomes compromised. For example, in Figure 11.2, the interior constituents appear less granular in (c) than (b), which may indicate a change in the internal composition of HIP. Therefore, by suspending cells in non-isosmotic conditions, it is possible to induce change in the biochemical composition of the cell and consequently, change its intermediate and/ or high frequency impedance responses (*e.g.*, due to changes in the composition/ ionic content of the cytoplasmic fluid or internal organelles).

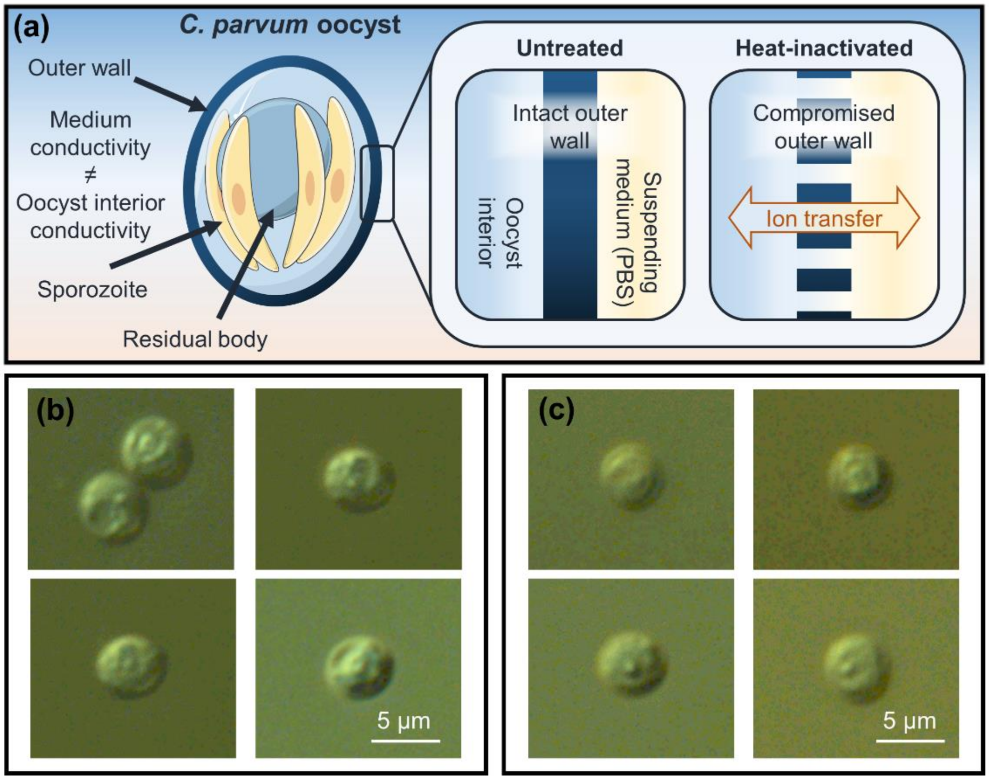

Figure 11.2: Diagram showing the structure of both the untreated (live) and heat-inactivated (non-viable) *C. parvum* oocysts in PBS. **(a)** Schematic showing hypothetical effect of heat-inactivation on oocysts suspended in PBS. The *C. parvum* oocyst generally consists of a trilaminar outer wall, which contains four naked, sporozoites and a membrane-enclosed residual body. Upon inactivation, the direction of ion transfer is influenced by buffer conductivity. **(b)** Untreated (UTP) *vs* **(c)** heat-inactivated (HIP) oocysts in PBS, viewed under oil immersion (100x) with DIC microscopy.

11.3 Impedance Analysis of Parasites

Impedance data gathered for four different UTP populations suspended in 0.5x PBS (σ_m = 0.76 S m^{-1}), at a reference frequency of 18.3 MHz are shown in Figure 11.3. A high reference frequency, beyond the β-relaxation frequency of the parasites, was selected so that the internal properties of the oocysts could be probed [11.15, 11.19]. Impedance magnitude (|Z|) is plotted on the *x*-axis and impedance phase (ΦZ) on the *y*-axis, where each data point represents a single oocyst and its colour reflects the data density. The data sets, and all data hereon in, were referenced to the impedance of the polystyrene beads to eliminate any drift in the measurement system. Previous analysis of the electrical properties of both UTP and

HIP by AC electrokinetic techniques required the use of a low conductive buffer such as deionised water to discern between the populations [11.5, 11.7, 11.10]. However, these methods had a poor limit of detection and performed measurements of whole cell populations. In contrast, MIC measures single cells suspended in buffer of physiological conductivity and has been previously shown to determine the viability of tumour cells [11.15]. Thus, a buffer conductivity of $\sigma_m = 0.76$ S m^{-1} – *i.e.*, the midpoint between the buffer conductivities typically reported for other AC electrokinetic analyses of these parasites and the typical operating buffer conductivities of MIC studies – was selected initially for impedance measurements.

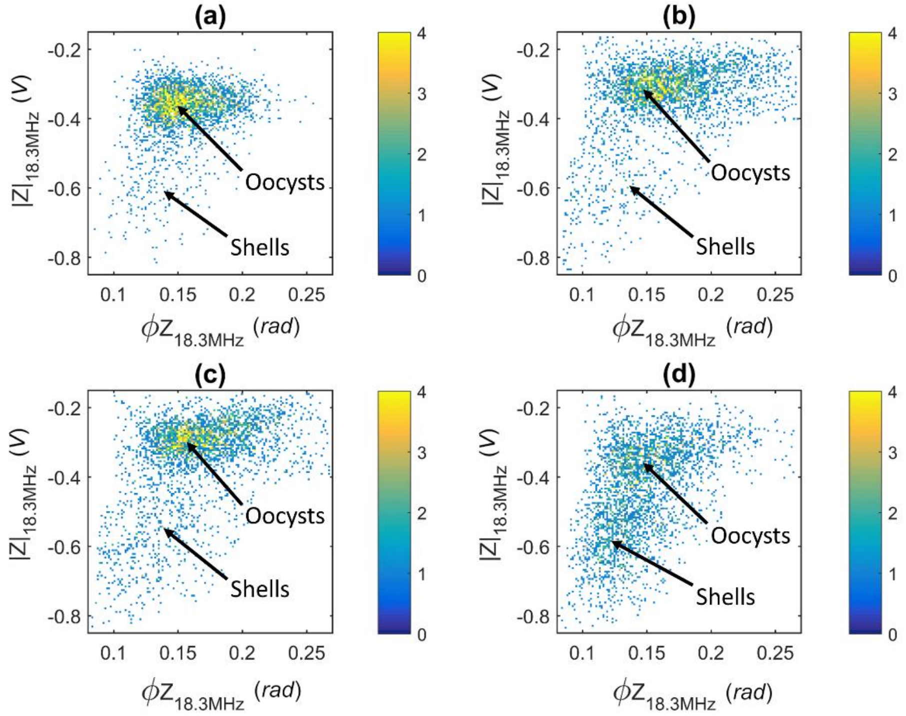

Figure 11.3: Impedance scatter data for four untreated *C. parvum* (UTP) samples at reference frequency. Impedance data was gathered in media of conductivity $\sigma_m = 0.76$ S m^{-1}. Each data point is a single oocyst and data point colour represents the data density. The first 3000 detected events are plotted in each figure subset and oocyst or shell populations are annotated. **(a)** A sample of calf-sourced oocysts (Iowa strain) was measured within 0-1 months of oocyst propagation. **(b)** Mouse-propagated oocysts (Iowa strain) were used within 1-2 months. **(c)** A second sample of calf-sourced oocysts (Iowa strain) was used within 1-2 months. **(d)** Calf-sourced *C. parvum* (Moredun strain) were measured within 2-3 months.

With environmental aging, *e.g.*, exposure to natural stressors like UV light and temperature variations or alternatively, sample transit and processing when used in a laboratory setting, some oocysts within a sample may become collapsed, distorted or even excysted [11.20]. In such a scenario, the infective sporozoites may be lost and consequently, oocysts become "empty shells" or "ghosts". Empty shells are routinely detected in environmental drinking-water samples [11.21] and the impedance data in Figure 11.3 shows the presence of such damaged/ excysted oocysts. The shells appear as a separate cluster below the main oocyst population and have lower impedance magnitude and phase on average. The subplots of Figure 11.3a – d are showing in ascending order of age. Interestingly, the youngest (a) and oldest (d) *C. parvum* samples have the least and most shells present respectively, which implies that shell presence increases with environmental age.

11.4 Frequency-dependent Modelling of Impedance Response

As previously described, impedance data reflects the dielectric properties of the system, namely its permittivity and conductivity (Figure 11.1). Generally, the dielectric behaviour of cells in suspension is defined by Maxwell's mixture theory (MMT) [11.22], which describes the complex permittivity of the suspension in terms of the cell complex permittivity, the suspending medium and the volume fraction [11.23]. Based on MMT, shell-based models have been extensively proposed to model the dielectric properties of cells in suspension [11.23-11.25] and to interpret experimental results in AC electrokinetics.

These shell-based models (see section 4.2) take into account the known structure of the suspended cell, with single shell models being used for cells with just a membrane and no relevant interior content, and double shell models being applied for more complex cells with relevant organelles (such as the nucleus or sporozoites in the case of *C. parvum)*. The frequency-dependent dielectric behaviour of these two different models can be given in terms of Debye relaxations [11.26], which describe the dielectric relaxation of the induced dipole moment within a cell/ particle under an AC field. Single shells typically have a single relaxation curve (due to the membrane β-dispersion, Figure 11.1a), and double shells have a double relaxation curve (the first relaxation associated with the membrane and the second with the interior organelles, Figure 11.1b) [11.16, 11.23]. Thus, the integrity and complexity of suspending cells can be inferred by fitting known data to these models.

The impedance response of UTP and HIP suspensions was analysed over a range of probe frequencies, from 250 kHz to 50 MHz, with a buffer conductivity of $\sigma_m = 0.76$ S m^{-1} - see Figure 11.4. The real ($\Re(Z)$) and imaginary ($\Im(Z)$) parts of impedance are plotted on the *y*-axes along the frequency spectrum used (in Log scale, *x*-axes). Each data point represents the mean of 1000 events per probe frequency.

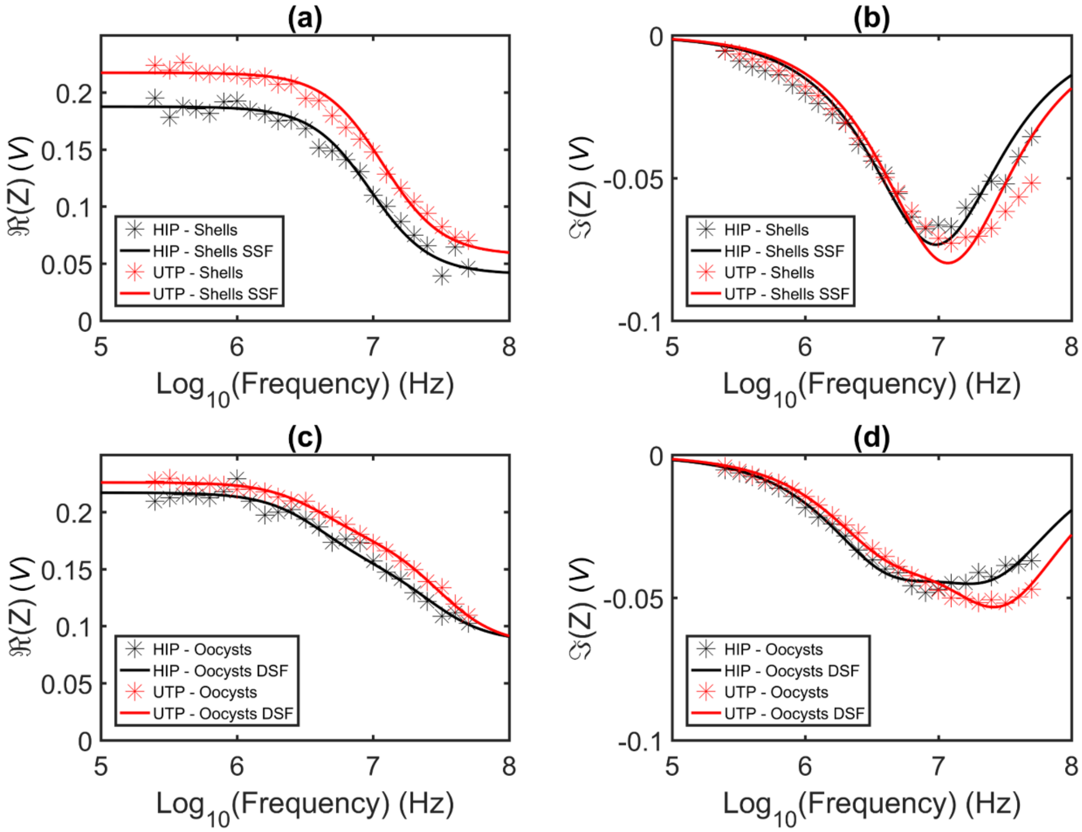

Figure 11.4: Impedance response of UTP and HIP suspensions along the probe frequency range - 250 kHz to 50 MHz, in a buffer conductivity of $\sigma_m = 0.76$ S m^{-1}. The mean value of the real ($\Re(Z)$) and imaginary ($\Im(Z)$) parts of the differential impedance signal for shells (**(a)** and **(b)**) and oocysts (**(c)** and **(d)**), respectively, is plotted (stars). The two sets of data were then modelled using a single shell fit (SSF) for shells (**(a)** and **(b)**) and a double shell fit (DSF) for oocysts (**(c)** and **(d)**), and plotted together with the data (solid lines).

The data of shells found in both HIP and UTP suspensions was firstly modelled using a single shell fit (SSF) – Figure 11.4a - b. As expected, the simple structure of the oocyst shell, where few/ no sporozoites and other organelles were present, fits well to a single relaxation of the membrane. Moreover, the heat inactivation of the suspension results in a physical disruption of the membrane of the shells, leading to an apparent reduction in the low frequency impedance (Figure 11.4a). In terms of the oocysts, an initial SSF was applied (Figure 11.5a), however the poor fit to the data (in comparison to the DSF in Figure 11.4 c-d) shows that the model clearly does not fully represent the intricacies of the oocyst structure. Hence, a double shell fit (DSF) was implemented, with the model clearly fitting to the data this time, *i.e.*, it correctly represents the relaxation the oocyst membrane (~1-10MHz) followed by the relaxation of the interior content (>10MHz). Furthermore, as seen in the case of shells, the heat inactivation and consequent membrane disruption causes a small drop in low frequency impedance (Figure 11.4c). These fits confirm that the two identified populations (Figure 11.3) are correctly labelled and that *C. parvum* shells can, thus, be excluded from future impedance analysis.

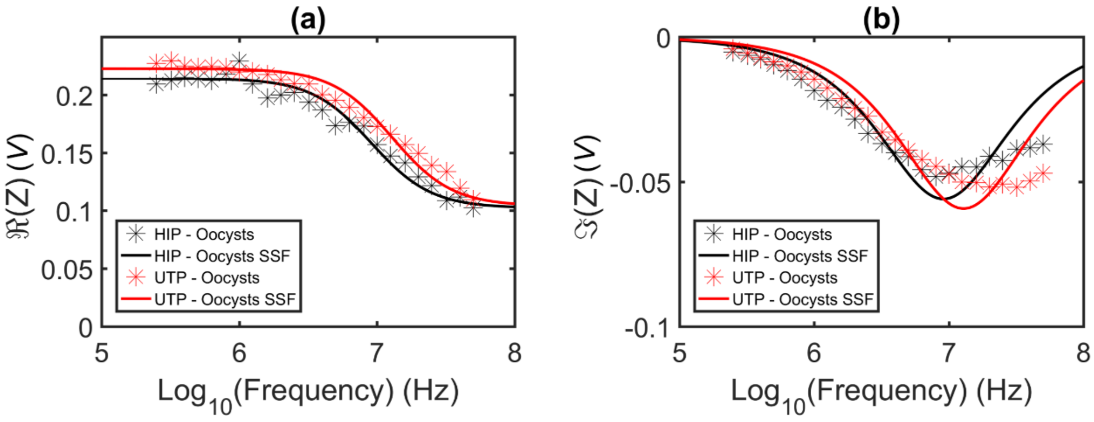

Figure 11.5: Single shell fit modelled to UTP and HIP impedance data along the probe frequency range - 250 kHz to 50 MHz, in a buffer conductivity of σ_m = 0.76 S m^{-1}. The mean values of the real ($\Re$(Z)) and imaginary ($\Im$(Z)) parts of the differential impedance signal for UTP **(a)** and HIP **(b)** are plotted (stars). The modelled single shell fits are indicated by solid lines.

11.5 Impedance Analysis of Parasites in PBS

The average impedance of all UTP or HIP populations across the probe frequency range, whilst suspended in a buffer of physiological conductivity (σ_m = 1.51 S m^{-1}), is shown in Figure 11.6a - b. By increasing buffer conductivity, the β-relaxation frequency of the parasites was shifted towards higher frequencies – see data in Figure 11.4c - d for lower conductivity comparison. This occurred as a consequence of charge build-up within the system and demonstrates that, within the probe frequency range, the applied signal penetrates further into the oocyst structure in low conductive buffer [11.16]. Despite this, a difference in the dielectric properties of UTP and HIP was apparent, especially at higher frequencies (see Figure 11.6c - e), whereby impedance was likely a function of the oocyst internal fluid (*i.e.*, the cytoplasmic fluid of the typical biological cell) or the complex oocyst interior. Previous works [11.5, 11.7, 11.10] using AC electrokinetic techniques and a single shell model have estimated the internal conductivity of UTP (often termed cytoplasmic conductivity – σ_{cyto}) to be 0.047 – 0.055 S m^{-1} when suspended in DI water. Although the single shell model is too simplistic for accurate approximation of the dielectric properties of the oocyst components (Figure 11.4), based on the reported values it can be assumed that the parasites are exposed to hyperosmotic conditions when suspended in buffer of physiological conductivity.

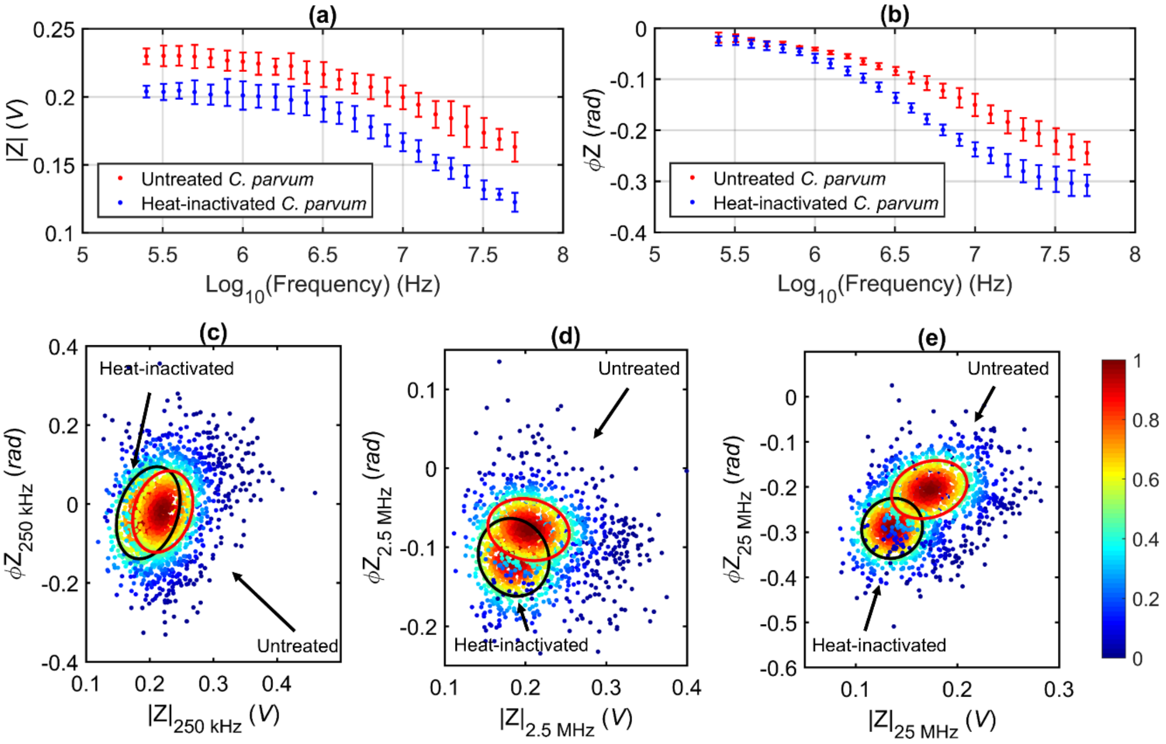

Figure 11.6: Impedance of *C. parvum* in PBS. **(a)** Impedance magnitude and **(b)** phase of untreated (red) and heat-inactivated (blue) *C. parvum* across the probe frequency range; data represents mean ± SD magnitude for all four *C. parvum* samples. The low, intermediate and high frequency impedance responses of untreated and heat-inactivated *C. parvum* are plotted together at **(c)** 250 kHz, **(d)** 2.5 MHz and **(e)** 25 MHz. The annotated confidence ellipses contain 50% of each population and the colour of each datapoint represents the normalized proximity of each event to the respective population mean. Untreated and heat-inactivated suspensions containing oocysts from all four stock samples were measured separately.

Generally, the *C. parvum* oocyst interior consists of four sporozoites – the infective agents of the oocyst – and a membrane-enclosed residual body. The residual body contains a large lipid body, numerous amylopectin granules, a crystalline protein inclusion, ribosomes and cytomembranes [11.27]. For HIP, the integrity and/ or composition of the internal fluid and interior organelles was presumably compromised, whereby conditions were less isosmotic than in the lower conductive buffer (σ_m = 0.76 S m^{-1}). Thus, a larger difference in the high frequency impedance responses of the parasite populations was measured in PBS (Figure 11.6). Due to the ability of the technology to probe different layers of the oocyst structure, impedance analysis enables clearer discrimination than flow cytometry – an equivalent, label-free method (Figure 11.7). The data in Fig 11.6a - b also indicates a shared impedance response, in terms of both magnitude and phase, regardless of strain or source of the *C. parvum* oocysts.

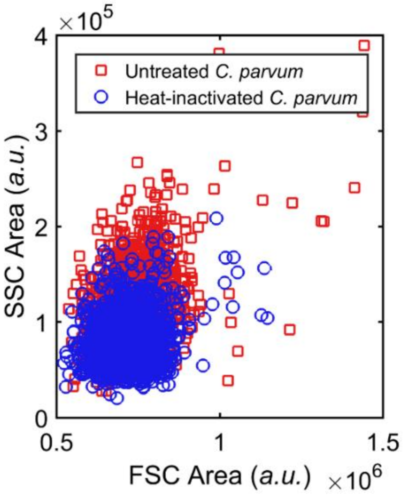

Figure 11.7: Conventional flow cytometry data (SSC *vs* FSC) for untreated and heat-inactivated *C. parvum* in PBS. Individual optical scatter data for viable or non-viable *C. parvum* are plotted together.

11.6 Discrimination of Untreated and Inactivated *C. parvum*

The suspension of oocyst populations in a high conductive, hyperosmotic buffer (5x PBS; σ_m = 7.10 S m^{-1}) gave rise to the largest difference in the impedance of UTP and HIP. Figure 11.8 shows the low, intermediate and high frequency impedance responses of the *C. parvum* populations in 5x PBS and demonstrates, again, that high frequency impedance measurement enabled improved discrimination of the parasite populations. The annotated confidence ellipses contain approximately 50% of the UTP or HIP populations and the colour of each data point indicates the normalized proximity of an event to the population mean – UTP and HIP samples were measured separately. The green line indicates the line of equal probability deviation between the populations (*i.e.*, where a detected event has equal chance of belonging to either population) and can be used when estimating confidence in the ability of the technology to discriminate between UTP and HIP. For example, at 50 MHz where the best result was achieved (Figure 11.8c), 91% of the events to the right of the equal probability deviation line were from the UTP sample and 92% of the events to the left were from the HIP sample. Thus, MIC enabled the identification of UTP or HIP with over 90% confidence in these experimental conditions. This capability would be useful for water utilities in, *e.g.*, a warning system which rapidly identifies single, viable, human-pathogenic *Cryptosporidium* oocysts in conjunction with EPA 1623.1 to reduce the requirement for skilled microscopists.

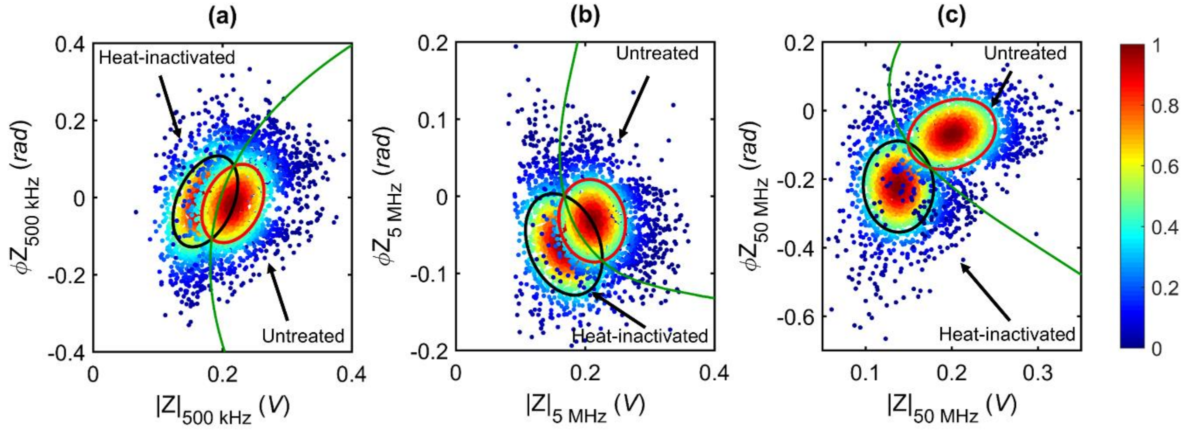

Figure 11.8: Frequency-dependent impedance response of *C. parvum* in 5x PBS. Low, intermediate and high frequency impedance data for untreated and heat-inactivated *C. parvum* are plotted together at **(a)** 500 kHz, **(b)** 5 MHz and **(c)** 50 MHz. Annotated confidence ellipses contain ~50% of untreated or heat-inactivated populations (1000 events plotted for each population). The green line indicates the regions of equal probability deviation between the two populations. The colour of each data point represents the normalized proximity of the event to the respective population mean.

Using the method described previously, the ability to accurately identify UTP or HIP from each individual sample was calculated when impedance was measured at a probe frequency of 50 MHz in 5x PBS. Table 11.1 shows the confidence values attained for the identification of each population – see section 10.6 for definition of sample abbreviations. Interestingly, UTP and HIP from the youngest sample (WC1) were identified with the greatest confidence, meanwhile oocyst populations from the oldest sample (MC) were identified with the least confidence. This finding may indicate that the presence of apparently viable oocysts (*i.e.*, still intact), but which were in fact non-viable and within the untreated sample, increased with sample age.

Table 11.1. Identification confidence for untreated or heat-inactivated *C. parvum* oocysts from samples of different age using electrical impedance data obtained at a frequency of 50 MHz in 5x PBS.

Sample	*Sample age (months)*	*Identification confidence (%)*	
		Untreated	*Heat-inactivated*
WC1	0-1	92	97
WM	1-2	91	92
WC2	1-2	92	92
MC	2-3	87	89

Notes: Sample abbreviations explained in section 10.6.

Population size limited to the first 500 detected oocysts (n = 500).

11.7 Species Analysis

The impedance of pathogens which are commonly isolated using EPA 1623.1 was measured to assess the suitability of MIC for the species- and genus-level discrimination of waterborne parasites. Specifically, samples containing *C. parvum* (CP), *C. muris* (CM) and *G. lamblia* (GL) suspended in PBS (σ_m = 1.61 S m^{-1}) were analysed. To properly gate and characterise the impedance properties of each population, samples were firstly measured independently - Figure 11.9. Using the cube root of the low frequency magnitude, which is proportional to particle diameter [11.15, 11.28], the average diameter of CP was approximated as 4.3 ± 0.3 µm, CM at 5.9 ± 0.4 µm and GL as 9.3 ± 0.4 µm, which correlates well with literature-reported dimensions [11.29, 11.30]. Additionally, using the ratio of pathogen to bead low frequency impedance magnitude and multiplying this by the known volume of our reference beads (180 fL), the average volume of CP was estimated as 42 ± 10 fL, CM as 107 ± 22 fL and GL as 410 ± 64 fL.

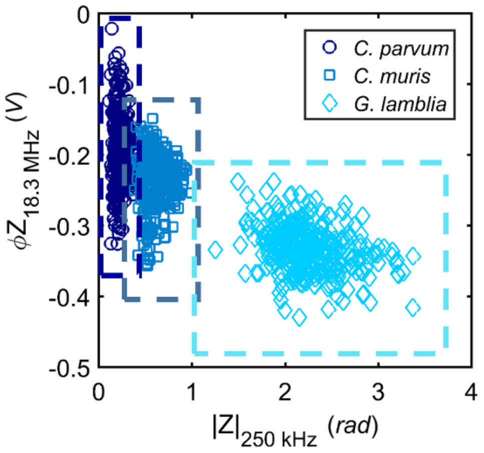

Figure 11.9: Low frequency magnitude (250 kHz) and high frequency phase data (18.3 MHz) for parasite suspensions. Impedance data for each population was measured independently but is plotted together – 1000 events are plotted. The gates (colour-coded, dashed lines) devised from independent sample analysis were used as a reference for future, mixed sample analysis.

Due to the differences in the dimensions of these pathogens [11.29, 11.30], plus detected variations in their internal structure/ composition, the plotting of low frequency magnitude (*e.g.*, 250 kHz) and high frequency phase (*e.g.*, 18.3 MHz) resulted in the largest difference between the populations. In Figure 11.10a, a total of 1000 data points are plotted that were obtained by measuring a mixed sample which contained all populations simultaneously. Using the gates that were devised upon independent analysis of each population, it was possible to discriminate CP with 98% confidence, CM with 93% confidence and GL with over 99% confidence based on the method described previously (section 11.6). Our findings suggest that impedance analysis allows the efficient discrimination of these pathogens, especially when compared to conventional flow cytometry (Figure 11.10b).

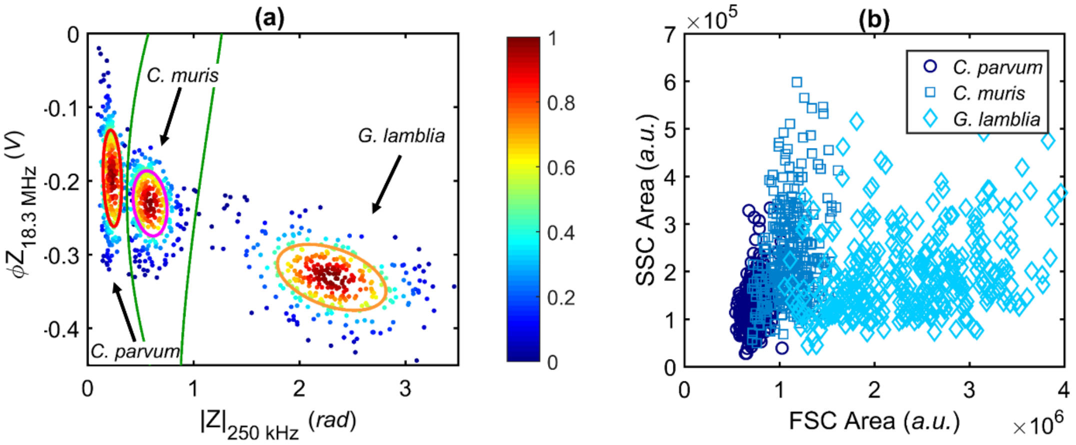

Figure 11.10: Label-free detection of waterborne parasites. **(a)** Impedance magnitude at 250 kHz *vs* phase at 18.3 MHz for all parasite species measured simultaneously in a mixed sample. Annotated confidence ellipses contain ~50% of each population. Green lines indicate regions of equal probability deviation between adjacent populations. The colour of each data point represents the normalized proximity of the event to the respective population mean. **(b)** Conventional flow cytometry data (SSC *vs* FSC) for all parasite species in PBS. Individual optical scatter data for each population plotted together. A total of 1000 events are plotted in both (a) and (b).

The species of *C. parvum* and *C. hominis* are estimated to be responsible for over 90% of human cases of cryptosporidiosis [11.31]. However, other species (*C. meleagridis*, *C. canis*, *C. cuniculus* and *C. felis*) have been associated with human infection, and although such cases are setting dependant, these species are also considered as “major human-pathogenic species” [11.29, 11.32]. In terms of oocyst dimensions, all of these “major” species show similarity and are typically reported as spheroidal oocysts within the range of 4.0-5.0 µm (minor axis) *x* 5.0-5.5 µm (major axis) [11.29]. Our results suggest that using MIC it may be possible to discriminate the major human-pathogenic species, with a high degree of certainty, from other species of *Cryptosporidium* that are not within this size range and which pose little or no risk to human health (as we have demonstrated with *C. parvum* and *C. muris*). Such species include (but not limited to) the larger *C. andersoni*, *C. baileyi* and *C. muris*, plus the smaller *C. xiaoi* and *C. ryanae* [11.29], which were all identified among the low-risk, contaminating species of UK drinking-water over a one-year period [11.9].

11.8 Conclusion and Outlook

In this Chapter, the impedance properties of *C. parvum* oocysts of varying source, strain and age were assessed, to identify that the presence of damaged/ excysted oocysts (termed shells) increased with environmental age. The impedance data of the oocyst and shell populations within each sample were fitted with single and double shell models to prove the natural existence of shells in each sample. Furthermore, this enabled the exclusion shell populations from the oocyst impedance data.

The findings of this Chapter also demonstrated that MIC can be a useful tool for the viability determination and species-level discrimination of *Cryptosporidium* oocysts. The data has shown that UTP and HIP can be identified with over 90% certainty using the high frequency impedance response in 5x PBS. This occurred because the ability to regulate ion transfer was lost upon loss of viability, resulting in an inward flux of ions, which ultimately enabled the efficient identification UTP or HIP in 5x PBS. In addition, single *C. parvum*, *C. muris* and *G. lamblia* (oo)cysts were identified with over 92% certainty using the low frequency magnitude *vs* high frequency phase response in PBS.

Immediate future work should be focused towards confirming that *C. parvum*, *C. muris* and *G. lamblia* can also be identified efficiently in 5x PBS. In PBS, these pathogens were discriminated using the low frequency impedance (250 kHz; a measure of oocyst volume) and the high frequency phase (18.3 MHz; a measure of the internal properties). If increasing buffer conductivity to 5x PBS then more charge will be present within the system. Therefore, the probe frequency signal should be increased to 40 – 50 MHz to penetrate the (oo)cyst structure and thus, facilitate the best possible identification of each pathogen.

For widespread use of this technique in water monitoring, this study should be extended to demonstrate that *Cryptosporidium* oocysts which have been inactivated by means other than heat-inactivation can be similarly discriminated from viable oocysts. Future work should also be extended to assessing the suitability of MIC for discriminating other species of *Cryptosporidium*, which pose/do not pose a significant risk to human health.

Given further validation with environmental samples, this technology could be implemented into the existing regulatory framework to enable rapid assessment of oocyst viability and thus provide a more accurate assessment of the risk posed to human health. For example, the existing detection method utilises immuno-magnetic separation (IMS) for parasite enrichment, giving a ~50 µL volume with recovered oocysts [11.2]. By increasing the conductivity of this product sample, it should be possible to discern between UTP and HIP using MIC. The MIC system could operate at an increased flow rate [11.28] of 80 µL min^{-1}, therefore it would be possible to process a sample in much less than an hour. Finally, it is also possible to view results in real-time, which would allow water utilities to rapidly identify potentially hazardous drinking-water.

11.9 Author Contributions

The following authors contributed to the completion of this work: John McGrath (JM), Carlos Honrado (CH), Dr. Daniel Spencer (DC), Ben Horton (BH), Dr. Helen Bridle (HB) and Prof. Hywel Morgan (HM). JM and HB are based at Heriot-Watt University (UK). CH, DC and HM are based at the University of Southampton (UK). BH is an employee of Moredun Scientific (UK). In order of contribution level, the following aspects of this work were completed by:

1. Designed and fabricated the system: DC HM
2. Conceived and designed the experiments: JM DC CH HM
3. Performed the experiments: JM CH BH
4. Analysed the data: JM CH DC
5. Contributed reagents/ materials/ analysis tools: HM HB
6. Wrote up results: JM CH DC HM HB

11.10 References

11.1. USEPA. Method 1623.1: C*ryptosporidium* and Gia*rdia in* Water by Filtration/IMS/FA: United States Environmental Protection Agency; 2012.

11.2. Bridle H, Kersaudy-Kerhoas M, Miller B, Gavriilidou D, Katzer F, Innes EA, et al. Detection of *Cryptosporidium* in miniaturised fluidic devices. water research. 2012;46(6):1641-61.

11.3. Scottish Water. Annual Water Quality Report 2013. 2013.

11.4. Environment and Heritage Service. Guidance for the Monitoring of *Cryptosporidium* in Treated Water Supplies in Northern Ireland. 2003.

11.5. Su Y-H, Tsegaye M, Varhue W, Liao K-T, Abebe LS, Smith JA, et al. Quantitative dielectrophoretic tracking for characterization and separation of persistent subpopulations of Cryptosporidium parvum. Analyst. 2014;139(1):66-73.

11.6. Quinn C, Archer G, Betts W, O'Neill J. Dose-dependent dielectrophoretic response of Cryptosporidium oocysts treated with ozone. Letters in applied microbiology. 1996;22(3):224-8.

11.7. Goater AD, Burt JP, Pethig R. A combined travelling wave dielectrophoresis and electrorotation device: applied to the concentration and viability determination of Cryptosporidium. Journal of Physics D-Applied Physics. 1997;30(18):L65.

11.8. Dalton C, Goater A, Burt J, Smith H. Analysis of parasites by electrorotation. Journal of Applied Microbiology. 2004;96(1):24-32.

11.9. Nichols R, Connelly L, Sullivan C, Smith H. Identification of Cryptosporidium species and genotypes in Scottish raw and drinking waters during a one-year monitoring period. Applied and environmental microbiology. 2010;76(17):5977-86.

11.10. Unni HN, Hartono D, Yung LYL, Ng MM-L, Lee HP, Khoo BC, et al. Characterization and separation of Cryptosporidium and Giardia cells using on-chip dielectrophoresis. Biomicrofluidics. 2012;6:012805.

11.11. Houssin T, Follet J, Follet A, Dei-Cas E, Senez V. Label-free analysis of water-polluting parasite by electrochemical impedance spectroscopy. Biosensors and bioelectronics. 2010;25(5):1122-9.

11.12. Smith HV, Nichols RAB. Cryptosporidium: Detection in water and food. Experimental Parasitology. 2010;124(1):61-79.

11.13. Bridge JW, Oliver DM, Chadwick D, Godfray HCJ, Heathwaite AL, Kay D, et al. Engaging with the water sector for public health benefits: waterborne pathogens and diseases in developed countries. Bulletin of the world Health Organization. 2010;88(11):873-5.

11.14. Schwan H, editor Electrical properties of tissues and cell suspensions: mechanisms and models. Engineering in Medicine and Biology Society, 1994 Engineering Advances: New Opportunities for Biomedical Engineers Proceedings of the 16th Annual International Conference of the IEEE; 1994: IEEE.

11.15. Spencer D, Hollis V, Morgan H. Microfluidic impedance cytometry of tumour cells in blood. Biomicrofluidics. 2014;8(6):064124.

11.16. Sun T, Morgan H. Single-cell microfluidic impedance cytometry: a review. Microfluidics and Nanofluidics. 2010;8(4):423-43.

11.17. Crowley JM. Electrical breakdown of bimolecular lipid membranes as an electromechanical instability. Biophysical journal. 1973;13(7):711.

11.18. Shafiee H, Sano MB, Henslee EA, Caldwell JL, Davalos RV. Selective isolation of live/dead cells using contactless dielectrophoresis (cDEP). Lab on a Chip. 2010;10(4):438-45.

11.19. Song H, Wang Y, Rosano JM, Prabhakarpandian B, Garson C, Pant K, et al. A microfluidic impedance flow cytometer for identification of differentiation state of stem cells. Lab on a Chip. 2013;13(12):2300-10.

11.20. Environment Agency. The Microbiology of Drinking Water (2010) - Part 14 - Methods for the isolation, identification and enumeration of Cryptosporidium oocysts and Giardia cysts. Methods for the Examination of Waters and Associated Materials; 2010.

11.21. Kostrzynska M, Sankey M, Haack E, Power C, Aldom J, Chagla A, et al. Three sample preparation protocols for polymerase chain reaction based detection of Cryptosporidium parvum in environmental samples. Journal of microbiological methods. 1999;35(1):65-71.

11.22. Maxwell JC. A treatise on electricity and magnetism: Clarendon press; 1881.

11.23. Morgan H, Green NG. AC Electrokinetics: Colloids and Nanoparticles: Research Studies Press; 2003.

11.24. Miller RD, Jones TB. Electro-orientation of ellipsoidal erythrocytes. Theory and experiment. Biophysical journal. 1993;64(5):1588.

11.25. Sun T, Green NG, Gawad S, Morgan H. Analytical electric field and sensitivity analysis for two microfluidic impedance cytometer designs. Iet Nanobiotechnology. 2007;1(5):69-79.

11.26. Debye P, Falkenhagen H. Dispersion of the Conductivity and Dielectric Constants of Strong Electrolytes, Phys: Z; 1928.

11.27. Fayer R, Xiao L. Cryptosporidium and Cryptosporidiosis, Second Edition: Taylor & Francis; 2012.

11.28. Spencer D, Elliott G, Morgan H. A sheath-less combined optical and impedance micro-cytometer. Lab on a Chip. 2014;14(16):3064-73.

11.29. Chalmers RM, Katzer F. Looking for Cryptosporidium: the application of advances in detection and diagnosis. Trends in Parasitology. 2013;29(5):237-51.

11.30. LeChevallier MW, Norton WD, Lee RG. Occurrence of Giardia and Cryptosporidium spp. in surface water supplies. Applied and Environmental Microbiology. 1991;57(9):2610-6.

11.31. Bouzid M, Hunter PR, Chalmers RM, Tyler KM. Cryptosporidium Pathogenicity and Virulence. Clinical Microbiology Reviews. 2013;26(1):115-34.

11.32. Fratamico P, Liu Y, Kathariou S. Genomes of Foodborne and Waterborne Pathogens: American Society of Microbiology; 2011.

Chapter 12 – Conclusions and Future Work

12.1 Introduction

In this chapter, I will summarise the findings of the whole research project with regards to the objectives set out in section 1.2 and make conclusions about the success of each approach used. The reader should return to the individual results chapters (*i.e.*, Chapters 7, 9 and 11) where conclusions were made concerning, *e.g.*, the specific experimental conditions of each approach which enabled the best results. Subsequently, I will recommend the ideal plan of future work that I would seek to undertake, based on the understanding gained throughout the course of this research, given sufficient time and resources. Again, the reader should revisit the individual results chapters for a more detailed outline of the recommended future work concerning each of the used, individual approaches.

The aim of this research project (Chapter 1) was to utilise microfluidics for the rapid, label-free sorting/ discrimination and detection of viable, human-pathogenic *Cryptosporidium* oocysts from non-viable and/ or non-human pathogenic *Cryptosporidium* oocysts (Chapter 2). Due to the size of the field of microfluidics, a variety of passive and/ or active sorting and/ or detection approaches could have been employed to meet the aims of the project (Chapter 3).

12.2 Microfluidic-enabled Force Spectroscopy

Using microfluidic-enabled force spectroscopy (MeFS; Chapter 5), a type of high-resolution scanning force microscopy in which the mechanical probe (or cantilever) can have syringe- or pipette-like function, we assessed whether passive microfluidic sorting systems could be used to satisfy the research aims (Chapter 6 and 7). Although the typical sizes of different *Cryptosporidium* species are reported in the literature (see Table 2.2), little is known about intra-species size variation. Furthermore, there are only a few articles in the literature which assess the deformability of *Cryptosporidium* oocysts (12.1-12.5) and the population sizes used by such researchers were generally too small to make reliable conclusions about oocyst deformability specifically.

Upon MeFS-based characterisation of the biomechanical properties (*i.e.,* size and deformability) of *Cryptosporidium* oocysts of different viability status and species, it was identified that size and/ or deformability distributions of live and temperature-inactivated (*i.e.*, heat- or freeze-inactivated oocysts) were overlapping. In addition, the size and deformability distributions of *C. parvum* (human-pathogenic) and *C. muris* (non-human pathogenic), while apparently different, also exhibited some overlap. Furthermore, it was identified that *C. muris* was larger and more deformable than *C. parvum*. The implications of this finding are that if using microfluidics which can potentially utilise size and deformability to sort particles, *e.g.*, deterministic lateral displacement (DLD) devices, *C. muris* would probably begin to deform under hydrodynamic force before *C. parvum*. Consequently, *C. muris* would effectively become smaller and the separation of *C. muris* and *C. parvum* would become even less efficient. Therefore, it was concluded that the passive, size- and/ or deformability-based microfluidics would not be developed for viability-based or species-based sorting of *Cryptosporidium*. On the other hand, MeFS could be used, instead of passive sorting microfluidics, by water utilities to more efficiently (but not completely) discriminate these populations. Given that less than 100 oocysts are typically recovered from a contaminated drinking-water sample in the UK using USEPA 1623.1 (12.6), MeFS could be used to analyse the biomechanical properties of all recovered oocysts in under two hours. The automation of the oocyst detection, immobilisation, measurement and data analysis procedures would make this method more attractive to water utilities. Nonetheless, this method does not satisfy all of the research objectives, as it is not a continuous-flow microfluidic technique, rather an AFM-based method with microfluidic capabilities.

12.3 Dielectrophoresis

Microfluidic sorting techniques which utilise active forces for particle separation were then sought to perform viability- and/ or species-based sorting of *Cryptosporidium*. Specifically, dielectrophoresis (DEP) – an AC electrokinetic-based sorting technique (Chapter 4) – was used because, firstly, several researchers have shown a difference in the dielectric responses of viable and non-viable *C. parvum* (12.7, 12.8). Secondly, the governing electrical forces which upon particles in DEP devices are influenced by particle size/ volume (12.9), thus, DEP could potentially perform both viability-based and species-based sorting.

In a low conductive electrolyte, viable and non-viable *C. parvum* were sorted in a DEP device (Chapter 8) based on differences in their dielectric properties at a signal frequency of 30 MHz (Chapter 9). Specifically, it was possible to sort untreated *C. parvum* with from heat-inactivated *C. parvum* with over 80% confidence. Despite this, the optimal sample flow rate was 12 µL hr^{-1}, which means that it would take 5 hours to process the ~50 µL product volume of USEPA 1623.1 in a single device. Device parallelisation would be required to reduce the sorting time and thus make the system more attractive to water utilities.

It was not possible to investigate DEP-based sorting of different *Cryptosporidium* species because, within the last few months of my studentship, the only known supplier of parasite suspensions of non/ minor risk human-pathogenic species required a 3-4 month lead time to propagate oocysts. Therefore, the DEP behaviour of more *Cryptosporidium* species should be analysed in future.

12.4 Microfluidic Impedance Cytometry

Microfluidic Impedance Cytometry (MIC) is an AC electrokinetics-based particle detection technology (Chapter 4) which enables the discrimination of suspended, single particles based on differences detected in their complex electric impedance responses to an AC field. Using this technology, untreated and heat-inactivated *C. parvum* oocysts were each identified with over 90% confidence (Chapters 10 and 11). Given that this finding was calculated based on impedance analysis of four *C. parvum* samples which differed in their age and/ or strain and/ or source, this is perhaps the most significant result of all detailed in this thesis. In addition, using MIC it was possible to identify oocysts of *C. parvum*, *C. muris* and *G. lamblia* (a protozoan pathogen which is also detected using the USEPA 1623.1 protocol) with over 90% confidence. As MIC is label-free, capable of high-throughput (flow rates of 40 $\mu L\ min^{-1}$ were used here) and requires minimal sample processing, this method is better equipped than DEP or MeFS to satisfy the objectives of this project.

12.5 Future Work

In the interests of satisfying the research objectives, publication of novel material and commercial output, I recommend that MIC technology is used in any follow-up studies that commence as a result of the findings detailed in this thesis. I believe that focus should initially be directed towards using existing technology to analyse *C. parvum* oocysts which have been inactivated using different treatments (*i.e.*, UV-, ozone-, freeze- and natural inactivation). Furthermore, the impedance properties of different species should be analysed using existing technology to validate/ verify that MIC can be used to discriminate between different species which vary in the level of risk that they pose to human health. A limiting factor however may be the ready availability of parasite suspensions. For example, to my knowledge it is only possible to source oocysts of *C. parvum*, *C. hominis*, *C. meleagridis*, *C. muris* and *C. bovis* from suppliers worldwide. Furthermore, it can often cost as much as $3750 dollars for a single sample (of *C. meleagridis* or *C. hominis* in this instance) at a concentration of 1×10^7 oocysts (Dr. Don Girouard, Division of Infectious Diseases, Tufts University, Arizona, personal communication, 31st August 2015).

In the long-term, I recommend that future work should be focused towards the development of an impedance-activated cell sorter which discriminates but also sorts (*i.e.*, like a FACS system) particles based on their impedance properties. For example, impedance detection could be coupled with a downstream sorting function to efficiently sort *Cryptosporidium* populations – *e.g.*, dielectrophoresis or acoustophoresis could be used to complete this function. Such a technology would likely be very useful to water utilities and would thus would potentially have significant commercial output. The technology could then also be used in many other cell discrimination/ sorting applications.

12.6 References

12.1. Considine RF, Drummond CJ, Dixon DR. Force of interaction between a biocolloid and an inorganic oxide: complexity of surface deformation, roughness, and brushlike behavior. Langmuir. 2001;17(20):6325-35.

12.2. Considine RF, Dixon DR, Drummond CJ. Oocysts of Cryptosporidium parvum and model sand surfaces in aqueous solutions: an atomic force microscope (AFM) study. Water Research. 2002;36(14):3421-8.

12.3. Tufenkji N, Dixon DR, Considine R, Drummond CJ. Multi-scale Cryptosporidium/sand interactions in water treatment. Water research. 2006;40(18):3315-31.

12.4. Byrd T, Walz J. Interaction force profiles between Cryptosporidium parvum oocysts and silica surfaces. Environmental science & technology. 2005;39(24):9574-82.

12.5. Byrd T, Walz J. Investigation of the interaction force between Cryptosporidium parvum oocysts and solid surfaces. Langmuir. 2007;23(14):7475-83.

12.6. Nichols R, Connelly L, Sullivan C, Smith H. Identification of Cryptosporidium species and genotypes in Scottish raw and drinking waters during a one-year monitoring period. Applied and environmental microbiology. 2010;76(17):5977-86.

12.7. Goater AD, Burt JP, Pethig R. A combined travelling wave dielectrophoresis and electrorotation device: applied to the concentration and viability determination of Cryptosporidium. Journal of Physics D-Applied Physics. 1997;30(18):L65.

12.8. Su Y-H, Tsegaye M, Varhue W, Liao K-T, Abebe LS, Smith JA, et al. Quantitative dielectrophoretic tracking for characterization and separation of persistent subpopulations of Cryptosporidium parvum. Analyst. 2014;139(1):66-73.

12.9. Pethig R. Review Article—Dielectrophoresis: Status of the theory, technology, and applications. Biomicrofluidics. 2010;4:022811.